



**MONASH** University

## **Chemical Diversity in Mid-Ocean Ridge Basalts**

**A geochemical excursion to the ultraslow – spreading Gakkel Ridge,  
Arctic Ocean**

by

**Marianne Richter**

(Diplom Geologist)

A thesis submitted for the degree of *Doctor of Philosophy* at

Monash University in 2019

School of Earth, Atmosphere and Environment, Faculty of Science



## **Copyright**

© *Marianne Richter* 2019

I certify that I have made all reasonable efforts to secure copyright permissions for third-party content included in this thesis and have not knowingly added copyright content to my work without the owner's permission.

## Abstract

Mid-ocean ridges extend over 55,000 km and produce mid-ocean ridge basalts (MORBs) that cover two-thirds of the Earth's crust. MORBs are partial melting products of the Earth's upper mantle and therefore carry information about their inaccessible source. Observed chemical variety in the basalts is interpreted to result of multiple processes that affect the basalt from its origin in the mantle to the oceanic crust. These include heterogeneities in the mantle composition, fractional crystallization or melt-rock interaction during magma ascent, but the exact contribution of each to the observed geochemical diversity in MORBs remains unclear.

This thesis aims to understand the chemical evolution of MORBs focussing on the early stages of magma formation in heterogeneous sources and magmatic differentiation. The ultraslow-spreading Gakkel Ridge has been selected as study area due to its unusual and geochemically diverse underlying mantle and its along-ridge variations in magmatic activity, crustal thickness, spreading rate and isotopic signature. Here, I present chemical (including platinum group elements) and radiogenic/stable isotope data of thirty six fresh basalts dredged from three distinct areas, the Western Volcanic Zone (WVZ), the Sparsely Magmatic Zone (SMZ) and the Eastern Volcanic Zone (EVZ).

Trace element and radiogenic isotope data indicate that the mantle beneath the Gakkel Ridge experienced two metasomatic enrichment events. The younger event is recorded in basalts from the Western Gakkel Ridge region, comprised of the WVZ and the SMZ, and is proposed to be linked to a fossil subduction zone that occurred in the area at ca. 140 - 125 Ma. The older enrichment event, however, is only recorded in basalts from the Eastern Gakkel Ridge region (includes solely the EVZ) and of unknown origin. These enriched mantle domains affect the geochemistry of the MORBs positively as shown by stable Fe isotope systematics (expressed as  $\delta^{57}\text{Fe}$ ). Iron isotope systematics further indicate the existence of two different magma evolution patterns at the Gakkel Ridge. Basalts from the EVZ and the SMZ ascend rapidly from the source to the crust with little fractionation, whereas basalts from the WVZ experienced a stronger fractionation, which is explained by melt transport through a magma chamber *en route* to the surface, in which replenishment, magma mixing and crystallisation occurs. Furthermore, unlike to previous expectations, platinum group element data suggests directly ascending magmas of the SMZ and the EVZ are sulfide undersaturated, while the fractionated WVZ magmas are sulfide saturated.

## **Declaration**

This thesis contains no material which has been accepted for the award of any other degree or diploma at any university or equivalent institution and that, to the best of my knowledge and belief, this thesis contains no material previously published or written by another person, except where due reference is made in the text of the thesis.

Signature:

Print Name: Marianne Richter

Date: 29/03/2019

## Thesis including published works declaration

I hereby declare that this thesis contains no material which has been accepted for the award of any other degree or diploma at any university or equivalent institution and that, to the best of my knowledge and belief, this thesis contains no material previously published or written by another person, except where due reference is made in the text of the thesis.

This thesis includes one submitted publication that is currently under review and three chapters formatted as papers that are not submitted yet. The core theme of the thesis is the investigation of the chemical diversity of ocean floor lavas based on basalts from the Gakkel Ridge in the Arctic Ocean. The ideas, development and writing up of all the papers in the thesis were the principal responsibility of myself, the student, working within the School of Earth, Atmosphere and Environment under the supervision of A/Prof. Dr. Oliver Nebel and A/Prof. Dr. Andrew Tomkins.

The inclusion of co-authors reflects the fact that the work came from active collaboration between researchers and acknowledges input into team-based research. This study is heavily laboratory-based, which is reflected by the contribution (2 - 5%) of some-authors. The co-authors helped with experimental (clean-lab) and instrumental set-up. The analytical work for chapter 6 has been done by external collaborators, resulting in a 5% contribution.

In the case of 4 chapters my contribution to the work involved the following:

Thesis Chapter	Publication Title	Status (published, in press, accepted or returned for revision, submitted)	Nature and % of student contribution	Co-author name(s) Nature and % of Co-author's contribution*	Co-author(s), Monash student Y/N*
Chapter 3	<i>A fossil subduction zone under the western Gakkel Ridge region, Arctic</i>	<i>Submitted, under review</i>	<i>71%. Concept and collecting data and writing first draft</i>	<i>1) Oliver Nebel, supervisory role 15%</i> <i>2) Roland Maas, Data analysis, input into manuscript 5%</i> <i>3) Yona Nebel-Jacobsen, Data analysis, input into manuscript 5%</i> <i>4) Henry J.B. Dick, providing samples, input into manuscript 2%</i> <i>5) Fabio A. Capitanio, geodynamics and editing, input into manuscript 2%</i>	<i>1) No</i> <i>2) No</i> <i>3) No</i> <i>4) No</i> <i>5) No</i>

Thesis including published works declaration

Chapter 4	<i>Elucidating the peculiar DupAl isotope signatures of Arctic mid-ocean ridge basalts</i>	<i>Not submitted</i>	<i>78%. Concept and collecting data and writing first draft</i>	<p>1) <i>Oliver Nebel, supervisory role 10%</i></p> <p>2) <i>Roland Maas, Data analysis, input into manuscript 5%</i></p> <p>3) <i>Yona Nebel-Jacobsen, Data analysis, input into manuscript 5%</i></p> <p>4) <i>Henry J.B. Dick, providing samples, input into manuscript 2%</i></p>	<p>1) <i>No</i></p> <p>2) <i>No</i></p> <p>3) <i>No</i></p> <p>4) <i>No</i></p>
Chapter 5	<i>The effect of spreading rate and source heterogeneity on iron isotope variability in ocean floor lavas at the ultra-slow spreading Gakkel Ridge, Arctic Ocean</i>	<i>Not submitted</i>	<i>83%. Concept and collecting data and writing first draft</i>	<p>1) <i>Oliver Nebel, supervisory role 10%</i></p> <p>2) <i>Yona Nebel-Jacobsen, Data analysis, input into manuscript 5%</i></p> <p>3) <i>Henry J.B. Dick, providing samples 2%</i></p>	<p>1) <i>No</i></p> <p>2) <i>No</i></p> <p>3) <i>No</i></p>
Chapter 6	<i>Sulfide undersaturated melts at the ultraslow-spreading Gakkel Ridge, Arctic Ocean</i>	<i>Not submitted</i>	<i>74%. Concept and collecting data and writing first draft</i>	<p>1) <i>Oliver Nebel, supervisory role 10%</i></p> <p>2) <i>Jung-Woo Park, Data analysis, input into manuscript 5%</i></p> <p>3) <i>James Dottin III., Data analysis, input into manuscript 5%</i></p> <p>4) <i>Andrew G. Tomkins, input into manuscript 2%,</i></p> <p>5) <i>Henry J.B. Dick, providing samples, input into manuscript 2%</i></p> <p>6) <i>James Farquhar, input into manuscript 2%</i></p>	<p>1) <i>No</i></p> <p>2) <i>No</i></p> <p>3) <i>No</i></p> <p>4) <i>No</i></p> <p>5) <i>No</i></p> <p>6) <i>No</i></p>

## Thesis including published works declaration

---

I have renumbered sections of submitted or published papers in order to generate a consistent presentation within the thesis.

**Student signature:** MARIANNE RICHTER      **Date:** 29/03/2019

The undersigned hereby certify that the above declaration correctly reflects the nature and extent of the student's and co-authors' contributions to this work. In instances where I am not the responsible author I have consulted with the responsible author to agree on the respective contributions of the authors.

**Main Supervisor signature:** OLIVER NEBEL      **Date:** 29/03/2019

### Acknowledgements

Wohooo, finally it's time to write the most important and exciting chapter of my thesis – the acknowledgements. I assume everyone is reading this 'chapter', because it's the first thing I would read. Therefore, just in advance, if you find any mistakes, keep them! They are yours! Get ready, get a coffee, sit down, enjoy and smile.

Let's get started....

First of all, I would like to thank my supervisor A/Prof. Dr. Oliver Ne(d)bel(n) (yes – it's really hard to spell your last name right) and my favourite Italian lab technician Massimo Raveggi. Without Massimo, who was asking me several times if I want to do a PhD, and Oliver giving me the opportunity, I would have never experienced the joys and falls of a PhD. I am extremely grateful for that, because I learned so many things over the past 3.5 – 4 years. Thank you Oliver, for always believing in me even though I was doubting myself quite often. It was a great pleasure and a lot of fun to work with you! I will always remember these times. Also thanks for being such a great friend/mentor/supervisor! Most importantly, I learned a few new German sayings. Actually, there is only one that I remember, because you said it most of the time when I knocked on your office door to ask you 'stupid' clean lab question. I didn't count how many, but you were sewing yourself quite a lot of buttons to your cheek to hang a piano there. Seems funny to me, but you probably would say '*isn't it fantastic*' (pronunciation on faaantastic)! I hope you (dor Isodob'm Äggsbärde) won't forget my great jokes 'HeHe'.

Furthermore, I'd like to thank Roland Maas. You've been setting me up in the clean lab in the beginning of my PhD, helped me to separate Pb from my precious samples and you pushed me a little bit towards my personal PhD goals. I remember our conversation in the first 6 month of my candidature, you asked me what I want to do in my PhD and I said I would like to understand 'mantle heterogeneity'. Actually, I didn't know that until I said it out loud.

Yona Nebel-Jacobsen - thank you for dragging me out of the office to play Doko (Doppelkopf – a german card game for those who don't know) most Tuesdays, to be my HIIT partner and running partner in Marysville, Great Ocean Road, Studley Park and at the Monash Campus. I also have to mention the horrific Roller Coaster Run at Mt. Dandenong – It was a great, but a tough run. Actually, I should not just mention the fun things besides my PhD. Thanks for your help in the clean lab and mass spec lab! I remember sitting with you on a Friday evening until 9 pm (which is early to finish a measurement, as I found out later) at the Neptune to get some of my first isotope data and one of the first data of the Isotopia lab, while everyone else celebrated the beginning of the weekend.

I would also like to thank Peter Cawood for listening to my Progress Review on a Sunday afternoon and giving me some helpful comments. Thank you to Wolfgang Bach and Elmar Albers for providing me samples from the Gakkal Ridge. Thanks to Henry Dick for providing me the samples from the Gakkal Ridge and thank you that I could stay at your place, while I was collecting the precious samples at WHOI. Thanks to Andy Tomkins for brief chats about my data and ideas. Thanks also to Fabio A. Capitano for brief chats about geodynamics. Thanks to Jung-Woo Park for analysing the PGE of my sample suite. Thank you to James Farquhar for agreeing

## Acknowledgements

---

to run S-Isotopes on my sample suite in your lab and thanks to James Dottin III for doing all the tedious lab work. Thank you Junnel Alegado for using your equipment in the thin section lab to speed up my thin section production (96! in total and I haven't even touched one for this thesis). Also thanks to Jim Driscoll and Julie Boyce for taking me on-board of the Outreach team. It was a great opportunity and I loved teaching kids/students about geo topics. It always helped me to simplify complex research findings and express ideas a little bit better. Also thanks to the admin team that works behind the scenes (Emily Tran, Katie Tran, Caroline Venn, Silvana Katragadda, Ada Han, Robert Oakleigh and Yhuzou Lin).

I would also thank my office mates (Rm 245). Andrea Rielli, thanks for all the laughter in the office during the first half of my PhD. I really missed those times in the second half of my PhD. Thanks also to Pablo Farias, Nathan Gardiner, Saskia Ruttor and Prassanna Gunnawardana for sharing an office and doing the 8 week office-exercise plan that I came up with while I was training for my longest run (23km) so far. I had a great time with all of you! Pablo, I was very happy that you moved into my office, after I was trying to convince you for 6 months. Thanks for all the great chats about life and listening to me whenever I had my moments of craziness. Never forget: Be strong, be wyld! To all of my office mates: Lime Gorillazz forever! "Wir sind die coolesten, wenn wir cruisen, wenn wir übern Monash Campus cruisen" (Lyrics changed from Massive Töne). Saskia can translate it for you guys.

Also, thanks to my Tuesday-Doko-crew Johanna Schick, Sonja Neske and Mathias 'Matze' Zeller. You always put a smile on my face, when I had a bad Tuesday. Even though I rarely won. I am probably the worst Doko player. Thanks to the Hillbillies Joel and Anung Samsu, for sharing a house in 'the sticks' and taking me back into running. Even though I am not a fast runner, I really enjoy running on trails! One day, I might sign up for an ultra-marathon. But only for 60 km. At the moment, I am not that crazy enough to run 100 km.

Also thanks to Lauren Wolfram, Jackson van den Hove, Emily Finch, Mathias & Katrin 'Schnatterinchen' Eglseder, Steph Mills, Roland Seubert, Ben Mather, Ruby Smith, Jack Simmons, Tephy Marillo-Sialer, Stefan Vollgger, Shannon Herely, Jonas Köpping (he is a great detective – you can hire him), Adriana Traviati, Lynn Wu, Megan Withers, Lachlan Grose, Sam Thiele, Dan Uehara, Agi Kiraly, Zachary Sudholz, Nicholas Gardiner and Elle Nebel for all the fun times during my PhD such as surfing, doing crafts, sailing, running, cycling, hiking, having BBQ's or picnics in the Botanical garden, having beverages at various places in the city or at home, having great dinners and further more. Special thanks to Ben Knight for all the coffee's from various places on campus, for always listening to me and for partially proof-reading my book of thoughts (aka PhD thesis). Thanks also to Julia Sen for all the great talks and your trust. Thanks to everyone, who I met during my journey!

I also would like to thank my family (Jana, Rainer, Martin, Lissy, Moritz, Lotte and Monika) and all my friends back home. Whenever I came home for a visit you always welcomed me and put me back on track. I am so glad to have such a good family and friends in my life. Also thanks to Marina Veter for doing a PhD in Sydney. It's great to have you in the same time zone and on the same continent.

## Acknowledgements

---

Last but not least, thank you to one of the most important person in my life – Martin. Thank you for accepting the journey to move to Australia. The first 1.5 year weren't easy for both of us. But hey, we both finished our PhD's and were motivating each other throughout the journey. I'm looking forward to see what the future brings and hope to explore a few more countries with you before settling down in our home country.

Thanks to everyone for reading the two pages. I hope your coffee/tea is still drinkable and you found what you wanted to find.

You're off the hook now.

Enjoy reading my thesis!



## Table of Contents

<b>Copyright</b> .....	<b>i</b>
<b>Abstract</b> .....	<b>ii</b>
<b>Declaration</b> .....	<b>iii</b>
<b>Thesis including published works declaration</b> .....	<b>iv</b>
<b>Acknowledgements</b> .....	<b>vii</b>
<b>Table of Contents</b> .....	<b>xi</b>
<b>List of Figures</b> .....	<b>xv</b>
<b>List of Tables</b> .....	<b>xvii</b>

### ***CHAPTER 1 - Introduction***..... **3**

1.1 Rationale .....	5
1.2 Ultraslow-spreading Gakkel Ridge, Arctic Ocean.....	8
1.2.1 Western Volcanic Zone (WVZ).....	9
1.2.2 Sparsley Magmatic Zone (SMZ) .....	9
1.2.3 Eastern Volcanic Zone (EVZ) .....	10
1.3 Indian-type mantle signature (DupAl anomaly) .....	10
1.4 Methodology .....	12
1.5 Thesis structure .....	13
1.5.1 Brief chapter description.....	14
1.6 References.....	17

### ***CHAPTER 2 - Samples and Methodology***..... **21**

2.1 Introduction.....	23
2.2 Samples .....	23
2.2.1 Sample preparation .....	23
2.3 Methodology .....	29
2.3.1 Major element and alteration .....	29
2.3.1.1 Alteration .....	30
2.3.2 Trace element.....	31
2.3.3 Comparison between whole-rock XRF glasses and volcanic glass shards .....	32
2.3.4 Comparison between LA-ICP-MS and X-ray fluorescence spectroscopy (XRF)/Electron Microprobe analyser (EMPA) .....	34
2.3.5 Platinum Group Elements (PGE).....	35
2.3.6 Isotope analysis.....	35

## Table of Contents

---

2.3.6.1 Fe isotopes .....	36
2.3.6.2 Hf isotopes .....	36
2.3.6.3 Sr isotopes .....	37
2.3.6.4 Pb isotopes .....	38
2.3.6.4 S isotopes .....	39
2.4 References .....	39
<b>CHAPTER 3 - A fossil subduction zone under the Western Gakkel Ridge region, Arctic Ocean..... 41</b>	
Abstract .....	43
3.1 Introduction.....	45
3.2 Results.....	46
3.3 Discussion.....	48
3.3.1 Ghost of a past subduction .....	48
3.3.2 Remnants of subducting slab mélanges.....	49
3.4 Conclusion .....	52
3.5 References.....	52
3.6 Methods .....	54
3.6.1 Samples.....	54
3.6.2 Major elements .....	54
3.6.3 Trace elements .....	55
3.6.4 Sr and Pb isotope ratios .....	55
3.7 Supplementary Information .....	56
3.8 Acknowledgements.....	56
Supplementary Information .....	57
SI - $\Delta\text{Th}/\text{Yb}$ and $\Delta 8^{*}/6^{*}$ calculations.....	59
SI - References.....	64
Supplementary Data Tables .....	65
<b>CHAPTER 4 - Elucidating the peculiar <i>DupAl</i> isotope signatures of Arctic mid-ocean ridge basalts ..... 73</b>	
Abstract .....	75
4.1 Introduction.....	77
4.1.1 Gakkel Ridge basalt and mantle source heterogeneity .....	77
4.2 Results.....	78

## Table of Contents

---

4.3 Discussion.....	82
4.3.1 Locus and isotopic nature of the mantle boundary .....	82
4.3.2 Implications for DupAl mantle in the Arctic and elsewhere .....	83
4.4 Conclusion .....	85
4.6 References.....	85
4.6 Supplementary Information .....	87
4.7 Acknowledgements.....	87
Supplementary Information .....	89
SI - Methods.....	91
SI - References.....	95
Supplementary Data Tables .....	97
<b><i>CHAPTER 5 - The effect of spreading rate and source heterogeneity on iron isotope variability in ocean floor lavas at the ultra-slow spreading Gakkel Ridge, Arctic Ocean.....</i></b>	
Abstract .....	105
5.1 Introduction.....	107
5.2 Methods.....	109
5.3 Results.....	111
5.3.1 Major element and trace elements .....	111
5.3.2 Iron isotopes .....	112
5.4 Discussion.....	114
5.4.1 The effect of fractional crystallisation on Fe isotope composition.....	114
5.4.2 Mantle source variability at the Gakkel Ridge .....	116
5.4.2.1 The Western Gakkel Ridge region.....	116
5.4.2.2 The Eastern Gakkel Ridge region.....	118
5.5 Conclusion .....	119
5.6 Acknowledgements.....	119
5.7 References.....	119
<b><i>CHAPTER 6 - Sulfide undersaturated melts at the ultraslow-spreading Gakkel Ridge, Arctic Ocean .....</i></b>	
Abstract .....	125
6.1 Introduction.....	127
6.2 Geological setting .....	128
6.3 Methods.....	129

## Table of Contents

---

6.3.1 Major element, trace element and S content of the volcanic glass.....	129
6.3.2 Whole rock PGE analysis.....	130
6.3.3 Sulfur isotope measurement.....	131
6.4 Results.....	134
6.4.1 Major element and S content of the volcanic glasses.....	134
6.4.2 Sulfur isotopes.....	134
6.4.3 Platinum group elements.....	135
6.5 Discussion.....	136
6.5.1 Effect of source composition on S isotopes.....	137
6.5.2 The effect of the MORB source on PGE concentration.....	138
6.5.3 Sulfide saturated versus sulfide undersaturated MORBs.....	139
6.6 Conclusion.....	142
6.7 Acknowledgements.....	143
6.8 References.....	143
Supplementary Data Tables.....	147
<b>CHAPTER 7 - Discussion, Outlook and Conclusion.....</b>	<b>155</b>
7.1 Introduction.....	157
PART I: Mantle heterogeneity reflected by radiogenic isotopes of MORBs.....	157
7.1.1 Mantle convection and chemical heterogeneity.....	157
7.1.2 Indian-type mantle/DupAl anomaly and other complexities.....	159
PART II: Magmatic differentiation in MORBs.....	161
7.2 Outlook.....	162
7.3 Conclusion.....	163
7.4 References.....	165

## List of Figures

Figure 1.1 - Schematic overview of the Earth's mantle.....	5
Figure 1.2 - Schematic overview of the main research question.....	7
Figure 1.3 - Geographical overview of the Gakkel Ridge location (a) and ridge segments (b).....	9
Figure 1.4 - $^{208}\text{Pb}/^{204}\text{Pb}$ vs $^{206}\text{Pb}/^{204}\text{Pb}$ plot of MORBs from the four major ocean basin. ....	11
Figure 1.5 - Schematic overview of the Fe isotope fractionation. ....	12
Figure 1.6 - Schematic overview of a mid-ocean spreading ridge showing the focus of the 4 main research chapters. ....	14
Figure 2.1 - Sample suite of the Western Volcanic Zone. ....	26
Figure 2.2 - Sample suite of the Sparsely Magmatic Zone. ....	27
Figure 2.3 - Sample suite of the Eastern Volcanic Zone.....	28
Figure 2.4 - Schematic overview of the main analytical work.....	29
Figure 2.5 - Alteration test. ....	30
Figure 2.6 - Epoxy mounts and backscattered image of two volcanic glass shards.....	32
Figure 2.7 - Comparison between volcanic glasses and whole-rock XRF glasses. ....	33
Figure 2.8 - Comparison of the major element composition of the basalts obtained by XRF and LA-ICP-MS analysis.....	34
Figure 2.9 - Comparison of the major element composition of the volcanic glasses obtained by XRF and LA-ICP-MS analysis. ....	35
Figure 2.10 - Picked rock chips for Pb isotope analysis'.....	38
Figure 3.1 - Geographical overview, sample localities and trace element patterns in modern MORB lavas from the western Gakkel Ridge.....	46
Figure 3.2 - $^{87}\text{Sr}/^{86}\text{Sr}$ vs Ba/Yb.....	47
Figure 3.3 - Paleogeography of the Gakkel Ridge region.....	49
Figure 3.4 - Th-Nb/Yb co-variation diagram and Pb isotope systematics.....	51
Supplementary Figure 3.1 - Variation of Zr/Nb, Ba/Yb and axial depth along the ridge .....	62
Supplementary Figure 3.2 - Zr/Nb, Th/Yb and Sr isotope ratios in Western Gakkel Ridge MORB. ....	63
Supplementary Figure 3.3 - Ba/Th in MORB from the Western Gakkel Ridge region.....	64
Figure 4.1 - $\text{K}_2\text{O}/\text{TiO}_2$ versus MgO plot. ....	78
Figure 4.2 - Along-ridge variation in Sr-Pb isotope and Ba/Th.....	80

## List of Figures

---

Figure 4.3 - Hf-Sr-Pb isotope systematics of the Gakkel Ridge basalts. ....	81
Figure 4.4 - $^{207}\text{Pb}/^{204}\text{Pb}$ versus $^{206}\text{Pb}/^{204}\text{Pb}$ diagram.....	83
Figure 4.5 - $^{208}\text{Pb}/^{206}\text{Pb}$ versus $^{207}\text{Pb}/^{206}\text{Pb}$ diagram.....	84
Supplementary Figure 4.1 - Trace element pattern of the EVZ at the Gakkel Ridge .....	93
Supplementary Figure 4.2 - $^{208}\text{Pb}/^{204}\text{Pb}$ versus $^{206}\text{Pb}/^{204}\text{Pb}$ diagram. ....	94
Figure 5.1 - Major and trace element versus iron isotope composition .....	111
Figure 5.2 - Zr/Nb versus $\text{Na}_{8,0}$ and $\delta^{57}\text{Fe}_{\text{prim}}$ . ....	112
Figure 5.3 - Rare Earth Element (REE) pattern versus $\delta^{57}\text{Fe}_{\text{prim}}$ .....	113
Figure 5.4 - Comparison of $\delta^{57}\text{Fe}$ from different locations and tectonic settings.....	114
Figure 5.5 - Spreading rate dependency on $\Delta^{57}\text{Fe}$ and Mg#. ....	115
Figure 5.6 - Simplified model (after Brandl et al., 2016; Nebel et al., 2015) of the upper mantle beneath the Western Gakkel Ridge region.....	117
Figure 6.1 - Sulfur concentration versus FeO and MgO content of the volcanic glasses. ....	134
Figure 6.2 - Comparison of sulfur isotope composition ( $\delta^{34}\text{S}$ ) of different tectonic settings. ...	135
Figure 6.3 - PGE (Os, Ir, Ru, Pt, Pd) pattern of the Gakkel basalts of all three ridge segments.....	136
Figure 6.4 - Platinum group elements versus Fe isotope composition.....	137
Figure 6.5 - Pd-Ir ratio, $\text{Na}_{8,0}$ and Cr versus REE pattern. ....	138
Figure 6.6 - Iridium, Ru and Cu versus Fe isotope systematics ( $\Delta^{57}\text{Fe}$ ).....	140
Figure 6.7 - Schematic overview of the melting process and fractionation at the Gakkel Ridge.....	141
Figure 7.1 - Schematic overview of all the findings in this thesis. ....	160

**List of Tables**

Table 2.1 - Sample locality. .... 24

Table 2.2 - Overview of the sample entire suite. .... 25

Table 2.3 - Iron isotope composition (given in ‰) of BHVO1 and BCR1. .... 36

Table 2.4 - Reference values of all analytical Hf isotope runs..... 37

Table 2.5 - Strontium isotope ratios of the analysed reference materials. . .... 37

Table 2.6 – Lead isotope values for BCR 2 during each analytical run. .... 39

Supplementary Table 3.1 - Sample location of the analysed Gakkel Ridge basalts. .... 60

Supplementary Table 3.2 - Sr-Pb isotope data for Gakkel Ridge basalts. .... 61

Supplementary Data Table 3.1 - Major and trace element data of the WVZ and SMZ basalts. . 67

Supplementary Data Table 3.2 - Trace element data of NIST 612 and NIST 610..... 70

Supplementary Data Table 3.3 - Trace element data BHVO2G and XRF glass blank. .... 71

Table 4.1 - Lead, Sr and Hf isotope data of whole rock basalts from the Gakkel Ridge ..... 79

Supplementary Table 4.1 - Major and trace elements of EVZ basalts..... 99

Supplementary Table 4.2 - Trace element data of NIST 612 and NIST 610. .... 101

Supplementary Table 4.3 - Trace element data of BHVO2G and the XRF glass blank. .... 102

Table 5.1 - Major and trace element and iron isotope data of the Gakkel Ridge basalts (whole rock) and volcanic glasses (VG)..... 108

Table 6.1 - Major element concentrations and S isotope ratios of the volcanic glasses. .... 132

Table 6.2 - Trace element, isotope and PGE data of the Gakkel basalts..... 133

Supplementary Data Table 6.1 - Trace element data of the volcanic glasses from the Gakkel Ridge. .... 149

Supplementary Data Table 6.2 - Trace element data of the reference sample NIST 612 and NIST 610..... 152

Supplementary Data Table 6.3 - Trace element data of the reference sample BHVO2G..... 153



*In memory of Roland, Käthe, Johanna and Lars*

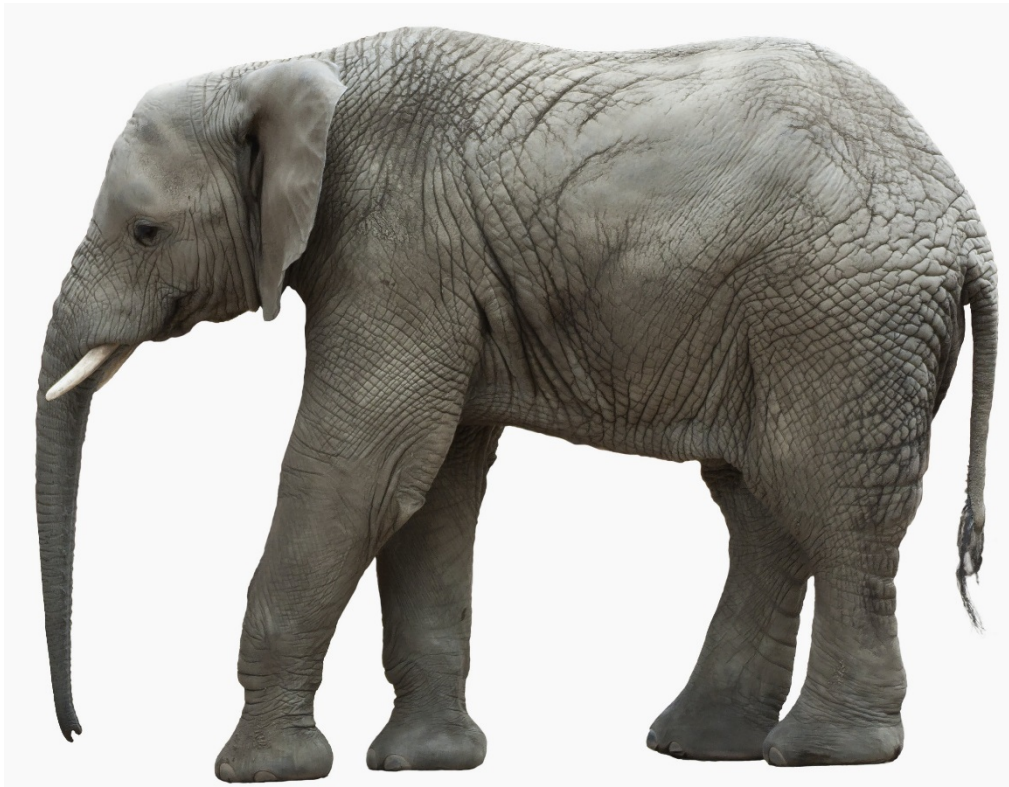
*“Ein Licht soll dir leuchten bis in die Ewigkeit*

*Zur Erinnerung an die Lebenszeit”*

*(Andreas Gabalier)*



# ANEKANTAVADA



*“The truth depends on one's point of view, and no single point of view comprises the complete truth. “*

*W. White (2015)*



# CHAPTER 1

## *Introduction*

---



*Photograph shows a curious polar bear that would like to explore the ocean. This is an analogue to my PhD. ([https://leballageecologique.com/wp-content/uploads/2012/10/ours\\_blanc\\_ocean\\_arctique-1.jpg](https://leballageecologique.com/wp-content/uploads/2012/10/ours_blanc_ocean_arctique-1.jpg))*

## 1.1 Rationale

Anekantavada - “the truth depends on one’s point of view and no single point of views comprises the complete truth” (White, 2015) – is often linked to an Indian parable, in which six blind men try to feel an elephant. One feels the leg and says it feels like a tree trunk and the second one feels the ear and says it feels like a leaf and so on. The same principle can be applied to the Earth sciences, where different disciplines (Geophysics, Geochemistry, Geodynamics, etc.) seek to understand the Earth’s mantle and “feel” different aspects. For instance, geophysicists “feel” the internal picture (e.g., hot and cold areas – slab no slab) or geochemists “feel” recycled crust; each single discipline has a different point of view.

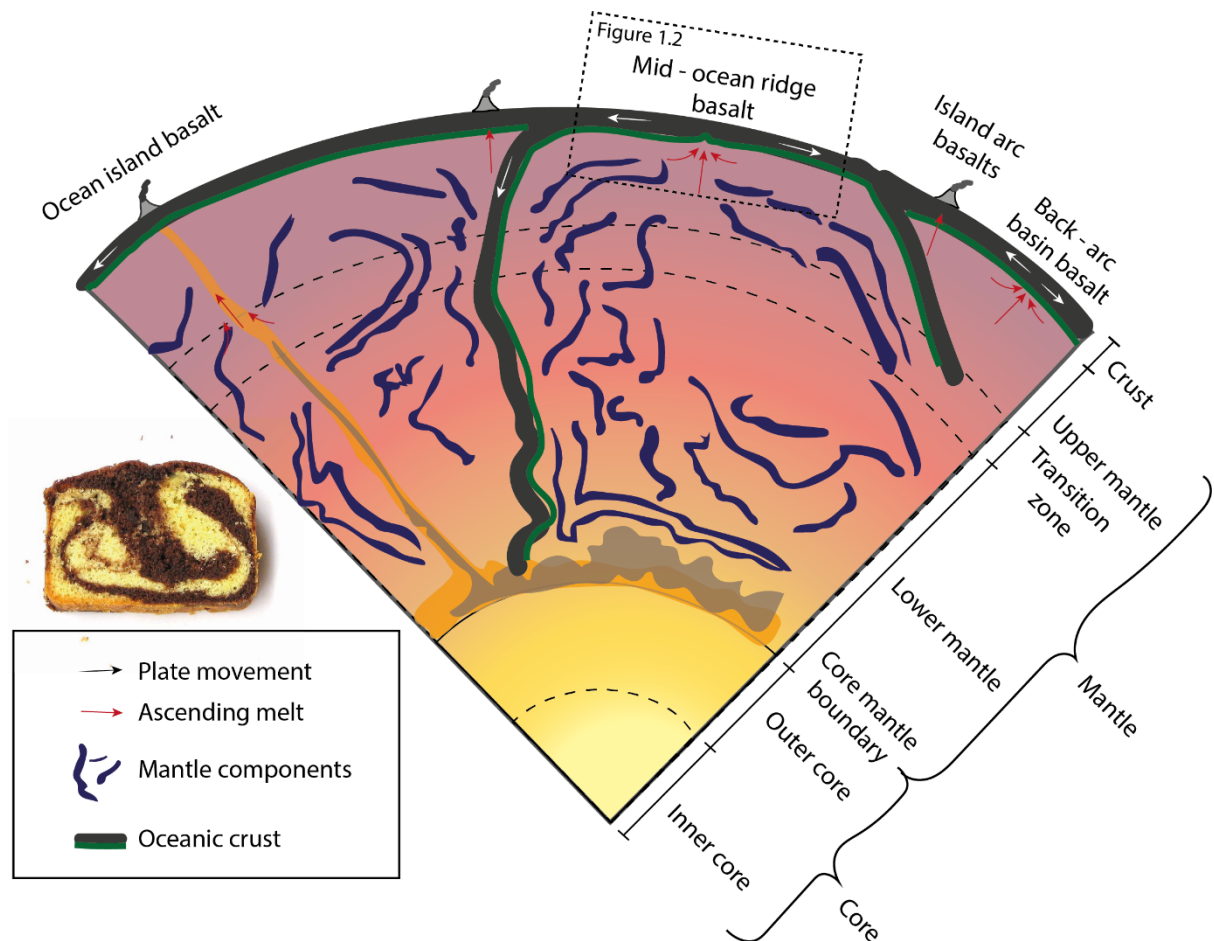


**Figure 1.1 - Schematic overview of the Earth’s mantle.** The schematic overview highlights the different ocean floor lavas; from left to right: ocean island basalts sample the lower mantle; mid-ocean ridge basalts that reveal information about the upper mantle; island arc and back-arc basin basalts provide insights into subduction zone processes. This study focusses on mid-ocean ridge basalts; highlighted by the dashed black box (Figure 1.2). The marble cake, on the left, represents the analogue of the Earth’s mantle, see text for further comments.

Simply put, the Earth's mantle can be imagined as a marble cake (Figure 1.1; Allegre and Turcotte, 1986; Kellogg and Turcotte, 1990), in which the yellow/vanilla part of the cake represents the depleted or ambient mantle and the chocolate streaks represents refractory and enriched mantle domains (Allègre and Turcotte, 1985; Wood, 1979; Zartman and Haines, 1988) that are integrated into the ambient mantle. Refractory mantle lithologies are thought to result from a series of partial melting events or re-fertilisation (Byerly and Lassiter, 2014; Liu et al., 2008; Salters et al., 2011; Sobolev and Shimizu, 1993; Stracke et al., 2011), whereas enriched mantle lithologies are thought to represent recycled material that has been brought into the mantle either in subduction zones, or by delamination of continental crust during continent collision or continental breakup (Hofmann, 2014; White, 2015). Melting and recycling processes modify the chemistry of the mantle and can be traced by radiogenic isotope studies in basalts (Anderson, 1968; Anderson, 2006; Hofmann, 2014; Mallick et al., 2014; Zindler and Hart, 1986), because the ascending magma inherits the geochemistry and therefore the isotopic composition of its source. The chemistry of magma is however not a direct reflection of the source, as a number of secondary processes will further modify the primary melt composition during ascent by e.g., fractional crystallization, magma chamber processes or wall-rock interaction; (Coogan and O'Hara, 2015; Gale et al., 2014; Langmuir et al., 2013; Lissenberg et al., 2019; O'Neill and Jenner, 2012). In turn, the chemical variability in ocean floor lavas (OFL) is controlled by both the source petrology and the superposition of petrogenetic processes from melt generation, ascent and extrusion, but to which extent each contributes to the geochemical diversity in basalts is still unclear (Matzen et al., 2017).

The aim of this study therefore is to better understand the processes that lead to geochemical diversity observed in OFL with focus on mid-ocean ridge basalts (MORBs; Figure 1.2). The overall research question is:

***“Why are MORBs geochemically diverse?”***

Mid-ocean ridge basalts are direct products of partial melting of the Earth's upper mantle, covering 65% of the Earth crust (Allègre et al., 1984; Brandl et al., 2016; Rubin et al., 2009). The geochemistry of MORBs is diverse and contributes fundamentally *“to the understanding of chemical and dynamic evolution of the Earth”* (Blusztajn et al., 2014). The chemistry of MORBs is affected by three different variables: (1) source heterogeneity, (2) partial melting/mantle temperature and (3) fractional crystallization (Gale et al., 2014).

Source heterogeneity is dependent on mantle convection and the geodynamic evolution of the mantle in a certain region (Hofmann, 2014; Kellogg and Turcotte, 1990; Richards and Engebretson, 1992), which causes a geochemically variety on large km-scale, but also in a smaller-scale within the mantle (e.g., Anderson, 2006; Byerly et al., 2017; Chen et al., 2016; Dupré and Allègre, 1983; Graham et al., 2006; Hart, 1984; Hofmann, 2003; Hofmann, 2014; Janney, 2005; Kellogg and Turcotte, 1990; Kim et al., 2017; le Roux et al., 2002; Mallick et al., 2014; White, 2015). Assuming similar melting conditions below a ridge segment, a heterogeneous source lithology produces chemically distinct MORBs. When melt rises from its source to the surface it interacts with its surroundings and is subject to fractional crystallization within magma chambers and dykes, which further affects the geochemistry of the MORB (Coogan and O'Hara, 2015; Gale et al., 2014; Lissenberg and Dick, 2008; O'Neill and Jenner, 2012; Rubin et al., 2009).

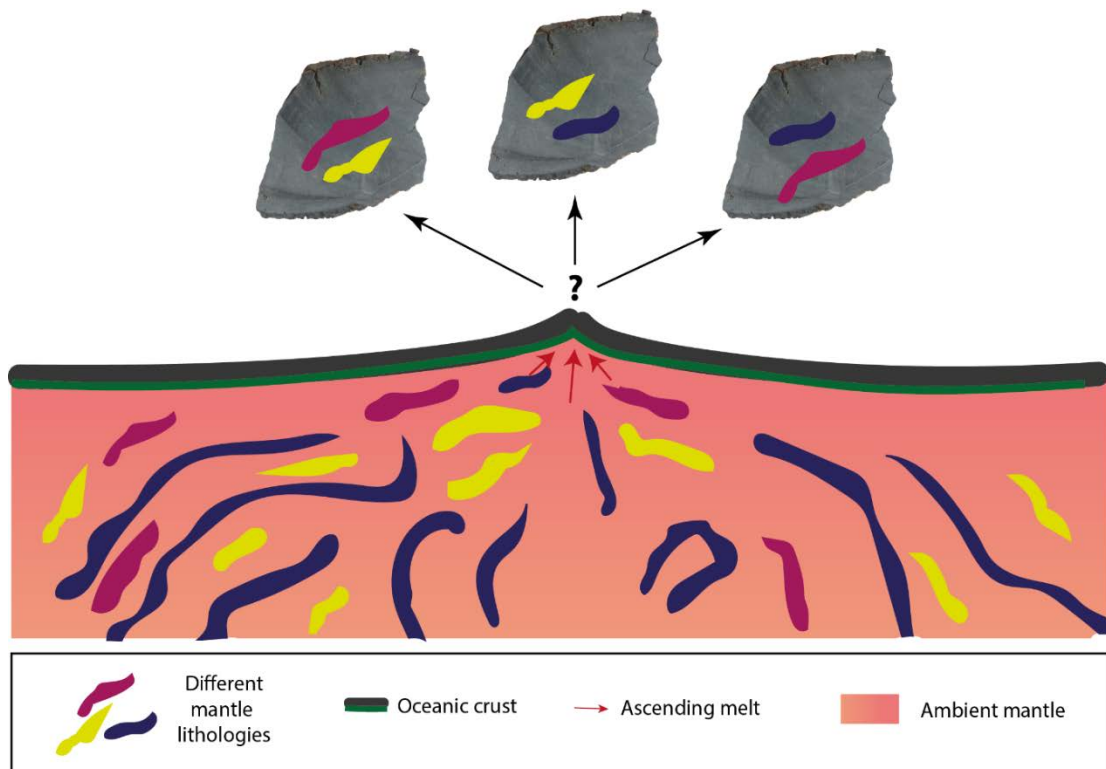


**Figure 1.2 - Schematic overview of the main research question.** The lower panel of the figure shows a mid-ocean ridge section with upper mantle and oceanic crust, zoomed in section from Figure 1.1. The upper mantle, as shown here, contains stripes of different mantle lithology, which are represented by different colours. MORBs are partial melting products of the Earth's upper mantle. Each mantle lithology has a different composition, which can be inherited into the MORB source. To which extent each component contributes to the chemical variability is unknown. The three basalts (same shape and sample) in the upper panel show three possibilities of MORB source variabilities. These, however, will be overprinted by secondary magma differentiation processes; changing the chemistry of MORBs.

The latter, however, also depends on the spreading rate. Globally, spreading rates vary between 6 mm/a (per annum) at the Gakkel Ridge in the Arctic Ocean to 150 mm/a at the Eastern Pacific rise in the Pacific Ocean. The global ridge system is divided into four

different ridge systems: ultraslow-spreading ridges ( $< 15$  mm/a), slow spreading ridges (15 mm/a – 30 mm/a), intermediate spreading ridges (30 mm/a – 70 mm/a) and fast spreading ridges ( $> 70$  mm/a). All but ultraslow-spreading ridges have a high magmatic activity, occurrence of transform faults, thick oceanic crust (up to 6 km) and the existence of magma chambers in common (Brandl et al., 2016). Within magma chambers three different processes can potentially affect MORB chemistry: (1) replenishment, (2) mixing and (3) fractional crystallization, defined as the so-called RTX processes (Coogan and O'Hara, 2015; O'Neill and Jenner, 2012).

In contrast, ultraslow-spreading ridges have only a small number of magmatic centres, lack transform faults and magma chambers due to low magmatic activity (Brandl et al., 2016; Dick et al., 2003). Therefore, the main characteristic feature of ultraslow-spreading ridges is the existence of an amagmatic ridge segment with mainly abyssal peridotite outcropping (Dick et al., 2003; Snow and Edmonds, 2007). Worldwide only two known ultraslow-spreading ridges exist, the Southwest Indian Ridge and the Gakkel Ridge in the Arctic Ocean (Snow and Edmonds, 2007). The low magmatic activity at ultraslow-spreading ridges is related to a colder thermal gradient in the mantle below. It is thought that conductive cooling is more efficient in upper crustal levels (1 km - 2 km; e.g., Standish et al., 2008) than it would be at spreading rates  $> 15$  mm/a, because of the absence of magma chambers. In such slow-spreading regimes the melt rises rapidly into the crustal level and erupts with minimal influence by crystal fractionation (Brandl et al., 2016; Phipps Morgan and Ghen, 1993). Rapid melt transfer with limited interaction and different melting process make basalts sourced from ultraslow-spreading ridges ideal to indirectly study the underlying mantle source and its link to chemical diversity in OFL.

In this thesis I focus on how a heterogeneous mantle and how magmatic differentiation process effects the geochemistry of OFL. The ultraslow-spreading Gakkel Ridge in the Arctic has been chosen as my study area, because of its geochemically diverse mantle (D'Errico et al., 2016; Liu et al., 2008; Stracke et al., 2011) and along-ridge changes in magmatic activity (Michael et al., 2003) and spreading rate (Dick et al., 2003); all factors that can potentially affect the geochemistry of MORBs.

## **1.2 Ultraslow-spreading Gakkel Ridge, Arctic Ocean**

The Gakkel Ridge in the Arctic Ocean extends for 1200 km from the northeast coast of Greenland to the northwest coast of Siberia (Figure 1.3a). Along-ridge variation in spreading rate (Dick et al., 2003), magmatic activity (Michael et al., 2003), isotope

signature (Goldstein et al., 2008) and crustal thickness (Schmidt-Aursch and Jokat, 2016) are the main characteristics of the Gakkel Ridge. Michael et al. (2003) divided the ultraslow-spreading Gakkel Ridge into three different segments. The westernmost ridge segment is the Western Volcanic Zone (WVZ), followed by the Sparsely Magmatic Zone (SMZ) and concludes with the easternmost ridge segment at the Eastern Volcanic Zone (EVZ). A brief description of each segment will be given in the following.

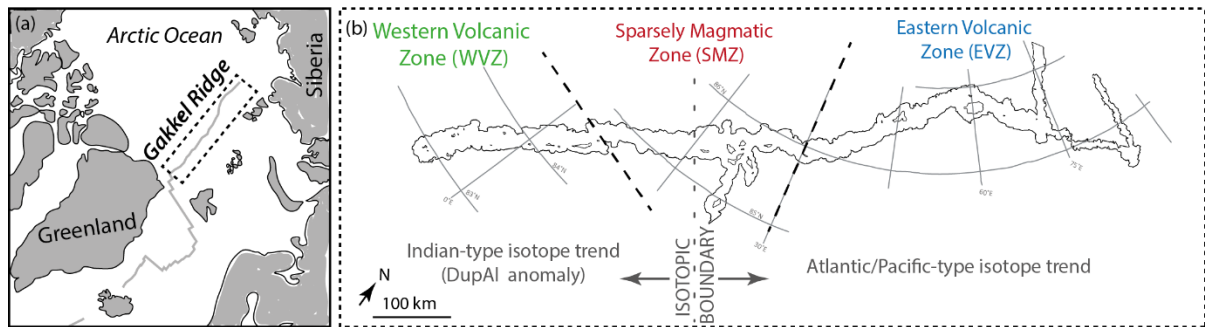


**Figure 1.3 - Geographical overview of the Gakkel Ridge location (a) and the ridge segments (b).** (b) shows the three different ridge segments of the Gakkel Ridge. The inclined black dotted lines highlight the boundary between the ridge segments and the vertical grey dashed line in the middle of the SMZ highlights the isotopic boundary distinguishing between Indian-type isotope trend (also referred to DupAl anomaly) in the west and Atlantic/Pacific-type isotope trend in the east.

### 1.2.1 Western Volcanic Zone (WVZ)

The WVZ extends for approximately 200 km (7°W to 3°E) and begins at the Lena trough (northern most part of the North Atlantic ridge). Five axial volcanic ridges (each 15 km – 50 km long) comprise the entire ridge segment. The axial depth ranges between 3700 – 4200 m. The ridge segment is characterised by robust magmatism and spreads at a rate of 14.5 mm/a in the west and 13.5 mm/a in the East. The chemistry of the WVZ basalts is characterised by a high concentration of large ion lithophile elements (e.g., Ba, Rb) and displays a radiogenic isotope signature akin to those observed in the Indian Ocean (high  $^{87}\text{Sr}/^{86}\text{Sr}$  and high  $^{208}\text{Pb}/^{204}\text{Pb}$ ; Goldstein et al., 2008; Mühe et al., 1993).

### 1.2.2 Sparsely Magmatic Zone (SMZ)

The second ridge segment is the SMZ, which ranges for 300 km from an abrupt change in axial depth by 1100 m lower than the most easterly point of the WVZ at 3°E (Michael et al., 2003) to 29°E. The abrupt change in ridge topography is linked to changes in ridge geometry, which may be due to changes in mantle lithology as observed (Standish et al., 2008; Whittaker et al., 2008). The SMZ is further characterised by an alternation of outcropping abyssal peridotites and volcanic edifices and is the least magmatic ridge segment of the Gakkel Ridge. Volcanic activity occurs only at approximately 12°E and

20°E. The limited magma production rate at the SMZ is furthermore linked to the slow spreading rate of the SMZ of approximately 12 mm/a.

The geochemistry of the SMZ is characterised by an extreme depleted mantle section close to the geomorphological boundary with the WVZ at 3°E (Salters and Dick, 2011). Furthermore, Goldstein et al. (2008) suggested an isotopic boundary in the middle of the SMZ at 15°E. Basalts, East of the isotopic boundary display an isotopic signature akin to Indian Ocean MORB (high  $^{208}\text{Pb}/^{204}\text{Pb}$  and high  $^{87}\text{Sr}/^{86}\text{Sr}$ ), whereas basalts west of the isotopic boundary show affinities with Atlantic/Pacific MORBs (Goldstein et al., 2008).

### ***1.2.3 Eastern Volcanic Zone (EVZ)***

The easternmost ridge segment, the EVZ is characterised by six 15 – 50 km large volcanic centres (100 km apart) at 31°E, 37°E, 55°E, 69°E and 85°E that spread over 700 km (Michael et al., 2003). In between each volcanic centre, abyssal peridotites are abundant. From east to west the spreading rate changes by almost 5 mm/a. In the West at 29°E the spreading rate is approximately at 11 mm/a and further to the East only 6 mm/a (Michael et al., 2003).

Previous studies on basalts and peridotites suggest an extremely heterogeneous mantle beneath the EVZ ranging from ultradepleted segments at 66°E to enriched ridge areas at 30°E (D'Errico et al., 2016; Liu et al., 2008; Stracke et al., 2011). It has been suggested that the mantle in the West has been metasomatically enriched and affected the MORB geochemistry, whereas further to the East (85°E) solely depleted MORB mantle is sampled. In addition, an unusual high hydrothermal activity with unknown origin has been described at 85°E (Edmonds et al., 2003; Jean-Baptiste and Fourné, 2004; Pedersen et al., 2010).

Lead and Sr isotope systematics of the EVZ basalts show affinities with Atlantic/Pacific MORB, similar to a West-SMZ ridge segment (Goldstein et al., 2008). In contradiction to this, Mühe et al. (1997) measured Sr and Pb isotopes on glass shards from the EVZ at 60°E, showing high radiogenic Sr isotope signature and Pb isotope signatures akin to Indian MORB (section 1.3).

### **1.3 Indian-type mantle signature (DupAl anomaly)**

Indian-type mantle signature (often referred to as DupAl anomaly), as found in basalts from the Gakkal Ridge, has generally been associated with basalts from the Indian Ocean in the Southern Hemisphere. Compared to OFL from the Atlantic and Pacific Ocean, basalts from the Indian Ocean and partially from the Arctic Ocean are characterised by a

high radiogenic Pb (in particular  $^{208}\text{Pb}/^{204}\text{Pb}$ ) and Sr isotope signature (Dupré and Allègre, 1983; Hart, 1984).

For a given  $^{206}\text{Pb}/^{204}\text{Pb}$ , basalts with Indian-type mantle signature show a high  $^{208}\text{Pb}/^{204}\text{Pb}$  (Figure 1.4), plotting above the Northern Hemisphere reference line (NHRL; Hart, 1984). The NHRL is used to better define the mantle source. Basalts from the Atlantic and the Pacific plot along the NHRL. Basalts with a high  $^{208}\text{Pb}/^{204}\text{Pb}$ , however, deviate ( $+\Delta 8/4$ ) from the NHRL, because of a higher Th/U in the source with  $^{232}\text{Th}$  being the parent nuclide of  $^{208}\text{Pb}$ .

Various studies have been conducted to explain the distinct isotopic signatures (high Th/U and Rb/Sr in the mantle source) of OFL from the Indian and Arctic Ocean. Three main models have been proposed to explain the distinct isotopic signature of the Indian-type mantle: (i) thermal upwelling from the core/mantle boundary, (ii) ancient subduction, or (iii) integration of sub-continental-lithospheric mantle (SCLM) into the MORB source as cause of continental break-up (e.g., Goldstein et al., 2008; le Roux et al., 2002; Mahoney et al., 1989; Rehkämper and Hofmann, 1997).

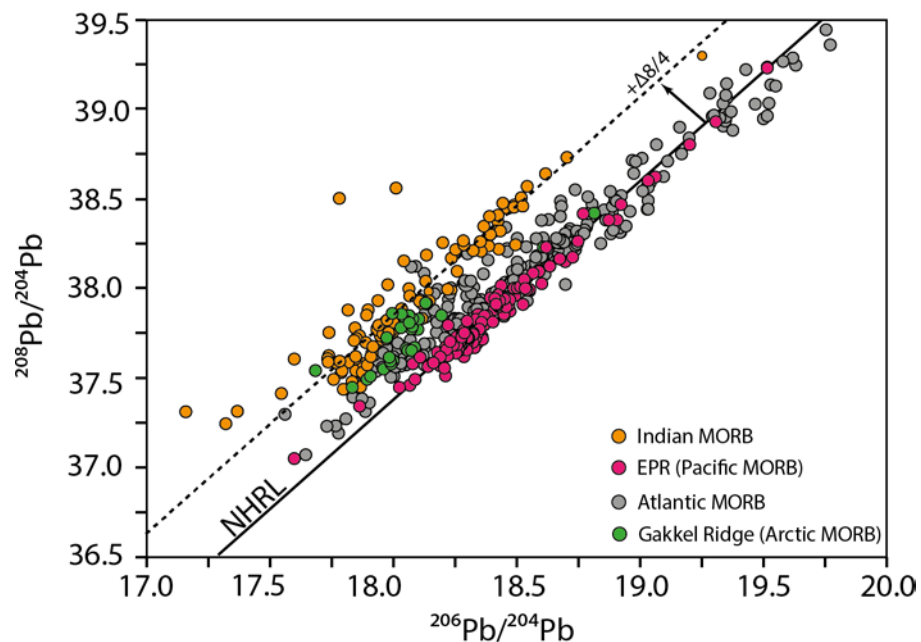


**Figure 1.4** -  $^{208}\text{Pb}/^{204}\text{Pb}$  vs  $^{206}\text{Pb}/^{204}\text{Pb}$  plot of MORBs from the four major ocean basin. The Northern Hemisphere Reference Line (NHRL; Hart 1984) is used as a reference line to distinguish source differences of ocean floor lavas (MORBs and ocean island basalts). Here, in this thesis, I focus on MORBs. The figure shows the four major oceans (in different colours) and the Pb isotope signature of the MORBs. The plot shows that the basalts from the Arctic Ocean (green dots) show an overlap with basalts from the Indian (orange dots) and Atlantic Ocean (grey dots). These basalts are reflected by a higher  $^{208}\text{Pb}/^{204}\text{Pb}$  for a given  $^{206}\text{Pb}/^{204}\text{Pb}$  than the basalts from the Atlantic and the Pacific Ocean (pink dots). As  $^{208}\text{Pb}/^{204}\text{Pb}$  is a function of Th/U, the figure suggests that the MORB source of the Indian and the Arctic Ocean (represented by the Gakkel Ridge) has a higher Th/U leading to a higher radiogenic  $^{208}\text{Pb}/^{204}\text{Pb}$  and  $+\Delta 8/4$ .

To explain the Indian-type mantle isotopic signature at the Gakkel Ridge, Goldstein et al. (2008) proposed that the SCLM became integrated into the MORB source due to the

break-up between Greenland and Spitsbergen at around 50 Ma (Blythe and Kleinspehn, 1998). This theory, however, is debated and does not explain other observed features, such as extreme mantle depletion (Liu et al., 2008; Stracke et al., 2011), source enrichment possibly due to metasomatism (Mühe et al., 1991) and homogeneous Pb isotope signatures in the Western Gakkel Ridge region (Blusztajn et al., 2014). Due to this controversy, I further aim to better constrain the mantle sources and the origin that leads to the elevated Th/U in Gakkel lavas.

#### 1.4 Methodology

To investigate the geochemical and isotopic diversity in the Gakkel basalts, 36 fresh basalts from all three ridge segments were analysed for their radiogenic (Pb, Sr, Hf), and stable (Fe, S) isotopic composition, as well as major and trace element composition, with subset of samples analysed with high-precision for their platinum group element (PGE) systematics.

Radiogenic isotope analysis will help to better characterize the MORB source and provide information about the timing (parent/daughter ratio), because radiogenic isotopes do not fractionate during crystal fractionation.

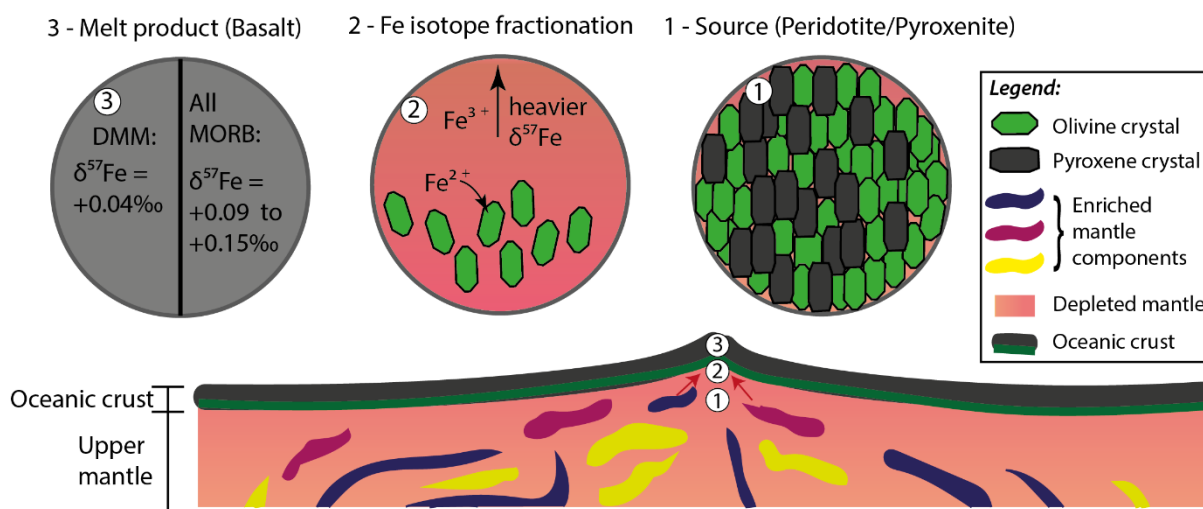


**Figure 1.5 - Schematic overview of the Fe isotope fractionation.** The lower panel represents a MORB section containing different mantle components (different colours). The red arrows indicate the melt flow from mantle source region to the crust. Each number (1, 2, 3) in the lower sketch represents the locality of the sketches in the upper panel. No.1 represents the MORB source, which can be either a peridotite or pyroxenite. No.2 represents the partial melt of the source with olivine fractionation and the incorporation of  $\text{Fe}^{2+}$  into the olivine. As result, the melt becomes progressively enriched in  $\text{Fe}^{3+}$  resulting in a heavier iron isotope signature ( $\delta^{57}\text{Fe}$ ). No.3 shows the iron isotope range of MORBs (data - Teng et al., 2013) and the depleted MORB mantle value (data - Craddock et al., 2013).

Stable isotopes, such as Fe, provide additional information about magmatic processes from source to crust due to isotopic fractionation during magma differentiation. In brief, iron is one of the most abundant elements in the Earth's mantle and a main

component of various minerals such as olivine, orthopyroxene, clinopyroxene, spinel, amphibole and garnet; and occurs in two different oxidation states ferrous ( $\text{Fe}^{2+}$ ) and ferric iron ( $\text{Fe}^{3+}$ ). Due to the different bonding in mineral structures,  $\text{Fe}^{2+}$  and  $\text{Fe}^{3+}$  behave differently and fractionate easily during magmatic crystallisation and fractionation (Weyer, 2008; Williams et al., 2004). Ferrous iron is more compatible than ferric iron and favours to be incorporated into olivine (Figure 1.5 No.2). Because olivine is the first mineral to crystallize, the amount of ferrous iron of the melt decreases and the melt becomes progressively enriched in ferric iron (Figure 1.5 No.3) as olivine crystals separate from the melt. Iron isotopes fractionate in tandem with this process. The iron isotope signature of a sample is given in the  $\delta$ -notation ( $\delta^{57}\text{Fe}$ ), which is strongly related to the  $\text{Fe}^{2+}$  and  $\text{Fe}^{3+}$  ratio of the melt. The same principles can be employed to understand magma differentiation processes during melt ascent or within magma chambers.

More details about the selected samples, the sample preparation and the analytical methods are described in chapter 2 or in each individual research chapter (chapters 3 – 6).

### **1.5 Thesis structure**

This thesis is organized into seven chapters, including an introductory chapter, methodology and a synthesis chapter summarizing the findings and their implications for the current understanding of the structure of the mantle below mid-ocean ridges, in particular for the Gakkel Ridge, and magmatic processes in MORBs. Chapters 3 – 6 are research chapters contributing to the overall research question. The chapters are formatted as stand-alone journal articles, which is an accepted format for a PhD thesis at Monash University, but results in some inevitable repetition of the introductory and methods section of each chapter. Despite that, chapter 3 has already been submitted for publications to Nature Communications. In each other chapter (chapters 4 - 6), I briefly state the journal that I will submit the manuscript to. The format of each chapter has been adjusted to maintain a consistent layout and reference style within the thesis. Supplementary material associated with each chapter and references to all cited literature are provided at the end of each chapter.

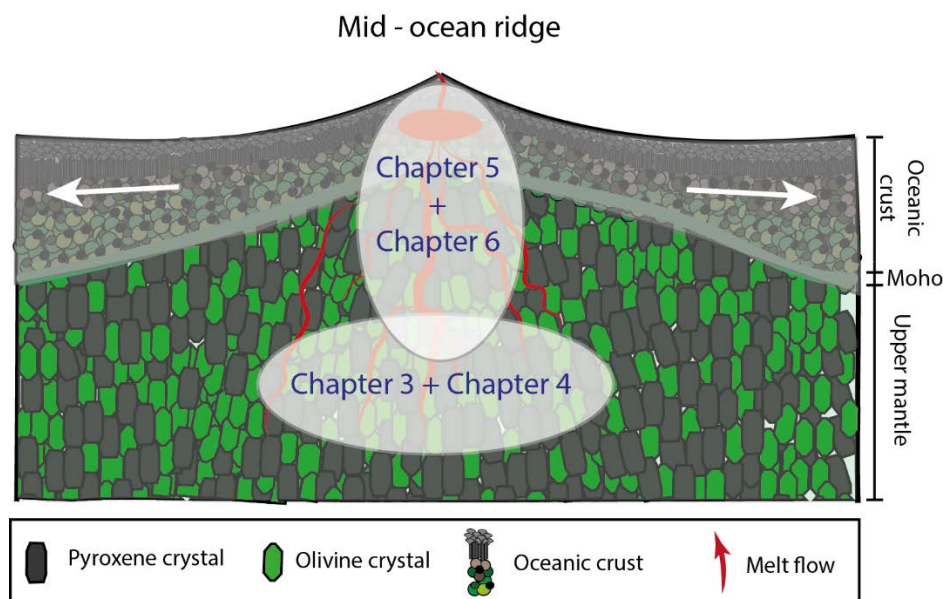


*Figure 1.6 - Schematic overview of a mid-ocean spreading ridge showing the focus of the 4 main research chapters.*

To address the overall research question, chapters 3 and 4 focus on the MORB source, whereas chapters 5 and 6 focus on the magmatic evolution of MORBs (Figure 1.6). This thesis structure is contrary to the common approach for magmatic and volcanic systems, because magmatic differentiation needs to be understood first, before investigating source composition. But as chapter 3 builds the foundation for chapters 4, 5 and 6; I choose the opposite approach. Having said this chapters 5 and 6, which deal with the understanding of magmatic and volcanic system, first discuss the magmatic differentiation and then I draw conclusions about the MORB source composition.

The Gakkel Ridge has been divided into two different along-strike regions: The Western Gakkel Ridge region (comprises of the WVZ and the SMZ) and (2) the Eastern Gakkel Ridge region (the EVZ only). The differentiation into these two regions is based Sr and Pb isotope signatures (Goldstein et al., 2008). Chapter 3 investigates the mantle source under the Western Gakkel Ridge region and Chapter 4 the Eastern Gakkel Ridge region. In Chapter 5, the findings from chapter 3 are linked with Fe isotope systematics and chapter 6 discusses the magmatic evolution of MORBs using PGE. A brief description of each chapter follows below.

### ***1.5.1 Brief chapter description***

**Chapter 3:** “A fossil subduction under the Western Gakkel Ridge region, Arctic Ocean”

This chapter discusses the distinct Pb and Sr isotopic signature found in Gakkel basalts from the WVZ and the SMZ ridge segment. As shown by Goldstein et al. (2008),

basalts from the WVZ and the SMZ are characterised by high radiogenic  $^{208}\text{Pb}/^{204}\text{Pb}$  and  $^{87}\text{Sr}/^{86}\text{Sr}$  isotope signature akin to ocean floor lavas from the Indian Ocean. In this study, new Sr and Pb isotope and trace element data of the Gakkel basalts will be presented. The data shows that basalts from the WVZ and SMZ display elevated concentrations of fluid-mobile elements (Ba, Th) and a depletion of highly incompatible elements (Zr, Nb), suggesting the occurrence of re-enrichment and depletion events in the mantle beneath the SMZ and the WVZ. Elevated Ba/Th, high  $^{208}\text{Pb}/^{204}\text{Pb}$ , high  $^{87}\text{Sr}/^{86}\text{Sr}$  isotope signatures in combination with low Zr/Nb are found in subduction zone settings, e.g., in active island arc and back-arc basin lavas from the Western Pacific (e.g., Escrig et al., 2009; Pearce and Stern, 2013; Ribeiro et al., 2013).

To explain the nature of the element ratios in Gakkel MORB, this chapter provides an alternative model to the pre-existing one from Goldstein et al. (2008). Here, I suggest that the observed geochemical signatures are linked to an old subduction zone, which had been active between 150 Ma and 125 Ma in the circumpolar region and modified the mantle in the study area. The data and observations are linked with palaeogeographic reconstructions (Alvey et al., 2008; Shephard et al., 2013) and seismic interpretations (Sokolov and Mazarovich, 2016).

#### **Chapter 4:** “*Elucidating the peculiar DupAl isotope signatures of Arctic mid-ocean ridge basalts*”

This study follows up on the findings of chapter 3 and discusses the nature of the Pb isotopic difference between the West and the East of the isotopic boundary with focus on MORB source of the basalts from the EVZ. New Sr and Pb isotope data for basalts from the EVZ and Hf isotope data of all Gakkel samples, studied here, are presented. The results confirm the existence of an isotopic boundary at 15°E, as Goldstein et al. (2008) suggested. The isotopic difference to the West and the East of the boundary is marked by an abrupt change in Pb isotopes and a decrease in Sr isotopes towards the EVZ boundary.

Furthermore, the data show a slight enrichment of  $^{208}\text{Pb}/^{204}\text{Pb}$  for a given  $^{206}\text{Pb}/^{204}\text{Pb}$  and in parts a higher  $^{87}\text{Sr}/^{86}\text{Sr}$  in the EVZ basalts, compared to Atlantic/Pacific MORB and a previous study at the Gakkel Ridge (Goldstein et al., 2008). The results presented here are, however, in line with data by Mühe et al. (1997), who suggested a re-enrichment by crustal fluids for EVZ basalts. Additionally, the enriched mantle area can be further linked to a depletion event that occurred ~2 Ga (Liu et al., 2008; Stracke et al., 2011; Warren and Shirey, 2012). It is possible that parts of the mantle beneath the EVZ has been affected by

crustal pollution to different extent and at different times to that in the Western Gakkel Ridge region. The similar, albeit not identical, overprint resulted in a pseudo-Indian-type mantle signature (high  $^{208}\text{Pb}/^{204}\text{Pb}$  and  $^{87}\text{Sr}/^{86}\text{Sr}$  isotope) in the EVZ basalts.

**Chapter 5:** “*Iron isotope variability in MORBs along the ultraslow-spreading Gakkel Ridge, Arctic Ocean*”

Chapter 5 discusses the effect of mantle source variability and magmatic differentiation on Fe isotope systematics. Previous studies showed a large variability in Fe isotope signatures of ocean floor lavas, suggesting that the range is not solely attributed to magmatic differentiation, but also to mantle source variability. The Gakkel Ridge is a suitable study area to investigate the iron isotope variability, because of its extremely heterogeneous mantle, changes in the magmatic activity and spreading rate from East to West, ranging from slow spreading rate from 6 mm/a to 14 mm/a, respectively, with an increase in magmatic activity. It is clear that with changing spreading rate and magma production rate, magmatic differentiation processes change (Rubin and Sinton, 2007; Standish et al., 2008). Iron isotope systematics from this study show that with increasing magmatic activity, magma chambers/magma lenses form in mid-crustal levels, where magma mixing and differentiation takes place and starts to affect the iron isotope composition in erupting lavas. The same likely accounts for changes in the chemistry of the basalts. Furthermore, the iron isotope variation in basalts from ultraslow-spreading ridges mainly reflects that of their mantle source, which contrasts with basalts from faster spreading ridges (>15 mm/a).

**Chapter 6:** “*Sulfide undersaturated melts at the ultraslow-spreading Gakkel Ridge, Arctic Ocean*”

Chapter 6 builds up on the findings of chapter 5 and discusses the geochemical behaviour of platinum group elements (PGE: Os, Ir, Ru, Pd, Pt) during MORB petrogenesis. In total, 16 basalt samples from all three ridge segments have been analysed for their PGE concentration. The results have been linked with Fe isotope systematics and show that Ir and Ru change their geochemical behaviour with changing magma differentiation processes. My findings indicate that magma, which rises through mid-crustal magma chambers *en route* to surface experiences S-saturation (reflected by WVZ basalts), as is commonly observed in MORB. However, magma that rises rapidly, such as at ultraslow-spreading ridges (reflected by SMZ and EVZ basalts), appears to be S-undersaturated. This

---

important finding links sulfur-saturation – a key aspect for the formation of magmatic sulphide deposits – to magma chamber processes.

## 1.6 References

- Allègre, C.J., Hamelin, B., Dupré, B., 1984. Statistical analysis of isotopic ratios in MORB: the mantle blob cluster model and the convective regime of the mantle. *Earth and Planetary Science Letters*, 71(1): 71-84.
- Allegre, C.J., Turcotte, D.L., 1986. Implications of a two-component marble-cake mantle. *Nature*, 323(6084): 123-127.
- Allègre, C.J., Turcotte, D.L., 1985. Geodynamic mixing in the mesosphere boundary layer and the origin of oceanic islands. *Geophysical Research Letters*, 12(4): 207-210.
- Alvey, A., Gaina, C., Kuszniir, N.J., Torsvik, T.H., 2008. Integrated crustal thickness mapping and plate reconstructions for the high Arctic. *Earth and Planetary Science Letters*, 274(3-4): 310-321.
- Anderson, D.L., 1968. Chemical inhomogeneity of the mantle. *Earth and Planetary Science Letters*, 5: 89-94.
- Anderson, D.L., 2006. Speculations on the nature and cause of mantle heterogeneity. *Tectonophysics*, 416(1-4): 7-22.
- Blusztajn, J., Shimizu, N., Warren, J.M., Dick, H.J.B., 2014. In-situ Pb isotopic analysis of sulfides in abyssal peridotites: New insights into heterogeneity and evolution of the oceanic upper mantle. *Geology*, 42(2): 159-162.
- Blythe, A.E., Kleinspehn, K.L., 1998. Tectonically versus climatically driven Cenozoic exhumation of the Eurasian plate margin, Svalbard: Fission track analyses. *Tectonics*, 17(4): 621-639.
- Brandl, P.A. et al., 2016. The timescales of magma evolution at mid-ocean ridges. *Lithos*, 240-243: 49-68.
- Byerly, B.L., Kareem, K., Bao, H., Byerly, G.R., 2017. Early Earth mantle heterogeneity revealed by light oxygen isotopes of Archaean komatiites. *Nature Geoscience*, 10(11): 871-875.
- Byerly, B.L., Lassiter, J.C., 2014. Isotopically ultradepleted domains in the convecting upper mantle: Implications for MORB petrogenesis. *Geology*, 42(3): 203-206.
- Chen, L., Tang, L., Yu, X., Dong, Y., 2016. Mantle source heterogeneity and magmatic evolution at Carlsberg Ridge (3.7°N): constrains from elemental and isotopic (Sr, Nd, Pb) data. *Marine Geophysical Research*: 1-14.
- Coogan, L.A., O'Hara, M.J., 2015. MORB differentiation: In situ crystallization in replenished-tapped magma chambers. *Geochimica et Cosmochimica Acta*, 158: 147-161.
- Craddock, P.R., Warren, J.M., Dauphas, N., 2013. Abyssal peridotites reveal the near-chondritic Fe isotopic composition of the Earth. *Earth and Planetary Science Letters*, 365: 63-76.
- D'Errico, M.E., Warren, J.M., Godard, M., 2016. Evidence for chemically heterogeneous Arctic mantle beneath the Gakkel Ridge. *Geochimica et Cosmochimica Acta*, 174: 291-312.
- Dick, H.J.B., Lin, J., Schouten, H., 2003. An ultraslow-spreading class of ocean ridge. *Nature*, 426(6965): 405-412.
- Dupré, B., Allègre, C.J., 1983. Pb-Sr isotope variation in Indian Ocean basalts and mixing phenomena. *Nature*, 303(5913): 142-146.
- Edmonds, H.N. et al., 2003. Discovery of abundant hydrothermal venting on the ultraslow-spreading Gakkel Ridge in the Arctic Ocean. *Nature*, 421(6920): 252-256.
- Escrig, S., Bézous, A., Goldstein, S.L., Langmuir, C.H., Michael, P.J., 2009. Mantle source variations beneath the Eastern Lau Spreading Center and the nature of subduction components in the Lau basin-Tonga arc system. *Geochemistry, Geophysics, Geosystems*, 10(4): n/a-n/a.
- Gale, A., Langmuir, C.H., Dalton, C.A., 2014. The Global Systematics of Ocean Ridge Basalts and their Origin. *Journal of Petrology*, 55(6): 1051-1082.
- Goldstein, S.L. et al., 2008. Origin of a 'Southern Hemisphere' geochemical signature in the Arctic upper mantle. *Nature*, 453(7191): 89-93.
- Graham, D.W., Blichert-Toft, J., Russo, C.J., Rubin, K.H., Albarede, F., 2006. Cryptic striations in the upper mantle revealed by hafnium isotopes in southeast Indian ridge basalts. *Nature*, 440(7081): 199-202.
- Hart, S.R., 1984. A large-scale isotope anomaly in the Southern Hemisphere mantle. *Nature*, 309(5971): 753-757.
- Hofmann, A., 2003. Sampling mantle heterogeneity through oceanic basalts: isotopes and trace elements. *Treatise on geochemistry*, 2: 61-101.
- Hofmann, A.W., 2014. Sampling Mantle Heterogeneity through Oceanic Basalts: Isotopes and Trace Elements. *Treatise on geochemistry*: 67-101.
- Janney, P.E., 2005. Hafnium Isotope and Trace Element Constraints on the Nature of Mantle Heterogeneity beneath the Central Southwest Indian Ridge (13 E to 47 E). *Journal of Petrology*, 46(12): 2427-2464.

- Jean-Baptiste, P., Fourré, E., 2004. Hydrothermal activity on Gakkel Ridge. *Nature*, 428: 36.
- Kellogg, L.H., Turcotte, D.L., 1990. Mixing and the distribution of heterogeneities in a chaotically convecting mantle. *Journal of Geophysical Research: Solid Earth*, 95(B1): 421-432.
- Kim, J. et al., 2017. Mantle heterogeneity in the source region of mid-ocean ridge basalts along the northern Central Indian Ridge (8°S-17°S). *Geochemistry, Geophysics, Geosystems*.
- Langmuir, C.H., Klein, E.M., Plank, T., 2013. Petrological Systematics of Mid-Ocean Ridge Basalts: Constraints on Melt Generation Beneath Ocean Ridges, Mantle Flow and Melt Generation at Mid-Ocean Ridges. American Geophysical Union, pp. 183-280.
- le Roux, P.J. et al., 2002. Mantle heterogeneity beneath the southern Mid-Atlantic Ridge: trace element evidence for contamination of ambient asthenospheric mantle. *Earth and Planetary Science Letters*, 203(1): 479-498.
- Lissenberg, C.J., Dick, H.J.B., 2008. Melt–rock reaction in the lower oceanic crust and its implications for the genesis of mid-ocean ridge basalt. *Earth and Planetary Science Letters*, 271(1): 311-325.
- Lissenberg, C.J., MacLeod, C.J., Bennett, E.N., 2019. Consequences of a crystal mush-dominated magma plumbing system: a mid-ocean ridge perspective. *Philosophical Transactions of the Royal Society A: Mathematical, Physical and Engineering Sciences*, 377(2139): 20180014.
- Liu, C.Z. et al., 2008. Ancient, highly heterogeneous mantle beneath Gakkel Ridge, Arctic Ocean. *Nature*, 452(7185): 311-6.
- Mahoney, J.J. et al., 1989. Isotopic and geochemical provinces of the western Indian Ocean Spreading Centers. *Journal of Geophysical Research: Solid Earth*, 94(B4): 4033-4052.
- Mallick, S., Dick, H.J.B., Sachi-Kocher, A., Salters, V.J.M., 2014. Isotope and trace element insights into heterogeneity of subridge mantle. *Geochemistry, Geophysics, Geosystems*, 15(6): 2438-2453.
- Matzen, A.K., Wood, B.J., Baker, M.B., Stolper, E.M., 2017. The roles of pyroxenite and peridotite in the mantle sources of oceanic basalts. *Nature Geoscience*.
- Michael, P.J. et al., 2003. Magmatic and amagmatic seafloor generation at the ultraslow-spreading Gakkel Ridge, Arctic Ocean. *Nature*, 423(6943): 956-961.
- Mühe, R., Bohrmann, H., Garbe-Schönberg, D., Kassens, H., 1997. E-MORB glasses from the Gakkel Ridge (Arctic Ocean) at 87°N: evidence for the Earth's most northerly volcanic activity. *Earth and Planetary Science Letters*, 152(1–4): 1-9.
- Mühe, R., Devey, C.W., Bohrmann, H., 1993. Isotope and trace element geochemistry of MORB from the Nansen-Gakkel Ridge at 86° north. *Earth and Planetary Science Letters*, 120(3–4): 103-109.
- Mühe, R.K., Bohrmann, H., Hörmann, P.K., Thiede, J., Stoffers, P., 1991. The Geology, Geophysics and Metallogeny of the Present-Day Oceans Spinifex basalts with komatiite-tholeiite trend from the Nansen-Gakkel Ridge (Arctic Ocean). *Tectonophysics*, 190(1): 95-108.
- O'Neill, H.S., Jenner, F.E., 2012. The global pattern of trace-element distributions in ocean floor basalts. *Nature*, 491(7426): 698-704.
- Pearce, J.A., Stern, R.J., 2013. Origin of Back-Arc Basin Magmas: Trace Element and Isotope Perspectives, Back-Arc Spreading Systems: Geological, Biological, Chemical, and Physical Interactions. American Geophysical Union, pp. 63-86.
- Pedersen, R.B. et al., 2010. Discovery of a black smoker vent field and vent fauna at the Arctic Mid-Ocean Ridge. *Nat Commun*, 1: 126.
- Phipps Morgan, J., Ghen, Y.J., 1993. Dependence of ridge-axis morphology on magma supply and spreading rate. *Nature*, 364: 706.
- Rehkämper, M., Hofmann, A.W., 1997. Recycled ocean crust and sediment in Indian Ocean MORB. *Earth and Planetary Science Letters*, 147(1–4): 93-106.
- Ribeiro, J.M. et al., 2013. Nature and distribution of slab-derived fluids and mantle sources beneath the Southeast Mariana forearc rift. *Geochemistry, Geophysics, Geosystems*, 14(10): 4585-4607.
- Richards, M.A., Engebretson, D.C., 1992. Large-scale mantle convection and the history of subduction. *Nature*, 355(6359): 437-440.
- Rubin, K.H., Sinton, J.M., 2007. Inferences on mid-ocean ridge thermal and magmatic structure from MORB compositions. *Earth and Planetary Science Letters*, 260(1-2): 257-276.
- Rubin, K.H., Sinton, J.M., MacLennan, J., Hellebrand, E., 2009. Magmatic filtering of mantle compositions at mid-ocean-ridge volcanoes. *Nature Geoscience*, 2: 321.
- Salters, V.J.M., Dick, H., 2011. Ultra Depleted Mantle at the Gakkel Ridge Based on Hafnium and Neodymium Isotopes, American Geophysical Union, Fall Meeting 2011, pp. V41G-02.
- Salters, V.J.M., Mallick, S., Hart, S.R., Langmuir, C.E., Stracke, A., 2011. Domains of depleted mantle: New evidence from hafnium and neodymium isotopes. *Geochemistry, Geophysics, Geosystems*, 12(8): n/a-n/a.
- Schmidt-Aursch, M.C., Jokat, W., 2016. 3D gravity modelling reveals off-axis crustal thickness variations along the western Gakkel Ridge (Arctic Ocean). *Tectonophysics*.

- Shephard, G.E., Müller, R.D., Seton, M., 2013. The tectonic evolution of the Arctic since Pangea breakup: Integrating constraints from surface geology and geophysics with mantle structure. *Earth-Science Reviews*, 124: 148-183.
- Snow, J.E., Edmonds, H.N., 2007. Ultraslow-Spreading Ridges Rapid Paradigm Changes. *Oceanography*, 20(1): 90-101.
- Sobolev, A.V., Shimizu, N., 1993. Ultra-depleted primary melt included in an olivine from the Mid-Atlantic Ridge. *Nature*, 363: 151.
- Sokolov, S.Y., Mazarovich, A.O., 2016. Cluster analysis of geological and geophysical parameters of the Arctic region as the base for geodynamic interpretation. *Geodynamics & Tectonophysics*, 7(1): 59 - 83.
- Standish, J.J., Dick, H.J.B., Michael, P.J., Melson, W.G., O'Hearn, T., 2008. MORB generation beneath the ultraslow-spreading Southwest Indian Ridge (9-25°E): Major element chemistry and the importance of process versus source. *Geochemistry, Geophysics, Geosystems*, 9(5): Q05004.
- Stracke, A. et al., 2011. Abyssal peridotite Hf isotopes identify extreme mantle depletion. *Earth and Planetary Science Letters*, 308(3-4): 359-368.
- Teng, F.-Z., Dauphas, N., Huang, S., Marty, B., 2013. Iron isotopic systematics of oceanic basalts. *Geochimica et Cosmochimica Acta*, 107: 12-26.
- Warren, J.M., Shirey, S.B., 2012. Lead and osmium isotopic constraints on the oceanic mantle from single abyssal peridotite sulfides. *Earth and Planetary Science Letters*, 359-360: 279-293.
- Weyer, S., 2008. What Drives Iron Isotope Fractionation in Magma? *Science*, 320(5883): 1600-1601.
- White, W.M., 2015. Isotopes, DUPAL, LLSVPs, and Anekantavada. *Chemical Geology*, 419: 10-28.
- Whittaker, J.M., Muller, R.D., Roest, W.R., Wessel, P., Smith, W.H., 2008. How supercontinents and superoceans affect seafloor roughness. *Nature*, 456(7224): 938-41.
- Williams, H.M. et al., 2004. Iron Isotope Fractionation and the Oxygen Fugacity of the Mantle. *Science*, 304(5677): 1656-1659.
- Wood, D.A., 1979. A variably veined suboceanic upper mantle—Genetic significance for mid-ocean ridge basalts from geochemical evidence. *Geology*, 7(10): 499-503.
- Zartman, R.E., Haines, S.M., 1988. The plumbotectonic model for Pb isotopic systematics among major terrestrial reservoirs—A case for bi-directional transport. *Geochimica et Cosmochimica Acta*, 52(6): 1327-1339.
- Zindler, A., Hart, S., 1986. Chemical Geodynamics. *Annual Review of Earth and Planetary Sciences*, 14(1): 493-571.



## CHAPTER 2

### *Samples and Methodology*

---



*Photograph shows the drill vessel in the Arctic Ocean.*

*(<https://www.renci.org/wp-content/uploads/2012/05/Arctic2011-485.png>)*

## 2.1 Introduction

This chapter provides an overview of the sample suite and the analytical methods. In total, thirty-six dredged ocean floor basalts and volcanic glass samples were investigated for major and trace elements, platinum group elements, and stable (Fe, S) and radiogenic (Pb, Sr, Hf) isotope compositions. An overview of each analysed sample and the available data is summarised in Table 2.1 and Table 2.2. To minimize repetitions in this thesis, only a brief outline of the analytical methodology is provided in this chapter. A detailed description of each of the applied methods will follow in the relevant research chapters (chapters 3 – 6), including sample preparation, analytical settings and analytical uncertainty.

## 2.2 Samples

As previously described, the Gakkel Ridge comprises three ridge segments, namely the Western Volcanic Zone (WVZ), the Sparsely Magmatic Zone (SMZ) and the Eastern Volcanic Zone (EVZ). In total, 36 dredged basalts were analysed, of which 17 are from the WVZ (Figure 2.1), 5 from the SMZ (Figure 2.2) and 14 from the EVZ (Figure 2.3). The samples used in this study were collected during five research cruises to the Arctic Ocean: Polarstern 59, Polarstern 66, Polarstern 86, Polarstern 101 and Healy 102.

The smaller number of samples from the SMZ, compared to the WVZ and the EVZ, is attributed to the smaller sample density and the lack of volcanic centres along this ridge segment. The selection criteria for the samples was the availability, the freshness (no alteration) of the sample (Figure 2.1 – 2.3); and the locality. The samples have a good spatial distribution across the entire ridge and are complementary to previous studies. The locality of each sample is provided in Table 2.1.

Out of 36 samples, 20 basalts contained a thin crust of volcanic glass, which has been carefully separated for element and isotope analysis and compared to with bulk rock basalt data of the same sample (section 2.2). Alteration and/or freshness of the samples is further discussed in section 2.2.

### 2.2.1 Sample preparation

Basalt samples were cut and any existing weathering manually ground off to reveal the fresh sample (dark-grey colour). Then, the samples were sonicated in ultrapure water to remove any particles from the grinding process and were crushed. Crushed rock fragments were handpicked (only material from the inside of the cut basalt slab) and placed into an agate mill for milling to yield fine sample powder.

*Table 2.1 – Sample locality.*

#	Sample name	Ridge segment	Latitude	Longitude	Spreading rate [mm/a]
1	HLY0102 D011 - 19	WVZ	82.60	-6.19	12.82
2	HLY0102 D8 - 12	WVZ	82.53	-6.16	12.82
3	PS 66 217-16 (B)	WVZ	82.86	-6.15	12.82
4	PS 86 -019 (B)	WVZ	82.53	-6.15	12.82
5	PS 86 - 67 (VG)	WVZ	82.53	-6.15	12.82
6	PS 86 - 044 (VG)	WVZ	82.53	-6.15	12.82
7	PS 59 216 (B)	WVZ	83.09	-6.10	12.82
8	PS 59 216-11 (B)	WVZ	83.09	-6.10	12.82
9	PS 59 216-13 (B)	WVZ	83.09	-6.10	12.82
10	HLY0102 D013 - 10	WVZ	83.20	-5.43	12.82
11	PS 59 231 - 14	WVZ	83.96	-0.40	12.51
12	PS 59 232 - 84	WVZ	84.17	0.88	12.31
13	HLY0102 D024 - 2	WVZ	84.55	1.39	12.03
14	HLY0102 D026 - 9	WVZ	84.28	2.34	12.31
15	HLY0102 D018 - 1	WVZ	83.42	2.54	12.70
16	PS 59 234 - 24	WVZ	84.57	3.13	12.03
17	PS 59 224 - 34	WVZ	83.38	3.66	12.70
18	PS 59 243 - 36	SMZ	84.97	10.15	11.67
19	HLY0102 D037 - 5	SMZ	85.18	11.30	11.67
20	HLY0102 D036 - 35	SMZ	85.16	12.20	11.67
21	HLY0102 D038 - 6	SMZ	85.19	12.42	11.67
22	PS 59 251 - 4	SMZ	85.71	20.23	11.39
23	PS 59 263 - 26	EVZ	86.04	30.63	11.09
24	HLY0102 D050 - 30	EVZ	86.20	37.47	11.09
25	HLY0102 D051 - 15	EVZ	86.33	43.29	11.09
26	PS 59 297 - 11	EVZ	86.67	46.86	10.75
27	PS 101 186 R1 (B)	EVZ	86.58	55.41	10.75
28	PS 101 186 (VG)	EVZ	86.58	55.41	10.75
29	PS 59 294 - 40	EVZ	86.90	56.41	10.75
30	PS 101 193 R1	EVZ	86.44	61.25	10.75
31	PS 101 203 R4	EVZ	86.53	61.37	10.75
32	PS 101 203 R5	EVZ	86.53	61.37	10.75
33	PS 101 203 R8	EVZ	86.53	61.37	10.75
34	PS 59 274 - 52	EVZ	86.73	66.76	10.75
35	HLY0102 D059 - 35	EVZ	86.27	70.59	11.09
36	HLY0102 D061 - 11	EVZ	85.38	84.60	10.31

Volcanic glass shards, used here, were thoroughly cleaned under a microscope and in an ultrasonic bath (mixture of ethanol + ultrapure water) to remove rust and any dust particles, prior the milling process.

## Chapter 2

**Table 2.2 – Overview of the entire sample suite.** This table provides a brief overview of the samples and geochemical analysis. The number (#) indicates the sample number, which is linked to Table 2.1. ME – Major elements; TE – Trace elements; PGE – Platinum group elements

#	Sample description				Geochemical analysis									
	Material (B - basalt; VG - volcanic glass)	Alteration (Yes/No)	Phenocrysts (Yes/No)	LOI	ME <sup>1</sup>	TE <sup>2</sup>	PGE <sup>3</sup>	S content in VG <sup>4</sup>	Isotopes					
									Pb <sup>2,5</sup>	Sr <sup>2</sup>	Hf <sup>2</sup>	Fe <sup>2</sup>	S <sup>6</sup>	
1	B; VG	No (fresh)	No	0.02	x	x	x	x	x	x	x	x	x	x
2	B; VG	Yes (slightly)	Yes (few disseminated; <1 mm)	-0.23	x	x	-	x	x	x	x	x	x	x
3	B; VG	No (fresh)	No	0.01	x	x	x	x	x	x	x	x	x	(x)
4	B	No (fresh)	No	-0.37	x	x	-	-	x	x	x	x	x	-
5	B; VG	No (fresh)	No	-0.58	x	x	x	x	x	x	x	x	x	-
6	B; VG	No (fresh)	No	-0.45	x	x	x	x	x	x	x	x	x	(x)
7	B; VG	No (fresh)	No	-0.17	x	x	-	x	x	x	x	x	x	-
8	B; VG	No (fresh)	No	-0.18	x	x	-	x	x	x	x	x	x	-
9	B	No (fresh)	No	-0.23	x	x	-	-	x	x	x	x	x	-
10	B	No (fresh)	No	1.48	x	x	-	-	x	x	x	x	x	-
11	B	No (fresh)	Yes (few disseminated; <0.5 cm)	0.11	x	x	-	-	x	x	x	x	x	-
12	B	No (fresh)	No	-0.06	x	x	x	-	x	x	x	x	x	-
13	B	Yes (slightly)	Yes (disseminated; <4 mm)	0.64	x	x	-	-	x	x	x	x	x	-
14	B; VG	No (fresh)	Yes (few disseminated; <2 mm)	-0.22	x	x	x	x	x	x	x	x	x	x
15	B	No (fresh)	Yes (few disseminated; <1 mm)	-0.18	x	x	-	-	x	x	x	x	x	-
16	B; VG	No (fresh)	Yes (few disseminated; <1 mm)	-0.25	x	x	-	x	x	x	x	x	x	(x)
17	B	Yes (slightly)	Yes (few disseminated; <0.5 cm)	1.71	x	x	x	-	x	x	x	x	x	-
18	B	Yes (slightly)	Yes (few disseminated; 0.5 cm)	0.30	x	x	-	-	x	x	x	x	x	-
19	B; VG	No (fresh)	No	-0.01	x	x	x	x	x	x	x	x	x	x
20	B; VG	No (fresh)	No	0.32	x	x	x	x	x	x	x	x	x	x
21	B; VG	No (fresh)	No	-0.02	x	x	x	x	x	x	x	x	x	(x)
22	B	Yes (slightly)	Yes (few disseminated; < 0.7 cm)	0.99	x	x	x	-	x	x	x	x	x	-
23	B	No (fresh)	Yes (disseminated; <4 mm)	0.69	x	x	x	-	x	x	x	x	x	-
24	B; VG	No (fresh)	No	-0.01	x	x	x	x	x	x	x	x	x	x
25	B; VG	No (fresh)	No	-0.21	x	x	-	x	-	x	x	x	x	-
26	B; VG	No (fresh)	Yes (few disseminated; <1 mm)	-0.53	x	x	x	x	x	x	x	-	x	-
27	B	No (fresh)	No	-0.05	x	x	-	-	x	x	x	x	x	-
28	B; VG	No (fresh)	No	-0.39	x	x	-	x	x	x	x	x	x	(x)
29	B; VG	No (fresh)	No	0.20	x	x	-	x	x	x	x	x	x	-
30	B	Yes (slightly)	Yes (few disseminated; <1 mm)	1.66	x	x	-	-	x	x	x	x	x	-
31	B	No (fresh)	Yes (up to 2 cm)	3.10	x	x	-	-	x	x	x	x	x	-
32	B	No (fresh)		2.93	x	x	-	-	x	x	x	x	x	-
33	B	No (fresh)	Yes (few disseminated; <1 mm)	3.11	x	x	-	-	x	x	x	x	x	-
34	B; VG	No (fresh)	Yes (few disseminated; <1 mm)	-0.37	x	x	x	x	x	x	x	x	x	-
35	B; VG	No (fresh)	No	-0.15	x	x	-	x	x	x	x	x	x	-
36	B; VG	No (fresh)	No	-0.26	x	x	x	x	x	x	x	x	x	x

(x) - awaiting data (Update: 12/2018)

1 - Analysis at Codes University, Tasmania, Australia (J. Thompson)

2 - LA-ICP-MS/MC-ICP-MS analysis at Monash Isotopia laboratory, Clayton, Australia

3 - Analysis at the University of Seoul, South Korea (J.-W. Park)

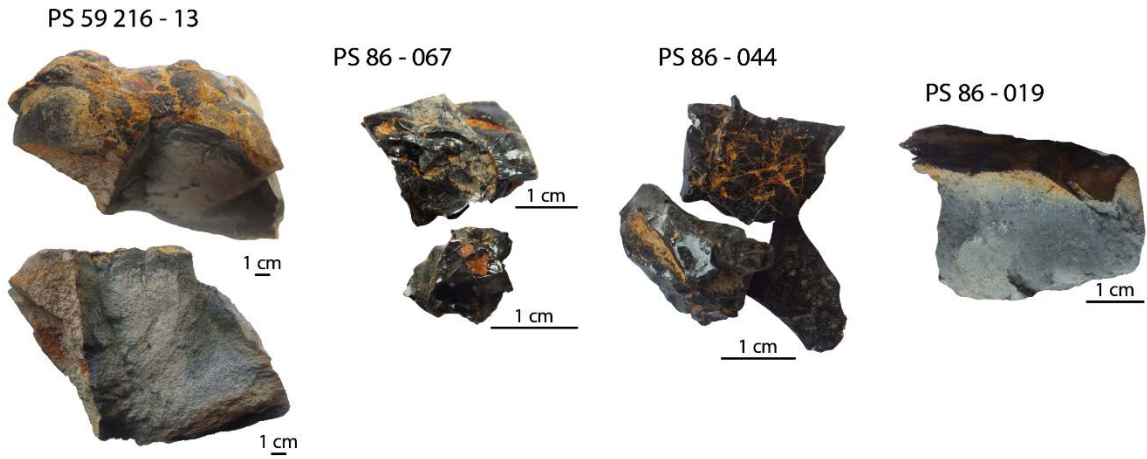
4 - Microprobe analysis at the CSIRO, Clayton, Australia (N. Wilson)

5 - MC-ICP-MS (Nu plasama) analysis at University of Melbourne, Parkville, Australia (R. Maas)

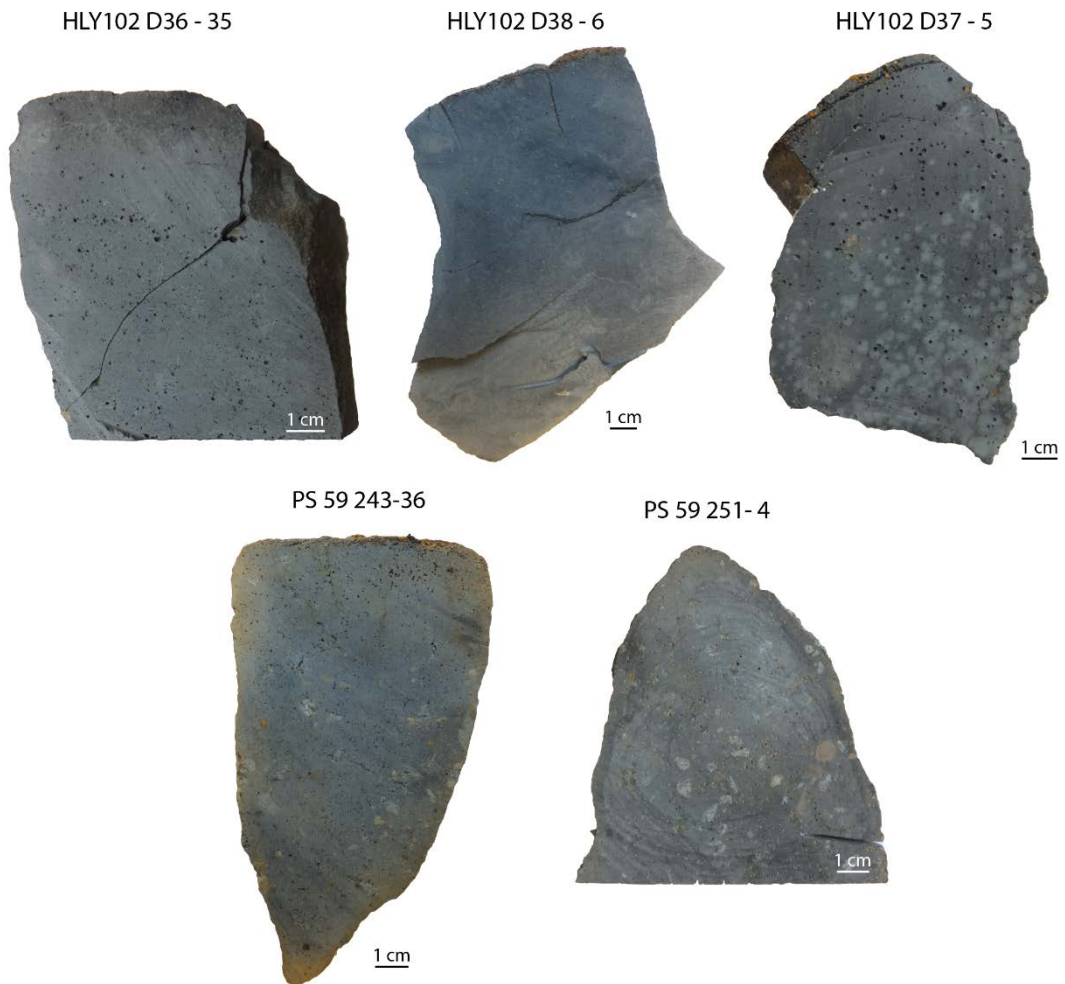
6 - MC-ICP-MS at the University of Maryland, Maryland, United States of America (J. Farquhar/J. Dotton III)



Figure 2.1: Sample suite of the Western Volcanic Zone.



*Figure 2.1: [continued]*



*Figure 2.2: Sample suite of the Sparsely Magmatic Zone.*

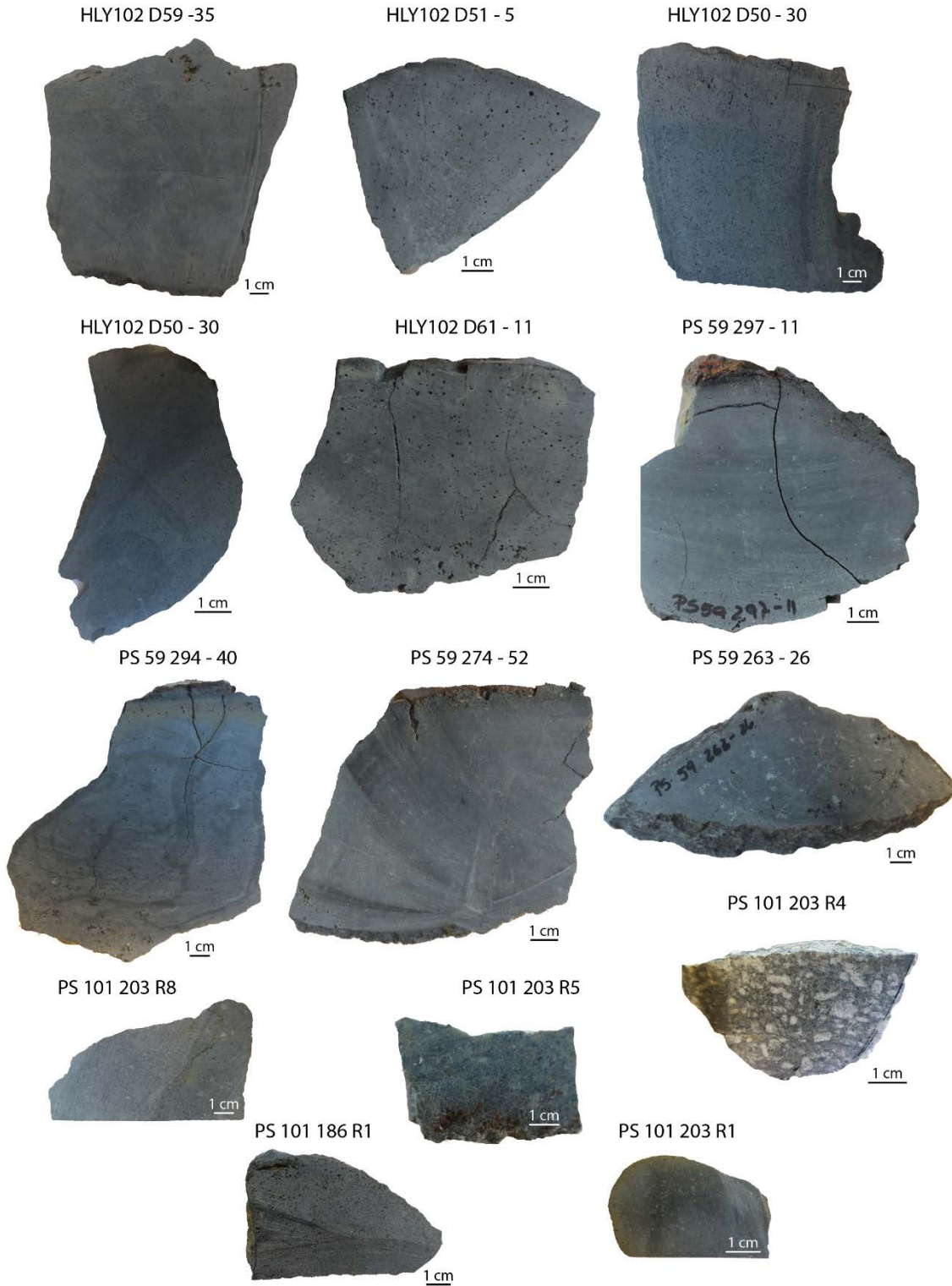


Figure 2.3: Sample suite of the Eastern Volcanic Zone.

## 2.3 Methodology

This section gives a broad overview of the applied methods and procedures (Figure 2.4). A fraction of the sample powder (~5 mg) has been used for major and trace element analysis (section 2.3.1 and 2.3.2) and only 100 mg of the powder has been dissolved in a mixture (1:5) of concentrated HF (24 M) and concentrated HNO<sub>3</sub> (16 M). From the digested sample Fe, Hf, Pb and Sr from the sample matrix were separated. In addition, S isotope and platinum group element (PGE) analyses were carried out on selected samples by external collaborators.

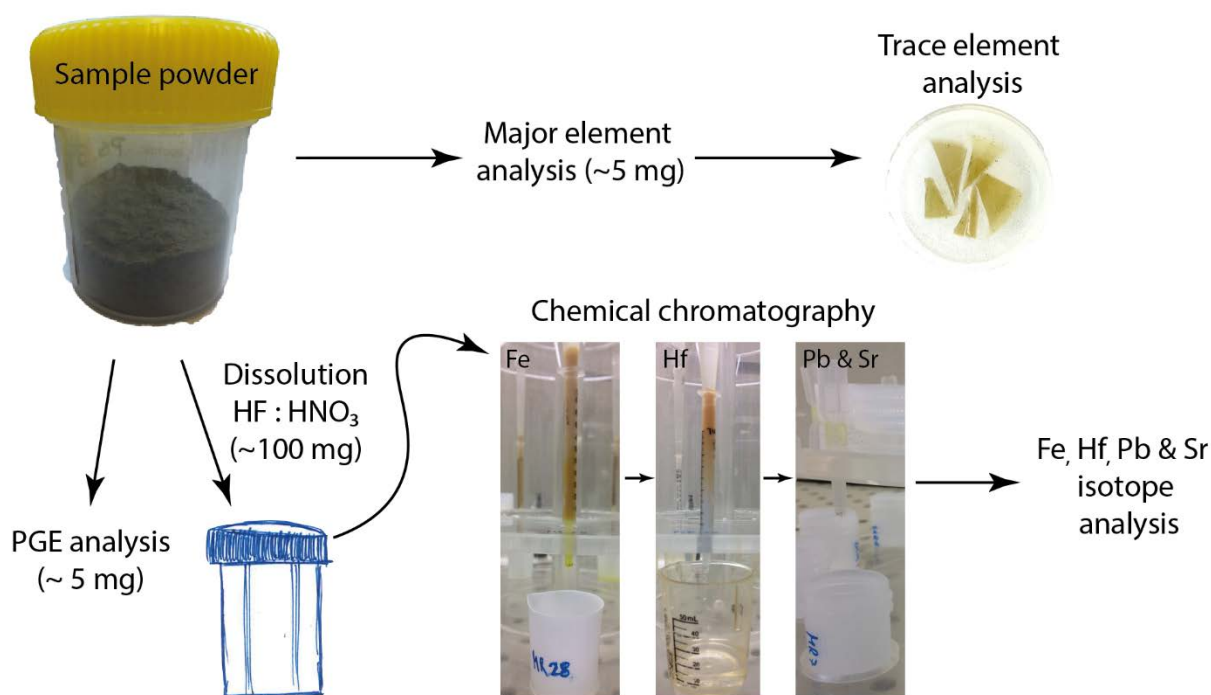


Figure 2.4 - Schematic overview of the main analytical work.

### 2.3.1 Major element and alteration

Basalt major element analysis was performed at the CODES (Centre for Ore Deposit and Earth Sciences) at the University of Tasmania by J. Thompson. Three milligrams of each sample as admixed with a Lithium: Borate flux and fused to glass. The flux used for this study is clean with little trace element contaminations, allowing trace element analysis of fragments of each XRF glass by laser ablation inductively coupled mass spectrometry (LA-ICP-MS, section 2.3.2). Major element concentration of the volcanic glass fragments was determined using an Electron Microprobe Jeol JXA 8530F (Hyperprobe) at the Commonwealth Science and Industry Research Organisation (CSIRO) in Melbourne. The analytical procedure for basalts and volcanic glasses is described in chapters 3 and 6, respectively.

## 2.3.1.1 Alteration

To account for any alteration of the basalt samples, loss on ignition (LOI, heating to approx. 1000°C) was determined for all whole-rock samples. LOI is an indicator of alteration in basalts. LOI values >3.2 wt.% indicate a low to moderate alteration (e.g. Sano et al., 2012). In general, basalts range between -1.0 wt.% and +1.0 wt.% (Francis, 1986; e.g., Sano et al., 2012). LOI for the basalts analysed in this study ranges between -0.58 wt.% and +3.11 wt.%, with only six out of 36 samples having a LOI of >1.0 wt.%. Negative LOI results from mass gain via oxidation of FeO to Fe<sub>2</sub>O<sub>3</sub> (Lechler and Desilets, 1987; Teklay et al., 2010).

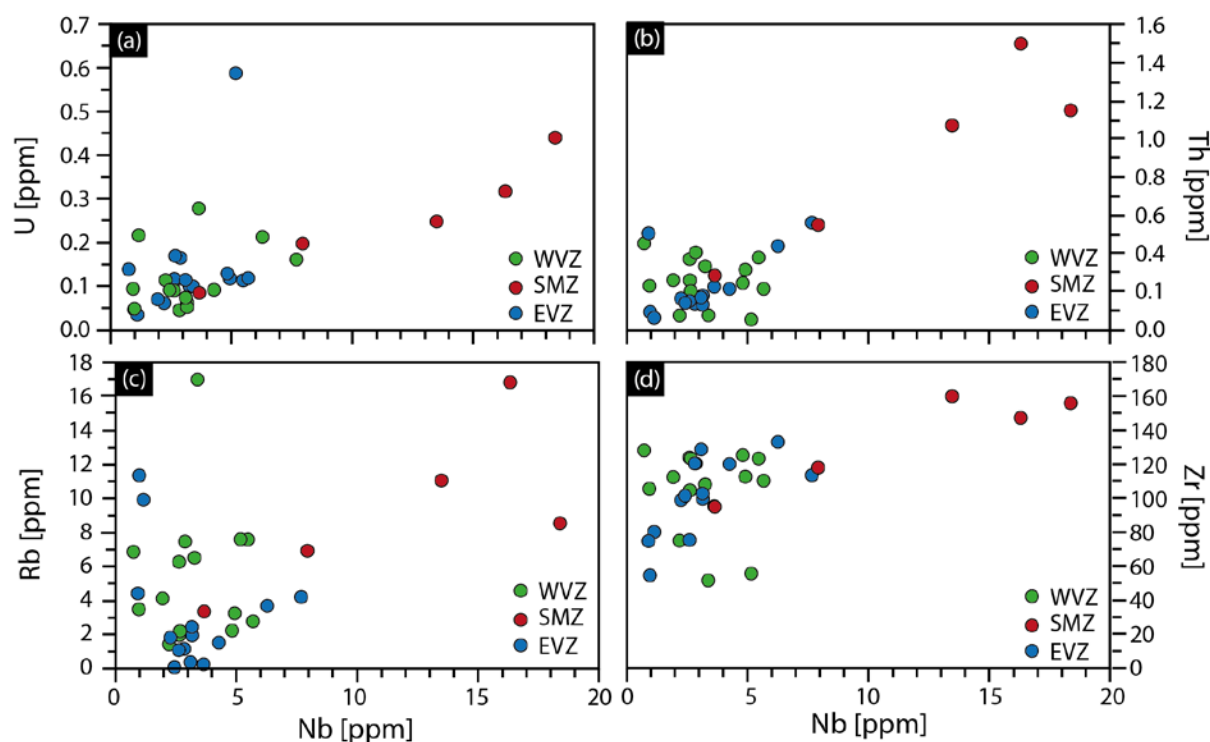


**Figure 2.5 – Alteration test.** Comparison of U (a), Th (b), Rb (c) and Zr (d) versus Nb. U (a) and Rb (c) are mobile elements and generally affected by alteration, compared to Th (b) and Zr (d). Niobium is an immobile element and not affected by any alteration effects.

To further evaluate the alteration of the basalts, mobile (U, Rb) and immobile (Th, Zr, Nb) elements (Kelley et al., 2003; Salters and Sachi-Kocher, 2010) that are affected by alteration (U and Rb) are compared in Figure 2.5. In this thesis, basalts are analysed for their Sr and Pb isotope signature. Rubidium (parent nuclide of Sr) and U (parent nuclide of Pb) are both thought to be mobile during alteration, which could result in a positive effect on Pb and Sr isotope ratios, because of a gain in Rb and U during alteration (Bach et al., 2001; Kelley et al., 2003; Staudigel et al., 1996).. The scatter, as shown in Figure 3.5, of U and Th versus Nb is similar, whereas Rb and Zr versus Nb show slight differences. Only a

few samples show a higher Rb for a given Nb value. The samples with a slightly higher scatter in Rb show a LOI of around 1 wt.%, which is in range of unaltered basalts and consistent with data from similar locality (Gale et al., 2013; Goldstein et al., 2008; Mühe et al., 1997). I therefore conclude that the variation of U and Rb, as well as Th and Zr, are due to source heterogeneity and magmatic processes. The effect of alteration is therefore negligible for Pb and Sr isotope studies on the Gakkel basalts.

### ***2.3.2 Trace element***

Trace element data was obtained from fragments of fused XRF glasses and volcanic glass fragments mounted in one-inch epoxy resin discs (Figure 2.6). The trace element analyses were measured in the Isotopia Laboratory at the School of Earth, Atmosphere and Environment, using an ASI RESOLUTION S-155 193nm laser coupled to ThermoFisher ICapQ/ICapTQ. The entire sample suite was measured over two analytical sessions. For the first run (161218 – whole rock XRF glasses; chapters 3 and 4) the laser was coupled with a ThermoFisher Scientific ICapQ quadrupole mass spectrometer, and for the second run (171216 – volcanic glasses, chapter 6) with a ThermoFisher ICapTQ triple-quadrupole mass spectrometer. Identical laser settings were applied in both analytical sessions, using a spot size of 80  $\mu\text{m}$ , a repetition rate of 10 Hz and a laser fluence  $\sim 5 \text{ mJ/cm}^2$ . Five volcanic glass samples were analysed in both analytical sessions for controlling the quality of the data.

During both analytical sessions, reference material NIST 610 (synthetic glass), NIST 612 (synthetic glass), BCR2G (basalt glass) and BHVO2G (basalt glass) were analysed two to three times in between a block of 20 unknowns. BCR2G was chosen as calibration reference sample and data was normalized on Si (obtained from XRF analysis). Furthermore, the reference material BHVO2G was used for data controlling. Uncertainty and precision of the main trace elements used in this study is provided in each individual research chapter, as well as operational settings and data evaluation are explained in chapters 3, 4 and 6.

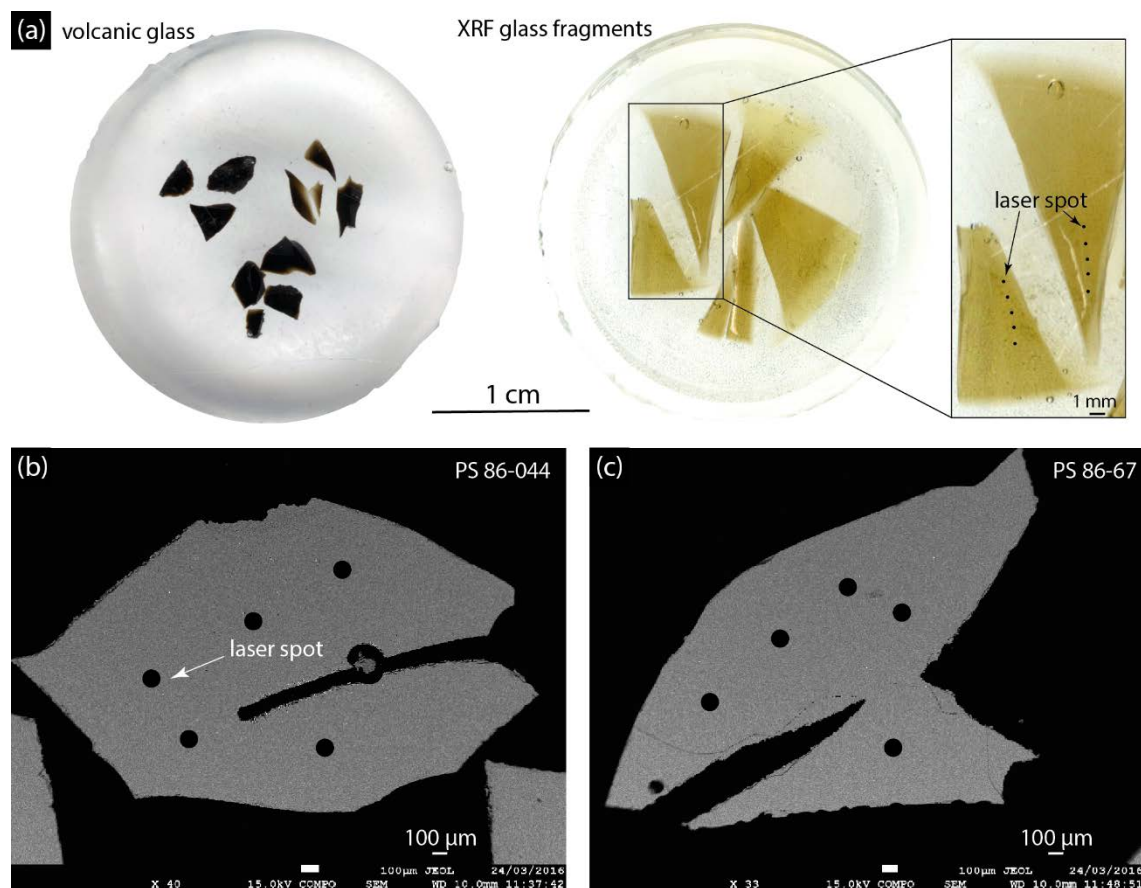


**Figure 2.6 - Epoxy mounts and backscattered image of two volcanic glass shards.** (a) The left epoxy mount shows volcanic glass samples and the left shows mounted fragments of the XRF glasses. The mounts have been polished down until 90% of the sample became visible under the microscope. The zoomed in section of the XRF glasses, on the right, shows the laser spots. The laser spots have been arranged in a line to gain an average composition of the XRF glass, to account for potential heterogeneity in the XRF glasses. (b) and (c) show backscattered images (obtained by Scanning electron microscope technique) and laser spot location of two volcanic glass shards from sample PS 86-044 and PS 86-67. The laser spots were set across the homogeneous glass shard.

### 2.3.3 Comparison between whole-rock XRF-glasses and volcanic glass shards

To further test the accuracy and reproducibility of the major and trace element data, as well as the homogeneity of the XRF glasses, the obtained data for of the whole-rock basalts (XRF glasses) have been compared with the volcanic glass shards of the corresponding sample. Figure 2.7 shows the comparison of the main major and trace element of the volcanic glasses and fused sample glasses used in this thesis. Major and trace element data shows a good correlation between the volcanic glasses and fused XRF glasses in particular for MgO, TiO<sub>2</sub>, FeO, K<sub>2</sub>O, CaO, Ba, Ni, Sr, Pb, Th, Zr, Rb and a moderate correlation for U. Only Cu shows a poor correlation of between the volcanic glass and XRF glass. This could be due to incomplete ionization of <sup>63</sup>Cu in the ICP-MS plasma or insufficient energy density during the ablation (e.g., Jackson and Günther, 2003).

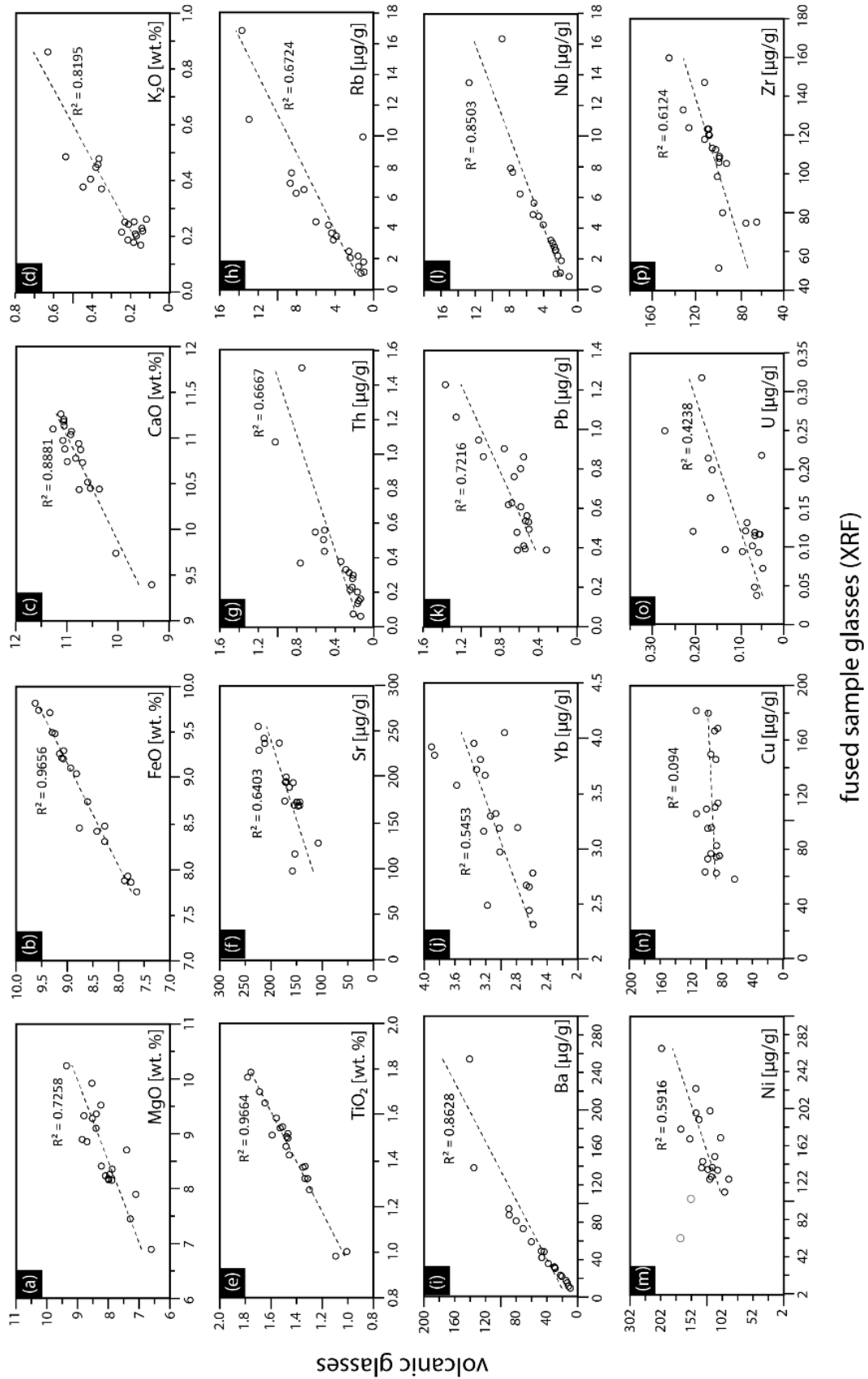


**Figure 2.7 – Comparison between volcanic glasses and whole-rock XRF glasses.** Major and trace element concentration that are mainly used in this thesis are presented in this figure. (a) MgO; (b) FeO; (c) CaO; (d) K<sub>2</sub>O; (e) TiO<sub>2</sub>; (f) Sr; (g) Th; (h) Rb; (i) Ba; (j) Yb; (k) Pb; (l) Nb; (m) Ni – the two light grey coloured dots are not included in the correlation,

because they appear as outlier; (n) Cu; (o) U; (p) Zr. All data has been plot together and has not been distinguished in different ridge segments. Data shown in this graph only shows the samples with available basalts and volcanic glass material.

### 2.3.4 Comparison between LA-ICP-MS and X-ray fluorescence spectroscopy (XRF)/Electron Microprobe analyser (EMPA)

Figures 2.9 and 2.10 show a comparison of major element content determined by both XRF/EMPA and LA-ICP-MS techniques for the fused XRF glasses and the volcanic glass shards. It has to be noted that only the trace element data determined by LA-ICP-MS is used in this study. The comparison, shown in Figures 2.9 and 2.10, is used to cross-check the techniques and the reproducibility of the data. Silica ( $\text{SiO}_2$  in wt.%; determined by XRF) was used to normalize the data obtained by LA-ICP-MS, therefore the correlation of  $\text{SiO}_2$  between both techniques is 1:1. The LA-ICP-MS data was given in  $\mu\text{g/g}$ , which has been converted to wt.% using a stoichiometric coefficient ( $\text{CaO} = 1.39919$ ;  $\text{MgO} = 1.65810$ ;  $\text{FeO} = 1.28649$ ;  $\text{Fe}_2\text{O}_3 = 1.42974$ ;  $\text{K}_2\text{O} = 1.20459$ ;  $\text{TiO}_2 = 1.66803$ ;  $\text{Na}_2\text{O} = 1.34796$ ) for comparison with major element data obtained by XRF/EMPA. Major element concentration of the whole rock basalts solely correlate moderately between XRF analysis and LA-ICP-MS, whereas major element data for volcanic glass correlate well between both techniques. The poor correlation for whole-rock basalts could be due to ablation material (absorption), insufficient ionization and/or a lower laser pulse energy.

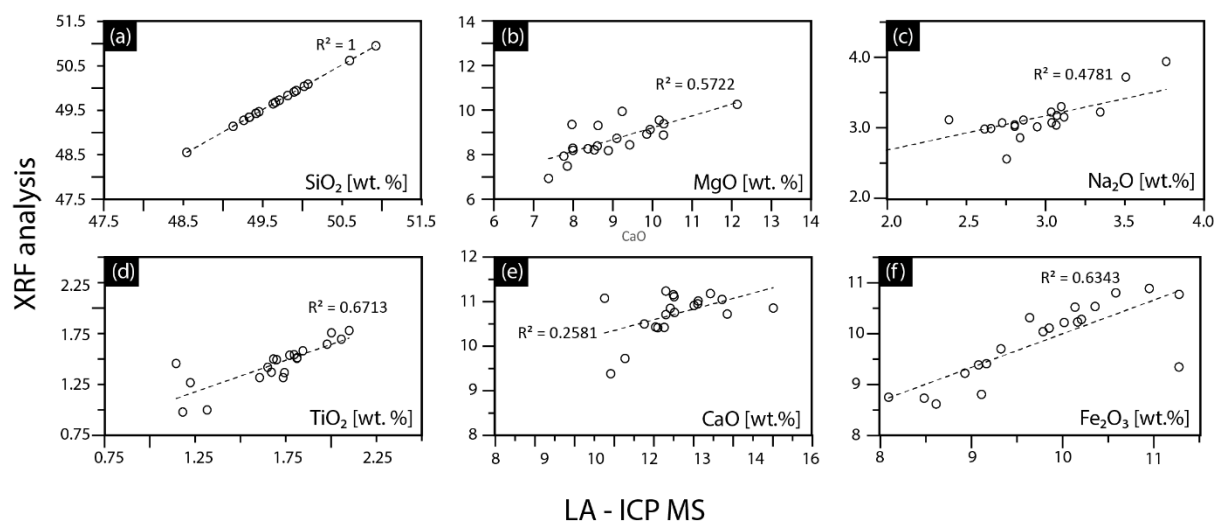


Figure 2.8 – Comparison of the major element composition of the basalts obtained by XRF and LA-ICP-MS analysis.

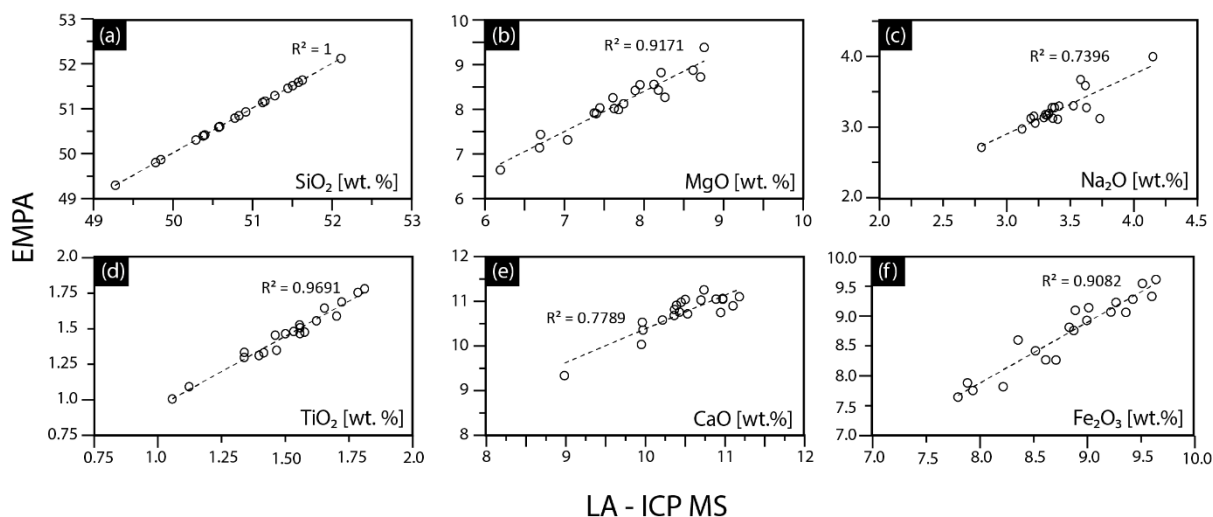


Figure 2.9 – Comparison of the major element composition of the volcanic glasses obtained by XRF and LA-ICP-MS analysis.

### 2.3.5 Platinum Group Elements (PGE)

Sixteen out of 36 samples were chosen for PGE analysis. Two milligrams of whole-rock sample powder was analysed for PGE at the University of Seoul by J.-W. Park. In brief, the sample powder was thoroughly mixed with a Ni, S and Na borax powder and fused to a sample-Ni-sulfide bead. After quenching, the bead was digested and PGE content measured with a Thermo Scientific ICAP-Q ICP-MS in the Korea Polar Research Institute, South Korea. In total two analytical session were performed. During the second analytical session, repeats were undertaken to test the accuracy and reproducibility of the analysis. In addition to this, TDB-1 was used as reference material in both analytical sessions. A detailed description of the method, operational settings and the PGE data is presented in chapter 6.

### 2.3.6 Isotope analysis

This section provides a brief overview of all isotope analyses undertaken in this thesis. For data control, BCR1 and BHVO1 (unless stated differently) were used as reference material for radiogenic isotope and Fe isotope analysis. For Fe, Hf, Sr and Pb isotope analysis, 100 mg sample powder of each basalt and reference material (BCR1 and BHVO1) was weighed and digested using a mixture of concentrated HF and concentrated HNO<sub>3</sub> (1:5). The dissolved sample was dried down several times and taken up in 2 ml 9M HCl for chromatographic separation. All samples were centrifuged before purification of iron, followed by Hf, Sr and Pb. After the chromatographic extraction, the samples were taken up in weak HNO<sub>3</sub> and measured in the Isotopia Laboratory at Monash University

using a ThermoFisher NeptunePlus multicollector ICP-MS. In addition to the radiogenic and iron isotope analysis, S isotope analysis on selected samples was obtained. For this, 1 mg of volcanic glass was processed and analysed at the University of Maryland in collaboration with J. Dottin III and J. Farquhar.

### 2.3.6.1 Fe isotopes

Iron has been separated from the sample matrix using the chemical purification procedure of Sossi et al. (2012) and Cheng et al. (2014). The measurements were collected in four analytical sessions (170530, 170725, 180425 and 180502) in solution mode. The samples were introduced via a glass spray chamber into the multicollector ICP-MS. Each sample was measured at least three times using standard-bracketing method, in which each sample analysis is bracketed in-between analysis of a reference sample. The international standard IRMM-542a (Craddock and Dauphas, 2011) was used as reference material. All Fe isotope data is given as  $\delta$ -notation and normalized to the IRMM-542a. Further analytical details and operational settings are described in chapter 5. Both measured reference materials are within 2SE uncertainty from the literature value. Iron isotope composition of the reference material BCR1 and BHVO1 are listed in Table 2.3.

**Table 2.3 - Iron isotope composition (given in ‰) of BHVO1 and BCR1.** The data are compared to literature data that measured BHVO1 (Sossi et al., 2012). For BCR 1 data can be roughly compared to BCR 2, because BCR 2 is the new reference material batch of BCR 1. BCR 2 data from Sossi et al. (2012).

Sample Name	Run	Measured		Uncertainty (2SE)	
		$\delta^{56}\text{Fe}$	$\delta^{57}\text{Fe}$	$\delta^{56}\text{Fe}$	$\delta^{57}\text{Fe}$
BHVO 1	170530	0.11	0.18	0.04	0.04
BHVO 1	170725	0.06	0.12	0.04	0.06
BHVO 1	180425	0.14	0.19	0.04	0.08
BHVO 1	180502	0.09	0.11	0.08	0.06
<i>Literature value</i>		0.10	0.16	0.07	0.04
BCR 1	170530	0.06	0.07	0.03	0.04
BCR 1	170725	0.08	0.10	0.02	0.02
BCR 1	180425	0.03	0.06	0.02	0.02
BCR 1	180502	0.12	0.16	0.01	0.04
<i>Literature value</i>		0.13	0.09	0.04	0.03

### 2.3.6.2 Hf isotopes

Hafnium has been extracted using the chemical separation method of Nebel et al. (2009). The samples were introduced via a Teledyne Cetac Technologies Aridus II into a ThermoFisher Neptune Plus and measured over two analytical sessions (170428 and

180718). Reproducibility and data control has been accounted by multiple measurements of JMC 475 and by the analysis of BCR1 and BHVO1 (Table 2.4). The results and a detailed description of sample handling is presented in chapter 4.

**Table 2.4 - Reference values of all analytical Hf isotope runs.** Literature data for BCR1 and BHVO1 are from Weis et al. (2007); and JMC457 data is from Blichert-Toft et al. (1997). n = number of analysis.

Sample Name	Run	$^{177}\text{Hf}/^{176}\text{Hf}$	
		Ratio	Uncertainty (ISE)
BCR 1	170428	0.282859	0.000011
BCR 1	180718	0.282876	0.000004
<i>Literature value</i>		0.282875	0.000008
BHVO1	170428	0.283094	0.000017
BHVO1	180718	-	-
<i>Literature value</i>		0.283106	0.000012
JMC 457	n = 8 170428	0.282167	0.000002
<i>Literature value</i>		0.282163	

### 2.3.6.3 Sr isotopes

Strontium was purified using a standard chromatographic extraction method with 3M HNO<sub>3</sub> and 0.01M HNO<sub>3</sub> (Pin et al., 1994) and measured over three analytical session (170522, 170801, 180815) using a wet solution mode. The samples were injected via a glass spray chamber into the multicollector ICP-MS. Data reproducibility was tested by multiple measurements of reference material SRM987, BCR 1 and BHVO 1 (Table 2.5). A detailed description of the Sr isotope method can be find in chapters 3 and 4.

**Table 2.5 – Strontium isotope ratios of the analysed reference materials.** BCR1 and BHVO1 were corrected to SRM 987 value. Reference values for BCR1, BHVO1 and SRM987 are from Weis et al. (2006) and GeoRem database ([http://georem.mpch-mainz.gwdg.de/sample\\_query.asp](http://georem.mpch-mainz.gwdg.de/sample_query.asp)).

Sample Name	Run	$^{87}\text{Sr}/^{86}\text{Sr}$	
		Ratio	Uncertainty (ISE)
BCR 1	170522	0.705003	0.000011
BCR 1	170801	0.705079	0.000006
BCR 1	180815	0.705085	0.000008
<i>Literature value</i>		0.705025	
BHVO1	170522	0.703492	0.000008
BHVO1	170801	0.703483	0.000007
BHVO1	180815	0.703571	0.000007
<i>Literature value</i>		0.703484	
SRM987	n = 13 170522	0.710269	0.000010
SRM987	n = 15 170801	0.710347	0.000008
SRM987	n = 10 180815	0.710326	0.000009
<i>Literature value</i>		0.710248	

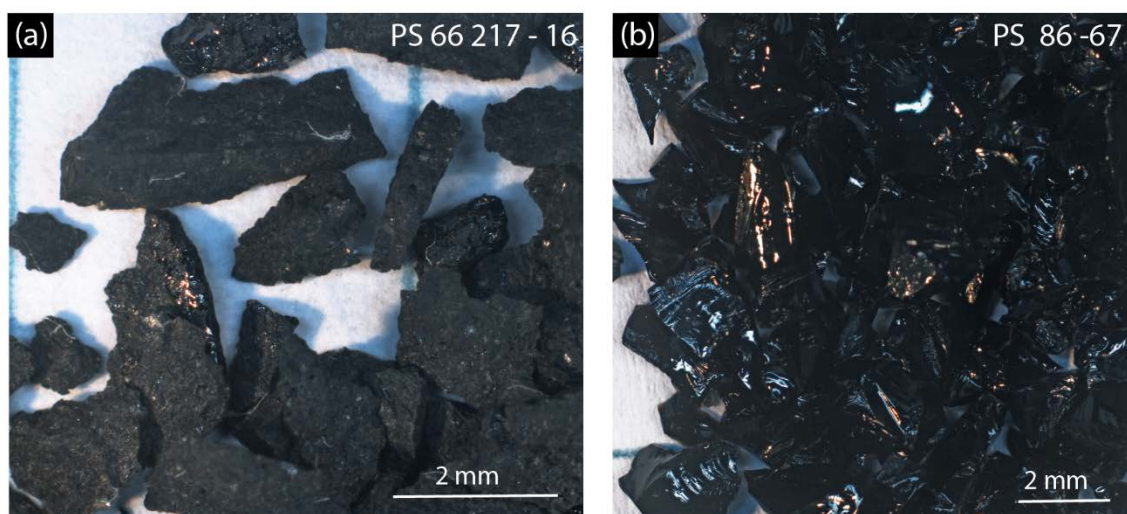


*Figure 2.10 - Picked rock chips for Pb isotope analysis. Sample PS 66 217 – 16 (a) and PS 86 – 67 (b) are shown as example.*

#### 2.3.6.4 Pb isotopes

The separation and analysis of Pb isotopes was undertaken in the School of Earth Sciences at the University of Melbourne (in collaboration with R. Maas) and in the Isotopia laboratory at the School of Earth, Atmosphere and Environment, Monash University. Both laboratories apply different chromatographic methods, which will be briefly mentioned in this section. However, each method is described in detail in chapters 3 and 4. In total, Pb isotopes were measured in three analytical sessions (160501; 170518; 180925). For the first two analytical sessions (160501; 170518), 400 mg rock chips (Figure 2.11) were picked and thoroughly cleaned in an ultrasonic bath in a mixture of ultrapure water and ethanol. For the chemical purification of Pb, the methodology as described in Maas et al. (2005) and Woodhead (2002) was followed. Prior chromatographic extraction of Pb the rock chips have been leached in 6M HCl (warm). The leachate has been removed from the beaker and the rock chips have been rinsed with MilliQ water. For the third analytical session (180925), 100 mg of sample powder was dissolved and Pb separated applying the methods of Pin et al. (2014). For Pb isotope analysis, reference material BCR2 (Table 2.6) was analysed to control the data.

**Table 2.6 – Lead isotope values for BCR 2 during each analytical run. Literature value is from GeoRem data base ([http://georem.mpch-mainz.gwdg.de/sample\\_query.asp](http://georem.mpch-mainz.gwdg.de/sample_query.asp)).**

Sample Name	Run	Ratio			Uncertainty (1SE)			
		$^{206}\text{Pb}/^{204}\text{Pb}$	$^{207}\text{Pb}/^{204}\text{Pb}$	$^{208}\text{Pb}/^{204}\text{Pb}$	$^{206}\text{Pb}/^{204}\text{Pb}$	$^{207}\text{Pb}/^{204}\text{Pb}$	$^{208}\text{Pb}/^{204}\text{Pb}$	
BHVO 1	180925	18.678	15.578	38.345	0.002	0.002	0.005	
<i>Literature value</i>		18.692	15.572	38.355				
BCR 2	170518	18.765	15.635	38.754	0.002	0.001	0.004	
BCR 2	180925	18.766	15.632	38.758	0.001	0.001	0.002	
<i>Literature value</i>		18.754	15.622	38.726				
SRM981	n = 13	160501	16.932	15.486	36.699	0.004	0.005	0.016
SRM981	n = 11	170518	16.945	15.503	36.731	0.001	0.001	0.002
SRM981	n = 8	180925	16.947	15.504	36.736	0.002	0.002	0.004
<i>Literature value</i>			16.941	15.499	36.722			

### 2.3.6.5 S isotopes

Nine samples out of 36 were selected for sulfur isotope analyses. These nine samples represent endmembers of each ridge segment, comprising the highest and the lowest sulfur concentration. All selected samples are volcanic glasses that were thoroughly cleaned in an ultrasonic bath to remove any dust particles or iron oxides prior to crushing to fine sample powder. The samples were digested in a Teflon apparatus and sulfur was extracted by gas chromatography (Labidi et al., 2012). Sulfur isotopes were determined using a dual-inlet ThermoFinnigan MAT gas source mass spectrometer in the Department of Geology at the University of Maryland, College Park. The sample preparation, sulfur extraction and S isotope measurement is described in detail by Labidi et al. (2012) and in chapter 6.

## 2.4 References

- Bach, W. et al., 2001. The geochemical consequences of late-stage low-grade alteration of lower ocean crust at the SW Indian Ridge: results from ODP Hole 735B (Leg 176). *Geochimica et Cosmochimica Acta*, 65(19): 3267-3287.
- Blichert-Toft, J., Chauvel, C., Albarède, F., 1997. Separation of Hf and Lu for high-precision isotope analysis of rock samples by magnetic sector-multiple collector ICP-MS. *Contributions to Mineralogy and Petrology*, 127(3): 248-260.
- Cheng, T., Nebel, O., Sossi, P.A., Chen, F., 2014. Refined separation of combined Fe-Hf from rock matrices for isotope analyses using AG-MP-1M and Ln-Spec chromatographic extraction resins. *MethodsX*, 1: 144-50.
- Craddock, P.R., Dauphas, N., 2011. Iron Isotopic Compositions of Geological Reference Materials and Chondrites. *Geostandards and Geoanalytical Research*, 35(1): 101-123.
- Francis, D., 1986. The pyroxene paradox in MORB glasses—a signature of picritic parental magmas? *Nature*, 319(6054): 586-589.
- Gale, A., Dalton, C.A., Langmuir, C.H., Su, Y., Schilling, J.-G., 2013. The mean composition of ocean ridge basalts. *Geochemistry, Geophysics, Geosystems*, 14(3): 489-518.

- Goldstein, S.L. et al., 2008. Origin of a 'Southern Hemisphere' geochemical signature in the Arctic upper mantle. *Nature*, 453(7191): 89-93.
- Jackson, S.E., Günther, D., 2003. The nature and sources of laser induced isotopic fractionation in laser ablation-multicollector-inductively coupled plasma-mass spectrometry. *Journal of Analytical Atomic Spectrometry*, 18(3): 205-212.
- Kelley, K.A., Plank, T., Ludden, J., Staudigel, H., 2003. Composition of altered oceanic crust at ODP Sites 801 and 1149. *Geochemistry, Geophysics, Geosystems*, 4(6).
- Labidi, J., Cartigny, P., Birck, J.L., Assayag, N., Bourrand, J.J., 2012. Determination of multiple sulfur isotopes in glasses: A reappraisal of the MORB  $\delta^{34}\text{S}$ . *Chemical Geology*, 334: 189-198.
- Lechler, P.J., Desilets, M.O., 1987. A review of the use of loss on ignition as a measurement of total volatiles in whole-rock analysis. *Chemical Geology*, 63(3): 341-344.
- Maas, R., Kamenetsky, M.B., Sobolev, A.V., Kamenetsky, V.S., Sobolev, N.V., 2005. Sr, Nd, and Pb isotope evidence for a mantle origin of alkali chlorides and carbonates in the Udachnaya kimberlite, Siberia. *Geology*, 33(7): 549.
- Mühe, R., Bohrmann, H., Garbe-Schönberg, D., Kassens, H., 1997. E-MORB glasses from the Gakkel Ridge (Arctic Ocean) at 87°N: evidence for the Earth's most northerly volcanic activity. *Earth and Planetary Science Letters*, 152(1-4): 1-9.
- Nebel, O., Morel, M.L.A., Vroon, P.Z., 2009. Isotope Dilution Determinations of Lu, Hf, Zr, Ta and W, and Hf Isotope Compositions of NIST SRM 610 and 612 Glass Wafers. *Geostandards and Geoanalytical Research*, 33(4): 487-499.
- Pin, C., Briot, D., Bassin, C., Poitrasson, F., 1994. Concomitant separation of strontium and samarium-neodymium for isotopic analysis in silicate samples, based on specific extraction chromatography. *Analytica Chimica Acta*, 298(2): 209-217.
- Pin, C., Gannoun, A., Dupont, A., 2014. Rapid, simultaneous separation of Sr, Pb, and Nd by extraction chromatography prior to isotope ratios determination by TIMS and MC-ICP-MS. *J. Anal. At. Spectrom.*, 29(10): 1858-1870.
- Salter, V.J.M., Sachi-Kocher, A., 2010. An ancient metasomatic source for the Walvis Ridge basalts. *Chemical Geology*, 273(3): 151-167.
- Sano, T. et al., 2012. Variety and origin of magmas on Shatsky Rise, northwest Pacific Ocean. *Geochemistry, Geophysics, Geosystems*, 13(8): n/a-n/a.
- Sossi, P.A., Foden, J.D., Halverson, G.P., 2012. Redox-controlled iron isotope fractionation during magmatic differentiation: an example from the Red Hill intrusion, S. Tasmania. *Contributions to Mineralogy and Petrology*, 164(5): 757-772.
- Staudigel, H., Plank, T., White, W.M., Schminke, H.-U., 1996. Geochemical fluxes during seafloor alteration of the basaltic upper oceanic crust: DSDP Sites 417 and 418. In: Bebout, G.E. (Ed.), *Subduction: Top to Bottom*. *Geophys. Monogr. Ser.* Washington, DC.
- Teklay, M., Scherer, E.E., Mezger, K., Danyushevsky, L., 2010. Geochemical characteristics and Sr-Nd-Hf isotope compositions of mantle xenoliths and host basalts from Assab, Eritrea: implications for the composition and thermal structure of the lithosphere beneath the Afar Depression. *Contributions to Mineralogy and Petrology*, 159(5): 731-751.
- Weis, D. et al., 2007. Hf isotope compositions of U.S. Geological Survey reference materials. *Geochemistry, Geophysics, Geosystems*, 8(6).
- Weis, D. et al., 2006. High-precision isotopic characterization of USGS reference materials by TIMS and MC-ICP-MS. *Geochemistry, Geophysics, Geosystems*, 7(8): n/a-n/a.
- Woodhead, J., 2002. A simple method for obtaining highly accurate Pb isotope data by MC-ICP-MS. *Journal of Analytical Atomic Spectrometry*, 17(10): 1381-1385.

## CHAPTER 3

### *A fossil subduction zone under the Western Gakkel Ridge region, Arctic Ocean*

*Marianne Richter*<sup>\*1,2</sup>, *Oliver Nebel*<sup>1,2</sup>, *Roland Maas*<sup>3</sup>, *Yona Nebel-Jacobsen*<sup>1,2</sup>, *Henry J.B. Dick*<sup>4</sup>, *Fabio A. Capitanio*<sup>2</sup>

<sup>1</sup> – Isotopia Laboratory, School of Earth, Atmosphere and Environment, Monash University, Clayton, Victoria, 3800, Australia

<sup>2</sup> - School of Earth, Atmosphere and Environment, Monash University, Clayton, Victoria, 3800, Australia

<sup>3</sup> – School of Earth Sciences, University of Melbourne, Parkville, Victoria, 3010, Australia

<sup>4</sup> – Department of Geology and Geophysics, Woods Hole Oceanographic Institution, Woods Hole, Massachusetts, 02543-1539, USA



*A curious polar bear that wants to know more about the mantle beneath the Gakkel Ridge.*

*(<http://polarbearsinternational.org/media/2967/d107411.jpg>)*

*This Manuscript has been submitted to Nature Communications (Feb'2019).*

**Abstract**

Earth's upper mantle, as sampled by ocean floor lavas (OFL) at oceanic spreading centres, has developed chemical heterogeneity over billions of years through focussed melt extraction and re-enrichment by recycled crustal components. Chemical and isotopic heterogeneity of OFL is dwarfed by the large compositional spectrum of lavas at convergent margins, identifying subduction zones as the major site for crustal recycling into and modification of the mantle. Here we show that seafloor lavas from the Western Gakkel Ridge in the Arctic Ocean have geochemical signatures that mirror that of an extensive, fossil subduction zone. Elemental depletion and re-enrichment patterns paired with high  $^{87}\text{Sr}/^{86}\text{Sr}$  and super-radiogenic  $^{208}\text{Pb}/^{204}\text{Pb}$  are distinct to OFL from Atlantic and Pacific Ocean spreading ridges and resemble a fossilised East-West arc to back-arc transition. A westward-dipping subduction zone further coincides with the reconstructed paleogeography of the Arctic in the Lower Cretaceous. Modelling of radiogenic ingrowth over timescales relevant to this subduction supports the link of Pb isotope anomalies and past subduction-related metasomatism, implying that subduction-modified mantle and its greater geodynamic structure survives convective homogenisation in the mantle for >125 million years.



### 3.1 Introduction

Compositional variations in the Earth's upper mantle, as sampled along oceanic spreading centres range from over thousands of kilometres (Hart, 1984; Meyzen et al., 2007) to the sub-kilometre scale (Standish et al., 2008). While many questions about the physical extent, age and chemical-mineralogical composition of mantle heterogeneity remain outstanding (Salters, 1996), it is clear that these form by a combination of earlier melting events and mantle re-enrichment associated with recycling of crustal components (Stracke, 2012). Well-known examples of compositionally diverse upper mantle include supra-subduction zone mantle, lithospheric mantle under cratons and possibly plume-infused mantle (Hofmann, 2014). Some ocean floor lavas (OFL) carry radiogenic isotopic signatures interpreted as either subduction-zone modified mantle (Andersen et al., 2015; Elliott et al., 2006; Nielsen et al., 2018; Rehkämper and Hofmann, 1997), relicts of ancient mantle plume activity (Dick and Zhou, 2014; Gibson and Richards, 2018), or remnants of cratonic lithospheric mantle (Goldstein et al., 2008; Meyzen et al., 2007). It remains unclear, however, for how long such heterogeneity can survive homogenisation by convection or remain stationary in the upper mantle (Hofmann, 2007; Widom, 2006), and to what extent they contribute to the chemical diversity in basalts along divergent plate boundaries.

Here we present geochemical evidence from dredged ocean floor lavas preserving remnants of a past subduction zone in the upper mantle. We assess the nature of the mantle source of mid-ocean ridge basalts (MORBs) at the Gakkel Ridge (Figures 3.1a and 3.1b) in the Arctic Ocean and place our results in context with the palaeogeographic reconstruction of the circumpolar region. The Gakkel Ridge is an area of reported extreme mantle heterogeneity (D'Errico et al., 2016; Liu et al., 2008) and exhibits along-ridge variations in axial depth (Michael et al., 2003), magma production rate (Dick and Zhou, 2014) and crustal thickness (Schmidt-Aursch and Jokat, 2016), all potential surface expressions of mantle source heterogeneity (Whittaker et al., 2008).

Furthermore, the Western Gakkel basalts have elevated  $^{87}\text{Sr}/^{86}\text{Sr}$  and  $^{208}\text{Pb}/^{204}\text{Pb}$  compared to Atlantic or Pacific Ocean lavas (Goldstein et al., 2008). The isotopic oddities in the Gakkel Ridge basalts are indicative of a crustal component (Goldstein et al., 2008; Rehkämper and Hofmann, 1997), which are accompanied by trace element signatures with incompatible element depletion and enrichment in fluid-mobile elements (Goldstein et al., 2008; Michael et al., 2003). Element depletion patterns in selected high-field strength elements (HFSE: Zr, Nb, Hf) is accompanied by enrichment in large ion lithophile element (LILE: Rb, Ba, Sr) concentrations, which in combination indicates a complex, two-stage history of the Gakkel Ridge MORB source (D'Errico et al., 2016; Liu et al., 2008; Stracke et al., 2011).

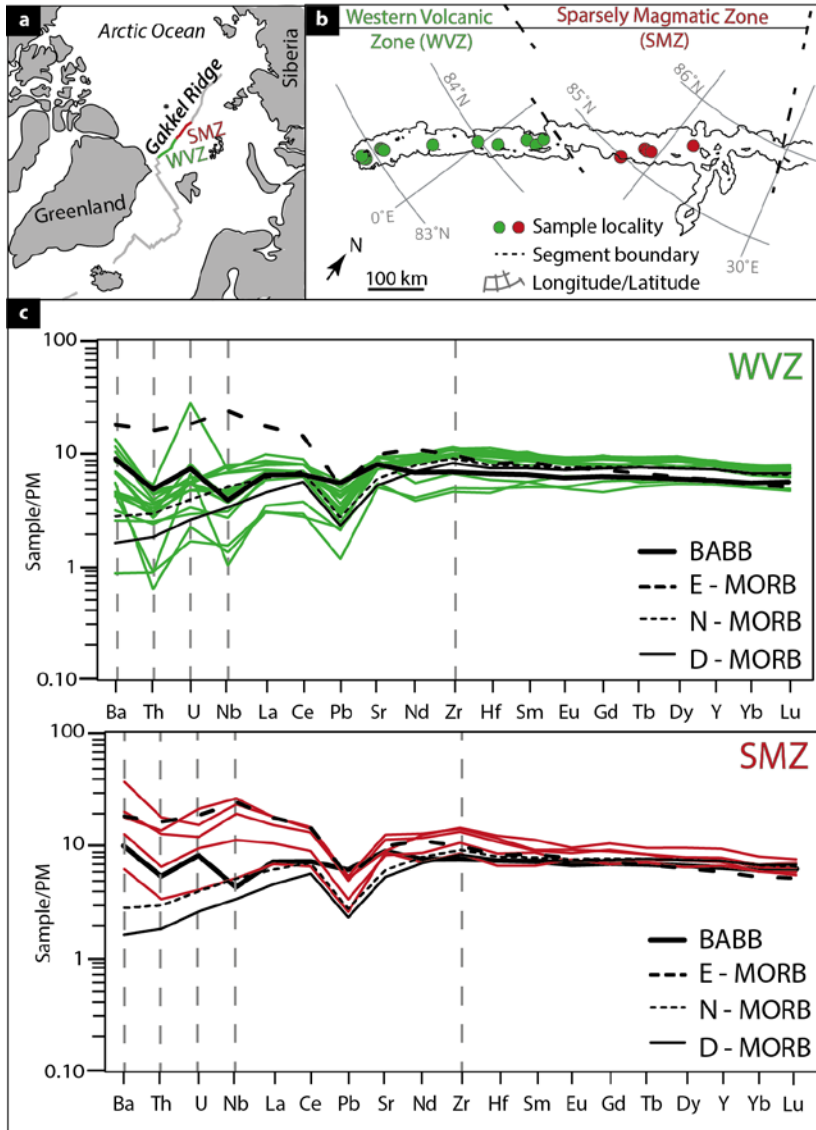


**Figure 3.1 - Geographical overview, sample localities and trace element patterns in modern MORB lavas from the western Gakkel Ridge.** (a) The Gakkel Ridge extends for ca.1800 km from the northwest coast of Greenland to the northern coast of Siberia. Note green and red sectors which correspond to sample localities in the Western Volcanic Zone, WVZ (green) and Sparsely Magmatic Zone, SMZ (red) in (b) for details of sampling sites see Supplementary Table 3.1. c, Western Gakkel Ridge MORBs show some overlap with the total range of global MORB (Gale et al., 2013), but generally follow a BABB trend (high Ba, Zr, low Th and Nb). Grey vertical dashed lines illustrate similarities to BABB. Trace element concentration normalised to primitive mantle (PM - primitive mantle; McDonough and Sun, 1995).

The geochemical anomalies in Gakkel Ridge lavas were previously ascribed to a sub-continental lithospheric mantle (SCLM) origin (Goldstein et al., 2008). In this model, SCLM underlying greater Greenland was detached and integrated into the upper mantle after continental break-up at around 50 Ma. The model from Goldstein and co-workers, however, was challenged on the basis of Pb isotope differences between Gakkel Ridge lavas and those from Spitsbergen (Blusztajn et al., 2014), with Spitsbergen xenoliths, derived from the lithospheric mantle, being isotopically distinct from those of sulphides in abyssal peridotites from the Gakkel Ridge (Blusztajn et al., 2014), leaving the origin of the

chemical anomaly in the mantle underpinning the Gakkel Ridge ambiguous.

## 3.2 Results

Our new trace element and isotopic results for dredged lavas from the Western Volcanic Zone (WVZ) and the Sparsely Magmatic Zone (SMZ; Figure 3.1b, Supplementary Table 3.1) of the Western Gakkel Ridge supports the inference of an extremely heterogeneous upper mantle

beneath the ridge similar to those found in abyssal peridotites (D'Errico et al., 2016; Liu et al., 2008). Gakkel Ridge lavas are enriched in LILE (e.g., Rb, Ba, Sr) and depleted in HFSE (e.g., Zr, Nb, Hf) (Figure 3.1c) compared to normal MORB. Lavas from the SMZ show higher incompatible trace element concentrations (e.g., Ba, Th, Nb, U, La, Ce) than those from the WVZ (Figure 3.1c). Both ridge segments, however, have elevated  $^{87}\text{Sr}/^{86}\text{Sr}$  and  $^{208}\text{Pb}/^{204}\text{Pb}$  compared to other OFL. Whilst our data is coherent with prior trace element and isotope signatures, the sum of new and old Gakkel Ridge data, combined with now available global ocean floor data, allows a more robust assessment of the origin of these signatures.

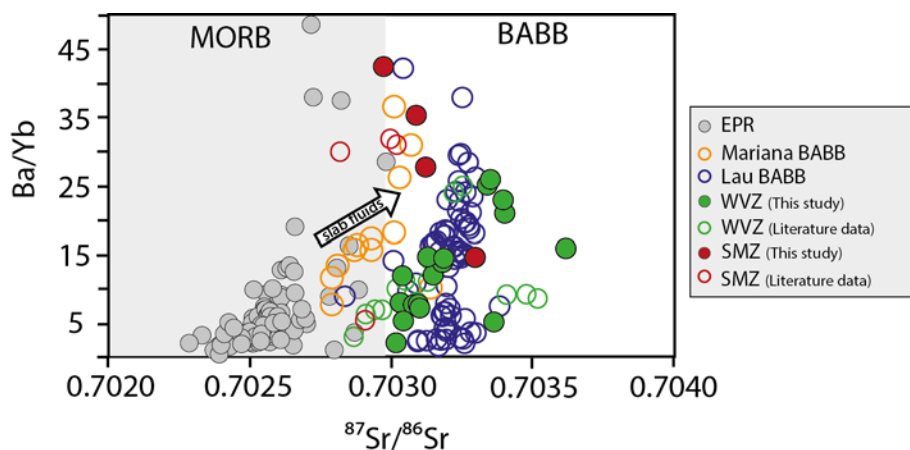


**Figure 3.2** -  $^{87}\text{Sr}/^{86}\text{Sr}$  vs  $\text{Ba}/\text{Yb}$ . Basalts from the western Gakkel Ridge (WVZ, SMZ) have high  $^{87}\text{Sr}/^{86}\text{Sr}$  (up to 0.7037) compared to MORB, similar to active island arcs and back-arc basins, such as the Lau and Mariana back-arc basin. High  $^{87}\text{Sr}/^{86}\text{Sr}$  and  $\text{Ba}/\text{Yb}$  ratio are explained by partial melting of a fluid-enriched mantle source. SMZ basalts tend to have higher  $\text{Ba}/\text{Yb}$  than WVZ basalts, implying a higher degree of source enrichment. Data from Gale et al. (2013).

The degree of prior melt extraction and re-enrichment of the Gakkel Ridge MORB source is assessed by comparing their LILE and HFSE concentrations with those in global MORB and convergent margin lavas. Zirconium/Nb (HFSE) is used as indicator for melt extraction (Pearce and Stern, 2013), with Zr being more incompatible during partial mantle melting than Nb. Melt extraction caused by partial (fluxed) melting thus lowers the Zr/Nb ratio in the mantle residue (Tiepolo et al., 2001), without being affected by fluid-borne metasomatism. Subsequent melt extraction from such a residual mantle source will produce melts with low Zr/Nb, which is essentially a memory of the past melting event, and is observed in basalts from both, the SMZ and the WVZ (Supplementary Figure 3.1b). Zirconium/Nb in WVZ lavas are systematically higher than in SMZ lavas, suggesting that the mantle beneath the SMZ experienced a melt extraction at higher degrees of melting. The higher degree of melting in the SMZ may thus be a function of fluid-triggered melting. Lavas from both ridge segments are also enriched in Ba, which is considered a fluid-mobile element, with Ba enrichment being more pronounced in the SMZ basalts. Gakkel Ridge lavas are also enriched in Th, which - in arc settings - is commonly attributed to subducted sediment (Hawkesworth et al., 1997). Elevated  $\text{Ba}/\text{Yb}$  (Figure 3.2; Supplementary Figure 3.2) and  $\text{Ba}/\text{Th}$  (Supplementary Figure 3.3) fall within or slightly outside the MORB field and correlate

broadly with elevated  $^{87}\text{Sr}/^{86}\text{Sr}$  (Figure 3.2, Supplementary Figure 3.2). For this, Eastern Pacific Rise basalts are used as MORB representative, because of no known influence of enriched mantle components in these ridge segments.

### 3.3 Discussion

#### 3.3.1 *Ghost of a past subduction*

A striking feature is the similarity of the aforementioned geochemical signatures observed at the Western Gakkel Ridge to those found in back-arc basin basalts (BABB) in the Western Pacific region. Both, Figure 3.1c and Figure 3.2 show an overlap of BABB with Mariana and Lau Basin back-arc lavas. It thus appears that Gakkel Ridge lavas originate from a source with low Zr/Nb as a record of prior melt depletion and subsequent re-enrichment evidenced through high Ba-Th and radiogenic Sr, likely through metasomatism under conditions similar to fluxed melting in a mantle wedge. The plausibility that Gakkel MORBs mirror chemical signatures that of BABB and/or mantle wedge will be further elaborated in the following.

Mantle (re-)enrichment (Ba-Th/Yb vs Sr isotope systematics) and melt extraction (lower Zr/Nb) in the source of the SMZ and the WVZ basalts resemble slab devolatilisation and the mobility of a slab component with Ba-Sr-Th, and subsequent fluxed melting of a hot mantle wedge to variable degrees (Spandler and Pirard, 2013). An important aspect is the similarity of the Gakkel Ridge basalt composition with back-arc rather than arc lavas from active subduction zones. Residual subduction signature, as is the case for the source of BABB, is expected in mantle with a subduction past with more subtle, yet clearly distinct signatures from non-modified MORB sources. Residual mantle with a subduction history is clearly distinct from active subduction zone magmatism, which carries the full slab component straight from slab to overlying arc. A second important aspect for this scenario is its geodynamic plausibility. The proposed subduction zone setting is ascribed here to the closure of the South Anuyi Ocean ~120 Ma ago (Figure 3.3). Paleoreconstructions of the Arctic Ocean suggest the activity of a westward-facing subduction zone between 145 Ma and 120 Ma (Figure 3.3a), concurrent with the closure of the South Anuyi Ocean (Shephard et al., 2013) with the SMZ as rear-arc and the WVZ as proposed back-arc regions (Figure 3.3b - c).

The latter is further supported by seismic tomography models from the Gakkel Ridge. S-wave tomography models show cold spots at one-third (boundary WVZ – SMZ) and central part (SMZ towards EVZ boundary) of the Gakkel Ridge (Sokolov and Mazarovich, 2016). The first cold spot has also been associated with a low magnetic field, suggested to be linked to a depleted mantle area (Sokolov and Mazarovich, 2016) presumably with low Fe concentration (< 7 wt.%). The area of proposed depletion is in-line with the recorded depletion (low Zr/Nb) in the SMZ basalts. The second cold spot, however, occurs at a depth of ~700 km in the central part of the ridge and is

interpreted as remnants of a westward dipping slab (Sokolov and Mazarovich, 2016) linked to the closure of the South Anuyi Ocean (Khain and Lomize, 1995). An additional line of supporting evidence is the chemistry of tholeiitic rocks from the Sverdup Basin in northern Canada, along the South Anuyi suture zone, show similar geochemical characteristics (high Th and low Nb) to the western Gakkel Ridge lavas. Basalts from the Sverdup Basin have previously been associated with an origin in an arc-/back-arc mantle (Shephard et al., 2016). In the following, we propose a mechanism that explains the arc- to back-arc-like geochemical characteristics observed in basalts.

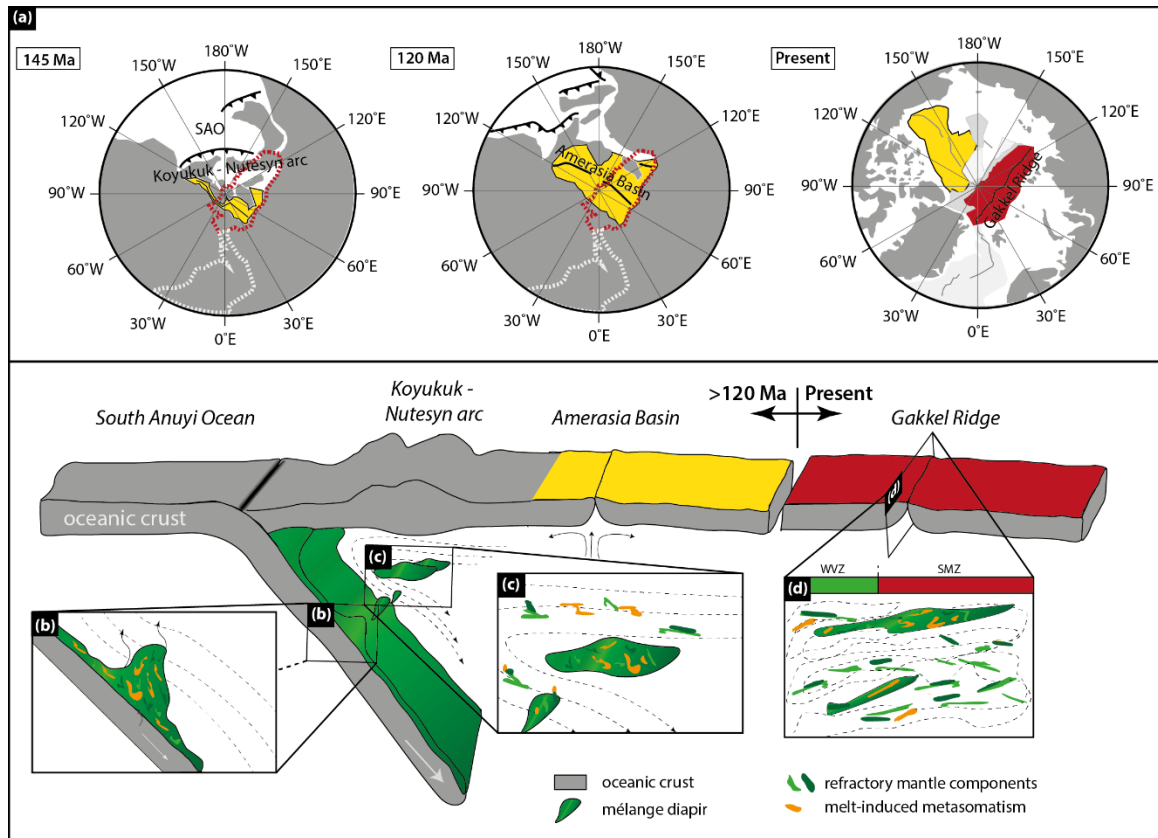


**Figure 3.3 - Paleogeography of the Gakkel Ridge region.** Palaeogeographic reconstructions show the Arctic region from 145 Ma to present. The upper panel is modified after (Alvey et al., 2008; Shephard et al., 2013) (a). Dashed red lines in the panels denote present location of the Gakkel Ridge, white dashed line is the North Atlantic ridge. The sketch in the lower panel suggests possible changes in shallow mantle structure at the time of subduction until the present day. The mechanism is explained in detail in the text. In brief, during subduction of the South Anuyi Ocean (SAO), mélangé-diapirs (b) ascend into the mantle wedge, forming the Koyukuk-Nutesyn volcanic arc (c) at 145 -120 Ma. A back-arc basin (Amerasia Basin) operated until about 120 Ma (Alvey et al., 2008). The original Gakkel Ridge at ca. 50 Ma was orthogonal to the pre-existing ridge/back-arc basin, due to the breakup of Greenland, Svalbard and the Eurasian plate. Changing mantle convection due to changes in plate motions after subduction ceased at 120 Ma led to stretching and shearing of the mélangé diapirs; (d), which is sampled by modern ridge magmatism in the western Gakkel Ridge.

### 3.3.2 Remnants of subducting slab mélanges

The physical form of inherited subduction-type Ba-Th vs. Sr isotope systematics in the Gakkel Ridge mantle is examined within a slab mélangé model (Marschall and Schumacher, 2012; Nielsen and Marschall, 2017). In this model, mélanges consisting of hydrous fluids from subducted oceanic crust, which form a thin veneer of subducted sediments and depleted mantle peridotites,

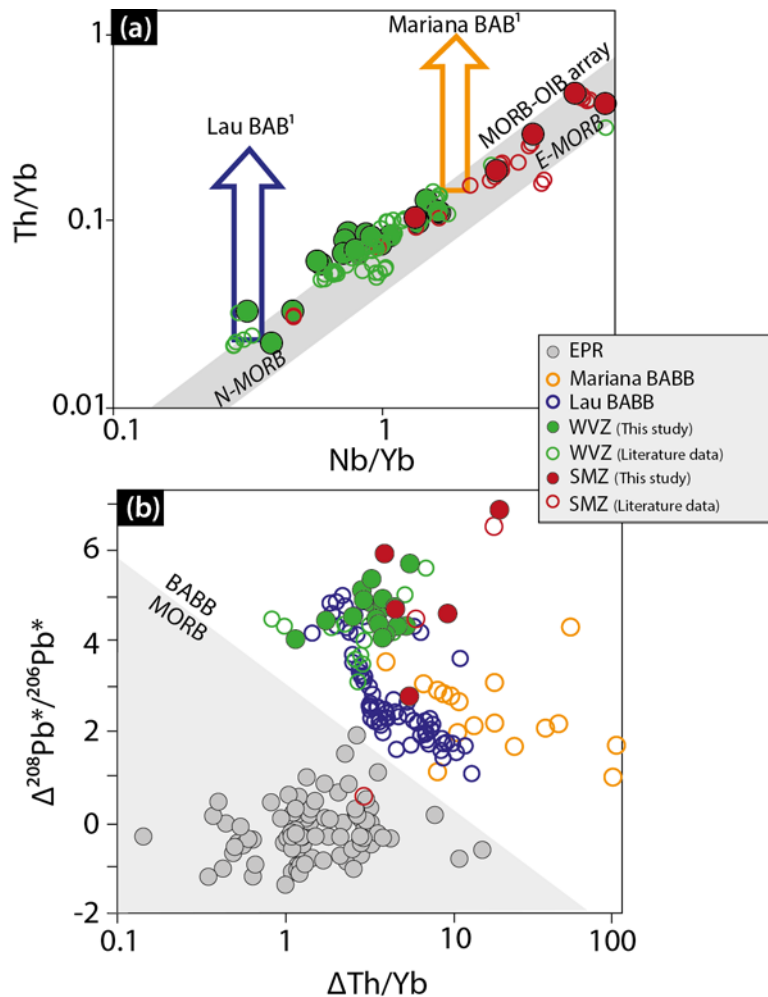
ascend diapirically (Nielsen and Marschall, 2017) into the mantle wedge due to buoyancy differences (Figure 3.3b). In the mantle wedge, the *mélange* diapirs undergo dehydration melting forming the source for arc magmas, leaving a depleted mantle (recorded in low Zr/Nb). The presence of *mélange* diapir remnants, marked by fossil melting residues of a former *mélange* plume (Figure 3.3c), provides a more plausible physical model for mantle metasomatism in the mantle wedge than a purely fluid-based metasomatic model, based on recently emerged evidence for physical residues of sediment melting in the centre of a former mantle wedge (Marschall and Schumacher, 2012). In the case of the Gakkel Ridge, we propose that changing mantle convection, as cause of changes in plate tectonic motions (Alvey et al., 2008; Gaina et al., 2014; Shephard et al., 2013), sheared the *mélange* residue to create elongated lenses of the depleted wedge plume/diapir (Figure 3.3d). Shearing of the *mélange* diapirs requires them to be almost dehydrated (Marschall and Schumacher, 2012) and have a similar density as the surrounding mantle, making these sections neutrally buoyant and stationary. Critical to this model is the delivery of Th into the mantle wedge, along with fluid-borne Ba-Sr.

Gakkel Ridge lavas have relatively high thorogenic Pb isotope ratios compared to global MORB, requiring a history of elevated Th/Pb and Th/U in their mantle source. Elevated Th/Yb in OFL are diagnostic for, and sensitive to, the influence of a subduction component in their mantle source (Pearce et al., 2005; Shu et al., 2019). The Th-Nb/Yb compositions of Gakkel Ridge basalts (Figure 3.4a) lie at the upper bound of the MORB field and combined with high  $^{208}\text{Pb}/^{206}\text{Pb}$  imply high time-integrated Th/U in its mantle source (Figure 3.4b). If high time-integrated Th/U existed in the mantle source beneath the present day Western Gakkel area since subduction ceased at ca. 120 Ma, as proposed by our model, elevated  $^{208}\text{Pb}/^{206}\text{Pb}$  may be explained as the result of local thorogenic ingrowth in high-Th/U zones inherited from fossil *mélange* rocks in the underlying mantle. Mass balance considerations have been used to infer that up to 70% of the original Th may be retained when subducted sediments undergo dehydration or partial melting (Hawkesworth, 1997). Assuming these high-Th/U residual *mélange* complexes remain within the upper mantle once subduction ceases, ingrown high  $^{208}\text{Pb}/^{206}\text{Pb}$  would be expected to be mobilised in younger melting episodes, such as the modern Gakkel Ridge MORB magmatism. A near identical component was traced for the Marianas rear arc (Pearce et al., 2005), adding further weight to this scenario.

Simple ingrowth modelling indicates that for timescales  $t = 125$  Ma (inferred for prior subduction activity in the Gakkel Ridge area), a  $^{232}\text{Th}/^{238}\text{U}$  ( $\kappa$ ) = 5.4 is sufficient to generate the observed preferential  $^{208}\text{Pb}$  isotope ingrowth assuming starting composition of Pb isotopes identical to the NHRL. This assumes that the basalts originate from a melt-depleted mantle with a U/Pb ( $\mu_{\text{DM}}$ ) = 6.5 (White, 1993) with U stripped off during primary melt extraction in the arc. The latter in combination with Th enrichment in residual assemblages leads to a Th/Pb ( $\omega$ ) of 35.1 in the sub-

ridge mantle. A considerable complication is the constantly high  $^{208}\text{Pb}/^{206}\text{Pb}$  in both SMZ and WMZ, so that a high average  $\kappa$  ( $\sim 5.4$ ) is required along the entire magmatically active ridge length. In addition, remarkably homogeneous Pb isotope compositions along the Gakkel Ridge length indicate a homogeneous distribution of Th/U in the mantle. Fossil diapir regions in the sub-ridge mantle, enriched in Th, occur most likely only locally (e.g., Th-rich accessory minerals formed during Lower Cretaceous mélangé diapir melting), and such domains are presumably higher in Th/U than required by the time-integrated *average* calculated  $\kappa$  for Gakkel Ridge lavas. A feasible solution to this conundrum is that partial melts are homogenised prior to eruption, possibly by diffusion in a melt network or in sub-oceanic magma ponds (O'Neill and Jenner, 2012). Indeed, only small amounts of an enriched  $^{208}\text{Pb}$  isotope component are sufficient to shift melts off the NHRL, whereas other signatures, such as element ratios or Sr isotopes are much less susceptible to change.

**Figure 3.4 Th-Nb/Yb co-variation diagram and Pb isotope systematics.** (a) Th-Nb/Yb (after Pearce, 2008) shows global MORB-OIB array (diagonal grey bar). The orange and dark blue arrow indicate Th/Yb data trends (at a given Nb/Yb) for Lau and Mariana BABB. Many Gakkel Ridge MORBs exceed Th/Yb in the MORB-OIB array at a given Nb/Yb, indicating Th enrichment. (b) Elevated mantle Th contents (higher  $\Delta\text{Th}/\text{Nb}$ ) contribute to high mantle Th/U, producing positive  $\Delta^{208}\text{Pb}^*/^{206}\text{Pb}^*$ .  $\Delta\text{Th}/\text{Nb}$  is the deviation from the lower boundary of the MORB-OIB array, and  $\Delta^{208}\text{Pb}^*/^{206}\text{Pb}^*$  is the difference in  $^{208}\text{Pb}/^{206}\text{Pb}$  from the Northern Hemisphere Reference Line (NHRL), see Supplementary Information for calculation. Mariana and BABB are from Gale et al. (2013). WVZ and SMZ literature data is compiled from Goldstein et al. (2008) and Gale et al. (2013).



Apparent similarities between the Gakkel Ridge and the Australian Antarctic Discordance (AAD), a prominent seafloor depression at the Southeast Indian Ridge between Australia and Antarctica, indicate that the proposed subduction feature in sub-ridge mantle is not a single oddity confined to the Arctic Ocean. The ridge depression along the AAD is coupled with lower magmatic activity and upper mantle depletion (Kempton et al., 2002; Whittaker et al., 2008) and Pb isotope

compositions along the depressed section of the ridge differ from those outside the AAD. These features have been tentatively linked to a stagnating slab residing in the upper mantle (Gurnis and Müller, 2003; Kempton et al., 2002) left behind from long-lived subduction along the Eastern Gondwana margin 150 - 260 Ma (Nebel et al., 2007), possibly providing another example of a sub-ridge fossil subduction system. Furthermore, Gakkel Ridge lavas not only share geochemical similarities in LILE, HFSE and Sr isotopes with those of arc-/back-arc lavas of Western Pacific subduction zones, e.g., the Mariana and Lau back-arc basins (Figure 3.4b), but also resemble their  $^{208}\text{Pb}/^{206}\text{Pb}$  (Th/U) systematics of Indian-type mantle, which in turn have compositions reminiscent of DupAl-type mantle (Nebel et al., 2007).

### 3.4 Conclusion

The preservation of a MORB suite with rear-arc (SMZ) to back-arc (WMZ) geochemical-isotopic signatures, and its link to the South Anuyi Ocean fossil subduction zone provide a lower bound to the survival time of subduction-modified mantle, possibly in the form of *mélange* diapirs/wedge plumes, after subduction cessation. As a consequence, mantle heterogeneity of enriched mantle components and melt depleted sections on the scale of subduction zones can survive convective homogenisation in the mantle for at least 120 Myr. The presence of these sections, stationary, in the upper Earth's mantle further implies that subduction leaves a chemical footprint, which, with time, can add to the chemical heterogeneity in global MORB without a deep mantle cycling.

### 3.5 References

- Alvey, A., Gaina, C., Kuznir, N.J., Torsvik, T.H., 2008. Integrated crustal thickness mapping and plate reconstructions for the high Arctic. *Earth and Planetary Science Letters*, 274(3-4): 310-321.
- Andersen, M.B. et al., 2015. The terrestrial uranium isotope cycle. *Nature*, 517(7534): 356-9.
- Blusztajn, J., Shimizu, N., Warren, J.M., Dick, H.J.B., 2014. In-situ Pb isotopic analysis of sulfides in abyssal peridotites: New insights into heterogeneity and evolution of the oceanic upper mantle. *Geology*, 42(2): 159-162.
- D'Errico, M.E., Warren, J.M., Godard, M., 2016. Evidence for chemically heterogeneous Arctic mantle beneath the Gakkel Ridge. *Geochimica et Cosmochimica Acta*, 174: 291-312.
- Dick, H.J.B., Zhou, H., 2014. Ocean rises are products of variable mantle composition, temperature and focused melting. *Nature Geoscience*, 8(1): 68-74.
- Elliott, T., Thomas, A., Jeffcoate, A., Niu, Y., 2006. Lithium isotope evidence for subduction-enriched mantle in the source of mid-ocean-ridge basalts. *Nature*, 443(7111): 565-8.
- Gaina, C., Medvedev, S., Torsvik, T.H., Koulakov, I., Werner, S.C., 2014. 4D Arctic: A Glimpse into the Structure and Evolution of the Arctic in the Light of New Geophysical Maps, Plate Tectonics and Tomographic Models. *Surv Geophys*, 35(5): 1095-1122.
- Gale, A., Dalton, C.A., Langmuir, C.H., Su, Y., Schilling, J.-G., 2013. The mean composition of ocean ridge basalts. *Geochemistry, Geophysics, Geosystems*, 14(3): 489-518.
- Gibson, S.A., Richards, M.A., 2018. Delivery of deep-sourced, volatile-rich plume material to the global ridge system. *Earth and Planetary Science Letters*, 499: 205-218.
- Goldstein, S.L. et al., 2008. Origin of a 'Southern Hemisphere' geochemical signature in the Arctic upper mantle. *Nature*, 453(7191): 89-93.
- Gurnis, M., Müller, R.D., 2003. Origin of the Australian–Antarctic Discordance from an ancient slab and mantle wedge. In: Hillis, R.R., Müller, R.D. (Eds.), *Evolution and Dynamics of the Australian Plate*. Geological Society of America.
- Hart, S.R., 1984. A large-scale isotope anomaly in the Southern Hemisphere mantle. *Nature*, 309(5971): 753-757.

- Hawkesworth, C.J., 1997. U-Th Isotopes in Arc Magmas: Implications for Element Transfer from the Subducted Crust. *Science*, 276(5312): 551-555.
- Hawkesworth, C.J., Turner, S.P., McDermott, F., Peate, D.W., van Calsteren, P., 1997. U-Th Isotopes in Arc Magmas: Implications for Element Transfer from the Subducted Crust. *Science*, 276(5312): 551-555.
- Hofmann, A.W., 2007. The lost continents. *Nature*, 448: 655.
- Hofmann, A.W., 2014. Sampling Mantle Heterogeneity through Oceanic Basalts: Isotopes and Trace Elements. *Treatise on geochemistry*: 67-101.
- Jenner, F.E., O'Neill, H.S.C., 2012. Analysis of 60 elements in 616 ocean floor basaltic glasses. *Geochemistry, Geophysics, Geosystems*, 13(2): Q02005.
- Jochum, K.P., Stoll, B., Herwig, K., Willbold, M., 2007. Validation of LA-ICP-MS trace element analysis of geological glasses using a new solid-state 193 nm Nd:YAG laser and matrix-matched calibration. *J. Anal. At. Spectrom.*, 22(2): 112-121.
- Jochum, K.P. et al., 2011. Determination of Reference Values for NIST SRM 610–617 Glasses Following ISO Guidelines. *Geostandards and Geoanalytical Research*, 35(4): 397-429.
- Jochum, K.P., Willbold, M., Raczek, I., Stoll, B., Herwig, K., 2005. Chemical Characterisation of the USGS Reference Glasses GSA - 1G, GSC - 1G, GSD - 1G, GSE - 1G, BCR - 2G, BHVO - 2G and BIR - 1G Using EPMA, ID - TIMS, ID - ICP - MS and LA - ICP - MS. *Geostandards and Geoanalytical Research*, 29(3): 285-302.
- Kempton, P.D. et al., 2002. Sr-Nd-Pb-Hf Isotope Results from ODP Leg 187: Evidence for Mantle Dynamics of the Australian-Antarctic Discordance and Origin of the Indian MORB Source. *Geochemistry, Geophysics, Geosystems*, 3(12): 1-35.
- Khain, V.E., Lomize, M.G., 1995. *Geotectonics and fundamentals of geodynamics*. MSU, Moscow.
- Liu, C.Z. et al., 2008. Ancient, highly heterogeneous mantle beneath Gakkel Ridge, Arctic Ocean. *Nature*, 452(7185): 311-6.
- Longerich, H.P., Jackson, S.E., Gunther, D., 1996. Inter-laboratory note. Laser ablation inductively coupled plasma mass spectrometric transient signal data acquisition and analyte concentration calculation. *Journal of Analytical Atomic Spectrometry*, 11(9): 899-904.
- Maas, R., Grew, E.S., Carson, C.J., 2015. Isotopic constraints (Pb, Rb-Sr, Sm-Nd) on the sources of Early Cambrian Pegmatites with Boron and Beryllium minerals in the Larsemann Hills, Prydz Bay, Antarctica. *The Canadian Mineralogist*, 53(2): 249-272.
- Marschall, H.R., Schumacher, J.C., 2012. Arc magmas sourced from mélange diapirs in subduction zones. *Nature Geoscience*, 5(12): 862-867.
- McArthur, J.M., 1994. Recent trends in strontium isotope stratigraphy. *Terra Nova*, 6(4): 331-358.
- McDonough, W.F., Sun, S.s., 1995. The composition of the Earth. *Chemical Geology*, 120(3): 223-253.
- Meyzen, C.M. et al., 2007. Isotopic portrayal of the Earth's upper mantle flow field. *Nature*, 447(7148): 1069-74.
- Michael, P.J. et al., 2003. Magmatic and amagmatic seafloor generation at the ultraslow-spreading Gakkel Ridge, Arctic Ocean. *Nature*, 423(6943): 956-961.
- Nebel, O. et al., 2007. Hf-Nd-Pb isotope evidence from Permian arc rocks for the long-term presence of the Indian-Pacific mantle boundary in the SW Pacific. *Earth and Planetary Science Letters*, 254(3-4): 377-392.
- Nielsen, S.G. et al., 2018. Barium isotope evidence for pervasive sediment recycling in the upper mantle. *Science Advances*, 4(7).
- Nielsen, S.G., Marschall, H.R., 2017. Geochemical evidence for mélange melting in global arcs. *Science Advances*, 3(4).
- O'Neill, H.S., Jenner, F.E., 2012. The global pattern of trace-element distributions in ocean floor basalts. *Nature*, 491(7426): 698-704.
- Pearce, J.A., 2008. Geochemical fingerprinting of oceanic basalts with applications to ophiolite classification and the search for Archean oceanic crust. *Lithos*, 100(1-4): 14-48.
- Pearce, J.A., Stern, R.J., 2013. Origin of Back-Arc Basin Magmas: Trace Element and Isotope Perspectives, *Back-Arc Spreading Systems: Geological, Biological, Chemical, and Physical Interactions*. American Geophysical Union, pp. 63-86.
- Pearce, J.A., Stern, R.J., Bloomer, S.H., Fryer, P., 2005. Geochemical mapping of the Mariana arc-basin system: Implications for the nature and distribution of subduction components. *Geochemistry, Geophysics, Geosystems*, 6(7): n/a-n/a.
- Pin, C., Briot, D., Bassin, C., Poitrasson, F., 1994. Concomitant separation of strontium and samarium-neodymium for isotopic analysis in silicate samples, based on specific extraction chromatography. *Analytica Chimica Acta*, 298(2): 209-217.

- Rehkämper, M., Hofmann, A.W., 1997. Recycled ocean crust and sediment in Indian Ocean MORB. *Earth and Planetary Science Letters*, 147(1–4): 93-106.
- Salters, V.J.M., 1996. The generation of mid-ocean ridge basalts from the Hf and Nd isotope perspective. *Earth and Planetary Science Letters*, 141(1): 109-123.
- Schmidt-Aursch, M.C., Jokat, W., 2016. 3D gravity modelling reveals off-axis crustal thickness variations along the western Gakkel Ridge (Arctic Ocean). *Tectonophysics*.
- Shephard, G.E., Müller, R.D., Seton, M., 2013. The tectonic evolution of the Arctic since Pangea breakup: Integrating constraints from surface geology and geophysics with mantle structure. *Earth-Science Reviews*, 124: 148-183.
- Shephard, G.E., Trønnes, R.G., Spakman, W., Panet, I., Gaina, C., 2016. Evidence for slab material under Greenland and links to Cretaceous High Arctic magmatism. *Geophysical Research Letters*, 43(8): 3717-3726.
- Shu, Y. et al., 2019. Closing the loop: subducted eclogites match thallium isotope compositions of ocean island basalts. *Geochimica et Cosmochimica Acta*.
- Sokolov, S.Y., Mazarovich, A.O., 2016. Cluster analysis of geological and geophysical parameters of the Arctic region as the base for geodynamic interpretation. *Geodynamics & Tectonophysics*, 7(1): 59 - 83.
- Spandler, C., Pirard, C., 2013. Element recycling from subducting slabs to arc crust: A review. *Lithos*, 170-171: 208-223.
- Standish, J.J., Dick, H.J.B., Michael, P.J., Melson, W.G., O'Hearn, T., 2008. MORB generation beneath the ultraslow-spreading Southwest Indian Ridge (9-25°E): Major element chemistry and the importance of process versus source. *Geochemistry, Geophysics, Geosystems*, 9(5): Q05004.
- Stracke, A., 2012. Earth's heterogeneous mantle: A product of convection-driven interaction between crust and mantle. *Chemical Geology*, 330-331: 274-299.
- Stracke, A. et al., 2011. Abyssal peridotite Hf isotopes identify extreme mantle depletion. *Earth and Planetary Science Letters*, 308(3-4): 359-368.
- Tiepolo, M. et al., 2001. Fractionation of Nb and Ta from Zr and Hf at Mantle Depths: the Role of Titanian Pargasite and Kaersutite. *Journal of Petrology*, 42(1): 221-232.
- White, W.M., 1993. 238U/204Pb in MORB and open system evolution of the depleted mantle. *Earth and Planetary Science Letters*, 115(1): 211-226.
- Whittaker, J.M., Muller, R.D., Roest, W.R., Wessel, P., Smith, W.H., 2008. How supercontinents and superoceans affect seafloor roughness. *Nature*, 456(7224): 938-41.
- Widom, E., 2006. Lost lithium found. *Nature*, 443: 516.
- Woodhead, J., 2002. A simple method for obtaining highly accurate Pb isotope data by MC-ICP-MS. *Journal of Analytical Atomic Spectrometry*, 17(10): 1381-1385.

## 3.6 Methods

### 3.6.1 Samples

Seventeen basalts (whole rock), including volcanic glasses, from the WVZ and five basalts from the SMZ have been analysed in this study. Prior to analysis, volcanic glass samples were ultrasonicated with ultrapure water and ethanol to remove loosely-held weathering minerals. Basalt specimens were sawn to remove weathering rinds, washed with ultrapure water in an ultrasonic bath and crushed in a jaw crusher. Rock chips and volcanic glass fragments were powdered in an agate swing mill.

### 3.6.2 Major elements

Major element concentration of 22 powder samples were determined on a PANalytical Axios Advanced WDS X-ray fluorescence (XRF) instrument equipped with a 4000W Rh X-ray tube at the School of Earth Sciences, University of Tasmania. 0.5 g of sample powder was mixed with 12:22 lithium metaborate and lithium tetraborate flux and fused using a Claisse M4 fluxer. Counting times for each element ranged from 4 to 68 seconds for a total analysis time of ~8 minutes per

sample. Loss on ignition (LOI) was determined on ~2 g of sample heated to 1000°C for 12 hours. Major element and LOI results are given in Supplementary Information (Data file).

### 3.6.3 Trace elements

Trace element concentrations for 20 basalt (fused discs used for XRF analysis) and 2 volcanic glass samples were determined by laser-ablation ICP-MS applying same analytical settings. The LA-ICP-MS analysis was performed at the Isotopia Laboratory at the School of Earth, Atmosphere and Environment, Monash University, using an ASI RESOLUTION SE 193nm ArF excimer laser coupled to ThermoFisher Scientific ICapQ (RF power = 1548 W; ablation cell gas flow = 550 mL min<sup>-1</sup> He + 0.06 mL min<sup>-1</sup> N<sub>2</sub>; auxiliary gas flow = 1.0 L min<sup>-1</sup> Ar). Oxide production (ThO<sup>+</sup>/Th<sup>+</sup>) was kept below <0.7 % and the Th/U was 0.98. Fragments of each fused disc mounted in 1-inch epoxy mounts were analysed for 42 elements (Na, Mg, Al, Si, Ca, Sc, Ti, V, Cr, Mn, Fe, Co, Ni, Zn, Ga, Rb, Sr, Y, Zr, Nb, Mo, Cs, Ba, La, Ce, Pr, Nd, Sm, Eu, Gd, Tb, Dy, Ho, Er, Tm, Yb, Lu, Hf, Ta, Pb, Th and U), using a spot size of 80 µm, a repetition rate of 10 Hz and an energy density of 3 J/cm<sup>2</sup>; four to five spots were measured on each fragment as a transect through the fragment. A single analysis comprised a 20s gas blank, 30s data acquisition and 20s washout. Blocks of twenty unknowns were bracketed by two to three ablations each of NIST 610, NIST 612, BCR2G and BHVO2G. BCR2G was used as calibration standard, and NIST 612 (Jochum et al., 2011), NIST 610 (Jochum et al., 2011) and BHVO2G (Jochum et al., 2005) were used as quality controls. All results for unknowns and quality controls are reported in Supplementary Data Tables 3.1 – 3.3. For the elements of particular interest here (Ba, Th, Nb, Zr, Yb), relative standard errors (%RSE) of 0.18 %, 0.93 %, 1.53 %, 2.3 % and 0.11 %, respectively, were obtained for a suite of sixteen analyses of the BHVO2G glass. Si (as determined by XRF) was used as internal calibration standard. Data were acquired in a time-resolved analysis mode and were reduced using a MS Excel spreadsheet developed at the Max Planck Institute for Chemistry (MPIC) Mainz, Germany (Jochum et al., 2007; Longerich et al., 1996). An important consideration in chemical analysis of fused discs is the blank of the flux material. The flux material contains 46.74 wt. % Si, and Na, Mg, Al, Ca, Ti and Fe range from 20 ppm (Mg) to 230 ppm (Ca). Apart from Sc, V, and Mn (5 ppm, 4 ppm and 8 ppm, respectively), all other measured elements are below 1 ppm (e.g. Ba 0.87 ppm, Nb 0.05 ppm, Zr 0.33 ppm; Th and Yb are below detection (Table S3.1c).

### 3.6.4 Sr and Pb isotope ratios

Pb isotope ratios were acquired for small (1 - 2 mm) chips picked under the microscope. Samples in the range 150 - 200 mg were weighed into Teflon beakers and leached with hot 6M HCl (60 min, 100°C). After removal of the leach solution and repeated rinsing with distilled water, residues were dissolved in 5:1 HF-HNO<sub>3</sub> (3 ml, 48 hrs, 100°C) on a hotplate. After evaporation of the acid, the residues were refluxed and dried twice with 2 ml of conc. HNO<sub>3</sub>, followed by dissolution with 6M

HCl. Lead was extracted using a double pass on small beds of AG1-X8 (100 – 200  $\mu\text{m}$ ) anion resin. The procedural blank was  $30 \pm 10$  pg Pb. Lead isotope ratios were measured on a Nu Plasma MC-ICP-MS at the University of Melbourne and on a ThermoFisher Neptune Plus MC-ICP-MS at the Isotopia Laboratory at Monash University. Instrumental mass bias was corrected using the thallium-doping technique of Woodhead (2002). This technique uses separate empirically determined Pb vs Tl isotope correlation lines for each Pb isotope ratio and produces external precisions in the sub-0.1% range (2sd). For example, USGS basalt BCR-2 (unleached) measured at University of Melbourne averages  $^{206}\text{Pb}/^{204}\text{Pb}$   $18.758 \pm 0.047\%$ ,  $^{207}\text{Pb}/^{204}\text{Pb}$   $15.619 \pm 0.066\%$ ,  $^{208}\text{Pb}/^{204}\text{Pb}$   $38.726 \pm 0.090\%$  (2sd,  $n = 47$ , Maas et al., 2015). A similar approach for the data acquired on the Monash University NeptunePlus yielded averages of  $16.941 \pm 0.039\%$ ,  $15.499 \pm 0.042\%$  and  $36.722 \pm 0.036\%$  (2sd,  $n = 11$ ) for SRM981. BCR2 averaged  $18.750 \pm 0.043\%$ ,  $15.615 \pm 0.051\%$  and  $38.691 \pm 0.041\%$  (2sd,  $n = 4$ ). These data are consistent with reference values (Jochum et al., 2007) (or <http://georem.mpch-mainz.gwdg.de>).

For Sr isotope analyses, ca. 100 mg of sample powder were dissolved as described above. Strontium was separated using EICHRON Sr spec (100 - 150  $\mu\text{m}$ ) following Pin et al. (1994). The procedural blank was negligible ( $\sim 60 \pm 20$  pg). Strontium isotope ratios were measured on a ThermoFisher NeptunePlus MC-ICP-MS at the Isotopia Laboratory at Monash University, with sample introduction via a glass spray chamber in wet-plasma mode. All measured signal intensities were corrected for memory and Rb-Kr isobars are required, and instrumental mass bias was corrected by internal normalisation to  $^{86}\text{Sr}/^{88}\text{Sr}$  of 0.1194, using the exponential law. Krypton interferences were corrected by using eight iterations of  $^{86}\text{Kr}/^{84}\text{Kr} = 0.30354$  to account for isobaric interferences on  $^{86}\text{Sr}$ .  $^{87}\text{Sr}/^{86}\text{Sr}$  in SRM987 averaged  $0.710347 \pm 0.000062$  (2sd;  $n = 15$ ), and  $^{87}\text{Sr}/^{86}\text{Sr}$  in all runs were calibrated to a more typical value ( $^{87}\text{Sr}/^{86}\text{Sr} = 0.710248$ ; McArthur, 1994).

### 3.7 Supplementary Information

Major and trace element concentrations data tables are provided in the Supplementary Data Tables.

### 3.8 Acknowledgements

The authors would like to acknowledge Jay Thompson from UTAS for undertaking the major element analysis and Massimo Raveggi from the Isotopia Laboratory for his help with LA-ICP-MS analysis. This work was supported by an ARC grant FT140101062 to O.N. H. Dick was supported by US National Science Foundation (Grant No. OCE-MG&G 8371300). M.R. was supported by a graduate scholarship of Monash University and the SEAE.

# **Supplementary Information**

**A fossil subduction zone under the western Gakkel Ridge region, Arctic Ocean**

Marianne Richter, Oliver Nebel, Roland Maas, Yona Nebel-Jacobsen, Henry J.B. Dick, Fabio A. Capitanio



**SI -  $\Delta Th/Yb$  and  $\Delta 8^*/6^*$  calculations**

$\Delta Th/Yb$  defines the deviation from the lowermost boundary of the MORB array in the Th-Nb-Yb diagram (Fig. 3.4a; Pearce, 2008). The low-Th/Yb high-Nb/Yb limit of the MORB array (Jenner and O'Neill, 2012), here referred as baseline, is described by the following equation (Eq. 1)

$$(Th/Yb)_{baseline} = 0.0555*(Nb/Yb) + 0.0113 \quad (Eq. 1)$$

Deviation ( $\Delta$ ) of Th/Yb in a given rock from this baseline are quantified by subtracting  $(Th/Yb)_{baseline}$  from the measured measured Th/Yb value (Eq. 2)

$$\Delta Th/Yb = [(Th/Yb)_{rock} - (Th/Yb)_{baseline}] \times 100 \quad (Eq. 2)$$

$\Delta 8^*/6^*$  represents the deviation of a measured Pb isotope composition from the Northern Hemisphere Reference Line (Hart, 1984) (NHRL) and the radiogenic Pb ingrowth  $(^{208}Pb^*/^{206}Pb^*)_{ingrowth}$  since the accretion of the Earth.  $(^{208}Pb^*/^{206}Pb^*)_{ingrowth}$  quantifies the increments of radiogenic  $^{208}Pb$  and  $^{206}Pb$  accumulated since Earth's accretion (Allègre et al., 1986) and is based on  $^{208}Pb/^{204}Pb$  and  $^{206}Pb/^{204}Pb$  in Canyon Diablo troilite (Tatsumoto, 1978) (CD). To calculate  $(^{208}Pb^*/^{206}Pb^*)_{ingrowth}$  the following equation (Eq. 3) has been used.

$$(^{208}Pb^*/^{206}Pb^*)_{ingrowth} = [(^{208}Pb/^{204}Pb)_{measured} - (^{208}Pb/^{206}Pb)_{CD}] / [(^{206}Pb/^{204}Pb)_{measured} - (^{206}Pb/^{204}Pb)_{CD}] \quad (Eq. 3)$$

$$(^{208}Pb^*/^{206}Pb^*)_{NHRL-CD} = [(^{208}Pb/^{204}Pb)_{NHRL} - (^{208}Pb/^{206}Pb)_{CD}] / [(^{206}Pb/^{204}Pb)_{measured} - (^{206}Pb/^{204}Pb)_{CD}] \quad (Eq. 4)$$

For determining the overall radiogenic ingrowth (Eq. 4), similar principle as (Eq. 2) has been applied

$$\Delta 8^*/6^* = [(^{208}Pb^*/^{206}Pb^*)_{ingrowth} - (^{208}Pb^*/^{206}Pb^*)_{NHRL-CD}] \times 100 \quad (Eq. 5)$$

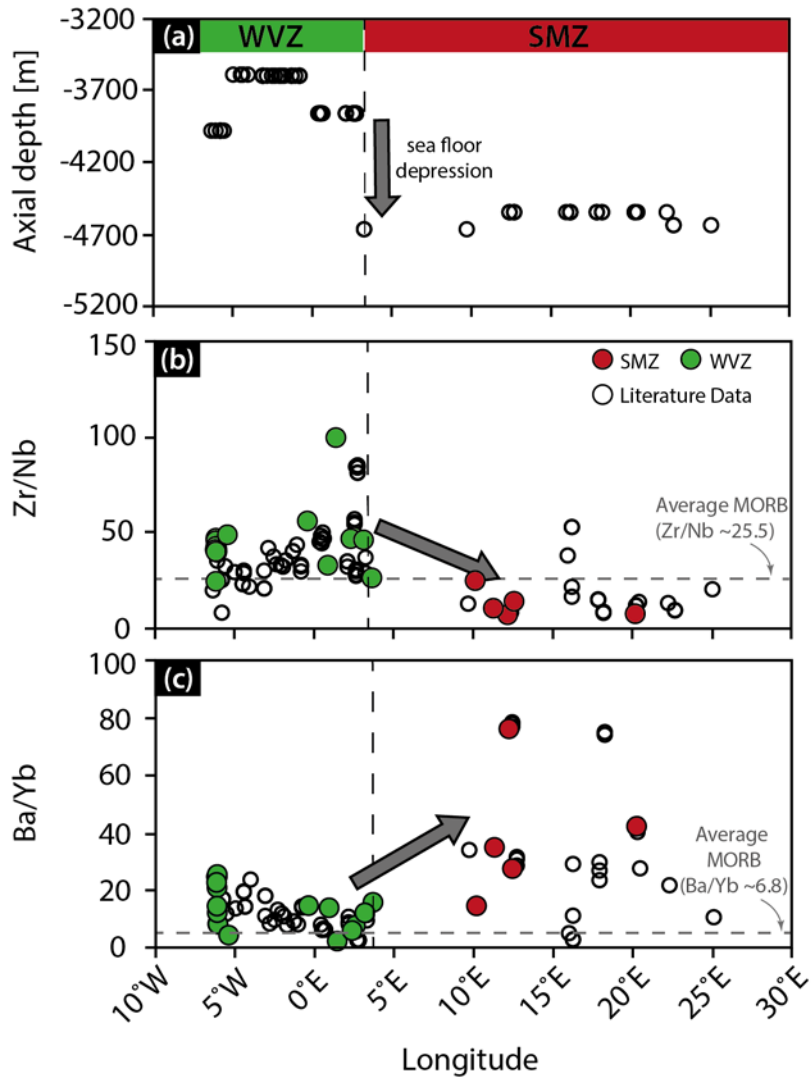
*Supplementary Table 3.1 - Sample location of the analysed Gakkel Ridge basalts.*

<b>Sample No.<sup>1</sup></b>	<b>Longitude</b>	<b>Latitude</b>	<b>Segment</b>
HLY0102 D011 - 19	82.60	-6.19	WVZ
PS 66 217-16 (B)	82.86	-6.15	WVZ
PS 86 -019 (B)	82.53	-6.15	WVZ
PS 86 - 67 (VG)	82.53	-6.15	WVZ
PS 86 - 044 (VG)	82.53	-6.15	WVZ
PS 59 216 (B)	83.09	-6.10	WVZ
PS 59 216-11 (B)	83.09	-6.10	WVZ
PS 59 216-13 (B)	83.09	-6.10	WVZ
HLY0102 D013 - 10	83.20	-5.43	WVZ
PS 59 231 - 14	83.96	-0.40	WVZ
PS 59 232 - 84	84.17	0.88	WVZ
HLY0102 D024 - 2	84.55	1.39	WVZ
HLY0102 D026 - 9	84.28	2.34	WVZ
HLY0102 D018 - 1	83.42	2.54	WVZ
PS 59 234 - 24	84.57	3.13	WVZ
PS 59 224 - 34	83.38	3.66	WVZ
PS 59 243 - 36	84.97	10.15	SMZ
HLY0102 D037 - 5	85.18	11.30	SMZ
HLY0102 D036 - 35	85.16	12.20	SMZ
HLY0102 D038 - 6	85.19	12.42	SMZ
PS 59 251 - 4	85.71	20.23	SMZ

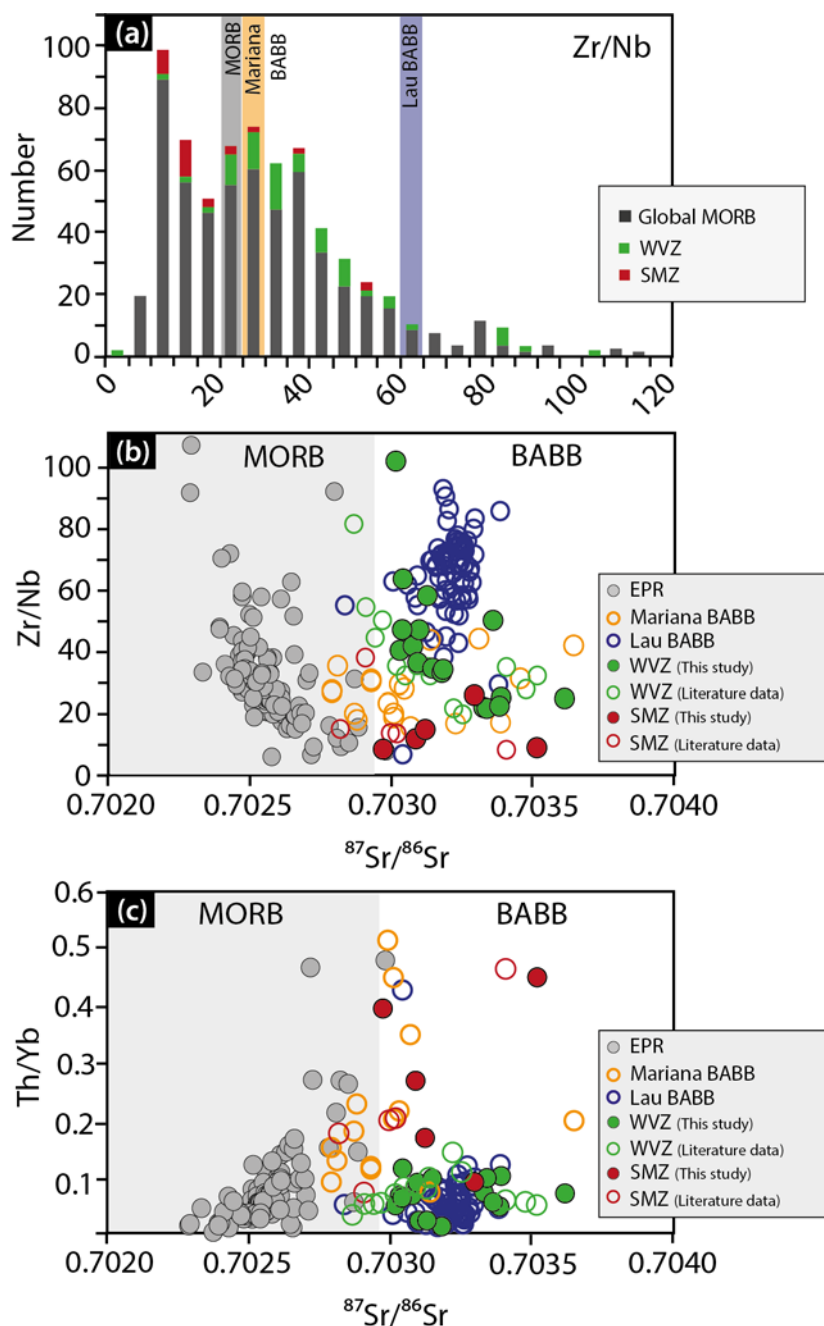
<sup>1</sup> (B) – Basalt; (VG) – Volcanic Glass

Supplementary Table 3.2 – Sr-Pb isotope data for Gakkel Ridge basalts. B – basalts; VG – volcanic glass

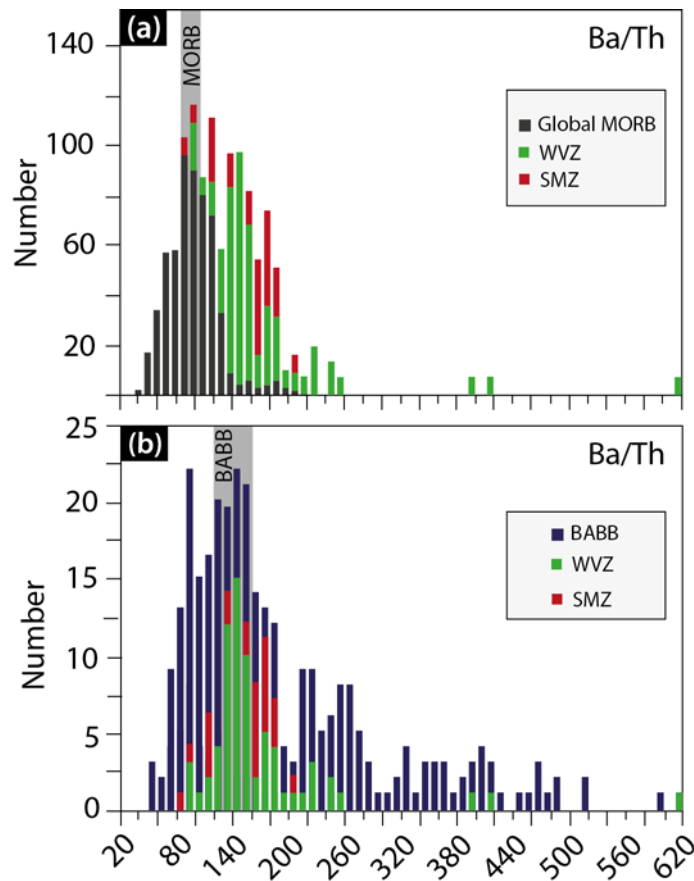
Sample Name	Segment	$^{206}\text{Pb}/^{204}\text{Pb}$	ISE	$^{207}\text{Pb}/^{204}\text{Pb}$	ISE	$^{208}\text{Pb}/^{204}\text{Pb}$	ISE	$\Delta 7/4$	$\Delta 8/4$	$^{176}\text{Hf}/^{177}\text{Hf}$	$\epsilon\text{Hf}$	$^{87}\text{Sr}/^{86}\text{Sr}$	ISE
HL Y0102 D011 - 19	WVZ	-	-	-	-	-	-	-	-	0.283234	15.88	0.703386	0.000007
HL Y0102 D8 - 12	WVZ	18.011	0.003	15.439	0.002	37.829	0.006	-0.44	42.68	0.283249	16.41	0.703186	0.000009
PS 66 217-16 (B)	WVZ	17.988	0.001	15.431	0.001	37.780	0.002	-1.41	40.51	0.283172	13.69	0.703392	0.000008
PS 86 -019 (B)	WVZ	17.889	0.001	15.414	0.001	37.678	0.002	-3.11	42.30	0.283034	8.81	0.703330	0.000008
PS 86 - 67 (VG)	WVZ	18.010	0.001	15.435	0.001	37.814	0.002	-1.00	41.29	0.283257	16.69	0.703148	0.000007
PS 86 - 044 (VG)	WVZ	17.866	0.001	15.415	0.001	37.666	0.002	-3.03	43.83	0.283229	15.70	0.703341	0.000011
PS 59 216 (B)	WVZ	18.064	0.001	15.443	0.001	37.845	0.002	-0.23	37.90	0.283156	13.12	0.703032	0.000009
PS 59 216-11 (B)	WVZ	18.043	0.001	15.438	0.001	37.819	0.002	-0.70	37.76	0.283034	8.81	0.703078	0.000005
PS 59 216-13 (B)	WVZ	18.059	0.001	15.437	0.001	37.824	0.002	-0.84	36.28	0.283261	16.83	0.703095	0.000010
HL Y0102 D013 - 10	WVZ	18.026	0.004	15.479	0.004	37.811	0.009	3.44	39.12	0.283247	16.34	0.703363	0.000008
PS 59 231 - 14	WVZ	18.082	0.003	15.458	0.003	37.843	0.007	0.66	35.42	0.283242	16.16	0.703129	0.000007
PS 59 232 - 84	WVZ	18.088	0.003	15.504	0.002	37.966	0.006	5.23	47.13	0.283269	17.12	0.703181	0.000007
HL Y0102 D024 - 2	WVZ	18.242	0.008	15.558	0.007	38.087	0.018	8.99	40.51	0.283218	15.31	0.703017	0.000007
HL Y0102 D026 - 9	WVZ	18.113	0.003	15.475	0.002	37.884	0.005	2.06	35.84	0.283260	16.80	0.703043	0.000007
HL Y0102 D018 - 1	WVZ	18.118	0.003	15.476	0.002	37.917	0.006	2.05	38.53	0.283158	13.19	0.703101	0.000009
PS 59 234 - 24	WVZ	18.066	0.003	15.459	0.002	37.859	0.006	0.94	38.97	0.283258	16.73	0.703040	0.000008
PS 59 224 - 34	WVZ	18.028	0.002	15.491	0.001	37.921	0.003	4.57	49.74	0.283286	17.72	0.703618	0.000007
PS 59 243 - 36	SMZ	17.873	0.004	15.447	0.003	37.774	0.009	1.84	53.88	0.283183	14.07	0.703297	0.000011
HL Y0102 D037 - 5	SMZ	17.952	0.001	15.458	0.001	37.293	0.002	2.05	-3.85	0.283381	21.08	0.703088	0.000008
HL Y0102 D036 - 35	SMZ	17.696	0.002	15.411	0.001	37.599	0.004	0.12	57.70	0.283321	18.95	0.703519	0.000010
HL Y0102 D038 - 6	SMZ	17.933	0.002	15.447	0.002	37.771	0.004	1.25	46.38	0.283201	14.71	0.703122	0.000006
PS 59 251 - 4	SMZ	18.308	0.003	15.526	0.002	38.011	0.006	5.08	24.99	0.283295	18.03	0.702973	0.000007



**Supplementary Figure 3.1 - Variation of Zr/Nb, Ba/Yb and axial depth along the ridge.** (a), The abrupt change in axial depth between the WVZ and SMZ could reflect a compositional break in the underlying mantle. Zr/Nb (b) and Ba/Yb (c) of both segments are inversely correlated with each other. Zr/Nb tends to be higher in WVZ than in SMZ, while Ba/Yb is higher in SMZ basalts, due to higher Ba (Michael et al., 2003). Low Zr/Nb in SMZ basalts reflects low Zr/Nb in their magma source, most likely a result of prior melt extraction (Michael et al., 2003). Ba enrichment in the same SMZ basalts would then require re-enrichment (by fluids) of this mantle domain. Dark-grey arrows indicate interpreted changes in Zr/Nb and Ba/Yb. Data sources from Gale et al. (2013). SMZ – Sparsely Magmatic Zone; WVZ – Western Volcanic Zone.



**Supplementary Figure 3.2 - Zr/Nb, Th/Yb and Sr isotope ratios in Western Gakkel Ridge MORB.** (a) Distribution of Zr/Nb in Western Gakkel Ridge MORB (data - this study and Gale et al., 2013) compared with MORB (data - Jenner and O'Neill, 2012). Zr/Nb in SMZ and WVZ basalts tend to lower and higher, respectively, than average Zr/Nb in MORB ( $n = 23$ , grey bar). Elevated Zr/Nb are also found in basalts from active back-arc basins (orange – Mariana BABB; blue – Lau BABB). (b) Zr/Nb shows weak correlations with  $^{87}\text{Sr}/^{86}\text{Sr}$ , e.g. high Zr/Nb in WVZ trends towards elevated  $^{87}\text{Sr}/^{86}\text{Sr}$  (as does Lau Basin BABB, indicating a crustal input). MORB show an opposite trend (high Zr/Nb towards lower  $^{87}\text{Sr}/^{86}\text{Sr}$ ). (c) Two different trends within the BABB are visible. Firstly, Lau BABB cluster at low Th/Yb and elevated  $^{87}\text{Sr}/^{86}\text{Sr}$  (0.7030 – 0.7035), similar to WVZ basalts. Secondly, Mariana BABB are enriched in Th which increases with increasing  $^{87}\text{Sr}/^{86}\text{Sr}$ , similar to basalts from the SMZ. The latter seems to extend the MORB trend. Elevated  $^{87}\text{Sr}/^{86}\text{Sr}$  reflect an input from subducted sediment, explanation see main text.



**Supplementary Figure 3.3 - Ba/Th in MORB from the Western Gakkel Ridge region.** Distribution of Ba/Th of the Western Gakkel Ridge MORBs (SMZ and WVZ) compared with MORB data (a) and BABB (b). Barium/Th in SMZ basalts is higher than in WVZ basalts, and Ba/Th in both ridge segments tend to be high compared to the global MORB distribution. Western Gakkel Ridge basalts, however, show a considerable overlap with Ba/Th in basalts erupted in active back-arc basins. MORB data is from Jenner and O'Neill (2012), BABB data from Gale et al. (2013), including Lau and Mariana BABB data. The grey bar represents the average Ba/Th concentration of MORB and BABB. Data for SMZ and WVZ is compiled from this study and Gale et al. (2013).

### SI - References

- Allègre, C.J., Dupré, B., Lewin, E., 1986. Thorium/uranium ratio of the Earth. *Chemical Geology*, 56(3): 219-227.
- Gale, A., Dalton, C.A., Langmuir, C.H., Su, Y., Schilling, J.-G., 2013. The mean composition of ocean ridge basalts. *Geochemistry, Geophysics, Geosystems*, 14(3): 489-518.
- Hart, S.R., 1984. A large-scale isotope anomaly in the Southern Hemisphere mantle. *Nature*, 309(5971): 753-757.
- Jenner, F.E., O'Neill, H.S.C., 2012. Analysis of 60 elements in 616 ocean floor basaltic glasses. *Geochemistry, Geophysics, Geosystems*, 13(2): Q02005.
- Michael, P.J. et al., 2003. Magmatic and amagmatic seafloor generation at the ultraslow-spreading Gakkel ridge, Arctic Ocean. *Nature*, 423(6943): 956-961.
- Pearce, J.A., 2008. Geochemical fingerprinting of oceanic basalts with applications to ophiolite classification and the search for Archean oceanic crust. *Lithos*, 100(1-4): 14-48.
- Tatsumoto, M., 1978. Isotopic composition of lead in oceanic basalt and its implication to mantle evolution. *Earth and Planetary Science Letters*, 38(1): 63-87.

## **Supplementary Data Tables**



Chapter 3 – Supplementary Data Tables

**Supplementary Table 3.1 – Major and trace element data of the WVZ and SMZ basalts. Major element data is given in wt.%, whereas the trace element data are given in ppm.**

<i>Sample Name</i>	<i>HLY0102 D011 - 19</i>	<i>HLY0102 D8 - 12</i>	<i>PS 66 217- 16 (B)</i>	<i>PS 86 -019 (B)</i>	<i>PS 86 - 67 (VG)</i>	<i>PS 86 - 044 (VG)</i>	<i>PS 59 216 (B)</i>	<i>PS 59 216- 11 (B)</i>
<i>Segment</i>	WVZ	WVZ	WVZ	WVZ	WVZ	WVZ	WVZ	WVZ
<i>MAJOR ELEMENTS</i>								
SiO <sub>2</sub>	49.66	49.81	49.71	50.26	50.02	50.59	49.89	49.45
TiO <sub>2</sub>	1.54	1.52	1.77	1.63	1.59	1.65	1.50	1.50
Al <sub>2</sub> O <sub>3</sub>	15.82	15.63	15.53	15.75	15.43	15.71	15.88	15.83
Fe <sub>2</sub> O <sub>3</sub>	10.05	10.30	10.54	10.13	10.55	10.24	10.33	10.23
MnO	0.17	0.18	0.18	0.17	0.18	0.16	0.18	0.17
MgO	8.35	8.41	7.89	8.37	8.23	8.18	8.25	8.16
CaO	10.73	11.04	10.52	10.58	10.87	10.44	11.26	11.18
Na <sub>2</sub> O	3.02	3.03	3.07	3.21	3.11	3.22	2.98	2.99
K <sub>2</sub> O	0.46	0.25	0.41	0.37	0.22	0.38	0.18	0.25
P <sub>2</sub> O <sub>5</sub>	0.15	0.15	0.17	0.17	0.16	0.17	0.14	0.14
Sum	99.98	100.09	99.79	100.26	99.77	100.31	100.44	99.73
<i>TRACE ELEMENTS</i>								
Na	20818	22764	20233	21528	21230	22530	19408	19709
Mg	52081	57000	47026	50661	50668	51648	48364	48418
Al	86802	91431	82473	85076	84387	87409	83997	84285
Si	232127	232837	232356	234916	233809	236477	233216	231151
Ca	88383	94234	84500	85718	89188	88085	88383	89744
Sc	38	41	38	37	40	39	38	38
Ti	10730	10985	12121	11405	11173	11974	10197	10304
V	286	312	310	300	312	311	289	293
Cr	321	345	296	309	294	303	323	322
Mn	1362	1425	1402	1374	1442	1414	1359	1387
Fe	68481	71432	70942	69479	72477	71133	67457	70106
Co	41.0	42.2	39.5	40.9	41.9	40.3	41.7	40.7
Ni	151.7	139.8	127.4	152.2	137.9	146.4	127.3	129.9
Zn	49.54	55.13	54.60	51.98	55.80	55.83	51.99	53.53
Ga	14.89	16.38	16.23	15.62	16.04	16.30	15.94	16.30
Rb	6.61	3.59	6.37	7.57	3.35	7.69	2.19	2.61
Sr	194.89	172.68	194.39	197.56	168.27	199.76	169.14	172.33
Y	33.06	35.51	37.56	35.71	36.94	36.60	35.45	35.89
Zr	108.37	105.72	124.10	120.66	112.88	123.48	106.34	109.48
Nb	4.88	3.15	4.99	5.53	3.32	5.74	2.69	2.68
Mo	1.07	0.27	36.20	1.17	0.75	0.71	1.45	0.69
Cs	0.11	0.02	0.04	0.05	0.02	0.09	0.04	0.03
Ba	73.95	49.30	82.09	94.66	49.92	95.13	33.13	32.73
La	5.19	4.64	5.64	6.18	4.88	5.93	4.57	4.64
Ce	12.38	11.51	14.37	14.40	12.37	14.35	12.00	11.98
Pr	2.01	2.03	2.40	2.41	2.12	2.37	2.06	2.13
Nd	11.28	11.03	12.95	13.22	11.98	12.61	12.27	12.21
Sm	3.88	3.52	4.44	4.11	3.90	4.65	3.96	4.12
Eu	1.38	1.41	1.56	1.50	1.42	1.43	1.44	1.52
Gd	4.88	4.84	5.64	5.73	5.54	5.32	5.55	5.33
Tb	0.82	0.87	1.01	0.94	0.98	0.93	0.94	0.96
Dy	5.61	6.50	6.98	6.52	6.39	6.38	6.37	6.46
Ho	1.11	1.30	1.39	1.33	1.36	1.32	1.37	1.35
Er	3.56	3.82	4.17	4.03	4.06	3.74	3.96	4.16
Tm	0.47	0.58	0.62	0.62	0.58	0.58	0.62	0.63
Yb	3.18	3.29	3.84	3.76	3.95	3.66	3.71	3.80
Lu	0.46	0.51	0.59	0.57	0.55	0.50	0.54	0.55
Hf	2.93	2.71	3.47	3.15	3.20	3.11	3.07	3.07
Ta	1.34	1.13	1.39	1.38	1.17	1.36	1.35	1.32
Pb	0.70	0.66	1.16	1.02	0.90	0.86	0.96	0.63
Th	0.33	0.23	0.37	0.41	0.32	0.38	0.30	0.28
U	0.13	0.11	0.12	0.11	0.10	0.12	0.11	0.12

Chapter 3 – Supplementary Data Tables

Supplementary Data Table 3.1 – [continued]

Sample Name	PS 59 216-13 (B)	HLY0102 D013 - 10	PS 59 231 - 14	PS 59 232 - 84	HLY0102 D024 - 2	HLY0102 D026 - 9	HLY0102 D018 - 1
Segment	WZ	WZ	WZ	WZ	WZ	WZ	WZ
<i>MAJOR ELEMENTS</i>							
SiO <sub>2</sub>	49.47	48.75	49.10	50.09	47.72	49.63	49.56
TiO <sub>2</sub>	1.51	1.63	1.79	1.53	1.11	1.70	1.71
Al <sub>2</sub> O <sub>3</sub>	16.04	15.24	16.12	15.60	19.25	15.48	15.79
Fe <sub>2</sub> O <sub>3</sub>	10.38	11.06	11.23	10.37	8.43	10.91	10.77
MnO	0.18	0.18	0.19	0.18	0.14	0.18	0.18
MgO	8.34	7.57	6.89	8.32	7.34	8.15	7.70
CaO	11.34	11.11	10.97	10.81	12.73	10.94	10.96
Na <sub>2</sub> O	2.99	2.90	3.04	3.09	2.77	3.01	3.11
K <sub>2</sub> O	0.24	0.32	0.34	0.35	0.11	0.22	0.25
P <sub>2</sub> O <sub>5</sub>	0.15	0.15	0.17	0.15	0.10	0.16	0.17
Sum	100.41	100.38	99.95	100.43	100.35	100.16	100.01
<i>TRACE ELEMENTS</i>							
Na	19413	19664	16084	23321	19227	21873	21529
Mg	48877	47021	55682	57514	46294	53764	48898
Al	83841	82630	97009	92734	106608	89138	87189
Si	231253	227880	229510	234127	223072	231982	231674
Ca	89272	89935	109697	94498	103518	93498	90141
Sc	38	39	47	40	33	42	38
Ti	10175	11280	7469	11433	7802	12449	11957
V	292	321	328	311	222	334	318
Cr	305	280	536	322	297	343	300
Mn	1378	1416	1966	1467	1084	1512	1432
Fe	69575	74197	75988	73326	56626	76641	73295
Co	40.3	42.9	47.1	44.3	38.7	43.4	40.0
Ni	131.4	115.5	115.2	152.2	126.2	137.1	117.6
Zn	51.86	57.53	60.39	55.59	42.77	55.71	60.93
Ga	15.76	16.73	15.93	16.64	13.18	16.08	16.52
Rb	2.06	2.88	7.69	4.22	1.53	2.30	2.34
Sr	170.18	154.94	107.22	176.41	185.32	168.74	171.71
Y	35.03	38.70	26.67	35.82	25.54	39.69	39.02
Zr	104.81	110.54	55.94	112.65	75.23	123.49	125.50
Nb	2.93	2.26	1.01	3.45	0.79	2.00	2.72
Mo	0.53	1.21	0.72	1.13	1.29	1.11	0.00
Cs	0.07	0.16	0.24	0.12	0.04	0.02	0.02
Ba	30.26	18.86	39.64	48.04	6.99	23.00	31.99
La	4.87	4.23	2.29	4.97	2.59	4.55	4.92
Ce	11.77	11.12	5.32	12.28	6.73	11.84	12.59
Pr	2.03	1.99	1.05	2.05	1.24	2.14	2.12
Nd	11.70	11.00	5.52	11.55	7.45	11.75	12.68
Sm	4.15	3.95	2.28	3.88	2.53	3.86	4.37
Eu	1.44	1.44	0.85	1.34	1.06	1.40	1.45
Gd	5.52	5.35	3.41	4.61	3.81	5.69	5.75
Tb	0.91	0.93	0.63	0.90	0.60	0.98	0.94
Dy	6.43	6.62	4.52	5.70	4.21	6.64	6.97
Ho	1.35	1.35	0.96	1.24	0.86	1.40	1.34
Er	3.85	4.18	2.67	3.64	2.73	4.23	4.12
Tm	0.61	0.58	0.44	0.47	0.40	0.61	0.61
Yb	3.47	3.91	2.60	3.34	2.47	3.57	3.92
Lu	0.52	0.55	0.42	0.47	0.35	0.55	0.55
Hf	3.04	2.90	1.52	2.59	1.82	3.05	3.27
Ta	1.23	1.09	1.07	1.12	0.86	0.98	1.03
Pb	0.85	0.56	0.31	0.67	0.49	0.63	0.69
Th	0.26	0.21	0.05	0.26	0.08	0.20	0.25
U	0.17	0.06	0.05	0.10	0.14	0.07	0.17

Chapter 3 – Supplementary Data Tables

Supplementary Data Table 3.1 – [continued]

<i>Sample Name</i>	<i>PS 59 234 - 24</i>	<i>PS 59 224 - 34</i>	<i>PS 59 243 - 36</i>	<i>HLY0102 D037 - 5</i>	<i>HLY0102 D036 - 35</i>	<i>HLY0102 D038 - 6</i>	<i>PS 59 251 - 4</i>
<i>Segment</i>	<i>WZ</i>	<i>WZ</i>	<i>SMZ</i>	<i>SMZ</i>	<i>SMZ</i>	<i>SMZ</i>	<i>SMZ</i>
<i>MAJOR ELEMENTS</i>							
SiO <sub>2</sub>	49.42	49.51	48.93	50.07	50.92	49.92	48.76
TiO <sub>2</sub>	1.46	1.74	1.19	1.79	1.55	1.42	1.72
Al <sub>2</sub> O <sub>3</sub>	15.38	15.52	18.03	15.79	16.28	16.11	15.42
Fe <sub>2</sub> O <sub>3</sub>	10.12	10.28	8.98	10.82	9.23	9.71	8.92
MnO	0.17	0.17	0.15	0.18	0.16	0.17	0.15
MgO	9.92	6.50	7.74	6.89	7.45	8.70	9.96
CaO	10.88	10.49	11.19	9.39	9.74	10.45	10.26
Na <sub>2</sub> O	2.94	3.16	3.21	3.93	3.71	3.30	3.22
K <sub>2</sub> O	0.21	0.49	0.24	0.49	0.86	0.48	0.68
P <sub>2</sub> O <sub>5</sub>	0.14	0.18	0.14	0.26	0.24	0.18	0.32
Sum	100.39	99.75	100.10	99.61	100.46	100.43	100.40
<i>TRACE ELEMENTS</i>							
Na	13376	23642	24354	27917	26026	23002	24216
Mg	55849	44229	52927	44696	47541	55050	66817
Al	96959	90506	106139	88760	90795	89140	90405
Si	230994	231445	228740	234029	238014	233342	227921
Ca	107816	89932	97106	78429	81015	86544	88400
Sc	43	39	37	36	35	36	35
Ti	6974	12843	8878	12706	10885	10010	12673
V	321	337	231	286	260	250	263
Cr	569	165	365	228	331	368	661
Mn	1919	1383	1271	1478	1269	1300	1209
Fe	68954	71745	63027	74073	62478	65249	61814
Co	47.7	40.7	39.5	37.7	35.6	39.4	55.8
Ni	106.1	78.2	155.9	113.4	139.9	172.1	303.8
Zn	49.04	62.24	43.34	62.87	50.43	50.42	56.20
Ga	15.20	16.60	14.70	17.93	15.90	15.59	15.42
Rb	17.09	6.96	3.46	11.16	16.93	7.02	8.64
Sr	115.96	191.57	182.82	188.80	236.98	172.57	261.25
Y	24.24	38.86	30.10	42.42	35.31	33.82	32.37
Zr	51.92	128.38	95.14	160.06	147.41	118.12	156.08
Nb	1.15	5.22	3.72	13.54	16.38	8.00	18.45
Mo	0.00	1.73	1.04	1.17	1.22	0.62	1.53
Cs	0.27	0.27	0.07	0.25	0.36	0.06	0.37
Ba	31.55	60.80	44.09	138.80	254.69	88.51	123.68
La	2.34	6.99	4.89	10.53	12.47	7.35	12.38
Ce	5.00	15.95	11.63	23.03	24.80	15.81	25.64
Pr	0.88	2.52	1.88	3.38	3.31	2.29	3.57
Nd	5.18	13.31	9.52	16.67	15.71	11.60	17.16
Sm	2.53	4.39	2.95	4.98	4.00	3.86	4.07
Eu	0.83	1.46	1.26	1.60	1.43	1.21	1.53
Gd	2.74	5.64	4.06	6.19	5.43	4.34	5.27
Tb	0.55	0.90	0.76	1.03	0.90	0.80	0.90
Dy	3.97	6.31	4.73	7.01	5.78	5.51	5.39
Ho	0.87	1.27	1.04	1.47	1.18	1.14	1.09
Er	2.63	3.84	3.05	4.52	3.59	3.42	3.30
Tm	0.43	0.57	0.48	0.60	0.51	0.49	0.48
Yb	2.49	3.74	2.92	3.92	3.32	3.16	2.89
Lu	0.36	0.55	0.40	0.56	0.52	0.47	0.43
Hf	1.39	3.04	2.03	3.74	3.31	2.61	3.54
Ta	1.08	1.09	1.02	1.62	1.76	1.40	1.91
Pb	0.51	0.76	0.58	1.04	1.00	0.71	1.08
Th	0.08	0.45	0.28	1.07	1.50	0.55	1.15
U	0.04	0.59	0.09	0.25	0.32	0.20	0.44

Supplementary Table 3.2 – Trace element data of NIST 612 and NIST 610. All values are given in ppm.

Element	NIST 612				NIST 610			
	Average (n = 32)	RSE (%)	Literature value	Relative error (%)	Average (n = 32)	RSE (%)	Literature value	Relative error (%)
Na	105295	1.4	101635	4.0	102794	1.4	102300	0.5
Mg	70	1.2	68	2.7	539	1.1	610	11.7
Al	11068	0.9	10744	2.9	10572	1.0	11626	9.1
Si	337024	0.0	337024	0.0	323001	0.0	323001	0.0
Ca	87831	1.0	85049	3.2	83812	1.0	81475	2.9
Sc	42.8	0.2	39.9	6.8	346	1.0	455	23.9
Ti	58.1	0.5	44.0	24.3	551	0.9	452	21.9
V	39.7	1.0	38.8	2.3	446	1.3	450	0.8
Cr	41.0	0.8	36.4	11.2	453	1.1	408	10.8
Mn	42.7	0.7	38.7	9.3	462	0.9	444	4.0
Fe	55.8	0.9	51.0	8.6	493	0.7	458	7.6
Co	35.5	0.5	35.5	0.1	407	0.8	410	0.7
Ni	41.8	0.4	38.8	7.1	487	0.4	441	5.9
Zn	28.8	1.7	39.1	35.7	362	1.4	460	27.0
Ga	37.9	0.7	36.9	2.6	445	0.8	433	2.7
Rb	31.0	1.0	31.4	1.4	383	1.5	426	11.0
Sr	88.9	1.0	78.4	11.8	506	1.1	516	1.9
Y	45.1	0.9	38.3	15.1	484	1.0	462	4.6
Zr	44.0	0.9	37.9	13.8	498	1.2	448	10.0
Nb	43.1	0.9	38.9	9.7	492	1.0	465	5.5
Mo	39.5	0.9	37.4	5.2	446	0.8	417	6.4
Cs	42.7	1.1	42.7	0.0	335	1.1	366	-9.3
Ba	41.6	1.2	39.3	5.6	469	1.3	452	3.6
La	38.7	1.1	36.0	7.1	418	1.2	440	5.3
Ce	40.8	1.1	38.4	5.8	432	1.2	453	4.9
Pr	41.0	1.1	37.9	7.6	433	1.2	448	3.4
Nd	39.6	1.1	35.5	10.4	473	1.1	430	9.1
Sm	42.2	1.1	37.7	10.6	498	1.1	453	9.1
Eu	38.9	1.2	35.6	8.4	433	1.4	447	3.1
Gd	42.7	1.2	37.3	12.6	495	1.2	449	9.2
Tb	42.5	1.2	37.6	11.5	446	1.3	437	2.1
Dy	41.4	1.2	35.5	14.3	493	1.3	437	11.3
Ho	43.2	1.2	38.3	11.3	453	1.4	449	1.0
Er	44.2	1.3	38.0	14.0	501	1.5	455	9.2
Tm	42.9	1.3	36.8	14.2	450	1.4	435	3.3
Yb	44.6	1.3	39.2	12.1	510	1.3	450	11.8
Lu	42.7	1.3	37.0	13.4	456	1.4	439	3.8
Hf	41.7	1.4	36.7	12.1	476	1.4	435	8.6
Ta	45.4	1.3	37.6	17.2	509	1.4	446	12.4
Pb	40.3	1.5	38.6	4.2	433	1.7	426	1.7
Th	42.8	1.6	37.8	11.6	460	1.7	457	0.6
U	39.1	1.6	37.4	4.3	429	1.7	462	7.6

*Supplementary Table 3.3 – Trace element data BHVO2G and XRF glass blank. All values are given in ppm.*

<i>Element</i>	<i>BHVO2G</i>				<i>Blank XRF glass</i>
	<i>Average (n = 16)</i>	<i>RSE (%)</i>	<i>Literature value</i>	<i>Relative error (%)</i>	<i>Average (n = 4)</i>
Na	16889	1.7	17805	5.42	35
Mg	43009	1.5	43001	0.02	20
Al	69771	1.2	71978	3.16	66
Si	230448	0.0	230448	0.00	218481
Ca	79385	1.3	81476	2.63	234
Sc	30.7	0.4	33.0	6.93	5.4
Ti	16719	1.5	16300	2.57	105
V	318	1.5	308	3.36	3.7
Cr	313	1.1	293	6.83	10.6
Mn	1313	0.9	1317	0.23	7.8
Fe	85760	0.9	87836	2.42	33.8
Co	45	0.7	44	1.57	0.25
Ni	130	0.7	116	12.05	0.98
Zn	96	1.7	102	5.63	0.67
Ga	22	0.8	22	0.24	0.13
Rb	9.1	1.1	9.2	1.56	0.10
Sr	385	2.3	396	2.82	0.43
Y	25.1	0.9	26	3.54	0.02
Zr	166.1	1.0	170	2.30	0.33
Nb	18.0	1.1	18.3	1.57	0.05
Mo	4.20	1.4	3.8	10.52	0.37
Cs	0.10	3.1	0.1	1.25	0.02
Ba	131.2	1.5	131	0.18	0.87
La	14.91	1.2	15.2	1.92	0.21
Ce	37.47	1.4	37.6	0.35	0.05
Pr	5.21	1.2	5.35	2.66	0.00
Nd	24.57	1.1	24.5	0.27	b.d.1
Sm	6.12	1.2	6.1	0.32	0.03
Eu	2.05	1.3	2.07	0.93	b.d.1
Gd	6.14	1.2	6.16	0.38	0.01
Tb	0.91	1.2	0.92	1.53	b.d.1
Dy	5.33	1.2	5.28	0.87	b.d.1
Ho	0.95	1.3	0.98	2.80	0.01
Er	2.53	1.4	2.56	1.30	b.d.1
Tm	0.33	1.3	0.34	3.72	0.03
Yb	2.01	1.5	2.01	0.11	b.d.1
Lu	0.28	1.9	0.279	0.44	b.d.1
Hf	4.33	1.6	4.32	0.30	b.d.1
Ta	1.15	1.5	1.15	0.36	0.55
Pb	1.84	1.9	1.7	8.14	0.10
Th	1.21	1.9	1.22	0.93	b.d.1
U	0.42	2.0	0.403	5.04	b.d.1



## CHAPTER 4

### *Elucidating the peculiar $\text{DupAl}$ isotope signatures of Arctic mid-ocean ridge basalts*

*Marianne Richter*<sup>\*1</sup>, *Oliver Nebel*<sup>1</sup>, *Roland Maas*<sup>2</sup>, *Yona Nebel-Jacobsen*<sup>1</sup>, *Henry J.B. Dick*<sup>3</sup>

<sup>1</sup> – Isotopia Laboratory, School of Earth, Atmosphere and Environment, Monash University, Clayton, Victoria, 3800, Australia

<sup>2</sup> – School of Earth Sciences, University of Melbourne, Parkville, Victoria, 3010, Australia

<sup>3</sup> – Department of Geology and Geophysics, Woods Hole Oceanographic Institution, Woods Hole, Massachusetts, 02543-1539, USA



*The photo shows snow covered mountain in the Arctic region, which are reflected in the water. The reflection ('pseudo' mountain) and the actual mountain reflects the findings in this study. (<https://si.huffpost.com/gen/2984270/images/o-ARCTIC-OCEAN-facebook.jpg>).*

*This manuscript is aimed for submission to Geology.*

**Abstract**

The ultraslow-spreading Gakkel Ridge in the Arctic Ocean exposes a geochemical boundary in the upper mantle identified by abrupt changes in radiogenic Pb isotopes at approximately 15 °E - 25°E. Basalts from the Western Gakkel Ridge region exhibit Indian-type or DupAl mantle isotope signatures exemplified through  $^{208}\text{Pb}/^{204}\text{Pb}$  versus  $^{206}\text{Pb}/^{204}\text{Pb}$  isotope covariations, which are clearly offset from the Northern Hemisphere Reference Line. In contrast, basalts from the Eastern Gakkel Ridge have been attributed to show affinities to Atlantic/Pacific-type mantle isotope signatures. Here, we present new radiogenic Hf-Sr-Pb isotope data of basalts dredged East of the isotopic boundary. New Pb isotope data from the Eastern Gakkel Ridge, in conjunction with published isotope data from the Western Gakkel Ridge region, show that the Eastern Gakkel Ridge basalts exhibit a clear Indian-type signature, yet clearly distinct from those at the Western Gakkel Ridge. Strontium-Pb isotope covariations indicate a pollution of the upper mantle that created a pseudo Indian-type mantle signature, which evolved independently in upper mantle regions underlying both ridge segments. We conclude that DupAl or Indian-type upper mantle can be preserved in defined upper mantle domains indefinitely and globally distributed signatures formed by a similar process, but not identical mantle pollution.



## 4.1 Introduction

Indian Ocean mid-ocean ridge basalts (MORB), together with MORBs from the Western Gakkel Ridge region in the Arctic Ocean, display systematically higher  $^{87}\text{Sr}/^{86}\text{Sr}$  and  $^{208}\text{Pb}/^{204}\text{Pb}$  isotopic signature (also called DupAl anomaly) compared to Atlantic/Pacific MORBs (Dupré and Allègre, 1983; Hart, 1984). Various theories exist explaining the DupAl anomaly, which include upwelling of anomalous hot mantle from the core-mantle boundary, modified mantle by subduction through sediment and oceanic crust derived fluids, or delaminated, recycled lower continental crust including sub-continental lithospheric mantle (SCLM) (Barling et al., 1994; Castillo, 1988; Dupré and Allègre, 1983; Escrig et al., 2004; Hanan et al., 2004; Hawkesworth et al., 1986; Kempton et al., 2002; Le Roex et al., 1989; Mahoney et al., 1989; Meyzen et al., 2005; Rehkämper and Hofmann, 1997; Zhang et al., 2005). To date, no satisfying unified model has been proposed to explain the DupAl anomaly.

Worldwide, only two known ridge segments, the Australian Antarctic Discordance (AAD; Klein et al., 1988) and the Western vs Eastern Gakkel Ridge (Goldstein et al., 2008), display an isotopic boundary between DupAl-type mantle and Atlantic/Pacific-type mantle, rendering these localities the most suitable to study the origin of these two distinct MORB isotopic signatures. Here, we focus on basalts from the Gakkel Ridge.

### 4.1.1 Gakkel Ridge basalt and mantle source heterogeneity

A characteristic feature of the Gakkel Ridge is its underlying mantle heterogeneity ranging from ultra-depleted, mainly confined to the East (Liu et al., 2008; Stracke et al., 2011), to enriched mantle in the West (D'Errico et al., 2016; Goldstein et al., 2008; Mühe et al., 1997; Wanless et al., 2014). Mantle heterogeneity in the East is complemented by differences in spreading rate, magmatic activity and in parts unusual hydrothermal activity of unknown origin (Edmonds et al., 2003; Jean-Baptiste and Fourré, 2004; Michael et al., 2003). The Gakkel Ridge consists of three ridge segments (Michael et al., 2003), namely the Western Volcanic Zone (WVZ), the Sparsely Magmatic Zone (SMZ) and the Eastern Volcanic Zone (EVZ). Goldstein et al. (2008) proposed an isotopic boundary based on the abrupt Pb isotopes changes in along the ridge between 12°E and 16°E in the middle of the SMZ. Existing data indicates that Sr isotopes decrease gradually from DupAl-type mantle signature in the Western Gakkel Ridge towards Atlantic/Pacific (A/P) MORB in the East (Goldstein et al., 2008).

The Western Gakkel Ridge with its DupAl signatures has been linked to crustal contamination (Goldstein et al., 2008) (Figure 3.2), yet with Pb isotope signatures coherent with mantle modification no older than 150 Ma. In contrast, ultra-depleted mantle in the East with affinities of A/P-type MORB displays an unusually high radiogenic Hf isotope signature of  $\epsilon_{\text{Hf}} > 100$  in refractory pyroxenites and high  $^{188}\text{Os}/^{189}\text{Os}$  ratio in clinopyroxene and sulphides from abyssal

peridotites, indicating an ancient depletion event at ca. 2 Ga (Liu et al., 2008; Stracke et al., 2011). Notable is that similar ultra-depleted components in abyssal peridotites can be found in every MOR setting (Brandon et al., 2000; Byerly and Lassiter, 2014; Harvey et al., 2006). It is assumed that abyssal peridotites reflect the MORB source, but only a few studies identified ancient depletion events that are inherited in MORB (Andres et al., 2004; Graham et al., 2006).

In this contribution, we study the nature of the mantle boundary at the Gakkel Ridge with inferences for the origin of both mantle segments. Basalts from WVZ and SMZ are comprised here in the Western Gakkel Ridge and samples from the EVZ are hereafter referred to as the Eastern Gakkel Ridge. Western Gakkel Ridge lavas were previously analysed for their major and trace elements, and Sr and Pb isotope ratios, which is presented in chapter 3 of this thesis. This dataset will be complemented with radiogenic Hf-isotope ratios and further present 14 samples from the Eastern Gakkel Ridge, analysed for their major and trace elements and Hf, Sr, Pb isotope ratios. The obtained data is shown in Table 4.1 and a full description of the methodology is provided in the Supplementary Information attached to this chapter.

## 4.2 Results

Major element composition of MORBs from the Gakkel Ridge range from primitive (MgO ~10 wt. %), for samples from the EVZ, to more evolved values (MgO ~7 wt.%) measured in basalts from the WVZ. Overall, the Gakkel MORBs display a higher  $K_2O/TiO_2$  than average global MORB values (Figure 4.1). Basalts from the EVZ and the WVZ range between D-MORB and N-MORB (Figure 3.1 and Supplementary Figure 4.1), whereas basalts from the SMZ vary between E-MORB and N-MORBs (Figure 3.1).

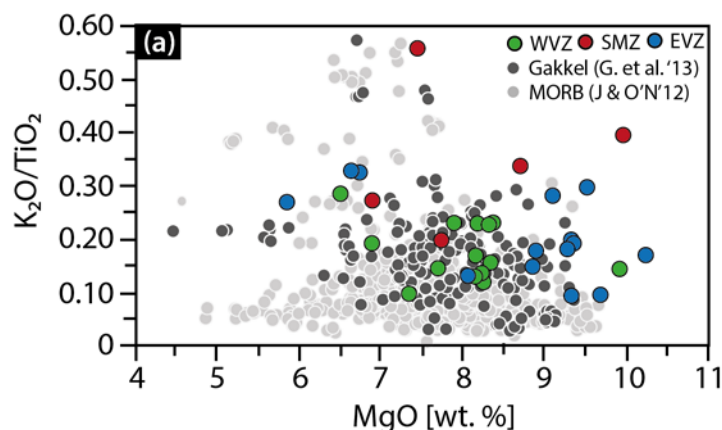


**Figure 4.1 -  $K_2O/TiO_2$  versus MgO plot.** On average Gakkel basalts have a higher  $K_2O/TiO_2$  than global MORB, suggesting an enrichment of the MORB source. MORB data from Jenner and O'Neill (2012) and data from Gakkel basalts are taken from Gale et al. (2014) have been used for comparison. Major element data from the WVZ and the SMZ basalts are taken from chapter 3.

Table 4.1 - Lead, Sr and Hf isotope data of whole rock basalts from the Gakkel Ridge.

Sample name	Ridge segment	Pb isotopes						Hf isotopes			Sr isotopes					
		$^{206}\text{Pb}/^{204}\text{Pb}$	ISE	$^{207}\text{Pb}/^{204}\text{Pb}$	ISE	$^{208}\text{Pb}/^{204}\text{Pb}$	ISE	$^{207}\text{Pb}/^{206}\text{Pb}$	$^{208}\text{Pb}/^{206}\text{Pb}$	$\Delta 7/4$	$\Delta 8/4$	$^{176}\text{Hf}/^{177}\text{Hf}$	ISE	$\epsilon_{\text{Hf}}$	$^{87}\text{Sr}/^{86}\text{Sr}$	ISE
HLY0102 D011 - 19*	WVZ	17.996	0.002	15.457	0.002	37.797	0.005	0.86	2.10	1.5	41.3	0.283234	0.000005	15.9	0.703386	0.000007
HLY0102 D8 - 12*	WVZ	18.011	0.003	15.454	0.002	37.829	0.006	0.86	2.10	1.1	42.7	0.283249	0.000005	16.4	0.703186	0.000009
PS 66 217-16 (B)*	WVZ	17.988	0.001	15.431	0.001	37.780	0.002	0.86	2.10	-1.0	40.5	0.283172	0.000004	13.7	0.703392	0.000008
PS 86 -019 (B)*	WVZ	17.889	0.001	15.414	0.001	37.678	0.002	0.86	2.11	-1.6	42.3	0.283084	0.000070	8.8	0.703333	0.000008
PS 86 - 67 (VG)*	WVZ	18.010	0.001	15.435	0.001	37.814	0.002	0.86	2.10	-0.8	41.3	0.283257	0.000004	16.7	0.703148	0.000007
PS 86 - 044 (VG)*	WVZ	17.866	0.001	15.415	0.001	37.666	0.002	0.86	2.11	-1.3	43.8	0.283229	0.000004	15.7	0.703341	0.000011
PS 59 216 (B)*	WVZ	18.064	0.001	15.443	0.001	37.845	0.002	0.85	2.10	-0.6	37.9	0.283156	0.000004	13.1	0.703032	0.000009
PS 59 216-11 (B)*	WVZ	18.043	0.001	15.438	0.001	37.819	0.002	0.86	2.10	-0.9	37.8	0.283034	0.000006	8.8	0.703078	0.000005
PS 59 216-13 (B)*	WVZ	18.059	0.001	15.437	0.001	37.824	0.002	0.85	2.09	-1.2	36.3	0.283261	0.000005	16.8	0.703095	0.000010
HLY0102 D013 - 10*	WVZ	18.026	0.004	15.469	0.004	37.811	0.009	0.86	2.10	2.4	39.1	0.283247	0.000006	16.3	0.703363	0.000008
PS 59 231 - 14*	WVZ	18.082	0.003	15.458	0.003	37.843	0.007	0.85	2.09	0.7	35.4	0.283242	0.000005	16.2	0.703129	0.000007
PS 59 232 - 84*	WVZ	18.088	0.003	15.504	0.002	37.966	0.006	0.86	2.10	5.2	47.1	0.283269	0.000005	17.1	0.703181	0.000007
HLY0102 D024 - 2*	WVZ	18.242	0.008	15.583	0.007	38.087	0.018	0.85	2.09	11.4	40.5	0.283218	0.000006	15.3	0.703017	0.000007
HLY0102 D026 - 9*	WVZ	18.113	0.003	15.476	0.002	37.884	0.005	0.85	2.09	2.1	35.8	0.283260	0.000005	16.8	0.703043	0.000007
HLY0102 D018 - 1*	WVZ	18.118	0.003	15.475	0.002	37.917	0.006	0.85	2.09	2.0	38.5	0.283158	0.000006	13.2	0.703101	0.000009
PS 59 234 - 24*	WVZ	18.066	0.003	15.459	0.002	37.859	0.006	0.86	2.10	0.9	39.0	0.283258	0.000004	16.7	0.70304	0.000008
PS 59 224 - 34*	WVZ	18.028	0.002	15.469	0.001	37.921	0.003	0.86	2.10	2.4	49.7	0.283286	0.000005	17.7	0.703618	0.000007
PS 59 243 - 36*	SMZ	17.873	0.004	15.447	0.003	37.743	0.009	0.86	2.11	1.8	50.7	0.283183	0.000005	14.1	0.703297	0.000011
HLY0102 D037 - 5*	SMZ	17.952	0.001	15.457	0.001	37.729	0.002	0.86	2.10	2.0	39.8	0.283381	0.000004	21.1	0.703088	0.000008
HLY0102 D036 - 35*	SMZ	17.696	0.002	15.410	0.001	37.599	0.004	0.87	2.12	0.1	57.7	0.283321	0.000007	19.0	0.703519	0.000010
HLY0102 D038 - 6*	SMZ	17.933	0.002	15.447	0.002	37.713	0.004	0.86	2.10	1.3	40.5	0.283201	0.000006	14.7	0.703122	0.000006
PS 59 251 - 4*	SMZ	18.308	0.003	15.526	0.002	38.011	0.006	0.85	2.08	5.1	25.0	0.283295	0.000004	18.0	0.702973	0.000007
PS 59 263 - 26	EVZ	18.235	0.004	15.522	0.003	37.969	0.008	0.85	2.08	5.4	29.6	0.283369	0.000008	20.7	0.702756	0.000007
HLY0102 D050 - 30	EVZ	17.872	0.002	15.488	0.002	37.567	0.004	0.87	2.10	5.9	33.2	0.283308	0.000005	18.5	0.702792	0.000007
HLY0102 D051 - 15	EVZ	-	-	-	-	-	-	-	-	-	-	0.283106	0.000010	11.4	0.702695	0.000008
PS 59 297 - 11	EVZ	18.254	0.006	15.535	0.005	38.034	0.012	0.85	2.08	6.5	33.8	0.283145	0.000006	12.7	0.703281	0.000007
PS 101 186 R1 Basalt	EVZ	18.096	0.006	15.490	0.005	37.789	0.011	0.86	2.09	3.7	28.3	0.283237	0.000007	16.0	0.702856	0.000008
PS 101 186 VG	EVZ	18.109	0.007	15.499	0.006	37.817	0.014	0.86	2.09	4.5	29.6	0.283244	0.000008	16.2	0.702775	0.000010
PS 59 294 - 40	EVZ	18.264	0.004	15.506	0.003	37.948	0.008	0.85	2.08	3.5	23.9	0.283234	0.000007	15.9	0.702979	0.000009
PS 101 193 R1	EVZ	18.068	0.005	15.482	0.004	37.766	0.010	0.86	2.09	3.3	29.5	0.283217	0.000006	15.3	0.703148	0.000013
PS 101 203 R4	EVZ	18.146	0.003	15.474	0.003	37.757	0.007	0.85	2.08	1.6	19.2	0.283230	0.000008	15.7	0.703498	0.000007
PS 101 203 R5	EVZ	18.111	0.007	15.481	0.006	37.757	0.016	0.85	2.08	2.7	23.4	0.283227	0.000008	15.6	0.703014	0.000008
PS 101 203 R8	EVZ	18.129	0.004	15.468	0.004	37.770	0.010	0.85	2.08	1.2	22.5	0.283224	0.000009	15.5	0.703276	0.000006
PS 59 274 - 52	EVZ	18.520	0.002	15.588	0.001	38.509	0.003	0.84	2.08	8.9	49.1	0.283023	0.000005	8.4	0.703794	0.000008
HLY0102 D059 - 35	EVZ	18.150	0.002	15.486	0.002	37.868	0.004	0.85	2.09	2.7	29.8	0.283088	0.000004	10.7	0.702843	0.000007
HLY0102 D061 - 11	EVZ	18.032	0.002	15.472	0.002	37.686	0.005	0.86	2.09	2.7	25.8	0.283215	0.000004	15.2	0.702638	0.000007

\* - Pb and Sr isotope data compiled from chapter 3

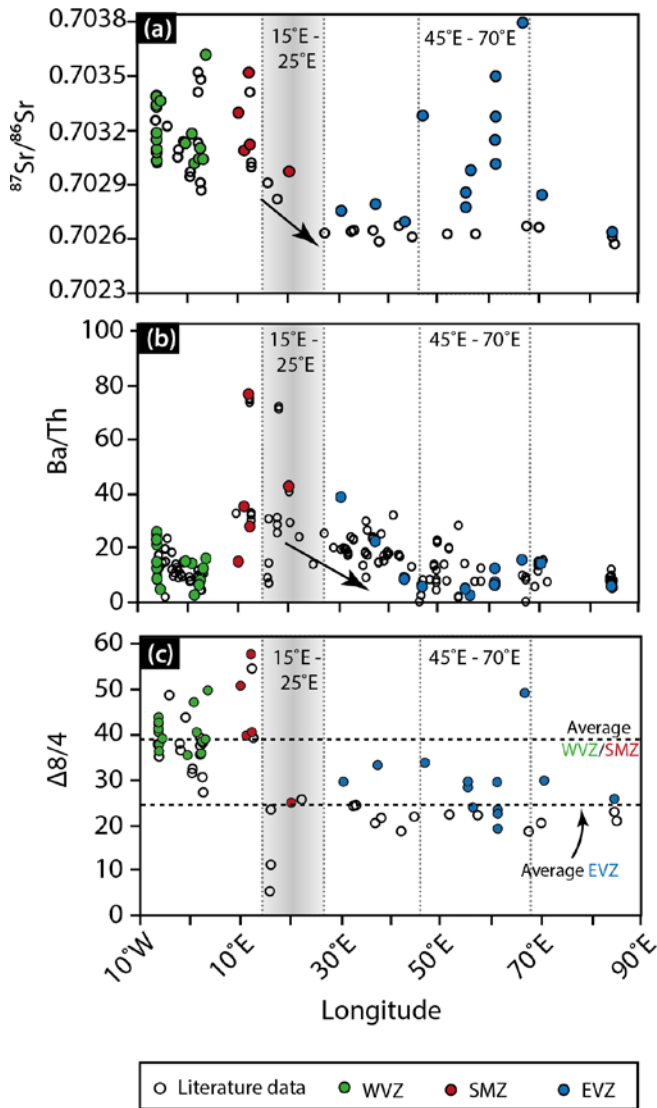


**Figure 4.2 - Along-ridge variation in Sr, Pb isotope and Ba/Th.** The light grey area (15°E to 25°E), east of the proposed isotopic boundary at 15°E, indicates the ridge segment with anomalous isotope and trace element signatures. (a) Variation of  $^{87}\text{Sr}/^{86}\text{Sr}$  of all three ridge segments. The Western Gakkel Ridge region displays Sr isotope values that covary with back-arc basins or island arc magmas (Figures 3.2 and 3.4). The black dashed horizontal line marks lower bound of back arc basin and island arc lavas. Strontium isotope values > 0.7030 suggest input from a crustal source. Basalts from the EVZ display high radiogenic  $^{87}\text{Sr}/^{86}\text{Sr}$  between 45°E and 70°E, suggesting a different crustal input than for basalts from the Western Gakkel Ridge region, because of a low Ba/Th in this area. (b) Ba/Th decreases (indicated by an error) towards the EVZ (until ~45°E), which is in line with decreasing  $^{87}\text{Sr}/^{86}\text{Sr}$  (see discussion for further explanation) until 25°E. In conjunction,  $\Delta 8/4$  (c) of the WVZ and the SMZ is higher than for basalts from the EVZ. The black dotted line marks the average  $\Delta 8/4$  for the Western and the Eastern Gakkel Ridge region. Gakkel Ridge data has been compiled from Gale et al. (2013) and chapter 3.

Lead isotopes, can be used as a tool to differentiate between distinct MORB isotope signatures, in particular to distinguish between and DupAl anomaly and A/P-type MORB. Data is presented in  $\Delta 8/4$ , which is the deviation of  $^{208}\text{Pb}/^{204}\text{Pb}$  from the Northern Hemisphere Reference line (NHRL; Hart, 1984) for a given  $^{206}\text{Pb}/^{204}\text{Pb}$ . Basalts with DupAl isotope signatures have a high radiogenic  $^{208}\text{Pb}/^{204}\text{Pb}$  for a given  $^{206}\text{Pb}/^{204}\text{Pb}$  resulting in a positive  $\Delta 8/4$ . Combined with literature values,  $\Delta 8/4$  of the Western Gakkel Ridge basalts have an average of +38.8, which is distinctively higher than basalts from the Eastern Gakkel Ridge with an average of +25.7 (Figure 4.2). Whilst this indicates a clear shift in the isotope signatures of the mantle at 15°E, A/P MORBs are on average four to ten times lower with  $\Delta 8/4_{\text{average}} = 0 \pm +8$  (calculated from Pb isotopes of Atlantic and Pacific MORBs; Gale et al., 2014).

DupAl basalts from the Western Gakkel Ridge region exhibit a  $^{87}\text{Sr}/^{86}\text{Sr}$  range from 0.7030 to 0.7035 (Figure 4.3, Table 4.1), similar to enriched Lau and Mariana back-arc Basin basalts

(Figures 3.2 and 3.4), but distinctly higher than A/P MORB (Gale et al., 2014). EVZ basalts display a broader range in  $^{87}\text{Sr}/^{86}\text{Sr}$  ranging from depleted (0.7026) to enriched (0.7038) values.

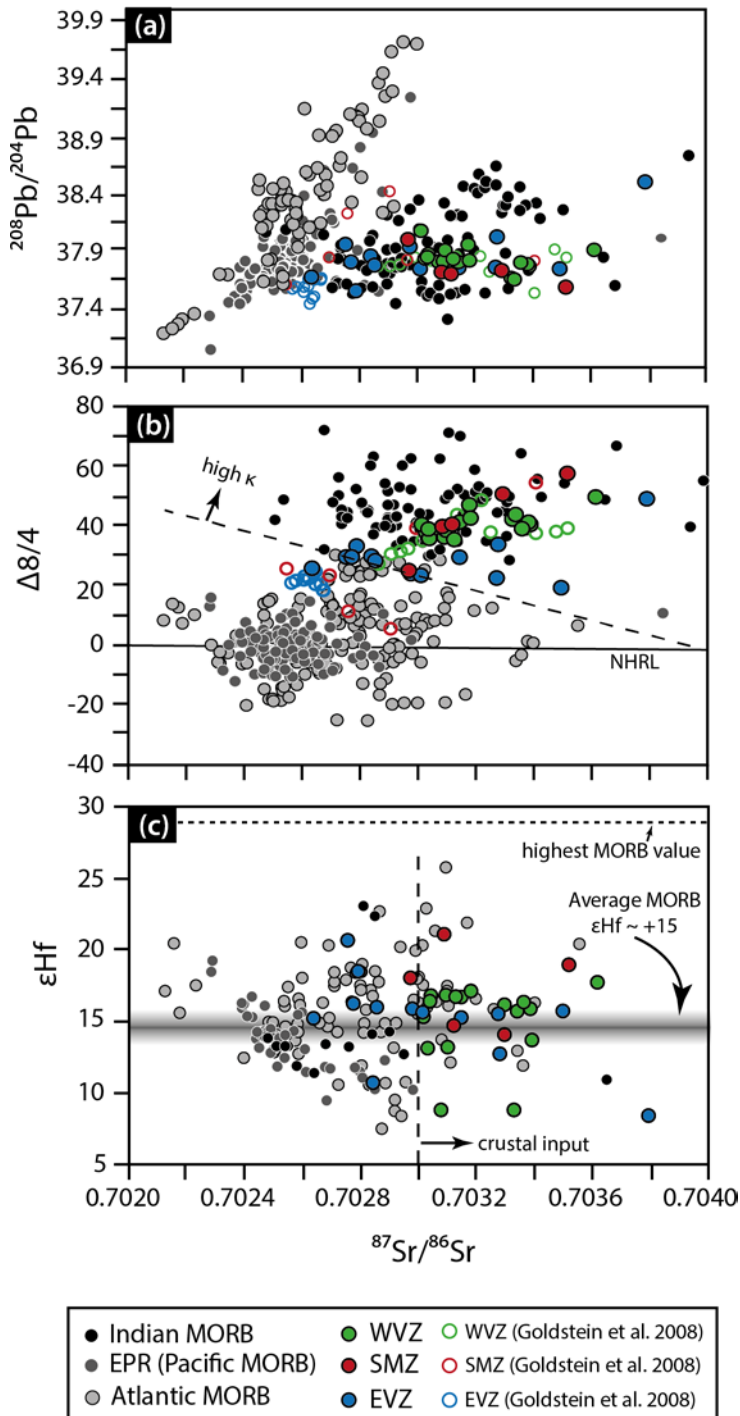


**Figure 4.3 Hf-Sr-Pb isotope systematics of the Gakkel Ridge basalts.** (a)  $^{208}\text{Pb}/^{204}\text{Pb}$  versus  $^{87}\text{Sr}/^{86}\text{Sr}$  shows two distinct trends of A/P-type MORBs ( $^{208}\text{Pb}/^{204}\text{Pb}$  increases with increasing  $^{87}\text{Sr}/^{86}\text{Sr}$ ) and Indian-type mantle MORBs (constant  $^{208}\text{Pb}/^{204}\text{Pb}$  values with increasing  $^{87}\text{Sr}/^{86}\text{Sr}$ ). The Gakkel Ridge MORBs plot within the range of Indian MORBs. The two distinct trends between A/P MORBs and Indian MORBs is not as clear for  $\Delta 8/4$  versus  $^{87}\text{Sr}/^{86}\text{Sr}$  (b). It is apparent that with increasing  $\Delta 8/4$  (suggesting a high thorogenic Pb) Sr isotopes increases too. The dashed line indicates the difference between A/P MORBs and Indian MORBs. Gakkel Ridge MORBs plot mainly within the Indian MORBs, whereas a few data points (from AAD) plot in the A/P MORB range. Hf-Sr systematics (c) do not show a clear distinction between Atlantic/Pacific and Indian MORBs. Basalts from the EVZ plot mainly within the A/P MORB range, whereby samples from the ridge segment between  $45^\circ\text{E}$  to  $\sim 70^\circ\text{E}$  ( $^{87}\text{Sr}/^{86}\text{Sr} > 0.7030$ ) plot within the Indian MORB range suggesting a crustal input (Figure 4.2, see discussion). The grey shaded horizontal bar indicates the highest measured MORB value (Hanan et al., 2004). The black shaded bar at  $\epsilon_{\text{Hf}} \sim +15 \pm 2$ , represents the average MORB value. The Gakkel basalts are compared with Indian, Atlantic and Pacific (EPR – Eastern Pacific Rise) MORBs. MORB data has been taken from Gale et al. (2014). Strontium and Pb isotope data for samples from the WVZ and the SMZ are taken from chapter 3.

Hafnium isotopes (here given in  $\epsilon_{\text{Hf}}$ ) of the Gakkel basalts range from +14.9 in the WVZ, +17.4 in basalts from the SMZ and +14.8 for basalts in the Eastern Gakkel Ridge region. The  $\epsilon_{\text{Hf}}$  values broadly coincide with average MORB ( $\epsilon_{\text{Hf}} \sim +14.1 \pm 2$ ; Figure 4.3c; Gale et al., 2014). Crucially, the Eastern Gakkel Ridge region lavas do not show any extreme Hf isotope values such as those previously reported in abyssal peridotites ( $\epsilon_{\text{Hf}} = +100$ ; Stracke et al., 2011).

## 4.3 Discussion

### 4.3.1 Locus and isotopic nature of the mantle boundary

A key aspect of the Sr isotope data in Gakkel Ridge basalts is that Sr isotope ratios are indistinguishable between 15°E - 25°E and the Eastern Gakkel Ridge region (Figure 4.2). Radiogenic Sr isotope values of the Western Gakkel Ridge were discussed in chapter 3 and it is argued for a source re-enrichment in this mantle area through a previous subduction event. Elevated Sr isotopes show a clear variability towards more radiogenic isotopes in the Eastern Gakkel Ridge lavas, mainly within the ridge segment from 45°E to ~ 70°E, suggesting a crustal component in their MORB source. These are seemingly unrelated to the Western Gakkel Ridge region due to the large distance between the regions with elevated Sr isotope signatures, suggesting an independent enrichment history. The observed variability is in line with previous observations of heterogeneous mantle sources beneath the Eastern Gakkel Ridge region (D'Errico et al., 2016; Hellebrand et al., 2002; Liu et al., 2008; Wanless et al., 2014), even though previous studies have not identified variable Sr isotope signatures (Goldstein et al., 2008).

Radiogenic Sr isotope signature within the ridge segment of 45°E to ~ 70°E coincide with extreme Hf isotopes ( $\epsilon_{\text{Hf}} \sim +100$ ) found in clinopyroxene separates from abyssal peridotite samples at around 65°E (Stracke et al., 2011). These exceed the most extreme reported MORB value fourfold with the highest Hf isotopes measured in global MORBs at  $\epsilon_{\text{Hf}} = +28.4$  (Figure 4.3c; Hanan et al., 2004). Indeed, the isotopic mismatch between MORBs and abyssal peridotites is a phenomenon observed in various locations (Byerly and Lassiter, 2014; Mallick et al., 2015; Warren, 2016). Byerly and Lassiter (2014) discussed different theories. In their “slag” hypothesis, ultra-depleted mantle domains are volumetrically small, oversampled by abyssal peridotites and are not represented in MORBs. Alternatively, ultra-depleted mantle domains are common (Salters et al., 2011), but too refractory to contribute to the chemistry of MORBs; which is also called ‘ghost’ hypothesis. It is plausible that a combination of ‘slag’ and ‘ghost’ hypotheses causes the isotopic mismatch between MORBs and abyssal peridotites with melts from ultra-depleted lithologies mixing with melts from isotopically enriched components, which results in intermediate isotopic compositions of the MORBs (Byerly and Lassiter, 2014). This hybrid hypothesis could explain the discrepancy between  $\epsilon_{\text{Hf}}$  of Gakkel MORBs and abyssal peridotites.

In addition to elevated Sr isotope in basalts and the extreme Hf isotope found in abyssal peridotites in the Eastern Gakkel Ridge region, basalts in this area also display higher  $^{207}\text{Pb}/^{204}\text{Pb}$  ratio for a given  $^{206}\text{Pb}/^{204}\text{Pb}$  than basalts from the Western Gakkel Ridge region (Figure 4.4). The higher  $^{207}\text{Pb}/^{204}\text{Pb}$  ratios and variability of Hf-Sr of the EVZ basalts suggests a distinct mantle source with a complex history of multiple melt extraction and re-fertilisation by crustal components. Previous studies indicated an ‘age’ for these events dating back to 2 Ga (Liu et al., 2008; Stracke et

al., 2011). Coupled  $^{238}\text{U}$ - $^{235}\text{U}$  decay demands that this feature is a function of time, and the extreme timeframe of  $\sim 2$  Ga can explain the offset of Eastern Gakkel Ridge lavas in  $^{207}\text{Pb}/^{204}\text{Pb}$  vs  $^{206}\text{Pb}/^{204}\text{Pb}$ , which lie towards the end of the Gakkel Ridge basalt spectrum, in line with sulfide Pb isotope signatures (Warren and Shirey, 2012).

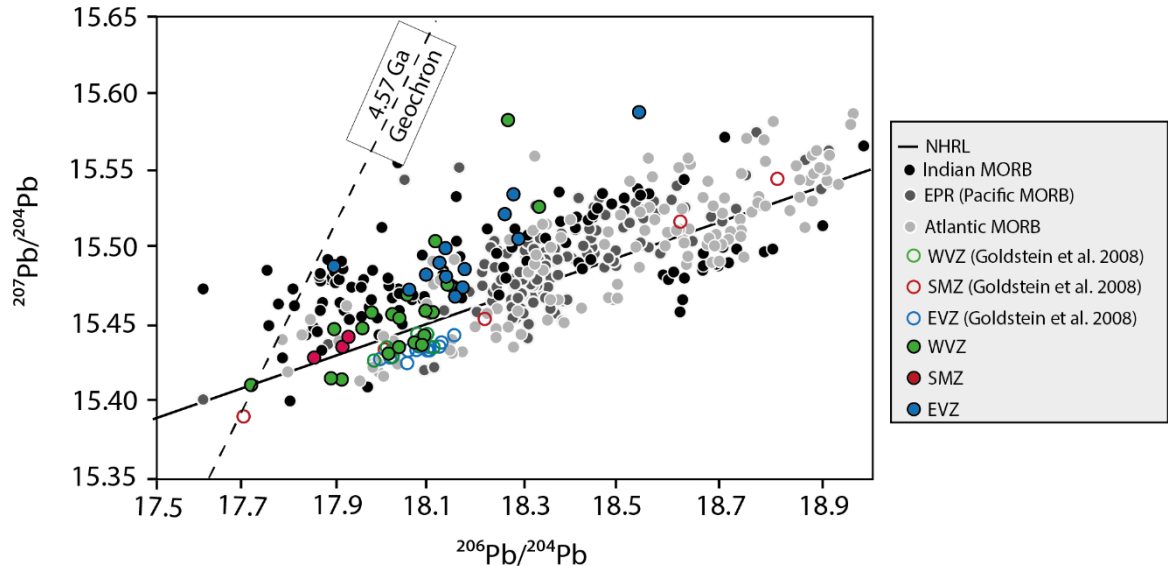


**Figure 4.4** -  $^{207}\text{Pb}/^{204}\text{Pb}$  versus  $^{206}\text{Pb}/^{204}\text{Pb}$  diagram. The difference in U/Pb between the Western Gakkel Ridge region and EVZ is not as clear as in Th/U ratio (Figure 4.3). Basalts from the EVZ display on average higher radiogenic  $^{207}\text{Pb}/^{204}\text{Pb}$  ratio than basalts from the Western Gakkel Ridge region for a given  $^{206}\text{Pb}/^{204}\text{Pb}$ , indicating  $^{207}\text{Pb}/^{204}\text{Pb}$  ratio is not significantly affected by the input of from fossil subduction zones that modified the mantle in this region.

In summary, the distinction between the Western and Eastern Gakkel Ridge is most definite in the Pb isotope system, yet combined all isotope systems require an ancient crustal overprint. In  $\Delta 8/4$  isotope space, a pronounced boundary is apparent at  $15^\circ\text{E}$  -  $25^\circ\text{E}$ , in line with previous suggestions within the SMZ (Goldstein et al., 2008). An abrupt drop from  $\Delta 8/4 = +57$  to  $+5$  within tens of kilometre (Figure 4.2c), in conjunction with slightly decreasing Sr isotope ratios at ca.  $25^\circ\text{E}$  marks a profound change in the mantle source of the basalts. The higher  $^{208}\text{Pb}/^{204}\text{Pb}$  for a given  $^{206}\text{Pb}/^{204}\text{Pb}$  in the Western Gakkel Ridge compared to the EVZ, imply a much higher time-integrated  $^{232}\text{Th}/^{238}\text{U}$  ( $k$ ) in the mantle beneath the Western Gakkel Ridge region (Figures 4.3 and 4.5).

### 4.3.2 Implications for DupAl mantle in the Arctic and elsewhere

Mantle sources of both Western and Eastern Gakkel Ridge lavas yield higher calculated  $k$ -values than Indian-type MORB (Figure 4.2b). The sharp drop in  $\Delta 8/4$  at the Gakkel Ridge does not separate “enriched” normal mantle from the West to “normal” depleted MORB mantle in the East, but suggest a differentiation of enriched mantle. This is different to what has been observed at the Australian Antarctic Discordance (AAD), an area of seafloor depression (Klein et al., 1988), and at the Australian-Antarctic Ridge in the Southern Ocean, which marks an area of distinct mantle domain between Zealandia and Antarctica (Park et al., 2019). At the AAD, a spatially sharp isotope

shift between Indian-type and A/P-type mantle marks the boundary of the so-called Indian mantle domain from Pacific mantle (Hanan et al., 2004; Klein et al., 1988). It is thus apparent that the entire Indian-type Gakkel Ridge has been subject to isotope modification albeit not in a single event, but by events that are separated by  $\sim 2$  Ga.

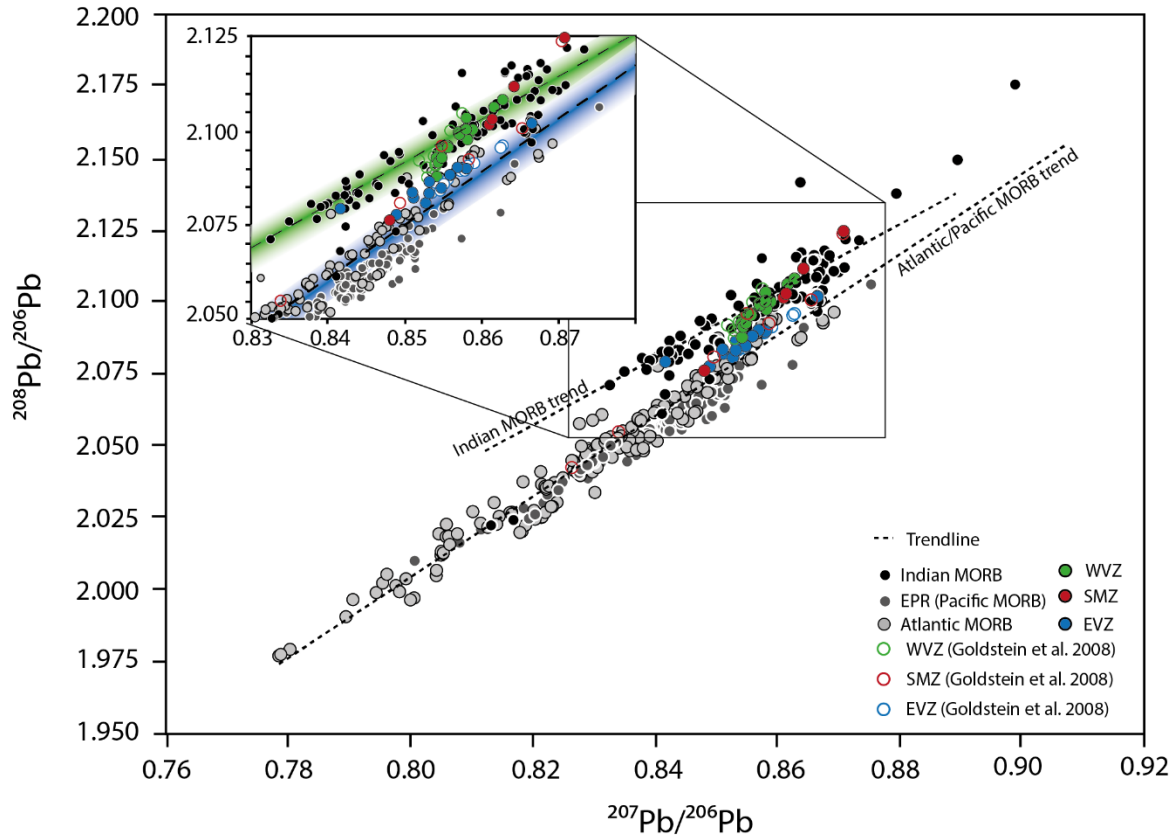


**Figure 4.5 -  $^{208}\text{Pb}/^{206}\text{Pb}$  versus  $^{207}\text{Pb}/^{206}\text{Pb}$  diagram.** The difference in U/Pb between the Western Gakkel Ridge region and EVZ is not as clear as in Th/U ratio (Figure 4.3). Basalts from the EVZ display on average higher radiogenic  $^{207}\text{Pb}/^{204}\text{Pb}$  ratio than basalts from the Western Gakkel Ridge region for a given  $^{206}\text{Pb}/^{204}\text{Pb}$ , indicating  $^{207}\text{Pb}/^{204}\text{Pb}$  ratio is not significantly affected by the input of from fossil subduction zones that modified the mantle in this region

Within global MORB, the preferential recycling of U over Th since the great oxidation event ca 2.2 Ga ago has been suggested to decrease mantle  $k$  (Th/U; Elliott et al., 1999), leading to the so-called kappa-conundrum with higher calculated  $k$  values (from Pb isotopes) than what is measured in MORBs. At the Gakkel Ridge, this phenomenon is reversed and requires excess Th in the mantle source of the basalts. Integration of subduction-modified mantle (metasomatised mantle) into the MORB source is a plausible scenario. Higher thorogenic Pb (high Th/U) can only be caused by ingrowth through Th decay. It is proposed that Th-rich residual mélangé rocks from a fossil subduction event of cryptic origin is the most likely source of thorogenic Pb (Supplementary Figure 4.2; Figure 3.4). Mantle shear and mixing may further promote heterogeneity in the source of these melts as indicated by elevated Ba/Th combined with decreasing Sr isotope signature between  $15^\circ\text{E}$  and  $25^\circ\text{E}$  (Figure 4.2). Indeed, Wanless et al. (2014) suggested that the MORB source is composed of DMM and a metasomatic component at around  $30^\circ\text{E}$ .

## 4.4 Conclusion

The overlap of Pb and Sr isotopes from the Western Gakkel Ridge MORB with those from the Indian Ocean may thus be coincidental in as much similar Th-U-Pb systematics for a given time leading to similar Pb isotope systematics. For the Eastern Gakkel Ridge, despite the longer time, this effect is much less pronounced with an apparently lower Th/Pb. Hence, both respective MORB sources at the Western and the Eastern Gakkel Ridge may be polluted by a similar process but at different times and to a different degree. Irrespective of these timescales this heterogeneity has prevailed in the upper mantle, indicating that mantle metasomatism, as a possible cause for this anomaly, can reside in the upper mantle indefinitely.

## 4.5 References

- Andres, M., Blichert-Toft, J., Schilling, J.-G., 2004. Nature of the depleted upper mantle beneath the Atlantic: evidence from Hf isotopes in normal mid-ocean ridge basalts from 79°N to 55°S. *Earth and Planetary Science Letters*, 225(1): 89-103.
- Barling, J., Goldstein, S.L., Nicholls, I., 1994. Geochemistry of Heard Island (Southern Indian Ocean): Characterization of an Enriched Mantle Component and Implications for Enrichment of the Sub-Indian Ocean Mantle. *Journal of Petrology*, 35(4): 1017-1053.
- Brandon, A.D., Snow, J.E., Walker, R.J., Morgan, J.W., Mock, T.D., 2000. 190Pt–186Os and 187Re–187Os systematics of abyssal peridotites. *Earth and Planetary Science Letters*, 177(3): 319-335.
- Byerly, B.L., Lassiter, J.C., 2014. Isotopically ultradepleted domains in the convecting upper mantle: Implications for MORB petrogenesis. *Geology*, 42(3): 203-206.
- Castillo, P., 1988. The Dupal anomaly as a trace of the upwelling lower mantle. *Nature*, 336(6200): 667-670.
- D'Errico, M.E., Warren, J.M., Godard, M., 2016. Evidence for chemically heterogeneous Arctic mantle beneath the Gakkel Ridge. *Geochimica et Cosmochimica Acta*, 174: 291-312.
- Dupré, B., Allègre, C.J., 1983. Pb-Sr isotope variation in Indian Ocean basalts and mixing phenomena. *Nature*, 303(5913): 142-146.
- Edmonds, H.N. et al., 2003. Discovery of abundant hydrothermal venting on the ultraslow-spreading Gakkel Ridge in the Arctic Ocean. *Nature*, 421(6920): 252-256.
- Elliott, T., Zindler, A., Bourdon, B., 1999. Exploring the kappa conundrum: the role of recycling in the lead isotope evolution of the mantle. *Earth and Planetary Science Letters*, 169(1–2): 129-145.
- Escrig, S., Capmas, F., Dupre, B., Allegre, C.J., 2004. Osmium isotopic constraints on the nature of the DUPAL anomaly from Indian mid-ocean-ridge basalts. *Nature*, 431(7004): 59-63.
- Foden, J., Sossi, P.A., Nebel, O., 2018. Controls on the iron isotopic composition of global arc magmas. *Earth and Planetary Science Letters*, 494: 190-201.
- Gale, A., Langmuir, C.H., Dalton, C.A., 2014. The Global Systematics of Ocean Ridge Basalts and their Origin. *Journal of Petrology*, 55(6): 1051-1082.
- Goldstein, S.L. et al., 2008. Origin of a 'Southern Hemisphere' geochemical signature in the Arctic upper mantle. *Nature*, 453(7191): 89-93.
- Graham, D.W., Blichert-Toft, J., Russo, C.J., Rubin, K.H., Albarede, F., 2006. Cryptic striations in the upper mantle revealed by hafnium isotopes in southeast Indian ridge basalts. *Nature*, 440(7081): 199-202.
- Hanan, B.B., Blichert-Toft, J., Pyle, D.G., Christie, D.M., 2004. Contrasting origins of the upper mantle revealed by hafnium and lead isotopes from the Southeast Indian Ridge. *Nature*, 432(7013): 91-94.
- Hart, S.R., 1984. A large-scale isotope anomaly in the Southern Hemisphere mantle. *Nature*, 309(5971): 753-757.
- Harvey, J. et al., 2006. Ancient melt extraction from the oceanic upper mantle revealed by Re–Os isotopes in abyssal peridotites from the Mid-Atlantic ridge. *Earth and Planetary Science Letters*, 244(3-4): 606-621.
- Hawkesworth, C.J., Mantovani, M.S.M., Taylor, P.N., Palacz, Z., 1986. Evidence from the Parana of south Brazil for a continental contribution to Dupal basalts. *Nature*, 322(6077): 356-359.
- Hellebrand, E., Snow, J.E., Mühe, R., 2002. Mantle melting beneath Gakkel Ridge (Arctic Ocean): abyssal peridotite spinel compositions. *Chemical Geology*, 182(2–4): 227-235.
- Jean-Baptiste, P., Fourré, E., 2004. Hydrothermal activity on Gakkel Ridge. *Nature*, 428: 36.

- Jenner, F.E., O'Neill, H.S.C., 2012. Analysis of 60 elements in 616 ocean floor basaltic glasses. *Geochemistry, Geophysics, Geosystems*, 13(2): Q02005.
- Kempton, P.D. et al., 2002. Sr-Nd-Pb-Hf Isotope Results from ODP Leg 187: Evidence for Mantle Dynamics of the Australian-Antarctic Discordance and Origin of the Indian MORB Source. *Geochemistry, Geophysics, Geosystems*, 3(12): 1-35.
- Klein, E.M., Langmuir, C.H., Zindler, A., Staudigel, H., Hamelin, B., 1988. Isotope evidence of a mantle convection boundary at the Australian-Antarctic Discordance. *Nature*, 333(6174): 623-629.
- Le Roex, A.P., Dick, H., Fisher, R.L., 1989. Petrology and Geochemistry of MORB from 25°E to 46°E along the Southwest Indian Ridge: Evidence for Contrasting Styles of Mantle Enrichment. *Journal of Petrology*, 30(4): 947-986.
- Liu, C.Z. et al., 2008. Ancient, highly heterogeneous mantle beneath Gakkel Ridge, Arctic Ocean. *Nature*, 452(7185): 311-6.
- Longerich, H.P., Jackson, S.E., Gunther, D., 1996. Inter-laboratory note. Laser ablation inductively coupled plasma mass spectrometric transient signal data acquisition and analyte concentration calculation. *Journal of Analytical Atomic Spectrometry*, 11(9): 899-904.
- Mahoney, J.J. et al., 1989. Isotopic and geochemical provinces of the western Indian Ocean Spreading Centers. *Journal of Geophysical Research: Solid Earth*, 94(B4): 4033-4052.
- Mallick, S., Standish, J.J., Bizimis, M., 2015. Constraints on the mantle mineralogy of an ultra-slow ridge: Hafnium isotopes in abyssal peridotites and basalts from the 9–25°E Southwest Indian Ridge. *Earth and Planetary Science Letters*, 410: 42-53.
- Meyzen, C.M. et al., 2005. New insights into the origin and distribution of the DUPAL isotope anomaly in the Indian Ocean mantle from MORB of the Southwest Indian Ridge. *Geochemistry, Geophysics, Geosystems*, 6(11): n/a-n/a.
- Michael, P.J. et al., 2003. Magmatic and amagmatic seafloor generation at the ultraslow-spreading Gakkel Ridge, Arctic Ocean. *Nature*, 423(6943): 956-961.
- Mühe, R., Bohrmann, H., Garbe-Schönberg, D., Kassens, H., 1997. E-MORB glasses from the Gakkel Ridge (Arctic Ocean) at 87°N: evidence for the Earth's most northerly volcanic activity. *Earth and Planetary Science Letters*, 152(1-4): 1-9.
- Park, S.-H. et al., 2019. An isotopically distinct Zealandia–Antarctic mantle domain in the Southern Ocean. *Nature Geoscience*.
- Rehkämper, M., Hofmann, A.W., 1997. Recycled ocean crust and sediment in Indian Ocean MORB. *Earth and Planetary Science Letters*, 147(1-4): 93-106.
- Salters, V.J.M., Mallick, S., Hart, S.R., Langmuir, C.E., Stracke, A., 2011. Domains of depleted mantle: New evidence from hafnium and neodymium isotopes. *Geochemistry, Geophysics, Geosystems*, 12(8): n/a-n/a.
- Salters, V.J.M., Stracke, A., 2004. Composition of the depleted mantle. *Geochemistry, Geophysics, Geosystems*, 5(5): n/a-n/a.
- Stracke, A. et al., 2011. Abyssal peridotite Hf isotopes identify extreme mantle depletion. *Earth and Planetary Science Letters*, 308(3-4): 359-368.
- Wanless, V.D., Behn, M.D., Shaw, A.M., Plank, T., 2014. Variations in melting dynamics and mantle compositions along the Eastern Volcanic Zone of the Gakkel Ridge: insights from olivine-hosted melt inclusions. *Contributions to Mineralogy and Petrology*, 167(5).
- Warren, J.M., 2016. Global variations in abyssal peridotite compositions. *Lithos*, 248-251: 193-219.
- Warren, J.M., Shirey, S.B., 2012. Lead and osmium isotopic constraints on the oceanic mantle from single abyssal peridotite sulfides. *Earth and Planetary Science Letters*, 359-360: 279-293.
- Zhang, S.Q. et al., 2005. Evidence for a Widespread Tethyan Upper Mantle with Indian-Ocean-Type Isotopic Characteristics. *Journal of Petrology*, 46(4): 829-858.

## 4.6 Supplementary Information

Major and trace element concentrations data tables are provided in the Supplementary Data Tables.

## 4.7 Acknowledgements

The authors would like to acknowledge Jay Thompson from UTAS for undertaking the major element analysis and Massimo Raveggi from the Isotopia Laboratory for his help with LA-ICP-MS analysis. This work was supported by an ARC grant FT140101062 to O.N. H. Dick was supported

by US National Science Foundation (Grant No. OCE-MG&G 8371300). M.R. was supported by a graduate scholarship of Monash University and the SEAE. The authors would like to thank Wolfgang Bach and Elmar Albers for providing additional samples from the Gakkal Ridge.



# **Supplementary Information**

## **Elucidating the peculiar $\text{D}_{\text{upAl}}$ isotope signatures of Arctic mid-ocean ridge basalts**

Marianne Richter, Oliver Nebel, Roland Maas, Yona Nebel-Jacobsen, Henry J.B. Dick



**SI - Methods**

Basalts analysed in this study have been crushed with a ceramic jaw crusher and milled in an agate mill to fine powder. Two grams of each sample has been admixed with a Li-Borate flux and fused to glass, which has been analysed for their major element composition at CODES University of Tasmania. A detailed description of the major element analysis can be found in chapter 3.

Trace element (Na, Mg, Al, Si, Ca, Sc, Ti, V, Cr, Mn, Fe, Co, Ni, Zn, Ga, Rb, Sr, Y, Zr, Nb, Mo, Cs, Ba, La, Ce, Pr, Nd, Sm, Eu, Gd, Tb, Dy, Ho, Er, Tm, Yb, Lu, Hf, Ta, Pb, Th and U) composition have been analysed on the fused Li-Borate glasses in the Isotopia Laboratory at Monash University, Australia. Fragments of each XRF glass were mounted in a 1-inch epoxy disc and five 80  $\mu\text{m}$  spots (aligned to transect the sample) were set on each fused glass fragment to analyse the trace element composition using an ASI RESolution SE 193nm ArF excimer laser coupled to a ThermoFisher ICapQ. Similar instrumental settings (10 Hz repetition rate; 3 J/cm<sup>2</sup>) as described in the previous chapter (chapter 3), have been applied for the EVZ samples. Each spot was measured using a background of 20 s, an ablation time of 30 s and a washout of 20 s. A set of 20 unknowns has been bracketed in a set of four reference materials (2 - 3 spots each). NIST 610, NIST 612, BCR2G and BHVO2G have been used as reference material to control the reproducibility, precision and accuracy during the analysis. Raw data has been processed using an in-house Microsoft Excel worksheet from the Max-Planck Institute for Chemistry (MPIC) in Mainz. Data reduction procedure is described by Longerich et al. (1996) and Jochum et al. (2007). The data has been normalised to BCR2G and a relative uncertainty for REE, U, Th and Pb below 3 % for BHVO2G has been achieved. The final trace element composition has been reduced by the blank composition of the fused glass blank. The trace element composition of each sample and uncertainty for each element is given in Supplementary Data Table 4.1. Trace element data of the reference material and fused glass blank is provided in Supplementary Data Table 4.2.

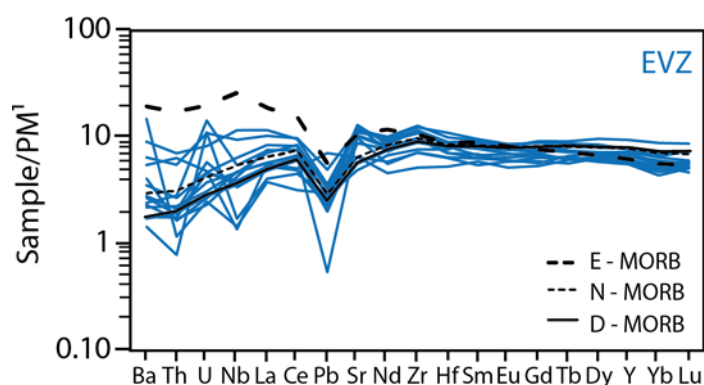
For Pb isotope chemistry, small (1 - 2 mm; 150 - 200 mg) rock chips hand-picked under the microscope were weighed into a Teflon beaker and leached with hot 6M HCl for 60 min on a hot plate at 100°C. After removal of the leach solution and repeated rinsing with distilled water, residues were dissolved in 5:1 HF-HNO<sub>3</sub> (3 ml, 100°C) on a hotplate for 48 hours. The acid was evaporated and remaining fluorides were refluxed and dried twice with 2 ml of concentrated HNO<sub>3</sub> and dissolved in 6M HCl. Pb was extracted from the samples using a double pass over small beds of AG1-X8 anion resin with a mesh size of 100 – 200  $\mu\text{m}$ . The procedural blank was 30  $\pm$  10 pg Pb. Lead isotope ratios were measured on a Nu plasma in the School of Earth Sciences at the University of Melbourne, and on a NeptunePlus MC-ICP-MS from Thermo Fisher Scientific in the Isotopia Laboratory at the School of Earth, Atmosphere and Environment, Monash University. Instrumental mass bias was corrected using the thallium-doping technique of Woodhead (2002). In

the School of Earth Sciences (University of Melbourne), the mass bias factors for each Pb isotope ratio were derived from Pb-Tl mass bias correlation lines based on results from >200 runs of SRM981.  $^{205}\text{Tl}/^{203}\text{Tl}$  in the running solution is assumed to be 2.3871, while SRM981 is assumed to have the following Pb isotope ratios  $^{206}\text{Pb}/^{204}\text{Pb}$ ,  $^{207}\text{Pb}/^{204}\text{Pb}$ ,  $^{208}\text{Pb}/^{204}\text{Pb} = 16.935/15.489/36.701/1$ . The long-term average for USGS basalt BCR-2 (unleached) is  $18.758 \pm 0.047\%$ ,  $15.619 \pm 0.066\%$ ,  $38.726 \pm 0.090\%$ . At the Monash Isotopia Facility SRM981 ( $n = 11$ ) yielded the following ratios  $^{206}\text{Pb}/^{204}\text{Pb}$ ,  $^{207}\text{Pb}/^{204}\text{Pb}$ ,  $^{208}\text{Pb}/^{204}\text{Pb} = 16.941 \pm 0.001$  (1SE),  $15.499 \pm 0.001$  (1SE),  $36.722 \pm 0.002$  (1SE) with a relative error of 0.02% compared to literature values of Taylor et al. (2015). For BCR2G ( $n = 4$ ) the following Pb isotopic ratios  $^{206}\text{Pb}/^{204}\text{Pb}$ ,  $^{207}\text{Pb}/^{204}\text{Pb}$ ,  $^{208}\text{Pb}/^{204}\text{Pb} = 18.750 \pm 0.002$  (1SE),  $15.615 \pm 0.002$  (1SE),  $38.691 \pm 0.004$  (1SE) were yielded with a relative error of 0.06%, 0.08%, 0.07% to the BCR-2 reference values (GeoReM, updated 02/2016), respectively.

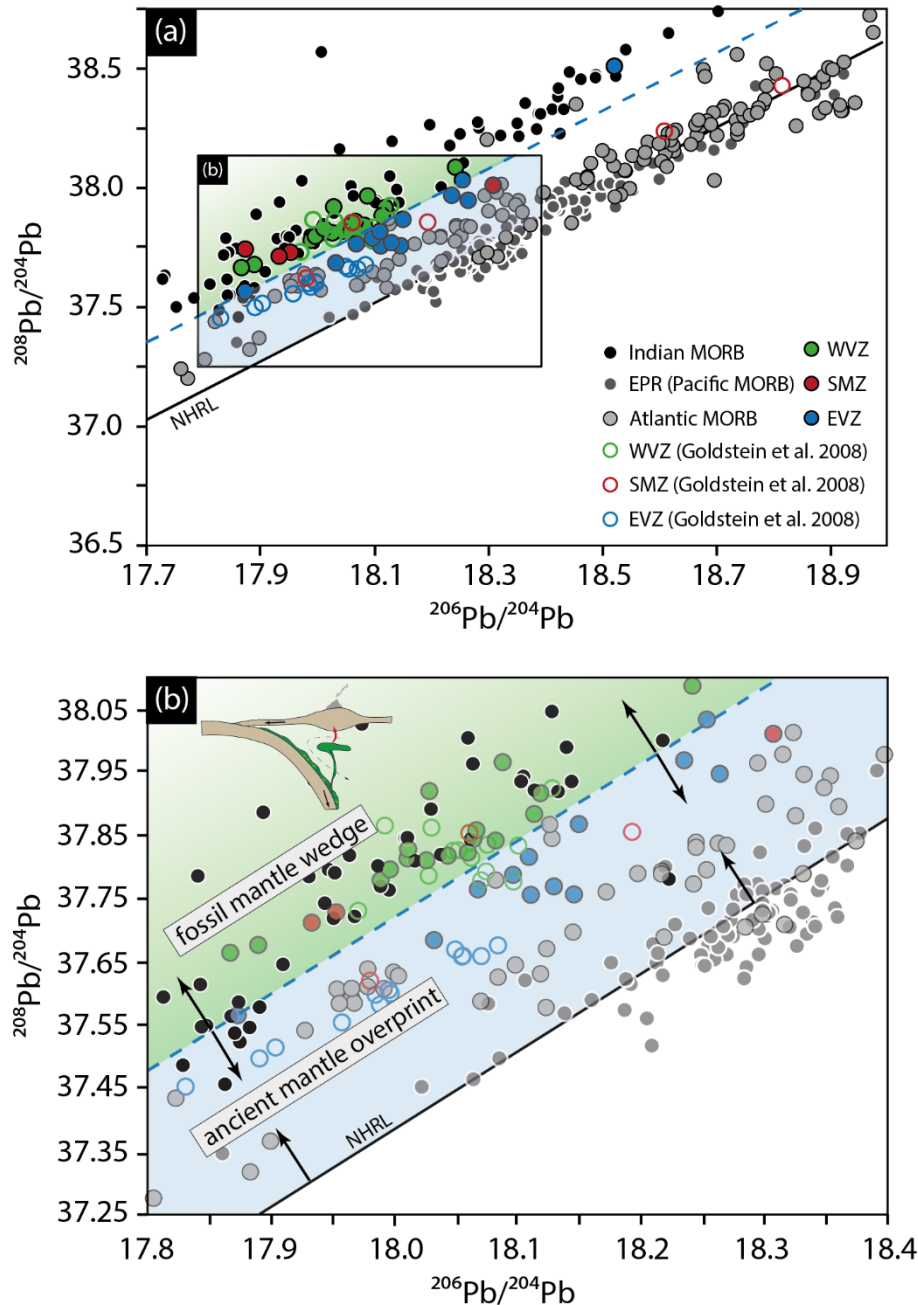
For Hf and Sr isotope analysis, approximately 100 mg of sample powder was weighted into a Teflon beaker and dissolved in a mixture of cHF and cHNO<sub>3</sub> (1:5 ratio, approx. 2ml) on a hotplate for 24 hours at 120°C. The acid was further evaporated and remaining fluorides were refluxed three-times with 5 drops of cHNO<sub>3</sub> and 1 - 2 drops of a weak mixture of 0.5M HF and 0.5M HCl.

For chromatographic extraction of Hf the chemical procedure of Nebel et al. (2009) has been followed using Eichrom Ln spec (100 - 200  $\mu\text{m}$  mesh size) resin. After the purification, the samples were taken up in a 0.24M HF and 0.32M HNO<sub>3</sub> mixture and introduced via a Teledyne Cetac Technologies Aridus II into a multicollector ICP-MS. Hafnium isotopes were analysed in two individual analytical sessions using a ThermoFisher NeptunePlus MC-ICP-MS at the Isotopia Laboratory at the School of Earth, Atmosphere and Environment, Monash University. Operational settings of the Aridus were set between 3.92 l/min and 5.37 l/min for the sweep gas (Ar) and for N<sub>2</sub> between 0.04 l/min – 0.06 l/min. Hafnium isotopes were measured in a low resolution mode and data was obtained during three blocks of 20 cycles with an integration time of 2.097 seconds. For data control, BCR1 and BHVO1 sample powder have been dissolved applying the same chromatic extraction as for the samples and analysed among the sample set. Hafnium isotope analyses of BCR1 and BHVO1 resulted in values of  $0.282859 \pm 11$  ( $n = 2$ ;  $1\sigma$  of the mean) and  $0.283094 \pm 17$  ( $n = 2$ ;  $1\sigma$  of the mean), respectively. Hafnium isotope values of BCR1 ( $0.282875 \pm 8$ ; Weis et al., 2007) and BHVO1 ( $0.283106 \pm 12$ ; Weis et al., 2007) deviate absolutely from their literature value by 0.000016 (relative uncertainty 0.006%) and 0.000012 (relative uncertainty 0.004%). Reproducibility was accounted by multiple measurements of JMC475 resulting in  $^{176}\text{Hf}/^{177}\text{Hf}$  of  $0.282168 \pm 4$  ( $n = 14$ ; 1SE) yielding in an absolute difference to literature value ( $0.282163 \pm 0.000009$ ; Blichert-Toft et al., 1997) of 0.000005 (relative uncertainty 0.002 %). The procedural blank is > 48 pg. All  $^{176}\text{Hf}/^{177}\text{Hf}$  are given as epsilon notation  $\epsilon_{\text{Hf}}$  that is defined as the deviation from the chondrite reservoir (CHUR) multiplied by 10000, for a given time.

Strontium was separated using Sr spec (100 – 150  $\mu\text{m}$  mesh size) applying a standard chromatographic extraction method with 3M  $\text{HNO}_3$  to elute the matrix and 0.01M  $\text{HNO}_3$  to extract Sr. Procedural blank was negligible ( $\sim 40 \pm 20$  pg). Strontium isotope measurements was performed with a glass chamber in a wet-solution mode resolution mode. Instrumental mass bias was corrected using the exponential law to  $^{86}\text{Sr}/^{88}\text{Sr}$  of 0.1194. To account for isobaric interferences on  $^{86}\text{Sr}$  with  $^{86}\text{Kr}$  of the gas, Kr interferences have been corrected to  $^{86}\text{Kr}/^{83}\text{Kr}$  of 1.50252 using six iterations. Reproducibility was monitored by repeated measurements of the US National Institute of Standards and Technology SRM987 standard yielded a  $0.710326 \pm 0.000018$  (2SE;  $n = 10$ ). All samples were corrected to  $^{87}\text{Sr}/^{86}\text{Sr} = 0.710248$  (McArthur, 1994). Among the sample set, reference material BCR1 and BHVO1 has been dissolved for chromatographic extraction of Sr for data control and chemical purification process. The measured Sr isotope values for BCR1 is  $0.705008 \pm 0.00010$  (1SE) and for BHVO1 is  $0.703494 \pm 0.000012$ , resulting in an absolute deviation to the recommended literature value of 0.000177 (BCR1 = 0.704960; USGS) and 0.000192 (BHVO1 = 0.703436; USGS), respectively.



**Supplementary Figure 4.1 - Trace element pattern of the EVZ at the Gakkel Ridge.** All data has been compared with enriched MORB (E-MORB); normal MORB (N-MORB) and depleted MORB (D-MORB). <sup>1</sup> – Data from Palme and O'Neill (2014).



**Supplementary Figure 4.2 -  $^{208}\text{Pb}/^{204}\text{Pb}$  versus  $^{206}\text{Pb}/^{204}\text{Pb}$  diagram.** (a) Comparison of the EVZ basalts with basalts from the Western Gakkal Ridge region (WVZ, SMZ) and the Atlantic/Pacific MORBs. Basalts from the EVZ display a higher Th/U than most of the Atlantic/Pacific MORBs, but a lower than basalts from the WVZ and SMZ. The blue dashed line marks the isotopic difference (isotopic boundary) between the Western Gakkal Ridge region and the EVZ and shows that the EVZ plot within the Atlantic/Pacific MORB, whereas the WVZ and SMZ within the Indian MORB field. (b) is a close-up to clarify the difference between SMZ, WVZ and EVZ. The high Th/U ratio observed in basalts from the Western Gakkal Ridge region and lower Th/U of the EVZ basalts marks a boundary between a mantle that has been overprinted by two separate re-enrichment processes. Different processes affects the MORB chemistry. Basalts showing an Indian-type mantle signature may sample remnants of a fossil mantle wedge, whereas the MORB source of the Atlantic/Pacific-type mantle is more homogenised containing refractory components and represents a mantle with an ancient overprint. MORB data from the Atlantic and Pacific basalts have been taken from Gale et al. (2014). Indian MORB data without samples  $> 125^\circ\text{E}$  from the Southeast Indian Ridge at the Australian Antarctic Discordance. Lead isotope data for samples from the WVZ and the SMZ has been compiled from chapter 3. The black line is the NHRL (Northern Hemisphere reference line; Hart, 1984) and has been used as reference.

**SI – References**

- Blichert-Toft, J., Chauvel, C., Albarède, F., 1997. Separation of Hf and Lu for high-precision isotope analysis of rock samples by magnetic sector-multiple collector ICP-MS. *Contributions to Mineralogy and Petrology*, 127(3): 248-260.
- Gale, A., Langmuir, C.H., Dalton, C.A., 2014. The Global Systematics of Ocean Ridge Basalts and their Origin. *Journal of Petrology*, 55(6): 1051-1082.
- Hart, S.R., 1984. A large-scale isotope anomaly in the Southern Hemisphere mantle. *Nature*, 309(5971): 753-757.
- Jenner, F.E., O'Neill, H.S.C., 2012. Analysis of 60 elements in 616 ocean floor basaltic glasses. *Geochemistry, Geophysics, Geosystems*, 13(2): Q02005.
- Jochum, K.P., Stoll, B., Herwig, K., Willbold, M., 2007. Validation of LA-ICP-MS trace element analysis of geological glasses using a new solid-state 193 nm Nd:YAG laser and matrix-matched calibration. *J. Anal. At. Spectrom.*, 22(2): 112-121.
- Longerich, H.P., Jackson, S.E., Gunther, D., 1996. Inter-laboratory note. Laser ablation inductively coupled plasma mass spectrometric transient signal data acquisition and analyte concentration calculation. *Journal of Analytical Atomic Spectrometry*, 11(9): 899-904.
- McArthur, J.M., 1994. Recent trends in strontium isotope stratigraphy. *Terra Nova*, 6(4): 331-358.
- Nebel, O., Morel, M.L.A., Vroon, P.Z., 2009. Isotope Dilution Determinations of Lu, Hf, Zr, Ta and W, and Hf Isotope Compositions of NIST SRM 610 and 612 Glass Wafers. *Geostandards and Geoanalytical Research*, 33(4): 487-499.
- Palme, H., O'Neill, H.S.C., 2014. Cosmochemical Estimates of Mantle Composition. 1-39.
- Taylor, R.N., Ishizuka, O., Michalik, A., Milton, J.A., Croudace, I.W., 2015. Evaluating the precision of Pb isotope measurement by mass spectrometry. *J. Anal. At. Spectrom.*, 30(1): 198-213.
- Weis, D. et al., 2007. Hf isotope compositions of U.S. Geological Survey reference materials. *Geochemistry, Geophysics, Geosystems*, 8(6).
- Woodhead, J., 2002. A simple method for obtaining highly accurate Pb isotope data by MC-ICP-MS. *Journal of Analytical Atomic Spectrometry*, 17(10): 1381-1385.



## **Supplementary Data Tables**



Chapter 4 – Supplementary Data Tables

**Supplementary Data Table 4.1 – Major and trace elements of the EVZ basalts.** Major element data is given in wt.%, whereas the trace element data are given in ppm. VG – Volcanic glass.

<i>Sample Name</i>	<i>PS 59 263 - 26</i>	<i>HLY0102 D050 - 30</i>	<i>HLY0102 D051 - 15</i>	<i>PS 59 297 - 11</i>	<i>PS 101 186 R1 Bas</i>	<i>PS 101 186 VG</i>	<i>PS 59 294 - 40</i>
<i>Segment</i>	<i>EVZ</i>	<i>EVZ</i>	<i>EVZ</i>	<i>EVZ</i>	<i>EVZ</i>	<i>EVZ</i>	<i>EVZ</i>
Longitude	86.0	86.2	86.3	86.7	86.6	86.6	86.9
Latitude	30.6	37.5	43.3	46.9	55.4	55.4	56.4
<i>MAJOR ELEMENTS</i>							
SiO <sub>2</sub>	49.7	49.3	49.4	47.8	49.1	49.3	48.5
TiO <sub>2</sub>	1.5	1.3	1.4	1.0	1.3	1.3	1.3
Al <sub>2</sub> O <sub>3</sub>	16.8	16.6	17.3	17.2	16.6	16.6	16.9
Fe <sub>2</sub> O <sub>3</sub>	9.9	8.6	8.7	10.8	8.8	8.9	9.4
MnO	0.2	0.1	0.1	0.2	0.1	0.1	0.2
MgO	6.7	9.1	8.9	10.2	9.3	9.3	9.3
CaO	10.8	11.0	11.2	10.7	11.1	11.0	11.1
Na <sub>2</sub> O	3.1	3.1	3.1	2.6	3.0	3.1	3.1
K <sub>2</sub> O	0.5	0.4	0.2	0.2	0.2	0.1	0.3
P <sub>2</sub> O <sub>5</sub>	0.2	0.2	0.2	0.1	0.1	0.1	0.1
LOI	0.7	0.0	-0.2	-0.5	0.0	-0.4	0.2
Sum	100.0	99.8	100.4	100.3	99.7	99.6	100.4
<i>TRACE ELEMENTS</i>							
Na	12928	23097	22515	20406	20782	20863	17703
Mg	55463	60068	59566	73295	52192	52934	48218
Al	98880	97005	101288	107543	88035	88486	84972
Si	232286	230258	230973	229744	229639	230502	226917
Ca	96393	93914	96214	99246	77079	77003	89648
Sc	39.0	31.9	32.0	35.9	21.2	19.8	41.7
Ti	7074	9633	10027	7894	7338	7479	10415
V	329	248	251	198	216	222	342
Cr	542	443	370	431	404	422	200
Mn	2198	1212	1211	1529	1023	1042	1941
Fe	73403	60238	59317	78894	56584	57593	78884
Co	47.5	41.4	40.1	53.4	38.1	36.6	47.3
Ni	91.2	197.9	169.8	267.6	190.7	183.8	62.7
Cu	112.0	145.8	62.7	181.4	77.0	89.4	63.6
Zn	66.0	45.5	46.2	52.2	39.3	41.9	68.9
Ga	15.2	14.7	15.1	14.5	14.6	13.8	17.0
Rb	11.4	4.2	1.5	1.1	1.8	0.1	9.9
Sr	128	236	242	193	173	172	97
Y	25.7	28.0	28.4	30.2	25.4	26.3	39.8
Zr	54.4	113.3	119.9	75.3	98.6	101.3	80.0
Nb	0.98	7.68	4.27	2.62	2.27	2.44	1.16
Mo	0.16	0.18	0.69	1.27	0.86	0.47	0.47
Cs	0.17	0.10	-0.02	0.12	0.04	0.11	0.30
Ba	96.1	59.0	23.3	17.7	11.9	11.8	9.6
La	2.45	7.44	5.39	3.41	3.16	3.37	2.63
Ce	5.33	15.81	13.68	8.14	10.59	10.59	7.55
Pr	0.96	2.19	2.27	1.29	1.76	1.81	1.49
Nd	5.85	11.52	11.83	7.12	9.68	9.81	8.54
Sm	2.45	3.60	3.36	2.62	3.22	2.81	3.74
Eu	0.82	1.19	1.19	0.96	1.10	1.09	1.28
Gd	3.00	4.04	4.22	3.18	3.60	3.91	5.09
Tb	0.62	0.75	0.75	0.67	0.66	0.63	0.92
Dy	4.35	4.69	4.69	4.91	4.19	4.50	6.61
Ho	0.94	0.91	0.97	1.05	0.92	0.93	1.39
Er	2.67	2.84	2.89	3.21	2.58	2.82	4.19
Tm	0.37	0.36	0.38	0.52	0.40	0.38	0.58

Chapter 4 – Supplementary Data Tables

Yb	2.49	2.65	2.78	3.19	2.44	2.47	4.05
Lu	0.39	0.40	0.39	0.51	0.32	0.37	0.60
Hf	1.53	2.47	2.50	1.87	2.38	2.34	2.21
Ta	0.57	0.74	0.54	0.58	0.16	0.11	0.44
Pb	0.52	0.63	0.48	0.39	0.39	0.35	0.49
Th	0.09	0.56	0.22	0.15	0.16	0.14	0.06
U	0.05	0.16	0.09	0.09	0.11	0.09	0.22

Supplementary Data Table 4.1 – [continued]

<i>Sample Name</i>	<i>PS 101 193 R1</i>	<i>PS 101 203 R4</i>	<i>PS 101 203 R5</i>	<i>PS 101 203 R8</i>	<i>PS 59 274 - 52</i>	<i>HLY0102 D059 - 35</i>	<i>HLY0102 D061 - 11</i>
<i>Segment</i>	<i>EVZ</i>	<i>EVZ</i>	<i>EVZ</i>	<i>EVZ</i>	<i>EVZ</i>	<i>EVZ</i>	<i>EVZ</i>
Longitude	86.4	86.5	86.5	86.5	86.7	86.3	85.4
Latitude	61.2	61.4	61.4	61.4	66.8	70.6	84.6
<i>MAJOR ELEMENTS</i>							
SiO <sub>2</sub>	46.2	49.0	48.7	48.8	49.1	49.3	49.3
TiO <sub>2</sub>	1.3	1.2	1.2	1.6	1.0	1.5	1.4
Al <sub>2</sub> O <sub>3</sub>	16.7	19.7	19.1	15.7	17.4	16.2	17.5
Fe <sub>2</sub> O <sub>3</sub>	9.6	6.9	7.3	9.5	9.4	9.4	8.8
MnO	0.1	0.1	0.1	0.2	0.2	0.2	0.2
MgO	9.7	5.8	6.6	8.1	9.4	9.5	8.9
CaO	11.3	9.1	9.2	8.3	10.8	10.4	11.1
Na <sub>2</sub> O	3.0	4.3	3.9	4.1	2.9	3.2	3.2
K <sub>2</sub> O	0.1	0.3	0.4	0.2	0.2	0.4	0.2
P <sub>2</sub> O <sub>5</sub>	0.2	0.1	0.1	0.2	0.1	0.2	0.2
LOI	1.7	3.1	2.9	3.1	-0.4	-0.2	-0.3
Sum	100.0	99.7	99.7	99.9	99.9	100.2	100.4
<i>TRACE ELEMENTS</i>							
Na	22074	30557	27566	29306	21035	22761	24795
Mg	57469	34544	39236	48200	62158	61470	62098
Al	92329	109767	106508	88259	99994	91498	106429
Si	216089	228813	227865	228277	223492	230576	230608
Ca	82926	66825	67557	60890	89716	86700	98306
Sc	20.3	18.5	18.1	24.2	29.2	29.0	29.0
Ti	7988	7169	7473	9558	7087	10872	10458
V	231	188	205	267	199	257	245
Cr	440	207	221	264	361	459	368
Mn	1085	939	965	1170	1244	1274	1270
Fe	64441	47318	50186	62881	63499	64100	63726
Co	42.2	26.7	25.7	36.7	44.0	42.3	41.8
Ni	242	63	60	90	200	224	180
Cu	77.0	80.8	63.8	83.7	106.1	82.8	110.9
Zn	43.5	40.5	38.6	48.0	42.6	50.2	45.2
Ga	15.0	13.7	15.6	15.0	14.4	15.2	17.1
Rb	0.2	1.9	2.4	0.4	4.4	3.7	1.2
Sr	204	254	200	218	127	229	255
Y	28.9	23.7	24.1	32.5	24.9	30.8	30.0
Zr	95.1	99.4	102.6	128.6	74.7	133.0	120.4
Nb	3.64	3.17	3.16	3.10	0.92	6.28	2.84
Mo	-	1.02	0.33	0.64	1.13	1.08	1.12
Cs	0.14	0.09	0.13	0.03	0.15	0.09	0.09
Ba	16.0	14.5	27.0	18.4	35.8	42.2	15.3
La	4.80	3.64	3.71	4.55	3.62	6.59	4.87
Ce	12.66	11.23	10.99	14.01	8.44	16.13	12.44
Pr	2.08	1.77	1.75	2.35	1.37	2.46	2.06
Nd	10.54	9.25	10.12	12.44	7.45	12.70	10.84

Chapter 4 – Supplementary Data Tables

Sm	3.25	2.86	2.65	3.97	2.27	3.87	3.74
Eu	1.19	0.93	1.01	1.35	0.93	1.29	1.30
Gd	4.26	3.57	3.74	4.91	3.31	5.03	4.50
Tb	0.73	0.64	0.63	0.88	0.57	0.75	0.74
Dy	4.95	4.04	4.35	5.86	4.38	4.98	4.95
Ho	1.00	0.84	0.87	1.23	0.82	1.05	0.94
Er	3.11	2.62	2.63	3.51	2.54	3.09	3.08
Tm	0.42	0.34	0.33	0.46	0.38	0.44	0.41
Yb	2.55	2.02	2.18	3.03	2.31	2.97	2.67
Lu	0.39	0.35	0.35	0.51	0.36	0.42	0.37
Hf	2.37	2.03	2.06	3.15	1.84	2.86	2.60
Ta	0.21	0.17	0.21	0.18	0.48	0.67	0.58
Pb	0.36	0.52	0.10	0.57	1.22	0.86	0.39
Th	0.23	0.18	0.13	0.17	0.51	0.44	0.14
U	0.28	0.06	0.05	0.07	0.09	0.21	0.05

Supplementary Data Table 4.2 – Trace element data of NIST 612 and NIST 610. All values are given in ppm.

Element	NIST 612				NIST 610			
	Average (n = 32)	RSE (%)	Literature value	Relative error (%)	Average (n = 32)	RSE (%)	Literature value	Relative error (%)
Na	105295	1.4	101635	4.0	102794	1.4	102300	0.5
Mg	70	1.2	68	2.7	539	1.1	610	11.7
Al	11068	0.9	10744	2.9	10572	1.0	11626	9.1
Si	337024	0.0	337024	0.0	323001	0.0	323001	0.0
Ca	87831	1.0	85049	3.2	83812	1.0	81475	2.9
Sc	42.8	0.2	39.9	6.8	346	1.0	455	23.9
Ti	58.1	0.5	44.0	24.3	551	0.9	452	21.9
V	39.7	1.0	38.8	2.3	446	1.3	450	0.8
Cr	41.0	0.8	36.4	11.2	453	1.1	408	10.9
Mn	42.7	0.7	38.7	9.3	462	0.9	444	4.0
Fe	55.8	0.9	51.0	8.6	493	0.7	458	7.6
Co	35.5	0.5	35.5	0.1	407	0.8	410	0.7
Ni	41.8	0.4	38.8	7.1	487	0.4	459	6.2
Cu	45.5	0.4	37.8	16.9	521	0.4	441	18.1
Zn	28.8	1.7	39.1	35.7	362	1.4	460	21.3
Ga	37.9	0.7	36.9	2.6	445	0.8	433	2.8
Rb	31.0	1.0	31.4	1.4	383	1.5	426	9.9
Sr	88.9	1.0	78.4	11.8	506	1.1	516	1.8
Y	45.1	0.9	38.3	15.1	484	1.0	462	4.8
Zr	44.0	0.9	37.9	13.8	498	1.2	448	11.1
Nb	43.1	0.9	38.9	9.7	492	1.0	465	5.8
Mo	39.5	0.9	37.4	5.2	446	0.8	417	6.8
Cs	42.7	1.1	42.7	0.0	335	1.1	366	8.5
Ba	41.6	1.2	39.3	5.6	469	1.3	452	3.8
La	38.7	1.1	36.0	7.1	418	1.2	440	5.0
Ce	40.8	1.1	38.4	5.8	432	1.2	453	4.7
Pr	41.0	1.1	37.9	7.6	433	1.2	448	3.3
Nd	39.6	1.1	35.5	10.4	473	1.1	430	10.0
Sm	42.2	1.1	37.7	10.6	498	1.1	453	10.0
Eu	38.9	1.2	35.6	8.4	433	1.4	447	3.0
Gd	42.7	1.2	37.3	12.6	495	1.2	449	10.2
Tb	42.5	1.2	37.6	11.5	446	1.3	437	2.1
Dy	41.4	1.2	35.5	14.3	493	1.3	437	12.7
Ho	43.2	1.2	38.3	11.3	453	1.4	449	1.0
Er	44.2	1.3	38.0	14.0	501	1.5	455	10.1
Tm	42.9	1.3	36.8	14.2	450	1.4	435	3.5
Yb	44.6	1.3	39.2	12.1	510	1.3	450	13.4

Chapter 4 – Supplementary Data Tables

Lu	42.7	1.3	37.0	13.4	456	1.4	439	4.0
Hf	41.7	1.4	36.7	12.1	476	1.4	435	9.4
Ta	45.4	1.3	37.6	17.2	509	1.4	446	14.2
Pb	40.3	1.5	38.6	4.2	433	1.7	426	1.7
Th	42.8	1.6	37.8	11.6	460	1.7	457	0.6
U	39.1	1.6	37.4	4.3	429	1.7	462	7.1

*Supplementary Data Table 4.3 - Trace element data of BHVO2G and the XRF glass blank. All values are given in ppm.*

Element	BHVO2G				Blank XRF glass
	Average (n = 16)	RSE (%)	Literature value	Relative error (%)	Average (n = 4)
Na	16889	1.7	17805	5.4	35
Mg	43009	1.5	43001	0.0	20
Al	69771	1.2	71978	3.2	66
Si	230448	0.0	230448	0.0	218481
Ca	79385	1.3	81476	2.6	234
Sc	31	0.4	33	6.9	5.4
Ti	16719	1.5	16300	2.6	105
V	318	1.5	308	3.4	3.68
Cr	313	1.1	293	6.8	10.6
Mn	1313	0.9	1317	0.2	8
Fe	85760	0.9	87836	2.4	33.8
Co	45	0.7	44	1.6	0.25
Ni	130	0.7	116	12.1	0.98
Cu	152	0.7	127	19.4	2.82
Zn	96	1.7	102	5.6	0.67
Ga	22.05	0.8	22	0.2	0.13
Rb	9.06	1.1	9.2	1.6	0.10
Sr	385	2.3	396	2.8	0.43
Y	25.1	0.9	26	3.5	0.02
Zr	166	1.0	170	2.3	0.33
Nb	18.0	1.1	18.3	1.6	0.05
Mo	4.2	1.4	3.8	10.5	0.37
Cs	0.1	3.1	0.1	1.3	0.02
Ba	131.2	1.5	131	0.2	0.87
La	14.91	1.2	15.2	1.9	0.21
Ce	37.47	1.4	37.6	0.3	0.05
Pr	5.21	1.2	5.35	2.7	0.00
Nd	24.57	1.1	24.5	0.3	b.d.1
Sm	6.12	1.2	6.1	0.3	0.03
Eu	2.05	1.3	2.07	0.9	b.d.1
Gd	6.14	1.2	6.16	0.4	0.01
Tb	0.91	1.2	0.92	1.5	b.d.1
Dy	5.33	1.2	5.28	0.9	b.d.1
Ho	0.95	1.3	0.98	2.8	0.01
Er	2.53	1.4	2.56	1.3	b.d.1
Tm	0.33	1.3	0.34	3.7	0.03
Yb	2.01	1.5	2.01	0.1	b.d.1
Lu	0.28	1.9	0.279	-0.4	b.d.1
Hf	4.33	1.6	4.32	0.3	b.d.1
Ta	1.15	1.5	1.15	0.4	0.55
Pb	1.84	1.9	1.7	8.1	0.10
Th	1.21	1.9	1.22	0.9	b.d.1
U	0.42	2.0	0.403	5.0	b.d.1

## CHAPTER 5

### *The effect of spreading rate and source heterogeneity on iron isotope variability in ocean floor lavas at the ultraslow-spreading Gakkel Ridge, Arctic Ocean*

*Marianne Richter*<sup>\*1</sup>, *Oliver Nebel*<sup>1</sup>, *Yona Nebel-Jacobsen*<sup>1</sup>, *Henry J.B. Dick*<sup>2</sup>

<sup>1</sup> – Isotopia Laboratory, School of Earth, Atmosphere and Environment, Monash University, Clayton, Victoria, 3800, Australia

<sup>2</sup> – Department of Geology and Geophysics, Woods Hole Oceanographic Institution, Woods Hole, Massachusetts, 02543-1539, USA



*Only the tips of icebergs are visible from the surface. To see what is below, we need to dive deeper. This image is an analogue for my thesis. With this PhD thesis, I only scratch the surface of a certain topic. But to understand its complexity, requires further research. ([https://c402277.ssl.cf1.rackcdn.com/photos/11158/images/story\\_full\\_width/Glacier287286.jpg?1458765745](https://c402277.ssl.cf1.rackcdn.com/photos/11158/images/story_full_width/Glacier287286.jpg?1458765745))*

*This manuscript is aimed for submission to Earth, Planetary and Science Letters.*

## **Abstract**

Ocean floor lavas from global oceanic ridges exhibit considerable variability in Fe isotope systematics that cannot be explained by igneous differentiation alone. It remains unclear if all or only parts of this variation is consequent to processes during the cooling of the lava towards the surface, or reflects heterogeneity in the Earth's upper mantle. Igneous differentiation in cooling melts from oceanic ridges has been proposed to be strongly affected by suboceanic magma slurries, with a complex interplay of fractional crystallisation, recharge of melts and evacuation of melts. The effect of this phenomenon should, however, be less pronounced in ridges with very slow spreading rates, which are considered to be fed directly by mantle-derived melts. We present new iron isotope data in dredged lavas from the ultraslow-spreading Gakkel Ridge in the Arctic Ocean to investigate the effect mantle source variability, suboceanic magma lenses and associated petrogenesis. Thirty-five basalts were analysed for their stable Fe isotopes (expressed as  $\delta^{57}\text{Fe}$  relative to IRMM-524a) from three ridge segments at the Gakkel Ridge. The Gakkel Ridge can be divided, based on radiogenic Pb-Sr isotopes, magmatic activity, and possibly thermal structure and spreading rate into the slow spreading Western Volcanic Zone (WVZ) and the ultraslow-spreading Sparsely Magmatic Zone (SMZ) and the Eastern Volcanic Zone (EVZ). Gakkel Ridge lavas range from  $\delta^{57}\text{Fe} = +0.10\text{‰}$  to  $+0.31\text{‰}$ , with samples from the SMZ displaying an average  $\delta^{57}\text{Fe}$  value of  $+0.22\text{‰} \pm 0.02\text{‰}$ . Basalts from the WVZ and the EVZ have an average  $\delta^{57}\text{Fe}$  of  $+0.17\text{‰} \pm 0.03\text{‰}$  and  $+0.16\text{‰} \pm 0.02\text{‰}$ , respectively. Calculated primitive  $\delta^{57}\text{Fe}$  of each sample (i.e., prior to olivine fractionation, expressed as  $\delta^{57}\text{Fe}_{\text{prim}}$ ) shows that the SMZ is, on average,  $0.04\text{‰}$  heavier than basalts from the EVZ and the WVZ, marking a higher degree of mantle depletion. The degree of isotope fractionation ( $\Delta^{57}\text{Fe}$ ), however, correlates with an increase in spreading rate (2 – 5 mm/a) and is interpreted here to be associated with the possible absence of magma lenses at upper crustal levels in the East and their presence in the West, respectively. At faster spreading rates ( $> 12\text{ mm/a}$ ; WVZ) more uniform  $\delta^{57}\text{Fe}$  indicate magma homogenization, along with an increase in  $\Delta^{57}\text{Fe}$  (crystal fractionation), which is ascribed here to processes in melt lenses or magma chambers. In contrast, at ultraslow-spreading rates ( $< 12\text{ mm/a}$ ; SMZ and EVZ),  $\delta^{57}\text{Fe}$  is highly variable, ascribed here to rapidly rising melts without homogenisation in a magma lens and with memory of the chemically diverse mantle source. It is inferred that the upper mantle is heterogeneous also in Fe isotopes, and that some of this heterogeneity is erased through magma reservoir homogenisation. However, the degree of Fe isotope variability in ocean floor lavas globally is too large so that this homogenisation appears to be imperfect. Variable degrees of mantle depletion still affect the Fe isotope signature of erupting lavas.



## 5.1 Introduction

The Earth's upper mantle is heterogeneous and consists of depleted and enriched lithologies formed by multiple cycles of melt extraction, fluid-borne metasomatism and potential relicts of subducted oceanic lithosphere and delaminated subcontinental lithospheric mantle (Chauvel et al., 2008; Hofmann, 2014; White, 2015; Zartman and Haines, 1988; Zindler and Hart, 1986). Mantle convection shears and blends areas of lithological variation and re-distributes these heterogeneities that range from the sub-kilometre to hundreds of kilometre scale (Agranier et al., 2005; Rubin et al., 2009). Mantle heterogeneities can be either investigated by studying abyssal peridotites (Warren, 2016) or by tracing them indirectly through geochemistry of ocean floor lavas, because melts are channelled through to the surface inheriting the chemical signature of its source (Rubin et al., 2009). Even though the nature of magmas derived from partial melting of the mantle is impacted by a number of processes that range from differences in melting conditions (pressure and temperature), igneous differentiation or melt mixing, underlying mantle source heterogeneity has a strong impact on the chemical diversity of mid-ocean ridge basalts (MORB) (Coogan and O'Hara, 2015; Mallick et al.; Meyzen et al., 2007; O'Neill and Jenner, 2012; Rubin et al., 2009). Deciphering the origin and extent of mantle heterogeneity, however, is challenging and requires well-defined chemical proxies that can be used to correct for secondary processes affecting the primary melt chemistry *en route* to the surface.

Recent developments in stable isotope geochemistry have revealed that Fe isotope compositions (expressed here as  $\delta^{57}\text{Fe}$  relative to IRMM-524A) in ocean floor lavas are affected by petrogenetic processes (Nebel et al., 2018; Weyer and Ionov, 2007; Williams et al., 2018) and source heterogeneity (Nebel et al., 2013). Iron is a major element in most mantle minerals, including olivine and pyroxene, and occurs as ferric ( $\text{Fe}^{3+}$ ) and ferrous ( $\text{Fe}^{2+}$ ) species in the  $f\text{O}_2$  range of the upper mantle and the crust. Bond theory predicts that ferrous iron is preferentially associated with lighter iron isotopes (Rustad and Yin, 2009; Sossi et al., 2017). Dependent on olivine-rich vs pyroxene-rich sections and possible mass transfer of Fe through partial melting in the mantle, variations in  $\delta^{57}\text{Fe}$  are expected (Sossi et al., 2016; Teng et al., 2013; Williams et al., 2009). Recorded pyroxenite and peridotite Fe isotope composition highlights variability of Fe isotopes of mantle xenoliths (Beard and Johnson, 2004; Craddock et al., 2013; Weyer and Ionov, 2007; Williams and Bizimis, 2014; Williams et al., 2009). This variability in mantle xenoliths can potentially translate in MORB chemistry (Craddock et al., 2013; Poitrasson et al., 2013). Whilst partial melting in the mantle adds a systematic shift of up to 0.05‰ in melts, dependent on the degree of melting, and ca. 0.02‰ towards lower  $\delta^{57}\text{Fe}$  in residual mantle (Foden et al., 2018; Nebel et al., 2015), it remains unclear to which degree mantle heterogeneity, resultant from melt depletion and re-enrichment, plays into the observed variations in MORBs.

**Table 5.1 – Major and trace element and iron isotope data of the Gakkel Ridge basalts (whole rock) and volcanic glasses (VG).  $\lambda 1$  and  $\lambda 2$  – calculated after O'Neill (2016);  $\lambda 1^l$  – estimated from Gale et al. (2013)**

Sample Name	Ridge segment	Latitude	Longitude	Spreading rate <sup>1</sup> [cm/a]	Na8.0	Mg#	Ni [ppm]	Zr/Nb	V/Sc	$\lambda 0$	$\lambda 1$	$\lambda 2$	$\delta^{56}\text{Fe}$	ISD	$\delta^{57}\text{Fe}$	ISD	$\delta^{57}\text{Fe}_{\text{prim}}$	$\Delta^{57}\text{Fe}$
HLX0102 D011 - 19	WVZ	82.6	-6.2	12.8	3.2	62.2	150.8	22.4	8.7	3.0	0.6	-29.7	0.11	0.01	0.13	0.03	0.09	0.039
HLX0102 D8 - 12	WVZ	82.5	-6.2	12.8	3.2	61.8	138.8	34.1	8.8	3.1	-0.7	-29.7	0.10	0.01	0.12	0.02	0.08	0.040
PS 66 217-16 (B)	WVZ	82.9	-6.2	12.8	3.0	59.7	126.4	25.1	9.5	3.2	0.0	-27.9	0.13	0.02	0.17	0.03	0.12	0.048
PS 86-019 (B)	WVZ	82.5	-6.2	12.8	3.4	62.1	151.2	22.0	9.2	3.2	0.4	-19.7	0.14	0.04	0.23	0.02	0.19	0.039
PS 86 - 67 (VG)	WVZ	82.5	-6.2	12.8	3.2	60.7	136.9	34.4	8.8	3.1	-0.7	-31.6	0.10	0.01	0.15	0.03	0.11	0.043
PS 86 - 044 (VG)	WVZ	82.5	-6.2	12.8	3.3	61.3	145.5	21.7	9.1	3.2	0.7	-29.1	0.15	0.02	0.24	0.01	0.20	0.041
PS 59 216 (B)	WVZ	83.1	-6.1	12.8	3.1	61.3	126.3	40.2	8.6	3.1	-0.9	-36.6	0.16	0.01	0.24	0.04	0.20	0.041
PS 59 216-11 (B)	WVZ	83.1	-6.1	12.8	3.1	61.2	128.9	41.6	8.8	3.1	-0.9	-34.8	0.09	0.03	0.14	0.03	0.10	0.041
PS 59 216-13 (B)	WVZ	83.1	-6.1	12.8	3.1	61.4	130.4	36.3	8.7	3.1	-0.6	-37.1	0.13	0.01	0.18	0.01	0.14	0.041
HLX0102 D013 - 10	WVZ	83.2	-5.4	12.8	2.7	57.6	114.6	49.9	9.4	3.1	-1.5	-37.6	0.08	0.01	0.10	0.03	0.05	0.055
PS 59 231 - 14	WVZ	84.0	-0.4	12.5	2.6	54.8	114.2	57.9	7.8	2.6	-3.8	-38.3	0.12	0.04	0.16	0.01	0.10	0.064
PS 59 232 - 84	WVZ	84.2	0.9	12.3	3.2	61.4	151.2	33.1	8.8	3.1	0.3	-31.4	0.09	0.02	0.16	0.03	0.12	0.041
HLX0102 D024 - 2	WVZ	84.6	1.4	12.0	2.5	63.3	125.2	101.3	8.0	2.7	-1.8	-47.0	0.08	0.02	0.12	0.03	0.09	0.035
HLX0102 D026 - 9	WVZ	84.3	2.3	12.3	3.1	59.7	136.1	63.3	9.0	3.1	-1.0	-38.9	0.08	0.02	0.16	0.05	0.11	0.047
HLX0102 D018 - 1	WVZ	83.4	2.5	12.7	3.0	58.6	116.6	46.9	9.5	3.2	-0.7	-36.9	0.17	0.03	0.23	0.01	0.18	0.051
PS 59 234 - 24	WVZ	84.6	3.1	12.0	3.7	66.0	105.2	46.9	8.4	2.6	-3.6	-32.6	0.12	0.02	0.16	0.02	0.14	0.024
PS 59 224 - 34	WVZ	83.4	3.7	12.7	2.6	55.6	77.2	24.8	10.0	3.2	1.3	-14.6	0.15	0.04	0.23	0.03	0.17	0.064
PS 59 243 - 36	SMZ	85.0	10.2	11.7	3.1	63.0	155.0	25.9	7.2	2.9	0.6	-15.0	0.13	0.01	0.18	0.03	0.14	0.035
HLX0102 D037 - 5	SMZ	85.2	11.3	11.7	3.5	55.8	112.4	11.8	9.2	3.4	3.1	-4.6	0.19	0.02	0.31	0.04	0.25	0.062
HLX0102 D036 - 35	SMZ	85.2	12.2	11.7	3.5	61.5	139.0	9.0	8.6	3.3	4.6	18.5	0.15	0.01	0.21	0.01	0.17	0.041
HLX0102 D038 - 6	SMZ	85.2	12.4	11.7	3.6	64.0	171.1	14.8	8.2	3.1	2.1	-1.7	0.14	0.04	0.21	0.03	0.18	0.032
PS 59 251 - 4	SMZ	85.7	20.2	11.4	4.0	68.9	302.8	8.5	8.9	3.2	5.7	6.6	0.12	0.01	0.18	0.01	0.17	0.013
PS 59 263 - 26	EVZ	86.0	30.6	11.1	2.6	57.4	91.2	55.4	8.4	2.6	-3.1	-33.0	0.12	0.02	0.13	0.02	0.07	0.057
HLX0102 D050 - 30	EVZ	86.2	37.5	11.1	3.6	67.6	197.9	14.7	7.8	3.0	3.4	-2.2	0.14	0.04	0.20	0.03	0.18	0.017
HLX0102 D051 - 15	EVZ	86.3	43.3	11.1	3.4	66.8	169.8	28.1	7.9	3.0	2.3	-20.1	0.08	0.01	0.11	0.02	0.09	0.020
PS 101 186 RI Basalt	EVZ	86.6	55.4	10.7	3.5	67.7	190.7	43.5	10.2	2.8	0.7	-43.3	0.12	0.02	0.15	0.01	0.14	0.017
PS 101 186 VG	EVZ	86.6	55.4	10.7	3.6	67.4	183.8	41.5	11.2	2.8	0.6	-33.9	0.10	0.02	0.13	0.01	0.12	0.019
PS 59 294 - 40	EVZ	86.9	56.4	10.7	3.6	66.4	62.7	69.1	8.2	3.0	-4.2	-51.1	0.09	0.02	0.14	0.04	0.12	0.021
PS 101 193 RI	EVZ	86.4	61.2	10.7	3.7	66.7	242.5	26.1	11.4	2.9	1.5	-25.8	0.10	0.01	0.14	0.02	0.12	0.020
PS 101 203 R4	EVZ	86.5	61.4	10.7	3.5	62.5	63.2	31.4	10.1	2.8	1.5	-31.5	0.07	0.01	0.10	0.01	0.06	0.040
PS 101 203 R5	EVZ	86.5	61.4	10.7	3.4	64.2	60.4	32.5	11.3	2.8	1.3	-31.2	0.14	0.03	0.19	0.03	0.15	0.033
PS 101 203 R8	EVZ	86.5	61.4	10.7	4.2	62.7	90.5	41.5	11.0	3.1	0.8	-35.0	0.17	0.03	0.28	0.02	0.24	0.036
PS 59 274 - 52	EVZ	86.7	66.8	10.7	3.4	66.4	200.1	81.0	6.8	2.7	-0.2	-13.4	0.07	0.02	0.10	0.01	0.08	0.021
HLX0102 D059 - 35	EVZ	86.3	70.6	11.1	3.7	66.7	224.2	21.2	8.8	3.1	2.7	-15.4	0.14	0.01	0.22	0.02	0.20	0.021
HLX0102 D061 - 11	EVZ	85.4	84.6	10.3	3.5	66.6	180.4	42.4	8.4	3.0	1.7	-33.7	0.14	0.01	0.23	0.02	0.21	0.023

The ultraslow-spreading Gakkel Ridge in the Arctic Ocean offers a unique opportunity to investigate the relationship between mantle source variability and magmatic evolution on Fe isotope signatures. The Gakkel Ridge is sourced by a heterogeneous mantle ranging from depleted to enriched sections (Blusztajn et al., 2014; Goldstein et al., 2008; Stracke et al., 2011), yet, as to its remote nature, is one of the least studied spreading ridges on Earth. Along-ridge spreading rates vary from 12 mm/a in the West to 6 mm/a in the East (Michael et al., 2003), placing it on the lowest end of the spectrum of global oceanic ridges, and thereby being an ideal location for the investigation of the influence of spreading rate on Fe isotopes. Variations in spreading rate are, in general, linked to different styles of magmatism caused by differences in mantle potential temperatures, rift geometry and kinematics (Dick and Zhou, 2014; Okino et al., 2002; Rubin and Sinton, 2007; Rubin et al., 2009; Sauter et al., 2004). The mantle beneath ultraslow-spreading ridges is colder promoting rapid melt transport through dikes from weak and small mantle upwelling cells (Brandl et al., 2016; Phipps Morgan and Ghen, 1993) into crustal levels, where melt migrates horizontally. Hence, during melt ascent, melt is not channelled through suboceanic magma lenses (or ‘chambers’), as has been promoted for global ridges elsewhere (O'Neill and Jenner, 2012). Potential variability in Fe isotope composition along the Gakkel Ridge with variable spreading rates and source heterogeneity can thus be placed into the context of crystal fractionation versus source composition.

### 5.2 Methods

Basalts analysed in this study originate from two different areas, which cover a spreading rate from 13 mm/a (Western Gakkel Ridge region) to 10.3 mm/a (Eastern Gakkel Ridge region). Twenty two basalts from the Western Gakkel Ridge region with known major and trace elements systematics and, in parts, radiogenic isotope systematics (chapters 3 and 4) have been chosen for this study. Additionally, thirteen basalts from the Eastern Volcanic Zone (EVZ) have been crushed in a ceramic jaw crusher, milled in an agate mill to fine powder and analysed for their major and trace element compositions. Data for major and trace elements are provided in chapter 4 (Supplementary Data Table 4.1). A detailed description of the sample locality is given in Table 5.1.

In brief, 0.5 g of sample powder has been admixed with 12:22 Li metaborate and lithium tetraborate flux. The mixture has been fused using a Claisse M4 fluxer. The fused sample disc has been analysed for their major element content using a PANanalytical Axios Advanced WDS X-ray fluorescence (XRF) instrument coupled with a 4000 W Rh X-ray tube at the School of Earth Sciences, University of Tasmania. Fragments of each fused sample discs have been mounted in 1-inch epoxy plugs and measured for the trace element content using laser ablation inductively coupled plasma mass spectrometer (LA-ICP-MS) in the Isotopia Laboratory at the School of Earth, Atmosphere and Environment, Monash University. Forty-two trace element compositions have

been determined using an ASI RESolution SE 193nm ArF excimer laser coupled to a ThermoFisher Scientific ICapQ. Spot size, repetition rate and energy density was set to 80  $\mu\text{m}$ , 10 Hz and 3  $\text{J}/\text{cm}^2$ , respectively. Four to five spots were measured on each fragment. A single analysis comprised of 20 s background signal, 30 s data acquisition and 20 s washout. For data reduction and control the reference glasses NIST 610, NIST 612, BCR2G and BHVO2G have been bracketed after blocks of twenty unknowns. BCR2G has been used as calibration standard. As internal calibration Si (determined by XRF) was used. Data has been acquired in a time-resolved analysis mode and were reduced using a Microsoft EXCEL spreadsheet developed at the Max Planck Institute for Chemistry (MPIC) Mainz, Germany (Jochum et al., 2007; Longerich et al., 1996).

Iron isotope measurements ( $\delta^{57}\text{Fe}$ ) have been carried out in the Isotopia facility at the School of Earth, Atmosphere and Environment at the Monash University, Australia. Circa 150 mg of each sample has been dissolved in a mix of concentrated HF:HNO<sub>3</sub> (ratio 1:5) and left for 24 hours on a hotplate at 100°C. After the digestion, the samples have been dried down three times, after adding three drops of concentrated HNO<sub>3</sub> and two drops of weak HCl-HF mixture to break the silica-calcium bonding. The samples were taken up in 2 ml of 9M HCl and have been then centrifuged to separate insoluble sample material (e.g., remaining Ca-fluorides), before the chemical separation of Fe from the rock matrix. For the Fe purification an anion resin AG1-X-8 resin (Bio-Rad 200 - 400  $\mu\text{m}$  mesh) was used to remove the matrix using the chromatographic procedure of Sossi et al. (2015) and Cheng et al. (2014). The extracted Fe has been introduced into the Ar plasma using a Thermo Scientific quartz cyclonic spray chamber. All samples were analysed in 2 % HNO<sub>3</sub> using a NeptunePlus MC-ICP-MS with <sup>53</sup>Cr, <sup>54</sup>Fe, <sup>56</sup>Fe, <sup>57</sup>Fe, <sup>58</sup>Fe, <sup>60</sup>Ni and <sup>61</sup>Ni ion beams measured simultaneously on Faraday cups (L4, L2, L1, C, H1, H2, H4) at medium resolution. Basalt samples have been analysed using the standard bracketing method. All data is reported relative to the international Fe isotope standard IRMM-524A (Craddock and Dauphas, 2011), which isotopically identical to IRMM-014 and is given in delta notation:

$$\delta^X\text{Fe (IRMM-524A)} = \left[ \frac{(^X\text{Fe}/^{54}\text{Fe}_{\text{sample}})}{(^X\text{Fe}/^{54}\text{Fe}_{\text{IRMM-524A}})} - 1 \right] \times 1000;$$

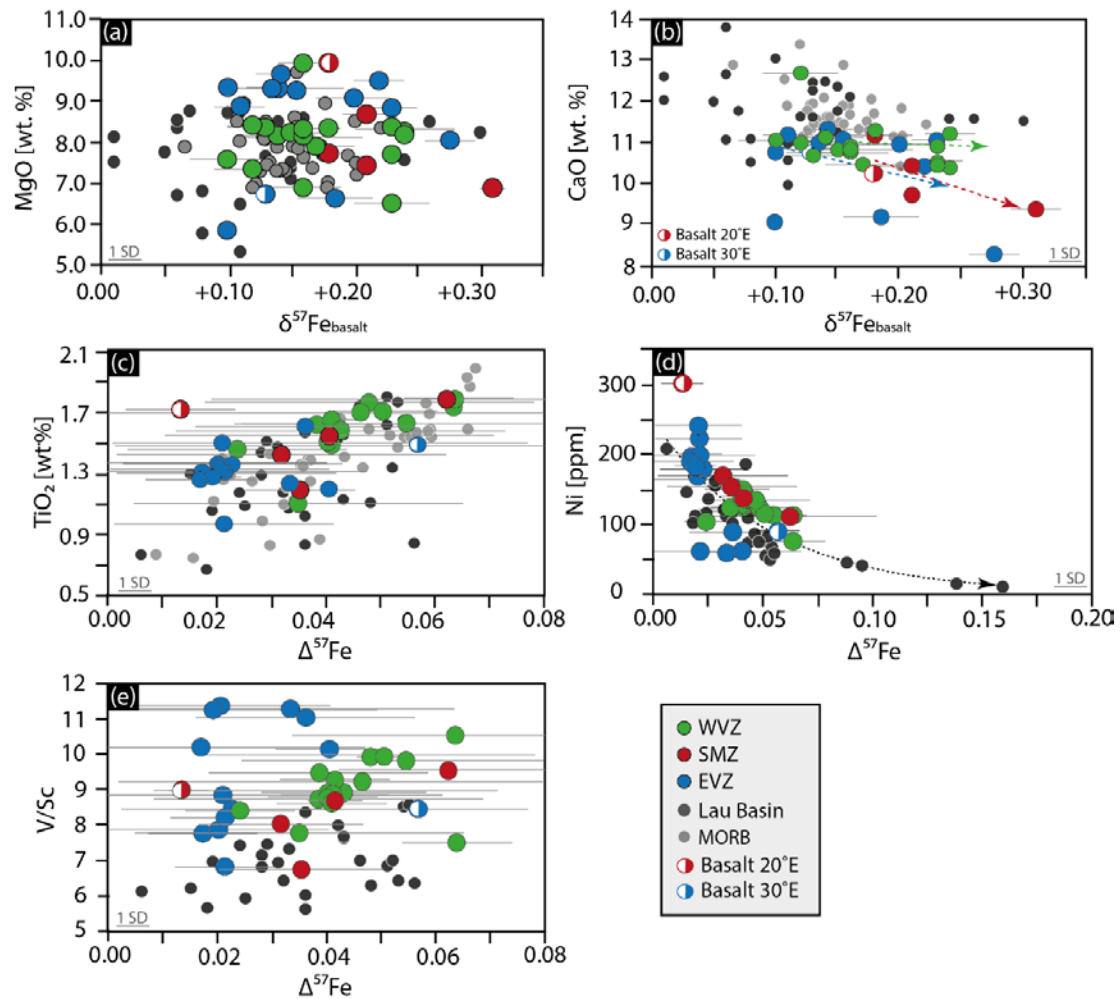
where <sup>X</sup>Fe refers to <sup>57</sup>Fe and <sup>56</sup>Fe, respectively, and <sup>X</sup>Fe/<sup>54</sup>Fe<sub>IRMM-524A</sub> is calculated as average from the bracketing standard values. Instrumental mass bias was further corrected in each analytical session by using a Ni ICP standard solution using the exponential fractionation law and assuming equal mass biases of Fe and Ni. The Ni solution has been admixed to the sample prior to isotope analyses and has been adjusted to 5 ppm Fe and 15 ppm Ni resulting in a ~700 mV for <sup>57</sup>Fe, respectively. Each sample has been measured for a minimum of three times. Iron isotopes are reported as  $\delta^{57}\text{Fe}$  and  $\delta^{57}\text{Fe}_{\text{prim}}$  in this study.  $\delta^{57}\text{Fe}$  corresponds to the measured value of the rock, whereas  $\delta^{57}\text{Fe}_{\text{prim}}$  is the corrected value that represents the composition of a primitive melt in equilibrium with mantle. A detailed description of the calculation for  $\delta^{57}\text{Fe}_{\text{prim}}$  is given in Sossi et

al. (2016) and Nebel et al. (2018). The uncertainty is given as 1sd (standard deviation) in this contribution. The reproducibility of the analysis has been tested by the analysis of BHVO2 and BCR2. BHVO2 yielded a  $\delta^{57}\text{Fe}$  of  $0.18\text{‰} \pm 0.02\text{‰}$  and BCR2 in a  $\delta^{57}\text{Fe}$   $0.05\text{‰} \pm 0.04\text{‰}$ , which is within analytical error to published literature values (Foden et al., 2018; Nebel et al., 2015). Data for each sample and reference material are given in Table 5.1.

## 5.3 Results

### 5.3.1 Major and trace elements

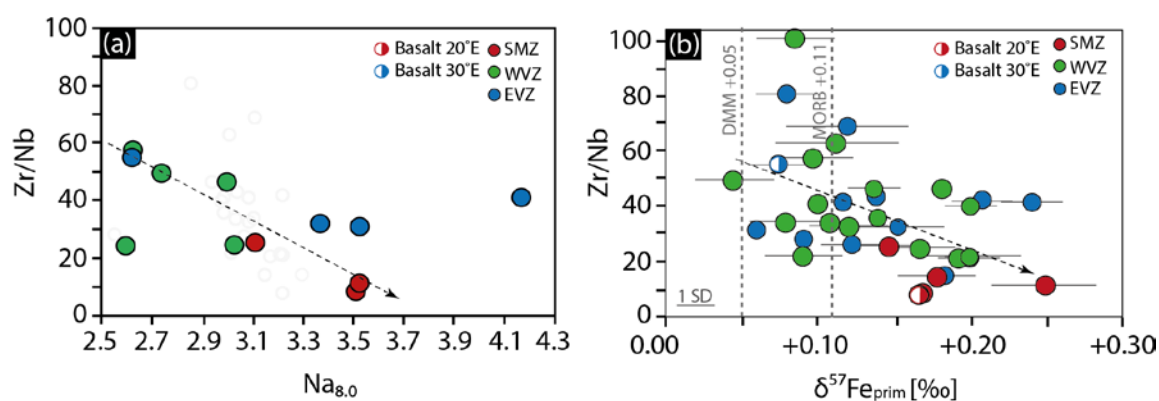
The most primitive Gakkel basalts with the highest MgO values are also characterised by high Ni concentration (average Ni = 174 ppm), low  $\text{TiO}_2$  (average 1.30 wt %), V/Sc ratio (average ratio = 7.74), whereas the more evolved basaltic melts have high  $\text{TiO}_2$  values (average = 1.79 wt %), higher V/Sc (average ratio = 8.90 wt %) and low Ni concentration (average Ni = 126 ppm) (Figure 5.1).



**Figure 5.1 - Major and trace element versus iron isotope composition.** MORB data from Teng et al. (2013) and data from the Lau Basin (Nebel et al., 2018) are used as comparison for the Gakkel Ridge region. (a) MgO versus  $\delta^{57}\text{Fe}$  shows no correlation. Basalts from the WVZ plot from depleted to enriched  $\delta^{57}\text{Fe}$ , whereas SMZ basalts plot towards positive values extending the existing MORB data base. (b) CaO versus  $\delta^{57}\text{Fe}$ . Basalts from the Gakkel Ridge have a lower CaO

compared to MORBs globally. Slight difference between the WVZ, and SMZ and EVZ visible. Basalts from the WVZ show no correlation, whereas basalts from the SMZ and EVZ have a negative co-variation suggesting possible compositional changes in the source. (c)  $\text{TiO}_2$  versus  $\Delta^{57}\text{Fe}$  shows an increase with increasing  $\Delta^{57}\text{Fe}$ . (d)  $\Delta^{57}\text{Fe}$  decreases exponentially with decreasing Ni content. (e)  $\text{V}/\text{Sc}$  versus  $\Delta^{57}\text{Fe}$  shows a negative co-variation for  $\Delta^{57}\text{Fe} < 0.04\text{‰}$  and a positive co-variation for  $\Delta^{57}\text{Fe} > 0.04\text{‰}$  suggesting an increase of pyroxene in the melt for basalts from the WVZ and the SMZ. Basalts from the EVZ plot scatter a  $0.02\text{‰}$  range showing no correlation.

Apart from the classification of the Gakkel basalts in primitive and evolved magmas, all basalts have high  $\text{Na}_{8.0}$ , which is the Na content of melts calculated at 8 wt.% MgO (Klein and Langmuir, 1987). The  $\text{Na}_{8.0}$  values show a negative trend with  $\text{Zr}/\text{Nb}$ , which is an indicator for mantle fertility (Figure 5.2).



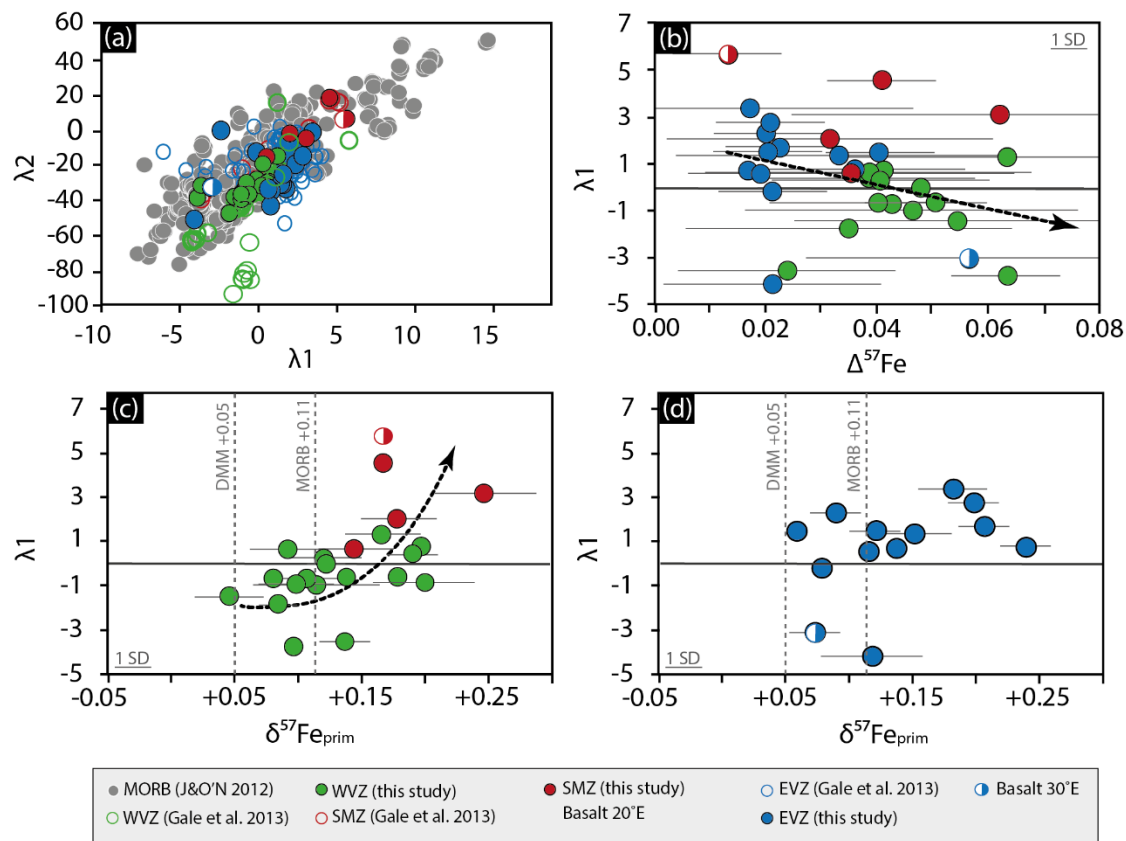
**Figure 5.2 -  $\text{Zr}/\text{Nb}$  versus  $\text{Na}_{8.0}$  and  $\delta^{57}\text{Fe}_{\text{prim}}$ .** With decreasing  $\text{Zr}/\text{Nb}$  increases the degree of partial melting ( $\text{Na}_{8.0}$ ) and  $\delta^{57}\text{Fe}_{\text{prim}}$  (b). Basalts from the SMZ have the lowest degree of partial melting linked to enriched mantle source (high  $\delta^{57}\text{Fe}_{\text{prim}}$ ). In comparison, basalts from the EVZ tend have a low degree of partial melting, which could be linked to the slow spreading rate and its lower geothermal gradient causing focussed melting from a deeper melt pool compared to the WVZ basalts that show higher degree of partial melting. The EVZ basalts show a wide range of  $\delta^{57}\text{Fe}_{\text{prim}}$  related to an extreme heterogeneous source. It has to be noted that solely basalts with  $\text{MgO} < 8.0\text{ wt. \%}$  were plotted and corrected for  $\text{Na}_{8.0}$ .

Figure 5.3 shows the REE pattern of basalts described as  $\lambda_1$  and  $\lambda_2$ , where  $\lambda_1$  describes the shape of the REE's and  $\lambda_2$  their curvature (O'Neill, 2016). Basalts from the WVZ show on average lower  $\lambda_1$  and  $\lambda_2$  values, compared to basalts from the SMZ displaying higher  $\lambda_1$  and  $\lambda_2$  values, meaning a slight depletion of LREE over HREE of the WVZ basalts. Basalts from the EVZ display low  $\text{Na}_{8.0}$ , similar to the SMZ basalts, but show a larger variability in  $\text{Zr}/\text{Nb}$ , indicating heterogeneity of the MORB source. Overall, the EVZ basalts show intermediate REE pattern plotting between the  $\lambda_1$  and  $\lambda_2$  range of the WVZ and the SMZ basalts.

### 5.3.2 Iron isotopes

The iron isotope composition of the Gakkel basalts range in  $\delta^{57}\text{Fe}$  from  $+0.10\text{‰} \pm 0.01\text{‰}$  to  $+0.31\text{‰} \pm 0.04\text{‰}$  (Table 5.1), with basalts from the SMZ displaying, on average, more positive  $\delta^{57}\text{Fe}$  values with  $+0.22\text{‰} \pm 0.02\text{‰}$  than basalts from the WVZ and the EVZ with  $\delta^{57}\text{Fe}$  values  $+0.17\text{‰} \pm 0.03\text{‰}$  and  $+0.16\text{‰} \pm 0.02\text{‰}$ , respectively (Figure 5.4). In order to assess the spread of Fe isotopes from the Gakkel Ridge MORBs, our results were compared to global MORBs (Teng et al., 2013) and basalts from the Lau Basin (Nebel et al., 2018). This allows for a direct comparison

with MORBs from faster spreading ridges and back-arc basin mantle to investigate (i) the role spreading rate, tentatively related to suboceanic magma chambers (Rubin and Sinton, 2007) and (ii) mantle source heterogeneity, such as metasomatic overprint or melt depletion as commonly found in subduction zones.



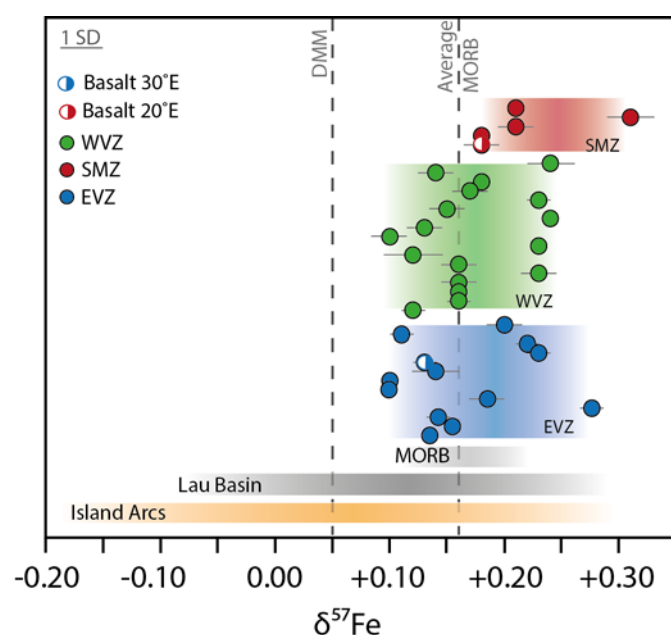
**Figure 5.3 - Rare Earth Element (REE) pattern versus  $\delta^{57}\text{Fe}_{\text{prim}}$ .** (a)  $\lambda_2$  versus  $\lambda_1$  shows that the WVZ basalts have lower values than basalts from the SMZ. Basalts from the EVZ plot between the WVZ and SMZ basalts. (b) Data show co-variation between  $\lambda_1$  and  $\Delta^{57}\text{Fe}$ . (c) and (d) show the dependence on  $\delta^{57}\text{Fe}_{\text{prim}}$  with  $\lambda_1$ . Basalts from the WVZ and the MZ display an exponential increase with  $\delta^{57}\text{Fe}_{\text{prim}}$ , whereas EVZ shows no co-variation. The two grey vertical dashed lines indicate a comparison with the DMM (Craddock et al., 2013) and MORB (Teng et al., 2013).  $\lambda_2$  versus  $\lambda_1$  has been calculated using the method of O'Neill (2016). MORB data have been plotted for comparison and calculated from Jenner and O'Neill (2012).

Figure 5.4 highlights that the iron isotope composition of the Gakkel MORBs spread twice as much as previously reported MORBs. These variations are low compared to basalts from the Lau Basin, which range by 0.4 ‰ (Nebel et al., 2018), and global arc basalts with variations of 0.5 ‰ (-0.19 ‰  $\pm$  0.03 ‰ to +0.31 ‰  $\pm$  0.09 ‰, Foden et al., 2018). During the magmatic ascend from the source to the crust, crystal fractionation, predominantly olivine from primitive melts, will result in a melt residue that is potentially more oxidised and isotopically modified. As melt fractionates *en route* to surface, the ratio of ferrous ( $\text{Fe}^{2+}$ ) versus ferric ( $\text{Fe}^{3+}$ ) iron decreases, and the physical removal of a preferential  $\text{Fe}^{2+}$ -species is accompanied by increasing  $\delta^{57}\text{Fe}$  (Teng et al., 2008; Teng et al., 2013; Weyer, 2008; Weyer and Ionov, 2007; Williams et al., 2004). To correct for this fractionation, to assess source variability, as outlined in section 5.2, olivine is incrementally added

to the melt until a composition that is in chemical equilibrium with a mantle of  $Mg\# = 74$  is achieved. This not only allows an approximation for the true Fe isotope nature of the melts at mantle depth ( $\delta^{57}Fe_{prim}$ ), but also creates a calculated measure for isotope fractionation through crystal fractionation, expressed here as  $\Delta^{57}Fe$  ( $\Delta^{57}Fe = \delta^{57}Fe - \delta^{57}Fe_{prim}$ ; Nebel et al., 2018; Sossi et al., 2016). Results show that the most primitive basalts ( $MgO \sim 10$  wt.%) exhibit a low  $\Delta^{57}Fe = 0.02$  ‰, and that the more evolved ( $MgO \sim 7$  wt.%) basalts yield expectedly higher  $\Delta^{57}Fe$  of  $> 0.04$  ‰; with the EVZ hosting the most primitive basalts and SMZ – WVZ the more evolved ones (Figure 5.2).

## 5.4 Discussion

Iron isotope retain a memory of magmatic processes that effects melts *en route* to the surface (Nebel et al., 2018; Teng et al., 2008; Teng et al., 2013; Weyer, 2008), linking traditional



**Figure 5.4 - Comparison of  $\delta^{57}Fe$  from different locations and tectonic settings.** The colour coding indicates the differences between each segment, location and tectonic setting. The  $\delta^{57}Fe$  of MORB composition, calculated from Teng et al. (2013), and depleted MORB mantle (Craddock et al., 2013) are given as a reference. Lau Basin data is from Nebel et al. (2018) and island arc data is from Foden et al. (2018).

major and trace element geochemistry with Fe isotopes offers additional insights into magmatic differentiation processes. In the following the effect of fractional crystallisation and source variability on Fe isotope composition will be discussed.

### 5.4.1 The effect of fractional crystallisation on Fe isotope composition

To discuss the effect of fractional crystallization of the basalts, we differentiate between evolved and primitive basaltic melt. As described in the results section, a higher  $\Delta^{57}Fe$  ( $> 0.04$  ‰) represents a more evolved melt, meaning that olivine has been removed

from the melt. By removing olivine from the system, the fractionated melt inherits more ferric iron and develops a positive  $\delta^{57}Fe$  and consecutively a higher  $\Delta^{57}Fe$ . On the other hand, basalts with low  $\Delta^{57}Fe$  ( $< 0.04$  ‰) are interpreted to reflect a more primitive melt. Primitive melts are further characterised by a high  $Mg\#$  (Shaw et al., 2010). Figure 5.5 shows that basalts with a low  $\Delta^{57}Fe$ , in particular the EVZ basalts and partially the SMZ basalts, have a high  $Mg\#$ . Both ( $\Delta^{57}Fe$  and  $Mg\#$ ), however, show an inverse correlation with increasing spreading rate, suggesting that fractional crystallisation has a greater influence on the Fe isotope composition at faster spreading ridges

compared to those with a slower spreading rate (Figure 5.5). Hereafter, we elaborate the differences in  $\Delta^{57}\text{Fe}$  in relation to different spreading rates (ultraslow and slow).

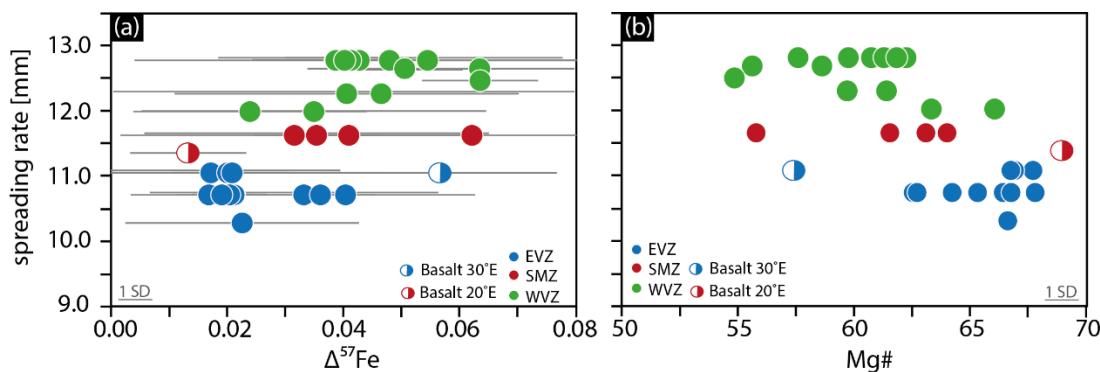


**Figure 5.5 - Spreading rate dependency on  $\Delta^{57}\text{Fe}$  and Mg#.** (a)  $\Delta^{57}\text{Fe}$  co-varies positively with increasing spreading rate, whereby magmatic processes at a spreading rate from 15 mm/a should be similar to the results from the WVZ. (b) Mg# decreases with increasing spreading rate suggesting an increase in magmatic differentiation. Changes in magmatic processes are visible within a spreading-rate variability of 3 mm/a.

Spreading ridges  $> 15$  mm/a are characterised by a high magmatic activity, higher mantle potential temperature and mid-crustal magma chambers (Brandl et al., 2016; Rubin and Sinton, 2007). Even though the spreading rate at the WVZ is slightly lower, basalts from the WVZ show characteristics of such fast spreading regimes, such as higher magmatic activity, thick oceanic crust and potential existence of a magma lens in mid-crustal levels. Seemingly, this translates into Fe isotopes, where WVZ basalts indicate a much stronger control of crystal fractionation ( $\Delta^{57}\text{Fe} > 0.04$  ‰; lower Mg#) than basalts from the EVZ and the SMZ. The WVZ ridge segment is also characterised by a high magmatic activity (Michael et al., 2003; Schmidt-Aursch and Jokat, 2016). We, therefore, suggest that melts at the WVZ travel through a mid-crustal magma lens or crystal zone, as suggested by Bennett et al. (2019), *en route* to the surface (Figure 5.6 profile A – A'). The higher magmatic activity at the WVZ could be further related to higher mantle temperatures beneath the ridge segment, which in turn increases melt production and promotes the formation of a magma chambers (Rubin and Sinton, 2007; Schmidt-Aursch and Jokat, 2016). Within a magma chamber crystal fractionation is accompanied by magmatic recharge and magma mixing (O'Neill and Jenner, 2012). Even though continuous magma recharge and homogenisation occurs in these chambers, the higher  $\Delta^{57}\text{Fe}$  of  $> 0.04$  ‰ indicate that crystal fractionation is a dominant process and that melts are tapped at various stages of this process.

Basalts with a  $\Delta^{57}\text{Fe}$  of  $< 0.04$  ‰ are linked to a spreading rate slower than  $< 12$  mm/a and occur in areas of low magmatic activity. The latter is typical for ultraslow-spreading rates (Dick et al., 2003; Michael et al., 2003; Rubin and Sinton, 2007), because of colder thermal upper mantle conditions (Bown and White, 1994; White et al., 2001). The cooler mantle thermal conditions causes the formation of a permeability barrier in deeper levels (i.e., in the upper mantle), where

melts may be pooled (Wanless et al., 2014). From there the melt can ascend rapidly to the crust with minor crystal fractionation or wall-rock-interaction (Figure 5.6 profile B-B'). The rapid melt transport suggest that primitive magma compositions can be preserved (Figure 5.6 profile B-B'). Notable is that basalts from the EVZ show high Mg# and no co-variation of trace elements (V/Sc; Figure 5.1e) with the degree of fractionation ( $\Delta^{57}\text{Fe}$ ). We therefore suggest that the Fe isotope compositions of the EVZ basalts closely resemble those of their mantle source with only minor crystal fractionation, wall-rock-interaction, and most critically no homogenization in suboceanic magma slurries.

Two basalts, one at 20°E and one at 30°E outlie from their respective ridge segment. The first sample at 20°E is from the SMZ (PS 59 251-4;  $\Delta^{57}\text{Fe} = 0.01 \text{ ‰}$ ) and shows high Mg#, Ni, TiO<sub>2</sub> and V/Sc ratio (Figure 5.1). The high Mg# and Ni content reflects a primary melt composition with a source having a higher modal amount of olivine. Titanium and V are preferably incorporated in pyroxene. The higher TiO<sub>2</sub> content and V/Sc suggest a higher modal amount of pyroxene. We interpret this sample to reflect the composition of a cumulate such as an olivine-rich gabbro. Cumulates typically occur in magma chambers or in small local magma lenses (Figure 5.6 profile B - B') at lower crustal level (Ross and Elthon, 1993). Melt ascending from lower crustal levels to the surface does not undergo much crystal fractionation or wall rock interaction, due to a rapid melt transport. The latter would explain the low  $\Delta^{57}\text{Fe}$  of 0.01 ‰, calculated for this sample. The second sample from the EVZ at 30°E shows a higher degree of fractionation ( $\Delta^{57}\text{Fe} > 0.04 \text{ ‰}$ ) and generally plots within the WVZ basalt range (Figure 5.1). The area around 30°E could be linked to an occurrence of a melt lens or crystal mush zone in crustal levels (Bennett et al., 2019), which increases  $\Delta^{57}\text{Fe}$  (as suggested for WVZ basalts).

#### ***5.4.2 Mantle source variability at the Gakkel Ridge***

As briefly discussed in the section above, crystal fractionation affects the iron isotope composition by 0.01 ‰ to 0.06 ‰. The iron isotope composition of the Gakkel MORBs, however, range over 0.2 ‰. The broad  $\delta^{57}\text{Fe}$  range suggest that the isotope variability must be inherited from a heterogeneous mantle source. To discuss the effect of source heterogeneity in the context of radiogenic isotope systematics, the samples are separated into two different regions, based on Sr and Pb isotopes (Goldstein et al., 2008). The first region is the Western Gakkel Ridge region, comprised of the WVZ and the SMZ, and the second region is the Eastern Gakkel Ridge region, solely comprised of the EVZ.

##### ***5.4.2.1 The Western Gakkel Ridge region***

Basalts from the WVZ and the SMZ differ in their major and trace element compositions (Figures 5.2 and 5.3), which may be related to mantle source heterogeneity. The WVZ basalts have a slightly low Na<sub>8,0</sub>, lower  $\delta^{57}\text{Fe}_{\text{prim}}$  and are slightly depleted in LREE compared to basalts from the

SMZ. Co-variations of REE pattern with  $\delta^{57}\text{Fe}_{\text{prim}}$ , the latter being the isotope signature of the mantle source, suggest that neither olivine nor pyroxene fractionation affects LREE/HREE composition of the basalts. Instead, the data suggest that the differences of the REE pattern are inherited from the mantle source. Dick and Zhou (2014) suggested that a high  $\text{Na}_{8.0}$  reflects source depletion by pre-existing partial melting events. Figure 5.2 indicates co-variations between decreasing  $\text{Na}_{8.0}$  and decreasing Zr/Nb. Combined, it is inferred here that the SMZ samples the most depleted mantle source, whereas the WVZ contains a more fertile, ordinary MORB source.

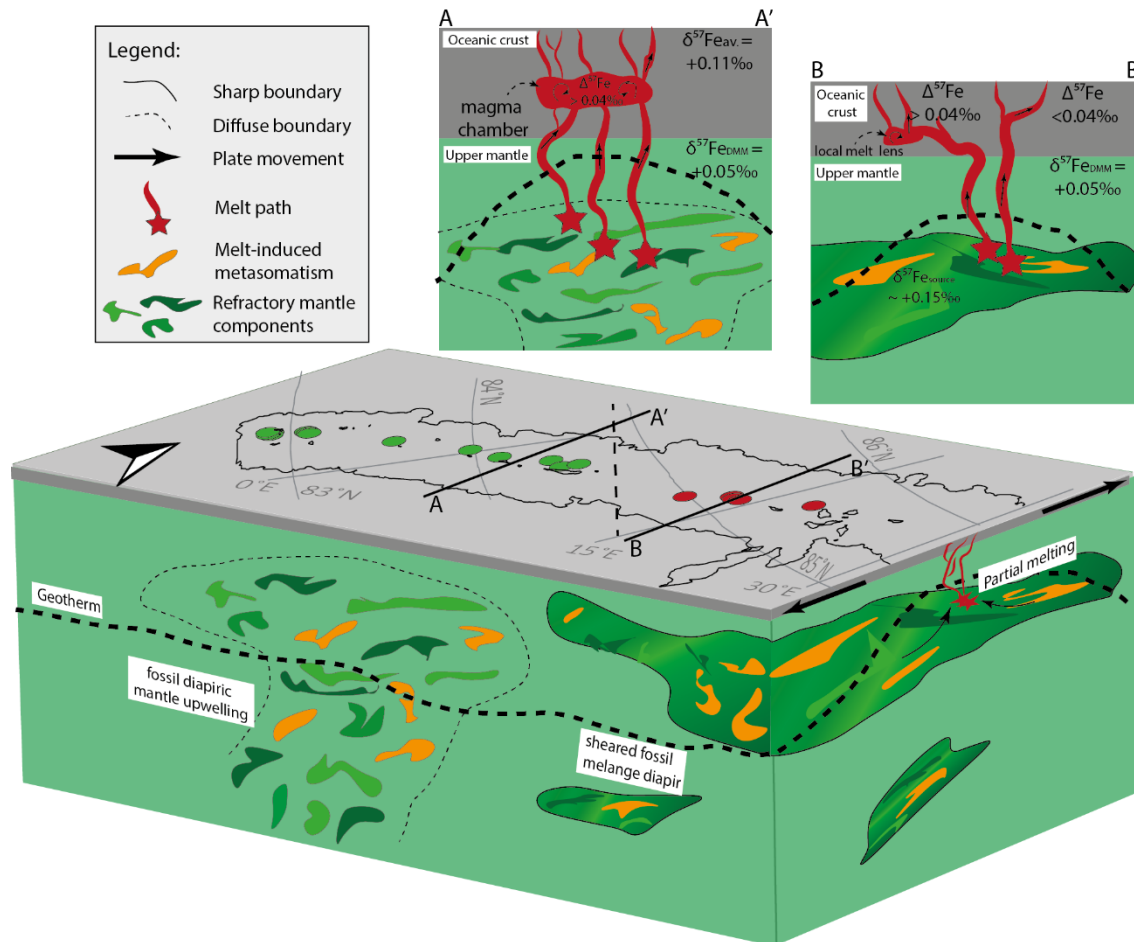


**Figure 5.6 - Simplified model (after Brandl et al., 2016; Nebel et al., 2015) of the upper mantle beneath the Western Gakkel Ridge region.** Basalts from the SMZ (red dots) sample a metasomatic enriched mantle domain, as suggested in chapter 3 it is possible that the SMZ resemble a fossil *mélange* diapir, from a pre-existing subduction zone in this area 120 Ma, whereas basalts from the WVZ sample upwelling mantle from a pre-existing back-arc basin (chapter 3). Two profiles in the upper part of the figure represent the melting process beneath the ridge segment. **Profile A-A'** shows a transect through the WVZ. Based on findings from this contribution, the profile shows a mid-crustal magma chamber that formed due to higher magmatic activity. Within the magma chamber homogenisation and crystal fractionation occurs which affects the iron isotope composition. Instead, **profile B-B'** represents the magmatic process for the EVZ and the SMZ. See text for further explanation. It has to be noted that the crustal thickness in the sketches between A – A' (thick crust – 4 to 7 km) and B – B' (thin crust – ~1.5 km) is different, because of difference in magmatic activity.

The isotopically heavy  $\delta^{57}\text{Fe}_{\text{prim}}$  ( $> 0.15$  ‰) in the SMZ and the WVZ basalts exceed values for other MORB samples outside analytical scatter and are thus due to an enrichment of heavy Fe isotopes in the mantle. Whilst mantle depletion, as indicated by  $\text{Na}_{8.0}$  and Zr/Nb lowers the Fe

isotope signatures of the mantle (Foden et al., 2018; Nebel et al., 2013; Nebel et al., 2018), enrichment in heavy Fe isotopes requires a physical component added to the mantle source of the basalts, and signals a direct disconnect between the two parameters. The effect of partial melting, even for very low degrees, is too small to elevate primitive melts to  $> 0.05$  ‰. This is also true for more oxidised mantle sections, where higher  $\text{Fe}^{3+}$ , which is considered to be more incompatible during mantle melting than  $\text{Fe}^{2+}$  (Canil et al., 1994; O'Neill et al., 2018), is more prevalent.

A solution to this conundrum and a feasible scenario for heavy Fe isotopes in the mantle are pyroxenites (Williams and Bizimis, 2014). Experimental and field studies have shown that small modal amounts ( $< 4$  %) of pyroxenite within a MORB source can significantly affect the trace element budget of extracted melts, in particular LREE (Hirschmann and Stolper, 1996; Lambart et al., 2013; Pertermann and Hirschmann, 2003; Warren, 2016). Hence, it is inferred here that pyroxenite is the reason for the elevated LREE in basalts with elevated  $\delta^{57}\text{Fe}_{\text{prim}}$ .

The source for the pyroxenitic assemblages with increased  $\delta^{57}\text{Fe}$  remain enigmatic. Clear is that metasomatic, likely melts or fluids must have enriched the MORB source in  $\text{Fe}^{3+}$ . Melting of these enriched mantle domains resulted in more positive  $\delta^{57}\text{Fe}$  than ordinary mantle. Metasomatic enrichment of the mantle must have occurred prior to mid-ocean ridge genesis, since heavy iron isotope signatures are not only prevalent in the SMZ but also the WVZ. Spreading rate is, however, not related to this feature, but rather associated to magma lenses that are seemingly not capable of erasing them.

#### 5.4.2.2 The Eastern Gakkel Ridge region

The Eastern Gakkel Ridge regions appears more heterogeneous in  $\delta^{57}\text{Fe}_{\text{prim}}$  than the WVZ and the SMZ. The iron isotopes composition of the EVZ ranges between  $+0.06$  ‰ to  $+0.24$  ‰, confirming the heterogeneous character of the mantle below EVZ ridge segment from other studies (Liu et al., 2008; Wanless et al., 2014). The variation in  $\delta^{57}\text{Fe}_{\text{prim}}$  does not only occur along the entire ridge segment, but also in samples from a single dredge. At  $61^\circ\text{E}$ , the iron isotope composition ranges from DMM-like values to highly enriched mantle values, implying that chemical heterogeneities also exist on a smaller scale (km - range). Magma mixing and mingling in suboceanic chambers or lenses potentially erases such heterogeneity (Rubin et al., 2009), such as for basalts from faster spreading segments ( $> 12$  mm/a).

Intriguing is that previous studies (Liu et al., 2008; Stracke et al., 2011) reported mantle sections that are extremely depleted at approximately  $65^\circ\text{E}$ . Melt-depleted mantle at convergent margins extends towards negative  $\delta^{57}\text{Fe}$  ( $< +0.05$  ‰). Basalt from the EVZ, however, do not show such light values in  $\delta^{57}\text{Fe}_{\text{prim}}$ . It remains unclear why this signature is not reflected in Fe isotopes, but such depletion is either also of localised nature, a rather unusual, rare find or do not contribute substantially to melt extruded at the ridge above (Byerly and Lassiter, 2014). Alternatively ultra-

depleted mantle lithologies are more abundant, but with very spatial limitations and no effect on  $\delta^{57}\text{Fe}$ .

## 5.5 Conclusion

This study assesses the effect of magmatic differentiation and mantle source heterogeneity on the Fe isotope composition of MORBs from the ultraslow-spreading Gakkel Ridge. We draw the following conclusions:

- (1) Crystal fractionation (monitored through  $\Delta^{57}\text{Fe}$ ) affects the  $\delta^{57}\text{Fe}$  by at least  $\sim 0.04$  ‰ at faster spreading rates ( $> 12$  mm/a). This process is ascribed here to the development of magma chambers in mid-crustal levels, where melt undergoes magma mixing and fractionation (Brandl et al., 2016; Rubin and Sinton, 2007). At ultraslow-spreading regimes with  $< 12$  mm/a,  $\delta^{57}\text{Fe}$  of basalts are mainly affected by its MORB source.
- (2) Mantle source variability (on large and small scale) effects the iron isotope composition causing a larger variability in  $\delta^{57}\text{Fe}$ , which is also reflected in trace element abundances and is not entirely erased through magma chamber processes.
- (3) Gakkel Ridge basalts extend the existing MORB database towards heavier values and demonstrate that MORB sources contain enriched mantle components (such as pyroxenite), which contribute to geochemical variation (especially REE) as suggested in previous studies (Byerly and Lassiter, 2014; Hirschmann and Stolper, 1996; Rosenthal et al., 2018). However, more detailed studies are required to further elucidate the role of pyroxenites in the source of MORB and their relation to Fe isotope systematics.

## 5.6 Acknowledgements

The authors would like to thank Jay Thompson from the University of Tasmania for undertaking major element analysis and Massimo Raveggi for his help with trace element analysis. This work was supported by an ARC grant FT140101062 to O.N. H. Dick was supported by US National Science Foundation (Grant No. OCE-MG&G 8371300). M.R. was supported by a graduate scholarship of Monash University and the SEAE. The authors would like to thank Elmar Albers and Wolfgang Bach for providing additional samples for this project.

## 5.7 References

- Agranier, A. et al., 2005. The spectra of isotopic heterogeneities along the mid-Atlantic Ridge. *Earth and Planetary Science Letters*, 238(1): 96-109.
- Beard, B.L., Johnson, C.M., 2004. Inter-mineral Fe isotope variations in mantle-derived rocks and implications for the Fe geochemical cycle. *Geochimica et Cosmochimica Acta*, 68(22): 4727-4743.

- Bennett, E.N., Lissenberg, C.J., Cashman, K.V., 2019. The significance of plagioclase textures in mid-ocean ridge basalt (Gakkel Ridge, Arctic Ocean). *Contributions to Mineralogy and Petrology*, 174(6): 49.
- Blusztajn, J., Shimizu, N., Warren, J.M., Dick, H.J.B., 2014. In-situ Pb isotopic analysis of sulfides in abyssal peridotites: New insights into heterogeneity and evolution of the oceanic upper mantle. *Geology*, 42(2): 159-162.
- Bown, J.W., White, R.S., 1994. Variation with spreading rate of oceanic crustal thickness and geochemistry. *Earth and Planetary Science Letters*, 121(3): 435-449.
- Brandl, P.A. et al., 2016. The timescales of magma evolution at mid-ocean ridges. *Lithos*, 240-243: 49-68.
- Byerly, B.L., Lassiter, J.C., 2014. Isotopically ultradepleted domains in the convecting upper mantle: Implications for MORB petrogenesis. *Geology*, 42(3): 203-206.
- Canil, D. et al., 1994. Ferric iron in peridotites and mantle oxidation states. *Earth and Planetary Science Letters*, 123(1): 205-220.
- Chauvel, C., Lewin, E., Carpentier, M., Arndt, N.T., Marini, J.-C., 2008. Role of recycled oceanic basalt and sediment in generating the Hf–Nd mantle array. *Nature Geoscience*, 1(1): 64-67.
- Cheng, T., Nebel, O., Sossi, P.A., Chen, F.K., 2014. Refined separation of combined Fe-Hf from rock matrices for isotope analyses using AG-MP-1M and Ln-Spec chromatographic extraction resins. *Methodsx*, 1: 144-150.
- Coogan, L.A., O'Hara, M.J., 2015. MORB differentiation: In situ crystallization in replenished-tapped magma chambers. *Geochimica et Cosmochimica Acta*, 158: 147-161.
- Craddock, P.R., Dauphas, N., 2011. Iron Isotopic Compositions of Geological Reference Materials and Chondrites. *Geostandards and Geoanalytical Research*, 35(1): 101-123.
- Craddock, P.R., Warren, J.M., Dauphas, N., 2013. Abyssal peridotites reveal the near-chondritic Fe isotopic composition of the Earth. *Earth and Planetary Science Letters*, 365: 63-76.
- Dick, H.J.B., Lin, J., Schouten, H., 2003. An ultraslow-spreading class of ocean ridge. *Nature*, 426(6965): 405-412.
- Dick, H.J.B., Zhou, H., 2014. Ocean rises are products of variable mantle composition, temperature and focused melting. *Nature Geoscience*, 8(1): 68-74.
- Foden, J., Sossi, P.A., Nebel, O., 2018. Controls on the iron isotopic composition of global arc magmas. *Earth and Planetary Science Letters*, 494: 190-201.
- Gale, A., Dalton, C.A., Langmuir, C.H., Su, Y., Schilling, J.-G., 2013. The mean composition of ocean ridge basalts. *Geochemistry, Geophysics, Geosystems*, 14(3): 489-518.
- Goldstein, S.L. et al., 2008. Origin of a 'Southern Hemisphere' geochemical signature in the Arctic upper mantle. *Nature*, 453(7191): 89-93.
- Hirschmann, M.M., Stolper, E.M., 1996. A possible role for garnet pyroxenite in the origin of the "garnet signature" in MORB. *Contributions to Mineralogy and Petrology*, 124(2): 185-208.
- Hofmann, A.W., 2014. Sampling Mantle Heterogeneity through Oceanic Basalts: Isotopes and Trace Elements. *Treatise on geochemistry*: 67-101.
- Jenner, F.E., O'Neill, H.S.C., 2012. Analysis of 60 elements in 616 ocean floor basaltic glasses. *Geochemistry, Geophysics, Geosystems*, 13(2): Q02005.
- Jochum, K.P., Stoll, B., Herwig, K., Willbold, M., 2007. Validation of LA-ICP-MS trace element analysis of geological glasses using a new solid-state 193 nm Nd:YAG laser and matrix-matched calibration. *J. Anal. At. Spectrom.*, 22(2): 112-121.
- Klein, E.M., Langmuir, C.H., 1987. Global correlations of ocean ridge basalt chemistry with axial depth and crustal thickness. *Journal of Geophysical Research: Solid Earth*, 92(B8): 8089-8115.
- Lambart, S., Laporte, D., Schiano, P., 2013. Markers of the pyroxenite contribution in the major-element compositions of oceanic basalts: Review of the experimental constraints. *Lithos*, 160-161: 14-36.
- Liu, C.Z. et al., 2008. Ancient, highly heterogeneous mantle beneath Gakkel Ridge, Arctic Ocean. *Nature*, 452(7185): 311-6.
- Longerich, H.P., Jackson, S.E., Gunther, D., 1996. Inter-laboratory note. Laser ablation inductively coupled plasma mass spectrometric transient signal data acquisition and analyte concentration calculation. *Journal of Analytical Atomic Spectrometry*, 11(9): 899-904.
- Mallick, S., Salters, V.J.M., Langmuir, C.H., *Geochemical Variability Along The Northern East Pacific Rise: Coincident Source Composition and Ridge Segmentation. Geochemistry, Geophysics, Geosystems*, 0(ja).
- Meyzen, C.M. et al., 2007. Isotopic portrayal of the Earth's upper mantle flow field. *Nature*, 447(7148): 1069-74.
- Michael, P.J. et al., 2003. Magmatic and amagmatic seafloor generation at the ultraslow-spreading Gakkel Ridge, Arctic Ocean. *Nature*, 423(6943): 956-961.

- Nebel, O., Arculus, R.J., Sossi, P.A., Jenner, F.E., Whan, T.H.E., 2013. Iron isotopic evidence for convective resurfacing of recycled arc-front mantle beneath back-arc basins. *Geophysical Research Letters*, 40(22): 5849-5853.
- Nebel, O. et al., 2015. Redox-variability and controls in subduction zones from an iron-isotope perspective. *Earth and Planetary Science Letters*, 432: 142-151.
- Nebel, O. et al., 2018. Iron isotope variability in ocean floor lavas and mantle sources in the Lau back-arc basin. *Geochimica et Cosmochimica Acta*, 241: 150-163.
- O'Neill, H.S., Jenner, F.E., 2012. The global pattern of trace-element distributions in ocean floor basalts. *Nature*, 491(7426): 698-704.
- O'Neill, H.S.C., Berry, A.J., Mallmann, G., 2018. The oxidation state of iron in Mid-Ocean Ridge Basaltic (MORB) glasses: Implications for their petrogenesis and oxygen fugacities. *Earth and Planetary Science Letters*, 504: 152-162.
- O'Neill, H.S.C., 2016. The Smoothness and Shapes of Chondrite-normalized Rare Earth Element Patterns in Basalts. *Journal of Petrology*, 57(8): 1463-1508.
- Okino, K. et al., 2002. Preliminary analysis of the Knipovich Ridge segmentation: influence of focused magmatism and ridge obliquity on an ultraslow-spreading system. *Earth and Planetary Science Letters*, 202(2): 275-288.
- Pertermann, M., Hirschmann, M.M., 2003. Partial melting experiments on a MORB-like pyroxenite between 2 and 3 GPa: Constraints on the presence of pyroxenite in basalt source regions from solidus location and melting rate. *Journal of Geophysical Research: Solid Earth*, 108(B2).
- Phipps Morgan, J., Ghen, Y.J., 1993. Dependence of ridge-axis morphology on magma supply and spreading rate. *Nature*, 364: 706.
- Poitrasson, F., Delpech, G., Grégoire, M., 2013. On the iron isotope heterogeneity of lithospheric mantle xenoliths: implications for mantle metasomatism, the origin of basalts and the iron isotope composition of the Earth. *Contributions to Mineralogy and Petrology*, 165(6): 1243-1258.
- Rosenthal, A. et al., 2018. Phase relations and melting of nominally 'dry' residual eclogites with variable CaO/Na<sub>2</sub>O from 3 to 5 GPa and 1250 to 1500 °C; implications for refertilisation of upwelling heterogeneous mantle. *Lithos*, 314-315: 506-519.
- Ross, K., Elthon, D., 1993. Cumulates from strongly depleted mid-ocean-ridge basalt. *Nature*, 365(6449): 826-829.
- Rubin, K.H., Sinton, J.M., 2007. Inferences on mid-ocean ridge thermal and magmatic structure from MORB compositions. *Earth and Planetary Science Letters*, 260(1-2): 257-276.
- Rubin, K.H., Sinton, J.M., MacLennan, J., Hellebrand, E., 2009. Magmatic filtering of mantle compositions at mid-ocean-ridge volcanoes. *Nature Geoscience*, 2: 321.
- Sauter, D. et al., 2004. Focused magmatism versus amagmatic spreading along the ultra-slow spreading Southwest Indian Ridge: Evidence from TOBI side scan sonar imagery. *Geochemistry, Geophysics, Geosystems*, 5(10): n/a-n/a.
- Schmidt-Aursch, M.C., Jokat, W., 2016. 3D gravity modelling reveals off-axis crustal thickness variations along the western Gakkel Ridge (Arctic Ocean). *Tectonophysics*.
- Shaw, A.M., Behn, M.D., Humphris, S.E., Sohn, R.A., Gregg, P.M., 2010. Deep pooling of low degree melts and volatile fluxes at the 85°E segment of the Gakkel Ridge: Evidence from olivine-hosted melt inclusions and glasses. *Earth and Planetary Science Letters*, 289(3-4): 311-322.
- Sossi, P.A., Halverson, G.P., Nebel, O., Eggins, S.M., 2015. Combined Separation of Cu, Fe and Zn from Rock Matrices and Improved Analytical Protocols for Stable Isotope Determination. *Geostandards and Geoanalytical Research*, 39(2): 129-149.
- Sossi, P.A., Nebel, O., Foden, J., 2016. Iron isotope systematics in planetary reservoirs. *Earth and Planetary Science Letters*, 452: 295-308.
- Stracke, A. et al., 2011. Abyssal peridotite Hf isotopes identify extreme mantle depletion. *Earth and Planetary Science Letters*, 308(3-4): 359-368.
- Teng, F.-Z., Dauphas, N., Helz, R.T., 2008. Iron Isotope Fractionation During Magmatic Differentiation in Kilauea Iki Lava Lake. *Science*, 320(5883): 1620-1622.
- Teng, F.-Z., Dauphas, N., Huang, S., Marty, B., 2013. Iron isotopic systematics of oceanic basalts. *Geochimica et Cosmochimica Acta*, 107: 12-26.
- Wanless, V.D., Behn, M.D., Shaw, A.M., Plank, T., 2014. Variations in melting dynamics and mantle compositions along the Eastern Volcanic Zone of the Gakkel Ridge: insights from olivine-hosted melt inclusions. *Contributions to Mineralogy and Petrology*, 167(5).
- Warren, J.M., 2016. Global variations in abyssal peridotite compositions. *Lithos*, 248-251: 193-219.
- Weyer, S., 2008. What Drives Iron Isotope Fractionation in Magma? *Science*, 320(5883): 1600-1601.
- Weyer, S., Ionov, D.A., 2007. Partial melting and melt percolation in the mantle: The message from Fe isotopes. *Earth and Planetary Science Letters*, 259(1-2): 119-133.

- White, R.S., Minshull, T.A., Bickle, M.J., Robinson, C.J., 2001. Melt Generation at Very Slow-Spreading Oceanic Ridges: Constraints from Geochemical and Geophysical Data. *Journal of Petrology*, 42(6): 1171-1196.
- White, W.M., 2015. Isotopes, DUPAL, LLSVPs, and Anekantavada. *Chemical Geology*, 419: 10-28.
- Williams, H.M., Bizimis, M., 2014. Iron isotope tracing of mantle heterogeneity within the source regions of oceanic basalts. *Earth and Planetary Science Letters*, 404: 396-407.
- Williams, H.M. et al., 2004. Iron Isotope Fractionation and the Oxygen Fugacity of the Mantle. *Science*, 304(5677): 1656-1659.
- Williams, H.M. et al., 2009. Fractionation of oxygen and iron isotopes by partial melting processes: Implications for the interpretation of stable isotope signatures in mafic rocks. *Earth and Planetary Science Letters*, 283(1-4): 156-166.
- Williams, H.M. et al., 2018. Interplay of crystal fractionation, sulfide saturation and oxygen fugacity on the iron isotope composition of arc lavas: An example from the Marianas. *Geochimica et Cosmochimica Acta*.
- Zartman, R.E., Haines, S.M., 1988. The plumbotectonic model for Pb isotopic systematics among major terrestrial reservoirs—A case for bi-directional transport. *Geochimica et Cosmochimica Acta*, 52(6): 1327-1339.
- Zindler, A., Hart, S., 1986. Chemical Geodynamics. *Annual Review of Earth and Planetary Sciences*, 14(1): 493-571.

## CHAPTER 6

### *Sulfide undersaturated melts at the ultraslow-spreading Gakkel Ridge, Arctic Ocean*

*Marianne Richter*<sup>\*1,2</sup>, *Oliver Nebel*<sup>1,2</sup>, *Jung-Woo Park*<sup>3</sup>, *James Dottin III*<sup>4</sup>, *Andrew G Tomkins*<sup>2</sup>, *Henry J.B. Dick*<sup>5</sup>, *James Farquhar*<sup>4</sup>

<sup>1</sup> – Isotopia Laboratory, School of Earth, Atmosphere and Environment, Monash University, Clayton, Victoria, 3800, Australia

<sup>2</sup> – School of Earth, Atmosphere and Environment, Monash University, Clayton, Victoria, 3800, Australia

<sup>3</sup> – School of Earth and Environmental Sciences, Seoul National University, Seoul 08826, South Korea

<sup>4</sup> – Department of Geology, University of Maryland, College Park, Maryland, 20740 USA

<sup>5</sup> – Department of Geology and Geophysics, Woods Hole Oceanographic Institution, Woods Hole, Massachusetts, 02543-1539, USA



*This image reflects saturation differences, such as between basalts. Is the basalt S-saturated or S-undersaturated?*

---

*This manuscript is aimed for submission to Earth, Planetary and Science Letters.*

**Abstract**

Ocean floor lavas from mid-ocean ridges are generally considered to be S-saturated. Sulfide saturation in mantle-derived melts is dependent on the melt generation (pressure, temperature) and the melt chemistry; in particular Fe content, the degree of melting and possibly mantle source depletion. Sulfur saturation of erupting ocean floor lavas has long been proposed to be affected by magmatic differentiation. Whether this occurs along a liquid line of descent or in suboceanic magma reservoirs remains unknown. Here, sixteen basalts from the ultraslow-spreading Gakkel Ridge in the Arctic Ocean, have been analysed for their platinum group element (PGE) concentration, of which nine were chosen for stable S isotope analysis with the aim to test if near-primitive MORBs are S-saturated. Ultraslow-spreading ridges produce rare, near-primitive MORBs (defined here with MgO > 8.5 wt.%) that supposedly have not been affected by magma reservoir processes. Our data show that the concentration of I-PGE (Ru-Ir) in near-primitive melt increases towards 8.5 wt.% MgO and then decreases along with magmatic differentiation, coincidental with a sharp drop in Cu concentration. It is proposed that primitive melts below the MgO threshold of 8.5 wt.% are sulfide undersaturated and that the increase in I-PGE concentration attributes to dissolution of monosulfides *en route* to the surface. More evolved erupting lavas appear to have reached S saturation, which is proposed here to be promoted by S incubation in steady-state magma chambers. This scenario is in line with a sudden drop in the Cu concentration, plausibly triggered by the segregation of Cu-sulfide phases at S saturation. We conclude that primitive magmas that rise to the surface are likely S-undersaturated, at least at the ultraslow-spreading Gakkel Ridge. Sulfide saturation, however, is achieved in more evolved MORBs with an S content at sulfide saturation similar to other MORB, proposed here to be associated with recharge-fractionation magma lenses, as observed in some Gakkel lavas.



## 6.1 Introduction

Magma erupting along mid ocean ridges are generally considered to be sulfide saturated (Keays, 1995; Reekie et al., 2019). The saturation in sulfur stems from the fact that mantle melts can solely dissolve ca. 350 ppm S at a pressure of ca. 3 GPa at sulfide saturation (termed sulfide content at sulfide saturation; SCSS) (Mavrogenes and O'Neill, 1999). At a lower pressure of ca. 1 GPa, which is the presumed pressure range for the MORB genesis, and a degree of melting of  $\leq 20\%$  primitive melts can presumably saturate in sulfur that originates from a mantle with ca. 200 - 250 ppm S (Lorand, 1990; O'Neill, 1991). During magma ascent, a drop in pressure and increasing Fe content through olivine fractionation will supposedly elevate the SCSS (Jugo, 2009; O'Neill and Mavrogenes, 2002; Smythe et al., 2017; Wykes et al., 2015). It remains unclear if the degree of fractionation and the associated increase in incompatible S is sufficient to keep melts S-saturated to counterbalance the elevated potential at SCSS. The latter process, however, seems plausible and likely, because of the S-saturated nature of MORB. At present, it is not known whether the S saturation is a function of suboceanic magma reservoirs, in which fractionation, replenishment and evacuation can act as an S incubator, or not.

Platinum group elements (PGE) are siderophile elements and in the absence of free metal have a highly chalcophile character (Bézos et al., 2005; Jenner, 2017; Patten et al., 2013). Together with other chalcophile elements (e.g., Cu, Se, Te), this group of elements are sensitive to the removal of sulfides in melts and are a potential tracer for sulfide saturation along a liquid line of descent (Ding and Dasgupta, 2018; Lee et al., 2012; e.g., Lissner et al., 2014). In the Earth's mantle, PGE's are preferably incorporated in iron-sulfides, tellurides, selenides or forming platinum group minerals (PGM); and can be divided in two sub-groups: I-PGE (Ir – PGE: Os, Ir, Ru) and P-PGE (Pt – PGE: Pt, Pd) (Barnes et al., 2015; Becker et al., 2006; Fiorentini et al., 2010; Fiorentini et al., 2011). During partial melting of the mantle, I-PGE are more compatible than P-PGE and are preferentially retained within the mantle source and incorporated into residual sulfides, PGM (Lorand et al., 2008) or PGE-rich alloys as inclusions in e.g., Cr-spinel (e.g., Ballhaus, 1995; Fleet and Stone, 1991; Lorand et al., 1999; Park et al., 2012), whereas P-PGE become enriched in the melt (Bézos et al., 2005). The decoupling of PGE's during mantle melting and MORB petrogenesis has been the focus in a range of studies (e.g., Bézos et al., 2005; Dale et al., 2008; McDonough and Sun, 1995; Palme and O'Neill, 2014). However, the complex geochemical behaviour of I- vs P-PGE and their affinities for sulfides vs silicates (Fleet et al., 1996; Fleet and Stone, 1991; Peach and Mathez, 1993), external parameter such as temperature, pressure, oxygen fugacity ( $fO_2$ ), sulfur fugacity ( $fS_2$ ) and sulfur availability in the mantle (Ding and Dasgupta, 2017; Ding and Dasgupta, 2018; Fleet and Stone, 1991; Jugo, 2009; Smythe et al., 2017; Williams et al., 2018; Wykes et al.,

2015), and ultimately prior melt depletion add further complexity causing substantial variations in PGE distribution that are, in combination, not well constrained.

In this study, we aim for an improved understanding of PGE behaviour during early MORB petrogenesis, with focus on ultraslow-spreading ridges and possible variable MORB sources. Rare, dredged seafloor basalts from the remote ultraslow-spreading Gakkel Ridge (6 - 15 mm/a) have been investigated for their PGE systematics complemented with S isotopes in selected samples. The ridge is known to be sourced by a heterogeneous mantle source (D'Errico et al., 2016; Goldstein et al., 2008; Liu et al., 2008; Stracke et al., 2011; Warren and Shirey, 2012) and with along-ridge variations in magmatic activity (Dick et al., 2003; Michael et al., 2003). Samples investigated here have previously been analysed for their major and trace elements, radiogenic isotopes (Sr, Pb, Hf) and Fe isotope systematics, making these rocks an ideal suite to investigate different aspects of S saturation.

## 6.2 Geological setting

The ultraslow-spreading Gakkel Ridge in the Arctic Ocean extends for 1200 km from the northeast coast of Greenland to the northwest coast of Siberia and is one of the youngest and least studied mid-ocean ridges on Earth (Dick et al., 2003). The spreading ridge started to open up at around 60 to 30 Ma ago when the continental plates Eurasia – Arctic and Greenland - Svalbard started to break apart (Alvey et al., 2008; Shephard et al., 2013). The Gakkel Ridge is divided in three different segments, the Western Volcanic Zone (WVZ), the Sparsely Magmatic Zone (SMZ) and the Eastern Volcanic Zone (EVZ) (Michael et al., 2003). The WVZ is characterised by a higher magmatic activity linked to a faster spreading rate (12 mm/a), whereas the SMZ and the EVZ have a low magmatic activity related to slower spreading rate ranging from 11 mm/a to 6 mm/a, respectively (Michael et al., 2003).

Besides changes in spreading rate and magmatic activity the Gakkel Ridge is separated into two chemically distinct areas (Goldstein et al., 2008), the Western and the Eastern Gakkel Ridge region. The Western Gakkel Ridge region (WVZ, SMZ) is characterized by more evolved MORBs displaying MgO content of 9.0 – 6.5 wt.% (Gale et al., 2014). Trace element and radiogenic isotope systematics show elevated Ba/Th and high radiogenic  $^{87}\text{Sr}/^{86}\text{Sr}$  and  $^{208}\text{Pb}/^{204}\text{Pb}$  ratios linked to re-enrichment events in the upper mantle region (Goldstein et al., 2008 and chapter 3). MORBs from the Eastern Gakkel Ridge region (EVZ) have primitive MgO values (~ 9.0 to 10.5 wt.%; Gale et al., 2014) and thought to result from congruent mantle melting (Wanless et al., 2014). Hafnium, Os and Pb isotope studies on abyssal peridotites of the Eastern Gakkel Ridge region suggested that the mantle has been affected by depletion and re-enrichment event that occurred 2 Ga (Liu et al., 2008; Stracke et al., 2011; Warren and Shirey, 2012).

## 6.3 Methods

Basalts of known major and trace element, as well as radiogenic isotope composition have been dredged from the ocean floor during five individual expeditions to the Arctic Ocean: Polarstern 59, Polarstern 66, PS 86, Polarstern 101 and Healy 102. Sixteen basalts were chosen for PGE analysis showing unusual high and low Ba/Th, Sr, Pb and Fe isotope signatures of each individual ridge segment from different locations. In total, twenty volcanic glasses from all three ridge segments combined were analysed for major/minor and trace element compositions of which 9 volcanic glass samples with highest and lowest sulfur concentration have been chosen for S-isotope analysis.

### *6.3.1 Major element, trace element and S content of the volcanic glass*

Major and minor (S) element concentration of the twenty volcanic glass fragments, mounted in one-inch epoxy resin discs, were determined using an Electron Microprobe Jeol JXA 8530F (Hyperprobe) at the Commonwealth Science and Industry Research Organisation (CSIRO) in Melbourne. The analyses were performed using an acceleration voltage of 15 kV, an emission current of 70  $\mu$ A and a beam current of 11 nA. The beam diameter was set to 20  $\mu$ m. The major and minor elements were measured using four different crystals: LIF (Fe, Mn), PETJ (P, Ti and K), AI (Na, Mg, Al and Si) and PETM (S). Ten to 12 spots were measured on each sample. The calculated average of all measured spots has been taken as the sulfur content of the volcanic glasses. Uncertainty is given in  $1\sigma$ . Major and minor element data is provided in Table 6.1.

The trace element composition of the volcanic glass were determined in the Monash Isotopia Laboratory at the School of Earth, Atmosphere and Environment. Forty-three trace elements (Na, Mg, Al, Si, Ca, Sc, Ti, V, Cr, Mn, Fe, Co, Ni, Cu, Zn, Ga, Rb, Sr, Y, Zr, Nb, Mo, Cs, Ba, La, Ce, Pr, Nd, Sm, Eu, Gd, Tb, Dy, Ho, Er, Tm, Yb, Lu, Hf, Ta, Pb, Th and U) were analysed using an ASI RESolution SE 193nm ArF excimer laser coupled to ThermoFisher Scientific ICapTQ (RF power = 1548 W; ablation cell gas flow = 550 ml/min He + 0.05 ml/min N<sub>2</sub>; nebulizer gas flow = 1.0049; auxillary gas flow 0.7718 L/min Ar). The oxide production (ThO<sup>+</sup>/Th<sup>+</sup>) rate was kept < 1 % and the Th/U (determined on NIST 610) was ~ 0.98. Five spots with a spot size of 80  $\mu$ m were set on each sample and were analysed using a repetition rate of 10 Hz and an energy density of 3.0 mJ (attenuator 50%). One single analysis comprised of 20 s background, 30 s ablation and 20 s of washout. Blocks of twenty unknowns were bracketed with a block of two to three analyses of NIST 610, NIST 612, BHVO2G, and BCR2G. BCR2G has been used for normalisation. To control the quality and reproducibility of the analysis, NIST 610, NIST 612 and BHVO2G has been used as reference material. Relative standard error (RSE) of Cu and REE for BHVO2G resulted in an uncertainty of 32 % to and < 2 %, respectively. The uncertainty of Cu is fairly large, but does not affect the trend shown in this study. The absolute deviation from the literature value

is on average 40 ppm (Jochum et al., 2005). However, data obtained during the analytical session is coherent with whole-rock basalt trace element data as discussed in chapter 2. Silica (determined by EMPA analysis) has been used as calibration standard. The laser ablation data was acquired in a time-resolved mode and reduced using an MS Excel spreadsheet developed at the Max Planck Institute for Chemistry (MPIC) Mainz, Germany. The data reduction method has been described by Jochum et al. (2007) and Longerich et al. (1996). Data and uncertainty is provided in the Supplementary Data Tables 6.1 and 6.2.

### 6.3.2 Whole rock PGE analysis

Sixteen samples from the Gakkel Ridge were analysed in two analytical sessions for their PGE concentration. Whole rock PGE (Os, Ir, Ru, Pd, Pt) were determined using a Ni-sulfide fire assay isotope dilution method as described by Park et al. (2012). Two grams of the whole rock sample powder has been admixed with, Ni, S and Na borax powder (S252-10, Fisher Scientific). The sample:Ni:S:Na-borax ratio was 10:1:0.5:10. All components were mixed thoroughly together and were spiked with a PGE-Re solution with  $^{99}\text{Ru}$ ,  $^{105}\text{Pd}$ ,  $^{185}\text{Re}$ ,  $^{190}\text{Os}$ ,  $^{191}\text{Ir}$ , and  $^{195}\text{Pt}$ . The admixture was fused in a preheated furnace at 1,100 °C for 20 min. Then, the quenched sample-Ni-sulfide beads were dissolved in 6M HCl and filtered through filter paper prior sample digestion in a mixture of concentrated  $\text{HNO}_3$  and concentrated HCl (aqua regia). After filtering, the solution was dried down to approximately 100  $\mu\text{l}$  and taken up in 5 ml of 2 %  $\text{HNO}_3$  for ICP-MS analysis.

The isotope analyses has been undertaken using a ThermoFisher Scientific ICapQ ICP-MS in the Korea Polar Research Institute, South Korea. The sensitivity of the instrument during the analysis was approximately  $2.5 \times 10^5$  cps/ppb for mass 115. Oxide production rate represented by  $\text{CeO/Ce}$  was  $< 1.9\%$ . Isobaric interferences during the analysis have been determined by analysing single element solutions containing Ni, Cu, Zn, Co, Hf, Mo, Zr, and Ta. The effects of the molecular isobaric interferences have been subtracted using measured argide and oxide production rates. The correction was negligible for all PGE's, but  $^{61}\text{Ni}^{40}\text{Ar}$  and  $^{62}\text{Ni}^{40}\text{Ar}$  interference on  $^{101}\text{Ru}$  and  $^{102}\text{Ru}$ , respectively was substantial for most samples mainly due to low Ru concentrations in the samples. The differences in Ru concentration before and after the correction range from 0.001 ppb to 0.031 ppb. Osmium, Ir, Ru, Pt and Pd concentrations were determined by isotope dilution using  $^{190}\text{Os}/^{189}\text{Os}$ ,  $^{191}\text{Ir}/^{193}\text{Ir}$ ,  $^{99}\text{Ru}/^{101}\text{Ru}$ ,  $^{195}\text{Pt}/^{194}\text{Pt}$  and  $^{105}\text{Pd}/^{108}\text{Pd}$  ratios, respectively. Ruthenium concentrations obtained using  $^{99}\text{Ru}/^{101}\text{Ru}$  and  $^{99}\text{Ru}/^{102}\text{Ru}$  are consistent with each other, exhibiting the validity of the interference correction.

Procedural blanks were determined on sample-free mixture of Ni, S and Na borax breads using 2 g of Na-borax, 0.5 g of Ni and 0.25 g of S. The procedural blank has been determined by an average of three individual analyses and has been then subtracted from the sample data. Average procedural blanks is 12 pg Os, 6.4 pg Ir, 8.9 pg Ru, 172 pg Pt, 82 pg and Pd, 4.3 pg. Below

determination limit calculated by 2 standard deviation of procedural blanks are 11 ppt Os, 3 ppt Ir, 5 ppt Ru, 69 ppt Pt and 17 ppt Pd for 2 g sample. To monitor the accuracy and precision of the analyses, reference sample TDB-1 was measured in each analytical session. The average PGE values for TDB-1 resulted in 0.080 ppb for Os, 0.073 ppb for Ir, 0.176 ppb for Ru, 5.034 ppb for Pt and 27.57 ppb for Pd which are in line with literature values (0.12 – 0.16 ppb for Os; 0.08 ppb – 0.15 ppb for Ir, 0.2 ppb – 0.33 ppb for Ru, 3.7 ppb – 5.8 ppb for Pt and 20 ppb – 25 ppb for Pd; (Meisel and Moser, 2004; Peucker-Ehrenbrink et al., 2003; Plessen and Erzinger, 1998; Tagle and Claeys, 2005), although Os is slightly lower. Furthermore, duplicate analyses were measured for the following samples: HLY102 D011 – 19; HLY 102 D036 – 35; HLY102 D037 – 5; HLY102 D038 – 6; PS59 – 251 -4 and yielded in a relative deviation of < 6% for Ru, Pt, Pd and < 30% for Ir and Os. Sample data and measured reference material values are given in Table 6.2.

### 6.3.3 Sulfur isotope measurement

Nine volcanic glass samples (4 from the WVZ, 2 samples from the SMZ and 3 samples from the EVZ) were processed using procedures similar to that described by Labidi et al. (2012). Circa 1 g of volcanic glass was thoroughly cleaned in an ultrasonic bath to remove any dust particles or iron oxides from the sample prior crushing to a fine powder ( $\sim <63 \mu\text{m}$ ) using a steel mortar and pestle. After crushing, the samples were weighed in and transferred into a Teflon Apparatus. Once in the apparatus, the samples were degassed with  $\text{N}_2$  for  $\sim 15$  minutes. After degassing, the samples were acidified and digested in heated 10 ml of 3.2M  $\text{CrCl}_2$ , 5 ml of 12M  $\text{HCl}$ , and 5 ml of 29M  $\text{HF}$ . The sulfides were released as  $\text{H}_2\text{S}$  and trapped as  $\text{Ag}_2\text{S}$  in an acidic  $\text{AgNO}_3$  trap solution. The captured  $\text{Ag}_2\text{S}$  was then rinsed and centrifuged six times with Milli-Q water and dried overnight in an oven at  $55^\circ\text{C}$ . Once dried, the samples were wrapped in aluminium foil and reacted with  $\text{F}_2$  in heated nickel tubes overnight, to produce  $\text{SF}_6$  (sulfurhexafluoride) The  $\text{SF}_6$  was then purified using a series of cryogenic techniques and a gas chromatograph.

Sulfur isotope compositions were determined using a dual-inlet ThermoFinnigan MAT gas source mass spectrometer in the Department of Geology at the University of Maryland, College Park. The sulfurhexafluoride was measured by monitoring  $\text{SF}_5^+$  ion beams at  $m/z$  of  $127^+$ ,  $128^+$ ,  $129^+$ , and  $131^+$ . Each sample was analysed as nine sets of eight, each 26 second cycles, and normalized to bracketed analyses of a single reservoir of the reference material, IAEA-S1. Uncertainty on the measurements are estimated using the long-term uncertainty ( $2\sigma$ ) of the IAEA-S1 reference material: 0.3‰, 0.008‰, and 0.3‰ for  $\delta^{34}\text{S}$ ,  $\Delta^{33}\text{S}$ , and  $\Delta^{36}\text{S}$  respectively. The data are reported relative to Canyon Diablo Troilite (CDT) using the calibration in Antonelli et al. (2014) and Dottin et al. (2018) for IAEA-S1:  $\delta^{33}\text{S} = -0.091 \text{‰}$ ,  $\delta^{34}\text{S} = -0.401 \text{‰}$ ,  $\delta^{36}\text{S} = -1.558 \text{‰}$ ,  $\Delta^{33}\text{S} = 0.116 \text{‰}$ ,  $\Delta^{36}\text{S} = -0.796 \text{‰}$ . Data and uncertainties are provided in Table 6.1.

Table 6.1 – Major element concentrations and S isotope ratios of the volcanic glasses.

Sample name	Ridge segment	Major element [wt.%]											S [ppm]				S - isotope [‰]			
		Na <sub>2</sub> O	MgO	Al <sub>2</sub> O <sub>3</sub>	SiO <sub>2</sub>	FeO	MnO	SO <sub>3</sub>	CaO	P <sub>2</sub> O <sub>5</sub>	TiO <sub>2</sub>	K <sub>2</sub> O	Total	$\delta^{34}\text{S}$	$\Delta^{34}\text{S}$	$\Delta^{36}\text{S}$	2 $\sigma$	2 $\sigma$	2 $\sigma$	
PS59 274 - 52	EVZ	2.98	8.40	16.71	51.14	8.77	0.16	0.24	10.84	0.07	1.10	0.22	100.62	977	-	-	-	-	-	
PS59 294 - 40	EVZ	3.28	8.80	16.75	49.79	8.42	0.14	0.24	11.06	0.12	1.34	0.12	100.06	964	-	-	-	-	-	
PS59 297 - 11	EVZ	2.73	9.36	17.32	49.28	9.34	0.17	0.24	11.00	0.12	1.01	0.15	100.72	949	-0.17	0.3	0.008	-0.25	0.3	
PS101 186	EVZ	3.20	8.52	16.51	50.60	7.89	0.15	0.22	11.28	0.14	1.30	0.15	99.95	888	-	-	-	-	-	
HLX0102 D61 - 11	EVZ	3.28	8.70	17.01	50.30	7.82	0.16	0.22	10.92	0.14	1.35	0.17	100.07	878	-0.58	0.3	0.023	0.008	0.02	0.3
HLX0102 D59 - 35	EVZ	3.13	8.24	16.61	51.52	8.27	0.15	0.24	10.77	0.19	1.59	0.39	101.09	955	-	-	-	-	-	
HLX0102 D50 - 30	EVZ	3.30	8.40	16.57	50.59	7.65	0.16	0.20	11.09	0.17	1.32	0.36	99.80	810	-0.92	0.3	0.004	0.008	-0.14	0.3
HLX0102 D51 - 15	EVZ	3.12	8.85	16.77	49.85	7.76	0.16	0.21	11.07	0.16	1.33	0.22	99.50	849	-	-	-	-	-	
HLX0102 D38 - 6	SMZ	3.58	7.41	15.67	50.79	8.61	0.15	0.25	10.55	0.18	1.46	0.37	99.01	982	-	-	-	-	-	
HLX0102 D36 - 35	SMZ	3.67	7.29	15.86	52.13	8.27	0.15	0.24	10.06	0.20	1.51	0.63	100.00	945	-0.82	0.3	0.006	0.008	-0.1	0.3
HLX0102 D37 - 5	SMZ	3.98	6.61	15.39	51.64	9.56	0.16	0.27	9.36	0.27	1.76	0.54	99.54	1079	0.28	0.3	0.024	0.008	-0.02	0.3
PS59 216 - 11	WVZ	3.18	7.99	15.34	50.84	9.08	0.18	0.27	11.07	0.14	1.47	0.19	99.75	1087	-	-	-	-	-	-
PS59 216	WVZ	3.13	7.96	15.54	51.46	9.07	0.17	0.27	11.13	0.15	1.48	0.19	100.55	1100	-	-	-	-	-	-
HLX0102 D8 - 12	WVZ	3.13	8.23	15.23	51.29	9.15	0.17	0.27	10.94	0.14	1.47	0.23	100.25	1069	-0.45	0.3	0.021	0.008	-0.17	0.3
HLX0102 D26 - 9	WVZ	3.16	7.89	14.99	50.41	9.63	0.18	0.29	10.78	0.17	1.69	0.14	99.32	1162	-0.84	0.3	0.018	0.008	-0.16	0.3
PS86 - 67	WVZ	3.14	8.10	15.20	51.59	9.29	0.17	0.28	10.74	0.13	1.56	0.25	100.45	1111	-0.66	0.3	0.018	0.008	-0.17	0.3
HLX0102 D11 - 19	WVZ	3.17	7.88	15.40	50.39	8.82	0.16	0.26	10.71	0.15	1.53	0.37	98.86	1056	-0.91	0.3	0.007	0.008	0.16	0.3
PS59 234 - 24	WVZ	3.06	8.53	15.53	51.17	8.94	0.16	0.27	11.05	0.14	1.48	0.18	100.52	1088	-	-	-	-	-	-
PS66 217 - 16	WVZ	3.30	7.11	15.37	50.93	9.24	0.16	0.29	10.60	0.15	1.78	0.41	99.36	1153	-	-	-	-	-	-
PS86 44	WVZ	3.28	8.01	15.30	50.39	9.11	0.15	0.26	10.38	0.16	1.65	0.45	99.13	1023	-	-	-	-	-	-

**Table 6.2 – Trace element, isotope and PGE data of the Gakkel basalts.** *B.D.L* – below detection limit; \*Peucker-Ehrenbrink et al. (2003); Plessen and Erzinger (1998); Tagle and Claeys (2005); Meisel and Moser (2004); 1 – data from chapter 3; 2 – data from chapter 5

Sample name	Ridge segment	Cr [ppm]	Cu [ppm]	Os [ppb]	Platinum group elements (PGE)										$\lambda I$	$\delta I$	$^{87}Sr/^{86}Sr$	$\delta^{57}Fe_{prim}$	2
					Ir [ppb]	Ru [ppb]	Pt [ppb]	Pd [ppb]	Pt/Ru	Pd/Ir	Ru/Ir	Ku/Ir	Ba/Th	1					
HLY0102 D061 - 11	EVZ	368	111	B.D.L.	B.D.L.	0.097	0.052	1.9	-	-	-	-	-	1.1	1.7	-33.7	0.7026378	0.21	0.02
PS 59 274 - 52	EVZ	361	106	B.D.L.	0.034	0.327	0.276	1.2	3.0	9.6	0.4	0.4	71	-0.2	-13.4	-13.4	0.7037942	0.08	0.01
PS 59 297 - 11	EVZ	431	181	B.D.L.	0.087	0.323	0.270	1.2	3.1	9.1	0.4	0.4	116	-2.5	-1.2	0.703281	-	-	
HLY0102 D050 - 30	EVZ	443	146	0.018	0.025	0.332	0.338	1.0	29.3	13.1	2.2	105	3.4	-2.2	0.7027919	0.18	0.02		
PS 59 263 - 26	EVZ	542	112	B.D.L.	B.D.L.	B.D.L.	0.025	-	-	-	-	1017	-3.1	-33.0	0.7027557	0.07	0.06		
PS 59 251 - 4	SMZ	650	99	B.D.L.	0.003	0.140	0.103	1.4	36.5	-	-	107	5.7	6.6	0.7029725	0.17	0.01		
	Rep	650	99	B.D.L.	0.005	B.D.L.	0.010	0.031	0.3	6.6	-	107	5.7	6.6	0.7029725	0.17	0.01		
HLY0102 D038 - 6	SMZ	358	169	B.D.L.	0.013	0.233	0.360	0.6	28.6	10.5	1.8	160	2.1	-1.7	0.703122	0.18	0.03		
	Rep	358	169	B.D.L.	0.009	0.024	0.230	0.354	0.6	37.6	9.7	2.5	160	2.1	-1.7	0.703122	0.18	0.03	
HLY0102 D036 - 35	SMZ	321	75	0.001	0.017	0.032	0.233	1.3	10.0	7.2	1.9	170	4.6	18.5	0.7035195	0.17	0.04		
	Rep	321	75	B.D.L.	0.014	0.034	0.229	1.4	11.8	6.8	2.4	170	4.6	18.5	0.7035195	0.17	0.04		
HLY0102 D037 - 5	SMZ	218	58	B.D.L.	0.004	0.000	0.068	0.111	0.6	30.5	199.0	0.1	129	3.1	-4.6	0.7030885	0.25	0.06	
	Rep	218	58	B.D.L.	B.D.L.	B.D.L.	0.104	-	-	-	-	129	3.1	-4.6	0.7030885	0.25	0.06		
PS 59 224 - 34	WVZ	154	84	B.D.L.	0.002	0.092	0.031	2.9	12.9	-	-	133	1.3	-14.6	0.7036177	0.17	0.06		
HLY0102 D026 - 9	WVZ	333	180	0.056	0.016	0.128	0.222	0.6	13.9	2.8	2.8	109	-1.0	-38.9	0.703043	0.11	0.05		
PS 59 232 - 84	WVZ	311	130	B.D.L.	B.D.L.	0.088	0.025	3.5	-	-	-	181	0.3	-31.4	0.7031812	0.12	0.04		
PS 86 - 67 (VG)	WVZ	284	150	0.030	0.025	0.042	0.071	0.097	0.7	3.9	1.7	156	-0.7	-31.6	0.703148	0.11	0.04		
PS 86 - 044 (VG)	WVZ	292	114	B.D.L.	0.005	0.008	B.D.L.	0.137	-	25.6	-	248	0.7	-29.1	0.703341	0.20	0.04		
PS 66 217-16 (B)	WVZ	286	75	B.D.L.	0.006	0.022	B.D.L.	0.079	-	12.4	-	3.5	219	0.0	-27.9	0.703392	0.12	0.05	
HLY0102 D8 - 12	WVZ	334	96	B.D.L.	B.D.L.	B.D.L.	B.D.L.	-	-	-	-	209	-0.7	-29.7	0.7031857	0.08	0.04		
HLY0102 D011 - 19	WVZ	310	167	0.012	0.015	0.032	0.201	1.3	10.1	6.3	2.1	219	0.6	-29.7	0.7033862	0.09	0.04		
	Rep	310	167	0.018	0.012	0.033	0.197	1.4	12.4	5.9	2.9	219	0.6	-29.7	0.7033862	0.09	0.04		
<b>Reference material</b>																			
TDB-1				0.067	0.083	0.185	4.803	23.196											
TDB-1				0.073	0.083	0.186	4.799	23.196											
TDB-1				0.087	0.055	0.147	5.182	30.269											
TDB-1				B.D.L	0.083	0.193	5.121	29.261											
<b>TDB-1 average</b>				<b>0.076</b>	<b>0.076</b>	<b>0.178</b>	<b>4.976</b>	<b>26.481</b>											
<b>1 <math>\sigma</math></b>				<b>0.010</b>	<b>0.014</b>	<b>0.021</b>	<b>0.204</b>	<b>3.815</b>											
<b>TDB value range*</b>																			
				0.106	0.08 - 0.15	0.2 - 0.33	3.7 - 5.8	20 - 25											

## 6.4 Results

### 6.4.1 Major elements and S content of the volcanic glasses

Similar to whole-rock analyses, volcanic glasses from the Gakkel Ridge show a primitive character of the EVZ samples displaying a high MgO (average of 9.0 wt%) and a low FeO content (average of 8.24 wt.%) (Figure 6.1). The primitive character of the EVZ volcanic glasses is further reflected in their low S concentration ranging between 844 ppm to 977 ppm; conform to previous S analysis on a different sample set (Shaw et al., 2010). In contrary to the EVZ samples, volcanic glasses from the Western Gakkel Ridge (WVZ, SMZ) region display a slightly lower MgO (7.10 – 7.97 wt. %) and slightly higher FeO (8.81 wt.% – 9.15 wt. %).

The evolved character of the samples from the Western Gakkel Ridge region is also reflected in a higher S concentration (> 1000 ppm). From East to West the sulfur concentration in the basalts increases, which could be an effect of increasing crystal fractionation, because FeO increases and MgO decreases with fractionation (Figure 6.1). The S-MgO trend in Figure 6.1b further indicates that the basaltic melt was S-saturated *en route* to the surface, because all samples co-align with the sulfur content at sulfide saturation (SCSS), as calculated by Smythe et al. (2017).

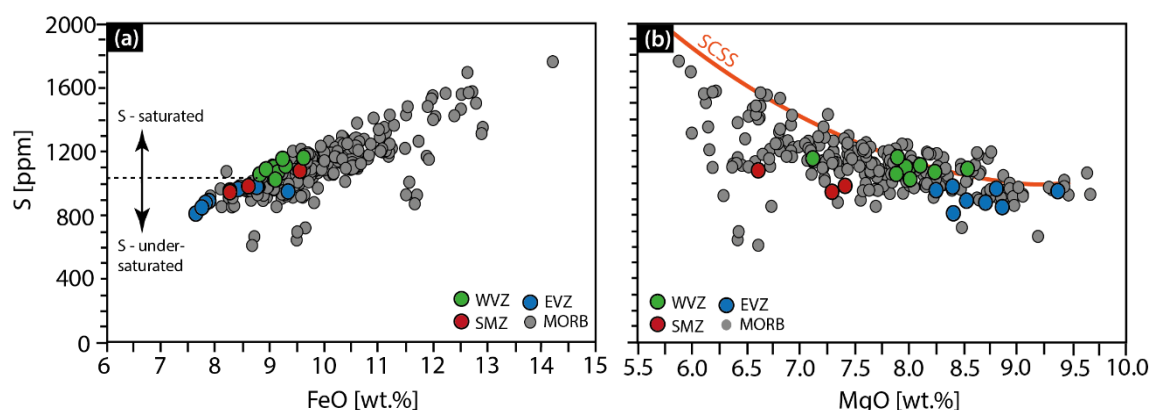


**Figure 6.1 - Sulfur concentration versus FeO and MgO content of the volcanic glasses. (a)** with increasing sulfur content FeO increases. Samples from the WVZ differentiate from the samples from the EVZ and SMZ. The dotted horizontal line marks the S concentration (1040 ppm), where sulfur-saturation occurred. This has been estimated from the Fe isotope systematics. **(b)** The measured volcanic glasses lie on the sulfur concentration at sulfide saturation (SCSS) line. SCSS has been determined by Smythe et al. (2017). Sulfur concentration increases with increasing fractionation. MORB data has been taken from Jenner and O'Neill (2012).

### 6.4.2 Sulfur isotopes

The sulfur isotope ( $\delta^{34}\text{S}$ ) ratio at the Gakkel Ridge does not change significantly between the segments ranging from  $-1.0\text{‰} \pm 0.3\text{‰}$  to  $+0.28\text{‰} \pm 0.3\text{‰}$  with an average of  $-0.56 \pm 0.3\text{‰}$  (Figure 6.2). Sulfur isotopes from the Gakkel Ridge deviate on average by  $+1.0\text{‰}$  from the depleted MORB mantle ( $\delta^{34}\text{S} = -1.44\text{‰} \pm 0.5\text{‰}$ ; Labidi et al., 2012; Labidi et al., 2014; Labidi et al., 2013). Even though the difference in  $\delta^{34}\text{S}$  of volcanic glasses among the three Gakkel Ridge segments is

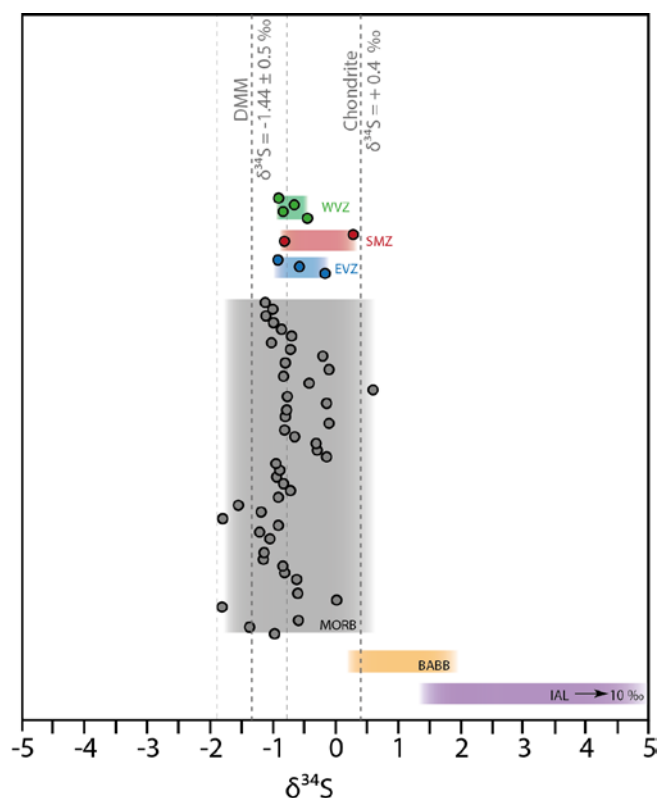


**Figure 6.2 - Comparison of sulfur isotope composition ( $\delta^{34}\text{S}$ ) of different tectonic settings.** The coloured squares represents different tectonic settings. Sulfur isotope composition of MORB from the three main oceanic basin are highlighted in grey. MORB data has been compiled from Labidi et al. (2012); Labidi et al. (2014); Labidi et al. (2013). In general,  $\delta^{34}\text{S}$  of MORBs ranges between DMM (Labidi et al., 2013) and chondrite value (Gao and Thiemens, 1993a; Gao and Thiemens, 1993b) highlighted as grey dashed vertical lines. MORB from the SMZ plot towards the upper boundary of MORB and lower boundary of Mariana back-arc basin basalts (BABB; Alt et al., 1993). Island arc lavas from the Mariana and Indonesian arc are plotted for comparison (Alt et al., 1993; de Hoog et al., 2001).

not significant, samples from the SMZ display a marginally heavier  $\delta^{34}\text{S}$  isotope signature ( $-0.27 \text{ ‰} \pm 0.3 \text{ ‰}$ ) than basalts from the WVZ ( $-0.72 \text{ ‰} \pm 0.3 \text{ ‰}$ ) and the EVZ ( $-0.56 \text{ ‰} \pm 0.3 \text{ ‰}$ ).

### 6.4.3 Platinum group elements

Whole rock PGE analysis shows a slight enrichment of Os in basalts from the WVZ and EVZ compared to global MORB. A few samples from the WVZ are slightly depleted in Ir, whereas samples from the EVZ show an inverse trend (Figure 6.3d). The data has been linked with iron isotopes of its source ( $\delta^{57}\text{Fe}_{\text{prim}}$ ; values taken from chapter 5; Figure 6.4), which can serve as an independent measure for the diversity of the source of the melts and igneous differentiation, especially with respect to magma chamber processes. Our result indicate a slightly different behaviour of I-PGE (Ir-Ru) with decreasing  $\delta^{57}\text{Fe}_{\text{prim}}$  (Figure 6.4a and 6.4b). Figure 6.4a shows a constant Ir concentration between  $\delta^{57}\text{Fe}_{\text{prim}} = +0.25 \text{ ‰}$  and  $+0.15 \text{ ‰}$ , whereas for  $\delta^{57}\text{Fe}_{\text{prim}} < +0.15 \text{ ‰}$  the Ir content in basalts slightly increases. Ruthenium shows an inverse trend. Between  $\delta^{57}\text{Fe}_{\text{prim}}$  of  $+0.25 \text{ ‰}$  and  $+0.15 \text{ ‰}$  Ru slightly increases and for  $\delta^{57}\text{Fe}_{\text{prim}} < +0.15 \text{ ‰}$  Ru shows constant values (Figure 6.4b). P-PGE, however, show no changes with  $\delta^{57}\text{Fe}_{\text{prim}}$  (Figure 6.4d).

To test whether the geochemical behaviour of the PGE changes due to magmatic differentiation;  $\Delta^{57}\text{Fe}$  has been calculated (calculation described by Nebel et al., 2018; Sossi et al., 2016), which provides the difference between the source (given as  $\delta^{57}\text{Fe}_{\text{prim}}$ ) and the basalt ( $\delta^{57}\text{Fe}$ ), which is used as an indicator for the degree of isotope fractionation. The I-PGE elements, Ir and Ru, increase with degree of fractionation (until  $\Delta^{57}\text{Fe}$  of  $< 0.04 \text{ ‰}$ ). For  $\Delta^{57}\text{Fe}$  values of  $> 0.04 \text{ ‰}$

the I-PGE decrease (Figures 6.5a and 6.5b), whereas P-PGE show no changes. The observed differences between P-PGE and I-PGE could be either related to differences within the mantle source or to magmatic differentiation, which will be discussed further.

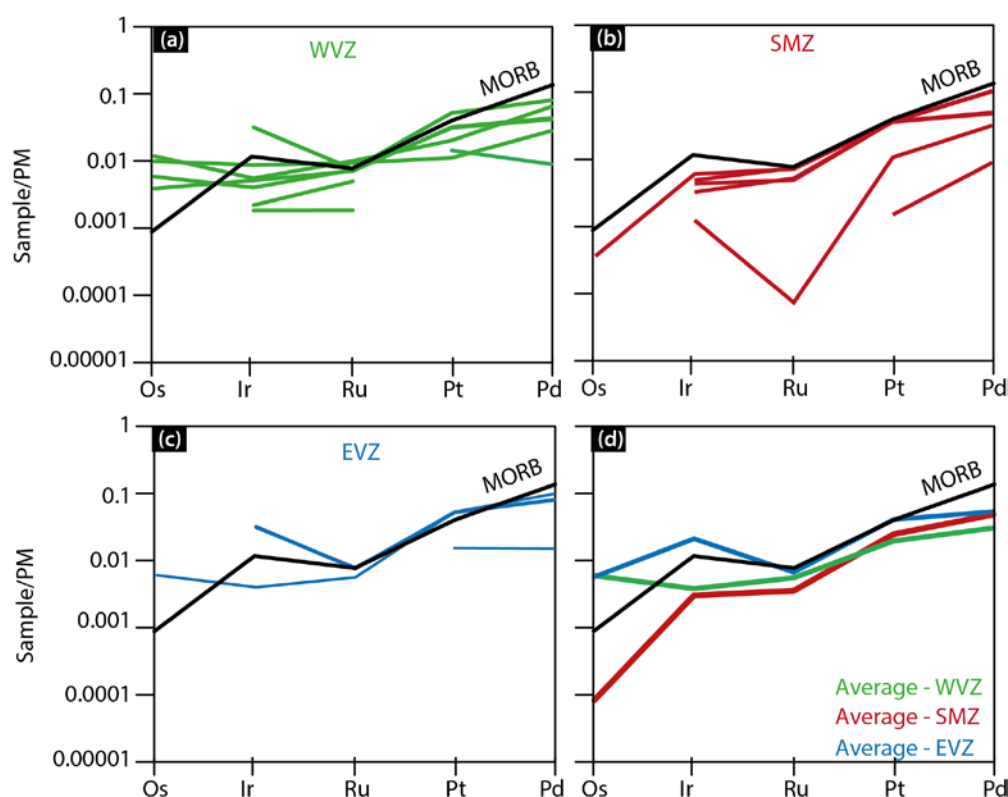


**Figure 6.3** - PGE (Os, Ir, Ru, Pt, Pd) pattern of the Gakkel basalts of all three ridge segments. (a) Western Volcanic Zone, (b) Sparsely Magmatic Zone, (c) Eastern Volcanic Zone and (d) shows the average of each ridge segment. All data has been normalized on primitive mantle values of McDonough and Sun (1995). MORB data compiled from Bézous et al. (2005) and Arevalo and McDonough (2010) has been plotted for comparison.

## 6.5 Discussion

Numerous studies reported geochemical behaviour of PGE in silicate/sulfide melt by changing different variables such as S concentration, source composition,  $fO_2$  and  $fS_2$  to investigate the geochemical behaviour of PGE during mantle melting (Ballhaus, 1995; Bézous et al., 2005; Fleet et al., 1996; Jenner, 2017; Jugo, 2009; Peach and Mathez, 1993; Reekie et al., 2019). Even though the S concentration in the mantle may affect the behaviour of PGE, basaltic melt that reaches the surface has a sulfur concentration ranging between 800 and 1100 ppm (Mavrogenes and O'Neill, 1999). This content is approximately half of the sulfur concentration expected after 10 % of melting a fertile mantle source (Lorand et al., 2013; Luguet et al., 2003; Mavrogenes and O'Neill, 1999), but is roughly the amount of S at sulfide saturation (Smythe et al., 2017), whereas the other half may retain in the residual mantle (Keays, 1995).

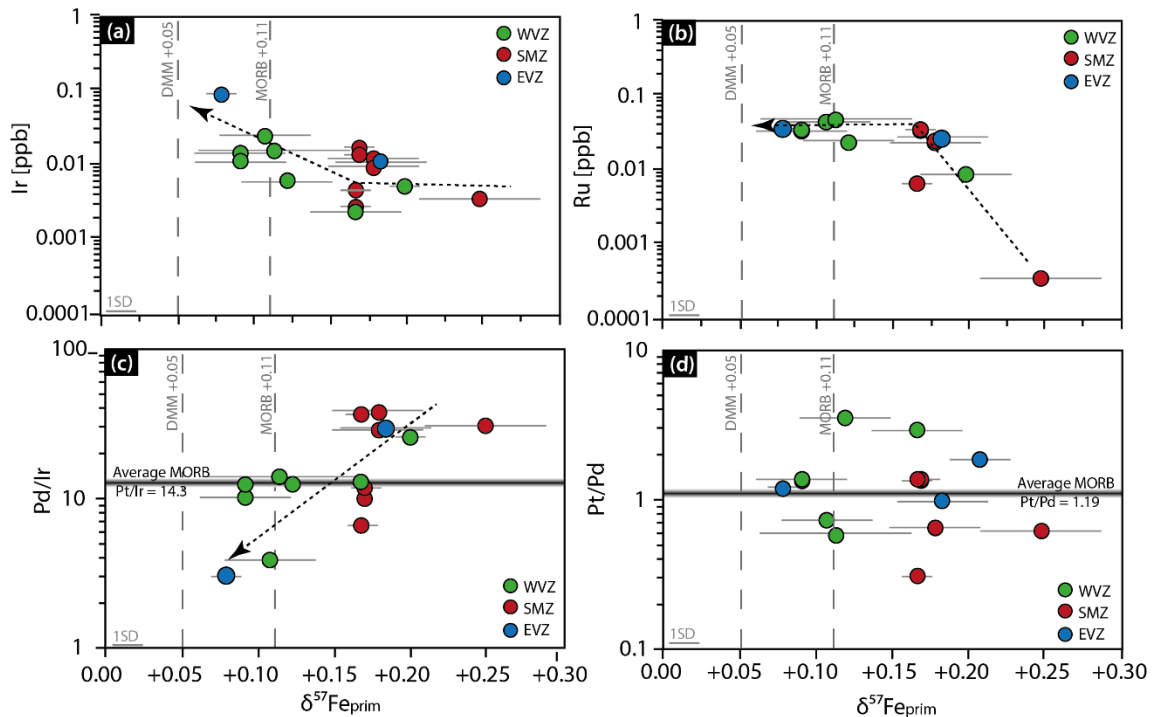


**Figure 6.4 – Platinum group elements versus Fe isotope composition.** (a) and (b) shows a slight difference in elemental concentration of Ir and Ru in the source, here represented as  $\delta^{57}\text{Fe}_{\text{prim}}$ . Ir and Ru show an increasing trend towards values of the average MORB (Teng et al., 2013) and DMM (Craddock et al., 2013). (c) Pd/Ir versus  $\delta^{57}\text{Fe}_{\text{prim}}$  shows a negative trend towards DMM values, compared to Ir and Ru, suggesting chemical behaviour change between P-PGE and I-PGE or the enrichment of I-PGE. (d) Pt-Pd, in contrary, show no correlation with change of MORB source. Average MORB ratios (Pd/Ir and Pt/Pd) have been plotted for comparison and calculated from Bézou et al. (2005). Trendlines are drawn by hand. Uncertainty is given in 2sd.

### 6.5.1 Effect of source composition on S isotopes

The Gakkel Ridge is not only the slowest spreading ridge on Earth, but also depicts a large heterogeneity in its underlying mantle ranging from enriched to depleted areas. It is thus essential to investigate if mantle depletion with a known effect on PGE abundances in extruding melts is affecting the concentrations in Gakkel Ridge lavas. Chemical differences in the source beneath the Western Gakkel Ridge region are apparent from radiogenic isotope systematics (Goldstein et al., 2008 and chapter 3), which may translate into differences in PGE concentrations in the basalts (Figure 6.4). The higher Fe isotope signature in basalts from the SMZ has been proposed to be linked to re-enrichment of the source during metasomatic overprint, as discussed in chapter 3. The source of this metasomatism is yet to be determined, but may be linked to crustal fluids.

Slab-derived fluids from subducting oceanic crust, which promote re-fertilisation of the mantle wedge, are also a carrier of sulfur (Tomkins and Evans, 2015). In the mantle sulfur occurs in two different oxidation states  $\text{S}^{2-}$  and  $\text{S}^{6+}$  and is mainly present in sulfides and sulfates (Hart and Gaetani, 2006; Jugo et al., 2005). At present, various studies used S-isotopes in conjunction with chalcophile and siderophile element systematics to trace mantle metasomatism in mantle peridotites and island arc basalts (de Hoog et al., 2001; e.g., Giuliani et al., 2016; Rielli et al., 2018). Only a few

studies analysed S-isotopes in MORBs showing that  $\delta^{34}\text{S}$  in MORBs may reveal insights of core-mantle differentiation processes (Labidi et al., 2014; Labidi et al., 2013) or potential recycling processes (Labidi et al., 2015). Samples from the Gakkel Ridge have an average  $\delta^{34}\text{S}$  of  $-0.56 \text{‰} \pm 0.3 \text{‰}$ . Even though this value is distinct from chondrites  $\delta^{34}\text{S} = +0.4 \text{‰} \pm 0.31 \text{‰}$  (Gao and Thiemens, 1993a; Gao and Thiemens, 1993b) and DMM  $\delta^{34}\text{S} = -1.4 \text{‰} \pm 0.5 \text{‰}$  (Labidi et al., 2014) (Figure 6.2), the Gakkel basalts, however, plot within the range of global MORB samples. It is thus concluded that the metasomatic enrichment has not affected sulfides in the source of the Gakkel Ridge.

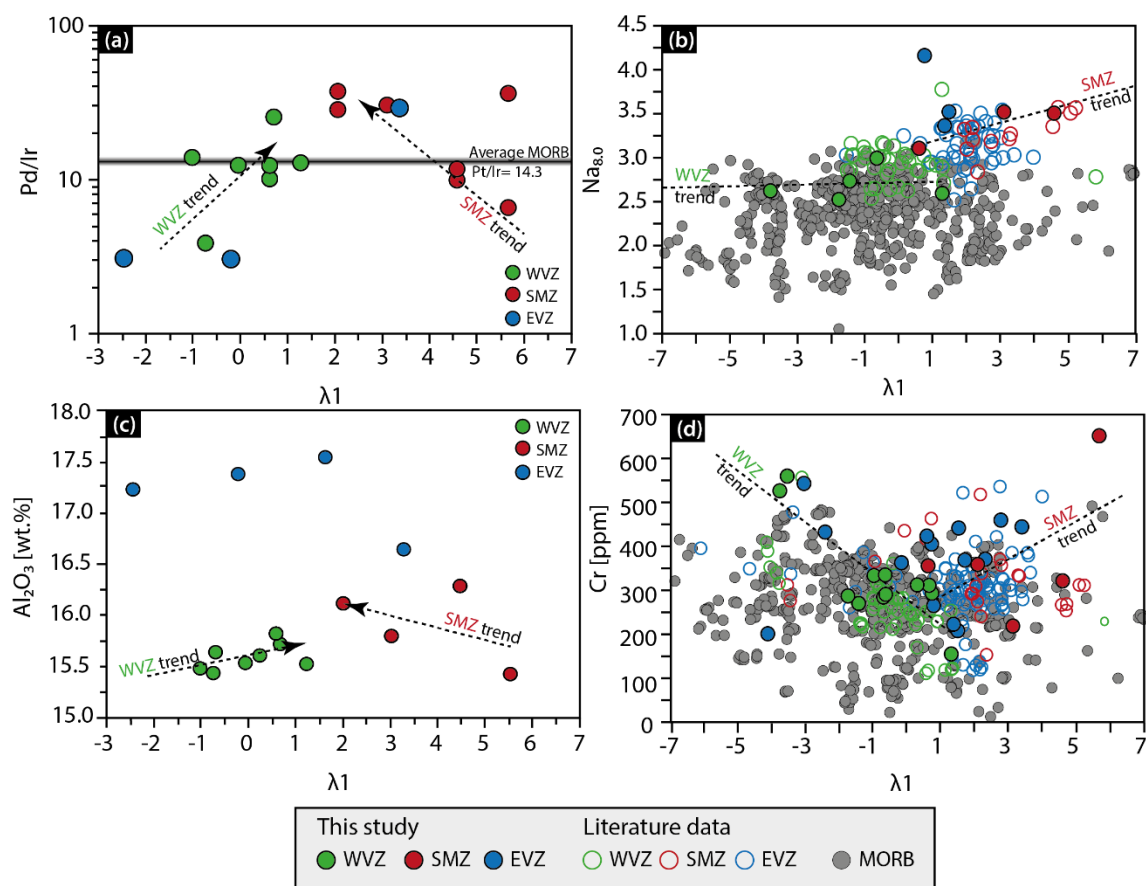


**Figure 6.5 - Pd-Ir ratio,  $\text{Na}_{8.0}$  and Cr versus REE pattern.** The REE pattern is given as  $\lambda_1$  and represents the shape of the REE pattern. The calculation for  $\lambda_1$  is given in O'Neill (2016). The higher  $\lambda_1$  the more depleted are, the basalts in LREE and the lower  $\lambda_1$  is, the more enriched the basalt in LREE. Two separate trends are visible from the data, which are linked to two individual ridge segments the WVZ and SMZ. (a) Pd/Ir in the SMZ trend increases with decreasing  $\lambda_1$  and for basalts in the WVZ, with increasing  $\lambda_1$  Pd/Ir increases. (b) WVZ and SMZ show inverse trends for the degree of melting  $\text{Na}_{8.0}$ . Only basalts with a MgO < 8 wt.% have been plotted (Klein and Langmuir, 1987) (c)  $\text{Al}_2\text{O}_3$  shows same trends as for Pd/Ir, whereas the Cr concentration (d) co-varies with  $\text{Na}_{8.0}$ . Both trends indicate that the source effects the MORB chemistry and magma chamber processes at faster spreading rate (>15 mm) diminish the source effect. MORB data from Jenner and O'Neill (2012).

### 6.5.2 The effect of the MORB source on PGE concentration

The opposing trend in iridium and ruthenium concentrations with increasingly lighter Fe and heavier Fe isotope, as shown in Figure 6.4, may not be related to source overprint, but to the degree of melting (Dale et al., 2008). Basalts from the SMZ, show, indeed a lower partial melting

degree (higher  $Na_{8,0}$ ) compared to WVZ basalts, as discussed in chapter 5. With increasing degree of melting Ru becomes first enriched and is then followed by Ir (Figures 6.4a and 6.4b). Such trends are not observed within P-PGE range (Figures 6.4c and 6.4d) and can be explained due to the difference in incompatibility between P-PGE and amongst I-PGE. To further test the behaviour of P-PGE and I-PGE, the Pd/Ir indicates an enrichment of P-PGE over I-PGE in basalts from the SMZ, which decreases towards depleted MORB mantle values (DMM,  $\delta^{57}Fe = +0.04 \text{ ‰}$ ; Craddock et al., 2013).

Different source chemistry can have further influence, not only on the partial melting degree, but also on unrelated elemental concentration of the basaltic liquid (Dick and Zhou, 2014; Rubin and Sinton, 2007; Standish et al., 2008; Sun and McDonough, 1989). Basalts from the SMZ show an enrichment in LREE (higher  $\lambda_1$ ), whereas the basalts from the WVZ show a depletion of LREE. During low degree partial melting (high  $Na_{8,0}$ ), LREE become slightly enriched due to higher incompatible behaviour over HREE (Figure 6.5b). Two different paths observed in Gakkel Ridge basalts, namely the SMZ trend and the WVZ trend (Figure 6.5). The SMZ trend is characterised by negative correlation of Pd/Ir and  $Al_2O_3$ ; and a positive correlation with  $Na_{8,0}$  and Cr concentration. In contrast, basalts from the WVZ show the opposite trend.

Irrespective of the variability in the source region of the PGE, it is clear that amongst the most primitive samples from the EVZ, Ir-Ru appear to slightly increase with increasing degrees of fractionation, until a sudden decrease at ca 8.5 wt.% MgO (Figure 6.6c).

### **6.5.3 Sulfide saturated versus sulfide undersaturated MORBs**

The pattern of increase and sudden decrease of Ir-Ru with increasing magmatic differentiation is mirrored by the chalcophile element Cu (Figure 6.6). This is apparent by the degree of fractionation as monitored by MgO or the stable Fe isotope composition of the samples that undergo fractionation as a function of olivine removal (expressed as  $\Delta^{57}Fe$ ). In chapter 5, it has been shown that  $\Delta^{57}Fe < 0.04 \text{ ‰}$  reflect olivine fractionation in the ultraslow part of the ridge (< 12 mm/a) until 8.5 wt.% MgO. An increase in spreading rate appears to promote the development of magma lenses/magma chamber and with this crystal fractionation (Coogan and O'Hara, 2015; O'Neill and Jenner, 2012; Rubin and Sinton, 2007), which is reflected by  $\Delta^{57}Fe > 0.04 \text{ ‰}$ . Figure 6.7 illustrates schematically the melt migration process from the source region (No. 1) to the crust (No. 3 and No. 4).

When melt rises from its parental source (No. 1), the melt inherits geochemical signatures of the ambient mantle, which will be carried in the melt to crustal levels. With increasing melting degree (lower  $Na_{8,0}$  values; Figure 6.6b) and melt migrating along grain boundaries, interstitial sulfides or platinum group minerals (Ir – Ru rich) can be completely exsolved in the upwards

migrating melt and may increase the sulfur and PGE content in the basaltic melt (No. 2). This process, however, is dependent on the available sulfur and oxygen fugacity of the source (Jugo, 2009). Within the most primitive melts  $> 8.5$  wt.% MgO, this process appears to be the most suitable to explain the increasing abundance of Ir-Ru in the melts. Such a dissolution of I-PGE can most plausibly counterbalance proposed formation of Ir-Ru rich phases such as laurite, which have been suggested to form during igneous differentiation. Primitive basalts from the EVZ form by congruent mantle melting (Wanless et al., 2014). Even though basalts from the SMZ show a slightly more evolved character than the EVZ basalts, it is expected that the melting mechanism is similar (No.1 and No. 2), because of the slow spreading rate, low magmatic activity and the absence of big magma chamber. In areas such as the EVZ and the SMZ melt rises rapidly from its source to crust, potentially with little crystal fractionation reflected by low  $\Delta^{57}\text{Fe}$  (chapter 5) and variable PGE and Cu concentration in particular in basalts from the EVZ (Figure 6.7). Assuming that Gakkel Ridge melts are directly derived from the mantle without further interaction *en route* to the crust, no secondary magma chamber process would interfere with these melts. It appears that fractional crystallisation observed here in lavas with  $> 8.5$  wt.% MgO (expressed through  $\Delta^{57}\text{Fe} < 0.04$ ) is not sufficient to overprint the trend in increasing I-PGE (No.4).

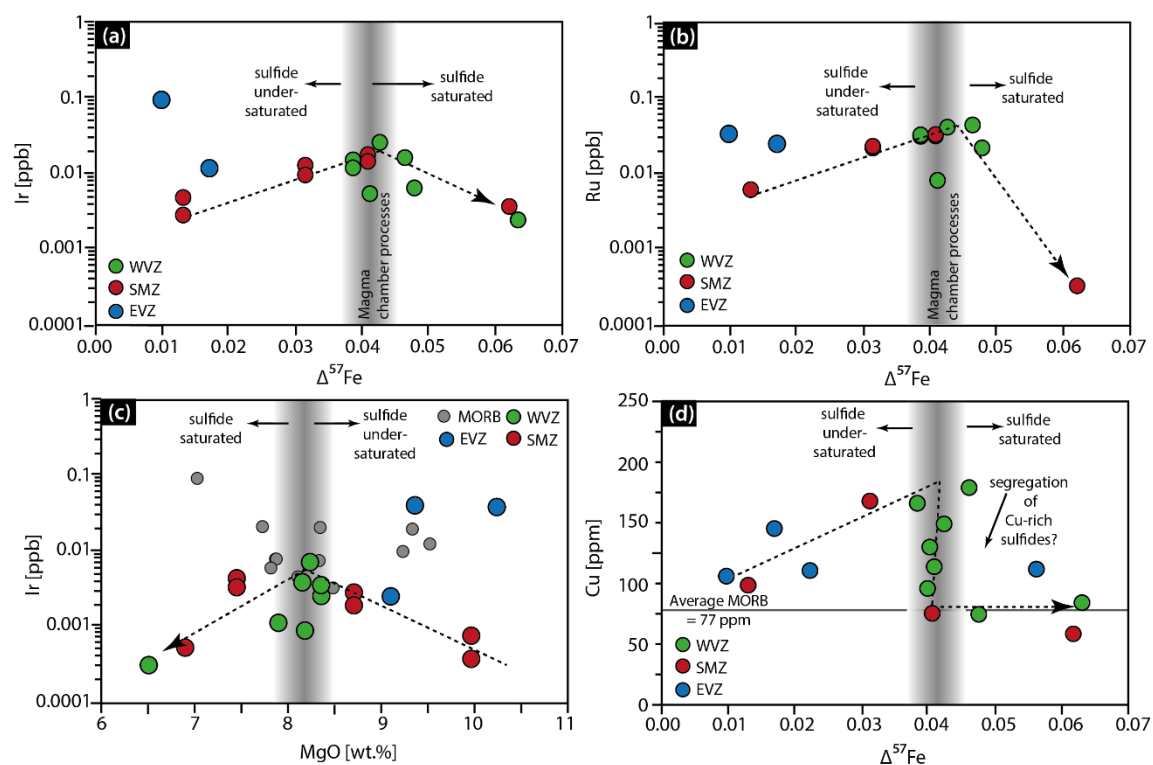


**Figure 6.6 - Iridium, Ru and Cu versus Fe isotope systematics ( $\Delta^{57}\text{Fe}$ ).** The higher  $\Delta^{57}\text{Fe}$  the more olivine fractionates out and the more evolved becomes the basaltic melt. The dotted lines indicate the development of Ir (a), Ru (b) and Cu (d) concentration of MORBs with increasing differentiation process. Between  $\Delta^{57}\text{Fe} = 0.04$  ‰ -  $0.05$  ‰, which equals a MgO content of  $< 8.5$  wt.% (c), the basaltic melt becomes sulfide saturated allowing the formation Cu-rich sulfides, which may incorporate I-PGE's (Ir and Ru) or promote the formation of Ir-Ru-rich alloys that segregate out of the melt and retain in the mantle or magma chamber/lenses.

Below this threshold, however, magma dynamics appear to change. Basalts with MgO < 8.5 wt.%, predominantly melts from the WVZ ridge segment with higher magma production rate appear to have been sourced from a magma chamber/lens beneath the ridge (Michael et al., 2003; Schmidt-Aursch and Jokat, 2016). The point of a sudden drop in I-PGE and Cu concentration (Figure 6.6) has been tentatively associated with the fractionation of these phases in a sulfide phase (Li and Audéat, 2015; Patten et al., 2013). In other words, this appears to be the point of sulfide saturation (No. 3) and inevitably implies that melts prior to this point are sulfide undersaturated (No. 4).

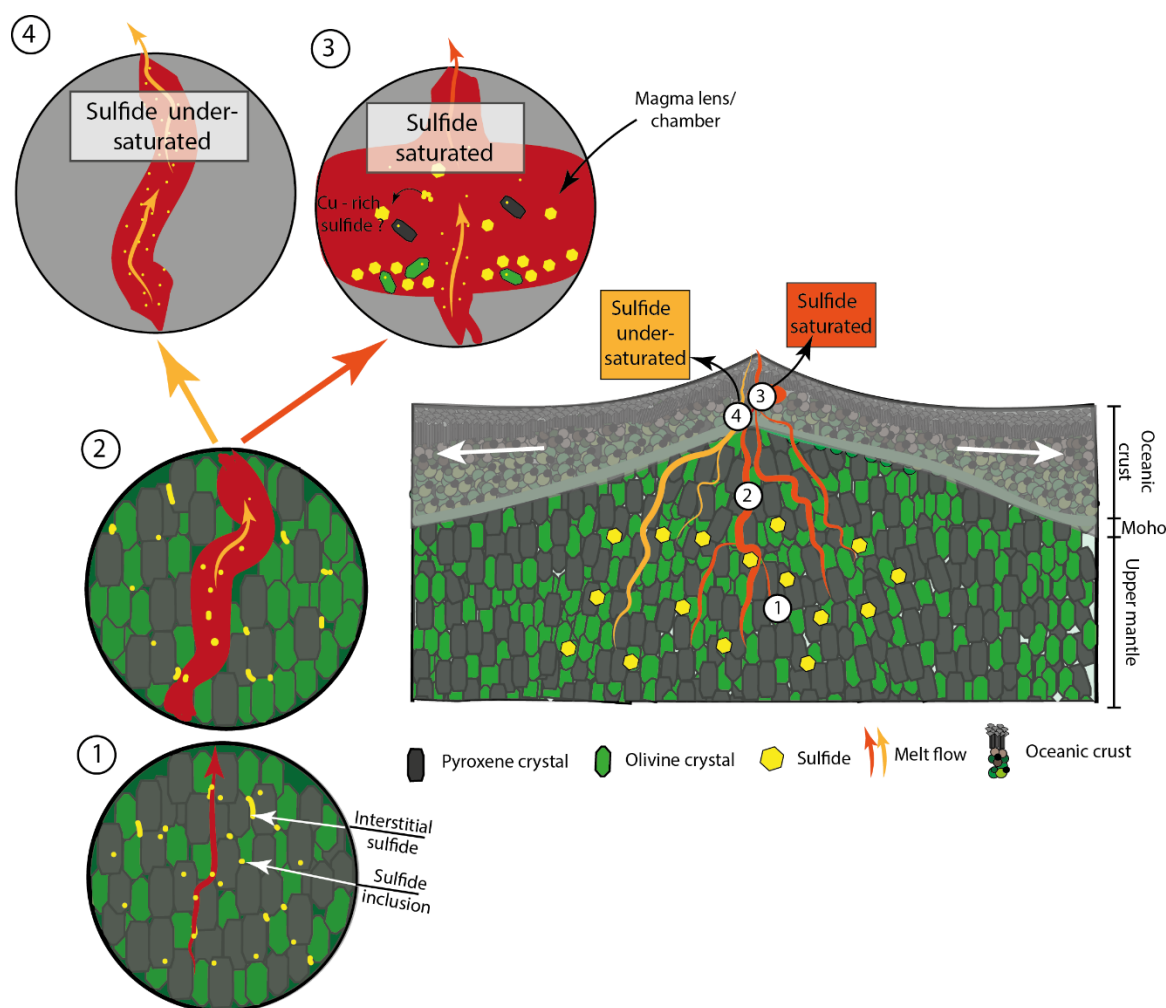


**Figure 6.7 - Schematic overview of the melting process and fractionation at the Gakkel Ridge.** In the source region, melt begins to form in melt pockets between networks of minerals. When enough melt has been produced, melt becomes buoyant and migrates along grain boundaries (1) towards upper levels. During its ascend the melt volume increases (No.2) by assimilating the ambient mantle. The melt network originates from different source region and migrate in two possible ways towards the surface, either melt migrates directly to the surface (No.4) or the melt pools in magma chambers (No.3). If the latter is the case, magma recharge, mixing and fractionation takes place. Melt that migrates from its source region to crust exsolves interstitial mineral phases, such as sulfide. A complete dissolution of sulfide can lead to an increase in sulfur concentration of the melt, which recharges magma chambers. Within the magma chambers sulfide saturation can be reached promoting sulfide - silicate segregation, which in turn results in formation of sulfide (Cu-rich?) and the erupting magma will appear sulfur-saturated. If No.4 is the case, only little fractionation occurs, which does not strongly affect the S concentration of the magma, resulting in S-undersaturated melt.

In relation to most MORBs, it seems that magma chamber processes are capable of enhancing S contents in lenses through recharge, evacuation and fractionation. Sulfur is incompatible in most phases during early MORB liquid fractionation, so that an incubation in magma chambers is a natural process for an undersaturated liquid.

It is likely that Cu-rich sulfide phases may form, because the partition coefficient of Cu increases if the melt becomes sulfide saturated during fractional differentiation (Reekie et al., 2019). I-PGE metals are then incorporated into the Cu-sulfides due to their chalcophile character or may form contemporaneous platinum group minerals (Ir-Ru rich) that form in the magma chamber. With ongoing crystallization in the magma chamber sulfide blebs can be interlocked in silicate minerals (Liu et al., 2009). Other studies suggest that fractional crystallization is key to keep magma saturated so that sulfides can precipitate (Holzheid and Grove, 2002). If Cu retains in Cu-rich sulfides within the magma chamber, and continuous sulfide formation and dissolution occurs within the magma chamber, then this would be a possible explanation for homogeneous Cu concentration in MORBs at around 77 ppm (Jenner, 2017). If most of the sulfur is consumed the partition coefficient of Cu decreases and Cu becomes incompatible again, enriching the melt with Cu (Lee et al., 2012) until recharge of magma chamber occurs, which may increase sulfur concentration to promote sulfur saturation and sulfide segregation.

From the Gakkel Ridge samples it is, however, clear that without magma chamber processes, mantle derived melts may be S-undersaturated. If this situation is unique to the Gakkel Ridge remains to be determined.

### 6.6 Conclusion

This study shows that basalts from the Gakkel Ridge appear sulfide undersaturated and sulfide saturated, which has been explained by different MORB evolution paths. Sulfur-undersaturated magma is linked to a direct melt transport from the source to the crust that is reflected by a primitive composition of the basalt ( $\text{MgO} > 8.5 \text{ wt.}\%$ ), a low degree of fractionation, increase in Ir-Ru and Cu concentration. The latter has been explained by dissolution of monosulfides *en route* to surface. On the other hand, magma that undergoes magma chamber processes during the melt ascend become sulfide saturated, due to replenishment and fractionation within a magma reservoir. This observation is in line with a sharp drop in Cu and decrease in Ir-Ru concentration, which is possibly caused by segregation of Cu-sulfide at S saturation.

---

## 6.7 Acknowledgements

This work was supported by an ARC grant FT140101062 to O.N. H. Dick was supported by US National Science Foundation (Grant No. OCE-MG&G 8371300). M.R. was supported by a graduate scholarship of Monash University and the SEAE.

## 6.8 References

- Alt, J.C., Shanks, W.C., Jackson, M.C., 1993. Cycling of sulfur in subduction zones: The geochemistry of sulfur in the Mariana Island Arc and back-arc trough. *Earth and Planetary Science Letters*, 119(4): 477-494.
- Alvey, A., Gaina, C., Kuznir, N.J., Torsvik, T.H., 2008. Integrated crustal thickness mapping and plate reconstructions for the high Arctic. *Earth and Planetary Science Letters*, 274(3-4): 310-321.
- Antonelli, M.A. et al., 2014. Early inner solar system origin for anomalous sulfur isotopes in differentiated protoplanets. *Proceedings of the National Academy of Sciences*, 111(50): 17749-17754.
- Arevalo, R., McDonough, W.F., 2010. Chemical variations and regional diversity observed in MORB. *Chemical Geology*, 271(1-2): 70-85.
- Ballhaus, C., 1995. Is the upper mantle metal-saturated? *Earth and Planetary Science Letters*, 132(1): 75-86.
- Barnes, S.J., Mungall, J.E., Maier, W.D., 2015. Platinum group elements in mantle melts and mantle samples. *Lithos*, 232: 395-417.
- Becker, H. et al., 2006. Highly siderophile element composition of the Earth's primitive upper mantle: Constraints from new data on peridotite massifs and xenoliths. *Geochimica et Cosmochimica Acta*, 70(17): 4528-4550.
- Bézos, A., Lorand, J.P., Humler, E., Gros, M., 2005. Platinum-group element systematics in Mid-Oceanic Ridge basaltic glasses from the Pacific, Atlantic, and Indian Oceans. *Geochimica et Cosmochimica Acta*, 69(10): 2613-2627.
- Coogan, L.A., O'Hara, M.J., 2015. MORB differentiation: In situ crystallization in replenished-tapped magma chambers. *Geochimica et Cosmochimica Acta*, 158: 147-161.
- Craddock, P.R., Warren, J.M., Dauphas, N., 2013. Abyssal peridotites reveal the near-chondritic Fe isotopic composition of the Earth. *Earth and Planetary Science Letters*, 365: 63-76.
- D'Errico, M.E., Warren, J.M., Godard, M., 2016. Evidence for chemically heterogeneous Arctic mantle beneath the Gakkel Ridge. *Geochimica et Cosmochimica Acta*, 174: 291-312.
- Dale, C.W., Luguét, A., Macpherson, C.G., Pearson, D.G., Hickey-Vargas, R., 2008. Extreme platinum-group element fractionation and variable Os isotope compositions in Philippine Sea Plate basalts: Tracing mantle source heterogeneity. *Chemical Geology*, 248(3-4): 213-238.
- de Hoog, J.C.M., Taylor, B.E., van Bergen, M.J., 2001. Sulfur isotope systematics of basaltic lavas from Indonesia: implications for the sulfur cycle in subduction zones. *Earth and Planetary Science Letters*, 189(3): 237-252.
- Dick, H.J.B., Lin, J., Schouten, H., 2003. An ultraslow-spreading class of ocean ridge. *Nature*, 426(6965): 405-412.
- Dick, H.J.B., Zhou, H., 2014. Ocean rises are products of variable mantle composition, temperature and focused melting. *Nature Geoscience*, 8(1): 68-74.
- Ding, S., Dasgupta, R., 2017. The fate of sulfide during decompression melting of peridotite – implications for sulfur inventory of the MORB-source depleted upper mantle. *Earth and Planetary Science Letters*, 459: 183-195.
- Ding, S., Dasgupta, R., 2018. Sulfur Inventory of Ocean Island Basalt Source Regions Constrained by Modeling the Fate of Sulfide during Decompression Melting of a Heterogeneous Mantle. *Journal of Petrology*, 59(7): 1281-1308.
- Dottin, J.W., Farquhar, J., Labidi, J., 2018. Multiple sulfur isotopic composition of main group pallasites support genetic links to IIIAB iron meteorites. *Geochimica et Cosmochimica Acta*, 224: 276-281.
- Fiorentini, M.L. et al., 2010. Platinum Group Element Geochemistry of Mineralized and Nonmineralized Komatiites and Basalts\*. *Economic Geology*, 105(4): 795-823.
- Fiorentini, M.L., Barnes, S.J., Maier, W.D., Burnham, O.M., Heggie, G., 2011. Global Variability in the Platinum-group Element Contents of Komatiites. *Journal of Petrology*, 52(1): 83-112.

- Fleet, M.E., Crocket, J.H., Stone, W.E., 1996. Partitioning of platinum-group elements (Os, Ir, Ru, Pt, Pd) and gold between sulfide liquid and basalt melt. *Geochimica et Cosmochimica Acta*, 60(13): 2397-2412.
- Fleet, M.E., Stone, W.E., 1991. Partitioning of platinum-group elements in the Fe-Ni-S system and their fractionation in nature. *Geochimica et Cosmochimica Acta*, 55(1): 245-253.
- Gale, A., Langmuir, C.H., Dalton, C.A., 2014. The Global Systematics of Ocean Ridge Basalts and their Origin. *Journal of Petrology*, 55(6): 1051-1082.
- Gao, X., Thiemens, M.H., 1993a. Isotopic composition and concentration of sulfur in carbonaceous chondrites. *Geochimica et Cosmochimica Acta*, 57(13): 3159-3169.
- Gao, X., Thiemens, M.H., 1993b. Variations of the isotopic composition of sulfur in enstatite and ordinary chondrites. *Geochimica et Cosmochimica Acta*, 57(13): 3171-3176.
- Giuliani, A. et al., 2016. Sulfur isotope composition of metasomatised mantle xenoliths from the Bultfontein kimberlite (Kimberley, South Africa): Contribution from subducted sediments and the effect of sulfide alteration on S isotope systematics. *Earth and Planetary Science Letters*, 445: 114-124.
- Goldstein, S.L. et al., 2008. Origin of a 'Southern Hemisphere' geochemical signature in the Arctic upper mantle. *Nature*, 453(7191): 89-93.
- Hart, S.R., Gaetani, G.A., 2006. Mantle Pb paradoxes: the sulfide solution. *Contributions to Mineralogy and Petrology*, 152(3): 295-308.
- Holzheid, A., Grove, T.L., 2002. Sulfur saturation limits in silicate melts and their implications for core formation scenarios for terrestrial planets. *American Mineralogist*, 87: 227 - 237.
- Jenner, F.E., 2017. Cumulate causes for the low contents of sulfide-loving elements in the continental crust. *Nature Geoscience*, 10: 524.
- Jenner, F.E., O'Neill, H.S.C., 2012. Analysis of 60 elements in 616 ocean floor basaltic glasses. *Geochemistry, Geophysics, Geosystems*, 13(2): Q02005.
- Jochum, K.P., Stoll, B., Herwig, K., Willbold, M., 2007. Validation of LA-ICP-MS trace element analysis of geological glasses using a new solid-state 193 nm Nd:YAG laser and matrix-matched calibration. *J. Anal. At. Spectrom.*, 22(2): 112-121.
- Jochum, K.P., Willbold, M., Raczek, I., Stoll, B., Herwig, K., 2005. Chemical Characterisation of the USGS Reference Glasses GSA - 1G, GSC - 1G, GSD - 1G, GSE - 1G, BCR - 2G, BHVO - 2G and BIR - 1G Using EPMA, ID - TIMS, ID - ICP - MS and LA - ICP - MS. *Geostandards and Geoanalytical Research*, 29(3): 285-302.
- Jugo, P.J., 2009. Sulfur content at sulfide saturation in oxidized magmas. *Geology*, 37(5): 415-418.
- Jugo, P.J., Luth, R.W., Richards, J.P., 2005. Experimental data on the speciation of sulfur as a function of oxygen fugacity in basaltic melts. *Geochimica et Cosmochimica Acta*, 69(2): 497-503.
- Keays, R.R., 1995. The role of komatiitic and picritic magmatism and S-saturation in the formation of ore deposits. *Lithos*, 34(1-3): 1-18.
- Klein, E.M., Langmuir, C.H., 1987. Global correlations of ocean ridge basalt chemistry with axial depth and crustal thickness. *Journal of Geophysical Research: Solid Earth*, 92(B8): 8089-8115.
- Labidi, J., Cartigny, P., Birck, J.L., Assayag, N., Bourrand, J.J., 2012. Determination of multiple sulfur isotopes in glasses: A reappraisal of the MORB  $\delta^{34}\text{S}$ . *Chemical Geology*, 334: 189-198.
- Labidi, J., Cartigny, P., Hamelin, C., Moreira, M., Dosso, L., 2014. Sulfur isotope budget ( $^{32}\text{S}$ ,  $^{33}\text{S}$ ,  $^{34}\text{S}$  and  $^{36}\text{S}$ ) in Pacific-Antarctic ridge basalts: A record of mantle source heterogeneity and hydrothermal sulfide assimilation. *Geochimica et Cosmochimica Acta*, 133: 47-67.
- Labidi, J., Cartigny, P., Jackson, M.G., 2015. Multiple sulfur isotope composition of oxidized Samoan melts and the implications of a sulfur isotope 'mantle array' in chemical geodynamics. *Earth and Planetary Science Letters*, 417: 28-39.
- Labidi, J., Cartigny, P., Moreira, M., 2013. Non-chondritic sulphur isotope composition of the terrestrial mantle. *Nature*, 501(7466): 208-11.
- Lee, C.-T.A. et al., 2012. Copper Systematics in Arc Magmas and Implications for Crust-Mantle Differentiation. *Science*, 336(6077): 64-68.
- Li, Y., Audétat, A., 2015. Effects of temperature, silicate melt composition, and oxygen fugacity on the partitioning of V, Mn, Co, Ni, Cu, Zn, As, Mo, Ag, Sn, Sb, W, Au, Pb, and Bi between sulfide phases and silicate melt. *Geochimica et Cosmochimica Acta*, 162: 25-45.
- Lissner, M. et al., 2014. Selenium and tellurium systematics in MORBs from the southern Mid-Atlantic Ridge (47-50°S). *Geochimica et Cosmochimica Acta*, 144: 379-402.
- Liu, C.-Z., Snow, J.E., Brüggemann, G., Hellebrand, E., Hofmann, A.W., 2009. Non-chondritic HSE budget in Earth's upper mantle evidenced by abyssal peridotites from Gakkel Ridge (Arctic Ocean). *Earth and Planetary Science Letters*, 283(1-4): 122-132.

- Liu, C.Z. et al., 2008. Ancient, highly heterogeneous mantle beneath Gakkel Ridge, Arctic Ocean. *Nature*, 452(7185): 311-6.
- Longerich, H.P., Jackson, S.E., Gunther, D., 1996. Inter-laboratory note. Laser ablation inductively coupled plasma mass spectrometric transient signal data acquisition and analyte concentration calculation. *Journal of Analytical Atomic Spectrometry*, 11(9): 899-904.
- Lorand, J.-P., Luguët, A., Alard, O., 2013. Platinum-group element systematics and petrogenetic processing of the continental upper mantle: A review. *Lithos*, 164-167: 2-21.
- Lorand, J.-P., Pattou, L., Gros, M., 1999. Fractionation of Platinum-group Elements and Gold in the Upper Mantle: a Detailed Study in Pyrenean Orogenic Lherzolites. *Journal of Petrology*, 40(6): 957-981.
- Lorand, J.P., 1990. Are spinel Iherzolite xenoliths representative of the abundance of sulfur in the upper mantle? *Geochimica et Cosmochimica Acta*, 54(5): 1487-1492.
- Lorand, J.P., Luguët, A., Alard, O., 2008. Platinum-Group Elements: A New Set of Key Tracers for the Earth's Interior. *Elements*, 4(4): 247-252.
- Luguët, A., Lorand, J.-P., Seyler, M., 2003. Sulfide petrology and highly siderophile element geochemistry of abyssal peridotites: a coupled study of samples from the Kane Fracture Zone (45°W 23°20N, MARK area, Atlantic Ocean). *Geochimica et Cosmochimica Acta*, 67(8): 1553-1570.
- Mavrogenes, J.A., O'Neill, H.S.C., 1999. The relative effects of pressure, temperature and oxygen fugacity on the solubility of sulfide in mafic magmas. *Geochimica et Cosmochimica Acta*, 63(7-8): 1173-1180.
- McDonough, W.F., Sun, S.s., 1995. The composition of the Earth. *Chemical Geology*, 120(3): 223-253.
- Meisel, T., Moser, J., 2004. Platinum-Group Element and Rhenium Concentrations in Low Abundance Reference Materials. *Geostandards and Geoanalytical Research*, 28(2): 233-250.
- Michael, P.J. et al., 2003. Magmatic and amagmatic seafloor generation at the ultraslow-spreading Gakkel Ridge, Arctic Ocean. *Nature*, 423(6943): 956-961.
- Nebel, O. et al., 2018. Iron isotope variability in ocean floor lavas and mantle sources in the Lau back-arc basin. *Geochimica et Cosmochimica Acta*, 241: 150-163.
- O'Neill, H.S., Jenner, F.E., 2012. The global pattern of trace-element distributions in ocean floor basalts. *Nature*, 491(7426): 698-704.
- O'Neill, H.S.C., 1991. The origin of the moon and the early history of the earth—A chemical model. Part 2: The earth. *Geochimica et Cosmochimica Acta*, 55(4): 1159-1172.
- O'Neill, H.S.C., 2016. The Smoothness and Shapes of Chondrite-normalized Rare Earth Element Patterns in Basalts. *Journal of Petrology*, 57(8): 1463-1508.
- O'Neill, H.S.C., Mavrogenes, J.A., 2002. The Sulfide Capacity and the Sulfur Content at Sulfide Saturation of Silicate Melts at 1400°C and 1 bar. *Journal of Petrology*, 43(6): 1049-1087.
- Palme, H., O'Neill, H.S.C., 2014. Cosmochemical Estimates of Mantle Composition. 1-39.
- Park, J.-W., Campbell, I.H., Eggins, S.M., 2012. Enrichment of Rh, Ru, Ir and Os in Cr spinels from oxidized magmas: Evidence from the Ambae volcano, Vanuatu. *Geochimica et Cosmochimica Acta*, 78: 28-50.
- Patten, C., Barnes, S.-J., Mathez, E.A., Jenner, F.E., 2013. Partition coefficients of chalcophile elements between sulfide and silicate melts and the early crystallization history of sulfide liquid: LA-ICP-MS analysis of MORB sulfide droplets. *Chemical Geology*, 358: 170-188.
- Peach, C.L., Mathez, E.A., 1993. Sulfide melt-silicate melt distribution coefficients for nickel and iron and implications for the distribution of other chalcophile elements. *Geochimica et Cosmochimica Acta*, 57(13): 3013-3021.
- Peucker-Ehrenbrink, B., Bach, W., Hart, S.R., Blusztajn, J.S., Abbruzzese, T., 2003. Rhenium-osmium isotope systematics and platinum group element concentrations in oceanic crust from DSDP/ODP Sites 504 and 417/418. *Geochemistry, Geophysics, Geosystems*, 4(7).
- Plessen, H.-G., Erzinger, J., 1998. Determination of the Platinum-Group Elements and Gold in Twenty Rock Reference Materials by Inductively Coupled Plasma-Mass Spectrometry (ICP-MS) after Pre-Concentration by Nickel Sulfide Fire Assay. *Geostandards Newsletter*, 22(2): 187-194.
- Reekie, C.D.J. et al., 2019. Sulfide resorption during crustal ascent and degassing of oceanic plateau basalts. *Nature Communications*, 10(1): 82.
- Rielli, A. et al., 2018. Sulfur isotope and PGE systematics of metasomatised mantle wedge. *Earth and Planetary Science Letters*, 497: 181-192.
- Rubin, K.H., Sinton, J.M., 2007. Inferences on mid-ocean ridge thermal and magmatic structure from MORB compositions. *Earth and Planetary Science Letters*, 260(1-2): 257-276.
- Schmidt-Aursch, M.C., Jokat, W., 2016. 3D gravity modelling reveals off-axis crustal thickness variations along the western Gakkel Ridge (Arctic Ocean). *Tectonophysics*.

- Shaw, A.M., Behn, M.D., Humphris, S.E., Sohn, R.A., Gregg, P.M., 2010. Deep pooling of low degree melts and volatile fluxes at the 85°E segment of the Gakkel Ridge: Evidence from olivine-hosted melt inclusions and glasses. *Earth and Planetary Science Letters*, 289(3-4): 311-322.
- Shephard, G.E., Müller, R.D., Seton, M., 2013. The tectonic evolution of the Arctic since Pangea breakup: Integrating constraints from surface geology and geophysics with mantle structure. *Earth-Science Reviews*, 124: 148-183.
- Smythe, D.J., Wood, B.J., Kiseeva, E.S., 2017. The S content of silicate melts at sulfide saturation: New experiments and a model incorporating the effects of sulfide composition. *American Mineralogist*, 102(4): 795-803.
- Sossi, P.A., Nebel, O., Foden, J., 2016. Iron isotope systematics in planetary reservoirs. *Earth and Planetary Science Letters*, 452: 295-308.
- Standish, J.J., Dick, H.J.B., Michael, P.J., Melson, W.G., O'Hearn, T., 2008. MORB generation beneath the ultraslow-spreading Southwest Indian Ridge (9-25°E): Major element chemistry and the importance of process versus source. *Geochemistry, Geophysics, Geosystems*, 9(5): Q05004.
- Stracke, A. et al., 2011. Abyssal peridotite Hf isotopes identify extreme mantle depletion. *Earth and Planetary Science Letters*, 308(3-4): 359-368.
- Sun, S.-s., McDonough, W.F., 1989. Chemical and isotopic systematics of oceanic basalts: implications for mantle composition and processes. *Geological Society, London, Special Publications*, 42(1): 313-345.
- Tagle, R., Claeys, P., 2005. An ordinary chondrite impactor for the Popigai crater, Siberia. *Geochimica et Cosmochimica Acta*, 69(11): 2877-2889.
- Teng, F.-Z., Dauphas, N., Huang, S., Marty, B., 2013. Iron isotopic systematics of oceanic basalts. *Geochimica et Cosmochimica Acta*, 107: 12-26.
- Tomkins, A.G., Evans, K.A., 2015. Separate zones of sulfate and sulfide release from subducted mafic oceanic crust. *Earth and Planetary Science Letters*, 428: 73-83.
- Wanless, V.D., Behn, M.D., Shaw, A.M., Plank, T., 2014. Variations in melting dynamics and mantle compositions along the Eastern Volcanic Zone of the Gakkel Ridge: insights from olivine-hosted melt inclusions. *Contributions to Mineralogy and Petrology*, 167(5).
- Warren, J.M., Shirey, S.B., 2012. Lead and osmium isotopic constraints on the oceanic mantle from single abyssal peridotite sulfides. *Earth and Planetary Science Letters*, 359-360: 279-293.
- Williams, H.M. et al., 2018. Interplay of crystal fractionation, sulfide saturation and oxygen fugacity on the iron isotope composition of arc lavas: An example from the Marianas. *Geochimica et Cosmochimica Acta*.
- Wykes, J.L., O'Neill, H.S.C., Mavrogenes, J.A., 2015. The Effect of FeO on the Sulfur Content at Sulfide Saturation (SCSS) and the Selenium Content at Selenide Saturation of Silicate Melts. *Journal of Petrology*, 56(7): 1407-1424.

## **Supplementary Data Tables**



## Chapter 6 – Supplementary Data Tables

*Supplementary Data Table 6.1 – Trace element data of the volcanic glasses from the Gakkel Ridge. Values are given in ppm.*

<i>Sample Name</i>	<i>PS59 274-52</i>	<i>PS59 294-40</i>	<i>PS59 297-11</i>	<i>PS101 186</i>	<i>HLY0102 D61-11</i>	<i>HLY0102 D59-35</i>	<i>HLY0102 D50-30</i>
<i>Segment</i>	<i>EVZ</i>	<i>EVZ</i>	<i>EVZ</i>	<i>EVZ</i>	<i>EVZ</i>	<i>EVZ</i>	<i>EVZ</i>
<i>TRACE ELEMENTS</i>							
Na	23065	24954	20710	24622	26803	27580	26048
Mg	47592	49556	52830	47954	52549	49850	49346
Al	86398	86545	89172	85749	92782	90350	88906
Si	239053	232738	230359	236516	235110	240817	236456
Ca	74222	75186	74815	76882	79481	78375	78570
Sc	34.2	33.1	35.7	32.1	31.1	33.1	32.0
Ti	6705	8006	6308	8004	8765	10182	8353
V	194	209	164	222	226	254	227
Cr	327	588	286	339	332	312	309
Mn	1286	1225	1355	1164	1203	1283	1147
Fe	68917	66151	74562	61231	63812	67632	60550
Co	44.2	42.0	49.4	38.5	41.6	41.7	39.5
Ni	122	170	201	140	169	145	145
Cu	114	102	114	95	89	88	88
Zn	62	62	61	59	60	66	57
Ga	16.4	17.2	15.8	16.4	17.9	18.6	16.8
Rb	6.0	1.1	1.3	1.0	1.0	4.4	4.7
Sr	108	158	157	173	225	224	212
Y	24.7	28.0	24.9	25.9	26.9	30.5	25.9
Zr	75	96	65	101	108	132	105
Nb	1.0	2.0	2.6	2.4	2.7	6.8	7.6
Mo	0.12	0.14	0.16	0.16	0.38	0.54	0.72
Cs	0.23	0.01	0.01	0.00	0.02	0.07	0.04
Ba	38.3	9.8	15.4	12.0	13.8	46.9	60.4
La	3.21	3.05	2.57	3.51	4.22	6.60	6.24
Ce	9.15	9.92	7.32	11.32	13.09	18.02	15.97
Pr	1.49	1.71	1.22	1.89	2.11	2.74	2.39
Nd	8.01	9.26	6.51	10.10	11.17	13.82	11.66
Sm	2.50	3.13	2.24	3.15	3.59	4.09	3.37
Eu	0.95	1.12	0.90	1.10	1.25	1.39	1.18
Gd	3.46	4.00	3.25	3.98	4.30	4.94	4.05
Tb	0.62	0.70	0.57	0.67	0.72	0.84	0.69
Dy	4.32	4.85	4.23	4.61	4.89	5.47	4.67
Ho	0.89	1.02	0.92	0.94	0.97	1.12	0.95
Er	2.71	3.11	2.82	2.82	2.92	3.32	2.82
Tm	0.38	0.43	0.40	0.38	0.40	0.47	0.40
Yb	2.58	2.95	2.78	2.63	2.67	3.01	2.63
Lu	0.39	0.45	0.43	0.39	0.42	0.45	0.39
Hf	1.99	2.36	1.60	2.43	2.60	3.11	2.48
Ta	0.07	0.12	0.17	0.15	0.19	0.45	0.46
Pb	1.38	0.51	0.33	0.55	0.63	0.98	0.69
Th	0.52	0.13	0.16	0.14	0.17	0.51	0.51
U	0.13	0.05	0.06	0.05	0.07	0.17	0.17

Chapter 6 – Supplementary Data Tables

Supplementary Data Table 6.1 – [continued]

<i>Sample Name</i>	<i>HLY0102 D51-15</i>	<i>HLY0102 D38-6</i>	<i>HLY0102 D36-35</i>	<i>HLY0102 D37-5</i>	<i>PS59 216-11</i>	<i>PS59 216</i>	<i>HLY0102 D8-12</i>
<i>Segment</i>	<i>EVZ</i>	<i>SMZ</i>	<i>SMZ</i>	<i>SMZ</i>	<i>WVZ</i>	<i>WVZ</i>	<i>WVZ</i>
<i>TRACE ELEMENTS</i>							
Na	25136	26739	26463	30654	24419	24854	23567
Mg	51982	40414	42465	37372	45998	46339	45901
Al	90303	81298	82693	81083	82320	84654	79184
Si	233038	237407	243673	241398	237652	240542	239769
Ca	78564	71328	71249	64324	77961	80051	74395
Sc	31.4	32.2	33.2	31.3	35.5	35.9	34.7
Ti	8464	8734	9320	10683	9317	9428	8974
V	224	227	249	253	275	278	268
Cr	307	276	268	197	299	305	300
Mn	1160	1228	1257	1382	1347	1366	1310
Fe	61622	64884	66891	73875	71602	72681	69991
Co	40.5	35.4	37.3	35.3	40.4	40.8	40.6
Ni	155	105	118	98	120	123	136
Cu	88	86	84	64	99	99	94
Zn	59	68	69	83	72	72	71
Ga	17.6	16.7	17.6	19.1	17.8	17.8	17.1
Rb	1.6	8.7	13.7	13.0	2.6	2.4	3.9
Sr	214	150	184	164	149	155	144
Y	25.6	31.2	30.5	38.0	32.4	32.7	30.9
Zr	107.7	112.2	112.1	144.4	98.6	98.9	92.2
Nb	4.05	7.86	8.88	12.72	2.59	2.66	2.94
Mo	0.34	0.51	0.59	0.71	0.30	0.26	0.15
Cs	0.01	0.14	0.20	0.18	0.03	0.04	0.04
Ba	22.5	89.3	140.8	135.2	30.3	30.4	43.9
La	4.77	6.30	6.93	9.61	3.66	3.64	3.48
Ce	13.84	15.79	16.63	22.63	11.11	11.27	10.51
Pr	2.15	2.39	2.45	3.25	1.92	1.91	1.78
Nd	11.20	12.08	12.51	16.02	10.79	10.73	10.15
Sm	3.24	3.60	3.67	4.57	3.56	3.58	3.36
Eu	1.18	1.23	1.29	1.54	1.27	1.30	1.22
Gd	4.12	4.66	4.77	5.82	4.81	4.81	4.52
Tb	0.70	0.81	0.80	0.98	0.83	0.84	0.79
Dy	4.62	5.52	5.43	6.80	5.77	5.88	5.55
Ho	0.93	1.16	1.12	1.41	1.20	1.21	1.15
Er	2.77	3.40	3.26	4.13	3.52	3.54	3.35
Tm	0.39	0.46	0.45	0.56	0.48	0.50	0.46
Yb	2.59	3.22	3.07	3.90	3.27	3.32	3.13
Lu	0.38	0.49	0.46	0.59	0.49	0.50	0.47
Hf	2.52	2.78	2.87	3.66	2.75	2.81	2.59
Ta	0.27	0.46	0.55	0.77	0.17	0.18	0.19
Pb	0.63	0.72	0.77	1.03	0.51	0.56	0.53
Th	0.24	0.61	0.75	1.02	0.22	0.21	0.22
U	0.09	0.16	0.19	0.27	0.07	0.07	0.06

## Chapter 6 – Supplementary Data Tables

*Supplementary Data Table 6.1 – [continued]*

<i>Sample Name</i>	<i>HLY0102 D26-9</i>	<i>PS86 67</i>	<i>HLY0102 D11-19</i>	<i>PS59 234-24</i>	<i>PS66 217-16</i>	<i>PS86 044</i>
<i>Segment</i>	WVZ	WVZ	WVZ	WVZ	WVZ	WVZ
<i>TRACE ELEMENTS</i>						
Na	23747	24329	24528	23825	25214	24806
Mg	44491	46720	44638	49011	40336	44911
Al	78450	79804	81423	81103	80626	79797
Si	235637	241162	235552	239189	238057	235543
Ca	74669	75395	74197	76606	73141	71390
Sc	35.5	35.5	34.0	34.7	34.7	33.8
Ti	10299	9704	9308	9168	10841	9895
V	293	287	262	267	292	270
Cr	282	272	287	355	272	261
Mn	1395	1367	1284	1303	1354	1291
Fe	74856	73187	68593	69859	71966	69026
Co	41.6	42.2	39.2	41.8	37.1	39.5
Ni	110	125	114	153	91	134
Cu	98	95	90	100	88	85
Zn	76	75	69	68	77	70
Ga	18.6	18.0	18.0	17.2	18.5	17.3
Rb	1.6	4.2	7.3	2.7	8.1	8.5
Sr	144	147	171	154	172	171
Y	34.6	32.9	29.4	31.3	36.2	31.6
Zr	109.6	101.8	98.8	99.1	126.4	108.4
Nb	1.93	3.15	4.55	2.56	5.25	5.14
Mo	0.19	0.15	0.20	0.31	0.49	0.39
Cs	0.01	0.07	0.10	0.04	0.24	0.12
Ba	20.8	47.5	71.1	29.4	80.2	89.7
La	3.60	3.91	4.14	3.69	5.56	4.63
Ce	11.47	11.66	12.24	11.22	15.66	13.28
Pr	2.03	2.01	2.03	1.93	2.60	2.19
Nd	11.44	11.05	10.97	10.60	13.88	12.11
Sm	3.83	3.57	3.54	3.63	4.46	3.72
Eu	1.34	1.30	1.24	1.26	1.58	1.32
Gd	5.05	4.85	4.40	4.66	5.65	4.80
Tb	0.89	0.84	0.77	0.78	1.02	0.84
Dy	6.12	5.82	5.26	5.51	6.59	5.69
Ho	1.27	1.20	1.06	1.14	1.42	1.18
Er	3.83	3.59	3.24	3.41	3.99	3.46
Tm	0.52	0.51	0.44	0.46	0.59	0.48
Yb	3.57	3.35	3.02	3.18	3.86	3.21
Lu	0.53	0.51	0.45	0.48	0.61	0.49
Hf	2.80	2.78	2.60	2.62	3.55	2.94
Ta	0.12	0.21	0.32	0.17	0.46	0.38
Pb	0.54	0.60	0.59	0.56	1.27	0.66
Th	0.17	0.26	0.29	0.21	0.76	0.34
U	0.05	0.07	0.08	0.06	0.21	0.09

Chapter 6 – Supplementary Data Tables

Supplementary Data Table 6.2 – Trace element data of the reference sample NIST 612 and NIST 610.

Element	NIST 612				NIST 610			
	Average (n = 22)	RSE (%)	Literature value	Relative error (%)	Average (n = 22)	RSE (%)	Literature value	Relative error (%)
Na	108541	3274	101635	6.4	105931	0.5	102300	3.5
Mg	65	3	68	-4.9	502	0.7	610	17.7
Al	11068	279	10744	2.9	10588	0.5	11626	8.9
Si	337024	0	337024	0.0	323001	0.0	323001	0.0
Ca	91989	2313	85049	7.5	87981	0.6	81475	8.0
Sc	42.7	1.0	39.9	6.5	318	1.9	455	30.1
Ti	375	18	44	88.3	-	-	-	-
V	39.6	1.4	38.8	2.1	459.2	0.7	450.0	2.0
Cr	42.0	1.3	36.4	13.3	470.5	0.7	408.0	15.3
Mn	40.7	1.5	38.7	5.0	470.6	0.8	444.0	6.0
Fe	54.4	2.9	51.0	6.3	493.9	0.9	458.0	7.8
Co	36.4	1.0	35.5	2.6	423.7	0.6	410.0	3.4
Ni	44.3	2.5	38.8	12.3	510.8	1.0	458.7	11.4
Cu	50.2	1.5	37.8	24.8	577.4	1.0	441.0	30.9
Zn	30.1	1.7	39.1	-29.8	372.6	0.8	460.0	19.0
Ga	38.5	1.5	36.9	4.2	458.6	0.7	433.0	5.9
Rb	31.6	1.1	31.4	0.8	421.0	0.8	425.7	1.1
Sr	83.0	3.2	78.4	5.5	542.5	0.8	515.5	5.2
Y	43.8	1.6	38.3	12.5	519.2	0.7	462.0	12.4
Zr	43.0	1.6	37.9	11.9	498.3	0.8	448.0	11.2
Nb	42.8	1.3	38.9	9.2	517.8	0.7	465.0	11.4
Mo	39.9	1.2	37.4	6.4	448.9	0.8	417.0	7.6
Cs	42.7	1.5	42.7	-0.1	369.1	0.7	366.0	0.8
Ba	41.5	1.6	39.3	5.2	471.7	0.8	452.0	4.4
La	37.8	1.4	36.0	4.8	464.7	0.5	440.0	5.6
Ce	40.7	1.5	38.4	5.6	487.7	0.6	453.0	7.7
Pr	40.6	1.8	37.9	6.7	485.2	0.5	448.0	8.3
Nd	38.9	1.7	35.5	8.7	470.9	0.8	430.0	9.5
Sm	40.6	1.6	37.7	7.1	486.2	0.7	453.0	7.3
Eu	36.7	1.6	35.6	3.1	462.2	0.7	447.0	3.4
Gd	40.7	1.9	37.3	8.3	476.3	0.9	449.0	6.1
Tb	40.6	1.7	37.6	7.4	473.0	0.6	437.0	8.2
Dy	40.0	1.9	35.5	11.2	483.1	0.8	437.0	10.5
Ho	41.6	1.8	38.3	7.9	482.5	0.5	449.0	7.5
Er	42.4	2.1	38.0	10.5	499.2	0.9	455.0	9.7
Tm	40.9	1.7	36.8	10.0	471.6	0.6	435.0	8.4
Yb	42.7	2.2	39.2	8.1	496.9	0.9	450.0	10.4
Lu	41.4	2.1	37.0	10.6	485.6	0.6	439.0	10.6
Hf	40.2	2.1	36.7	8.7	468.3	1.0	435.0	7.7
Ta	43.6	1.8	37.6	13.8	533.1	0.5	446.0	19.5
Pb	40.0	1.9	38.6	3.6	440.1	0.8	426.0	3.3
Th	41.2	2.1	37.8	8.3	485.4	0.6	457.2	6.2
U	38.9	1.9	37.4	3.8	466.2	0.7	461.5	1.0

## Chapter 6 – Supplementary Data Tables

*Supplementary Data Table 6.3 – Trace element data of the reference sample BHVO2G. Values are given in ppm.*

Element	BHVO2G		
	Average (n = 13)	Literature value	Relative error (%)
Na	17635	17805	1.0
Mg	44078	43001	2.5
Al	73027	71978	1.5
Si	241422	230448	4.8
Ca	82522	81476	1.3
Sc	32.0	33.0	3.0
Ti	17360	16300	6.5
V	323	308	4.9
Cr	327	293	11.5
Mn	1352	1317	2.7
Fe	88463	87836	0.7
Co	46.4	44.0	5.4
Ni	139	116	19.8
Cu	168	127	32.7
Zn	99	102	3.4
Ga	22.5	22.0	2.4
Rb	9	9	1.0
Sr	403	396	1.7
Y	25.6	26.0	1.4
Zr	170	170	0.2
Nb	18.3	18.3	0.1
Mo	4.2	3.8	10.9
Cs	0.1	0.1	11.1
Ba	133.5	131.0	1.9
La	15.1	15.2	0.7
Ce	38.1	37.6	1.2
Pr	5.3	5.4	0.7
Nd	24.9	24.5	1.8
Sm	6.2	6.1	1.6
Eu	2.0	2.1	2.6
Gd	6.3	6.2	2.1
Tb	0.9	0.9	0.3
Dy	5.4	5.3	3.0
Ho	1.0	1.0	0.2
Er	2.6	2.6	2.0
Tm	0.3	0.3	5.6
Yb	2.0	2.0	1.9
Lu	0.3	0.3	0.9
Hf	4.5	4.3	4.0
Ta	1.2	1.2	1.7
Pb	1.8	1.7	6.6
Th	1.2	1.2	1.5
U	0.4	0.4	6.0



## CHAPTER 7

### *Discussion, Outlook and Conclusion*

---



*Photograph shows a polar bear that looks into the future. ([https://cdn-images-medium.com/max/1200/1\\*99Uumr75xSMSFGU0k296oQ.jpeg](https://cdn-images-medium.com/max/1200/1*99Uumr75xSMSFGU0k296oQ.jpeg))*

## 7.1 Introduction

This thesis aims to better understand the processes that lead to the geochemical and isotopic diversity observed in MORBs. As addressed in the introduction, the chemistry of MORBs depends on its source, the degree of magmatic differentiation and wall-rock interaction. Two main aspects were addressed in this thesis, namely the source composition and the magmatic differentiation. In the following, I will synthesize the findings of the individual research chapters (chapters 3 – 6) and briefly discuss the implications for our general understanding of MORB formation. The discussion is therefore divided into two parts. Part I addresses recycling process within the upper mantle that create chemical and isotope distinct mantle domains, and part II focusses on the magmatic evolution of MORBs at ultraslow spreading ridges. All findings have been schematically summarized in Figure 7.1.

### ***PART I: Mantle heterogeneity reflected by radiogenic isotopes of MORBs***

Based on Pb and Sr isotopes (Goldstein et al., 2008), the Gakkel Ridge has been divided into two different regions, the Western Gakkel Ridge region (chapter 3), comprised of the Western Volcanic Zone and the Sparsely Magmatic Zone, and the Eastern Gakkel Ridge region, which comprises the EVZ (chapter 4). Basalts from both regions display elevated  $^{87}\text{Sr}/^{86}\text{Sr}$  and  $^{208}\text{Pb}/^{204}\text{Pb}$  isotope signatures akin to Indian-type mantle signature. Basalts from the Western Gakkel Ridge region inherit chemical characteristics of a subduction modified mantle. The latter is linked to a subduction event that occurred in the area 140 – 120 Ma ago, the conclusion based on palaeogeographic reconstructions (Alvey et al., 2008; Shephard et al., 2013) and is supported by seismic interpretations (Sokolov and Mazarovich, 2016) in the circumpolar region. Contrary to this, the mantle beneath the Eastern Gakkel Ridge region appears to have been polluted by a similar event, but at a different time. Osmium, Hf and Pb isotope studies on mineral separates from abyssal peridotites suggest that the mantle in the Eastern Gakkel Ridge region has been affected by a depletion event at ~2 Ga (Liu et al., 2008; Stracke et al., 2011; Warren and Shirey, 2012).

The result from both chapters indicate that evidence for the geological events, which polluted the mantle can survive in the upper mantle for up to 2 Ga, and can be the cause for distinct isotopic signatures in basalts sourced from such a mantle (Indian-type mantle signature).

#### ***7.1.1 Mantle convection and chemical heterogeneity***

Geochemically diverse mantle domains are interpreted to be the result of recycling processes into the mantle (Hofmann, 2014; White, 2015), which creates heterogeneities that range from thousands of kilometres (Hart, 1984; e.g., Meyzen et al., 2007) to that on a sub-kilometre scale (Agranier et al., 2005; Graham et al., 2006; e.g., Shirey et al., 1987; e.g., Standish et al., 2008).

Widom (2006) expressed that “*the precise nature of this recycling process, including the ultimate fate of recycled crust and its influence on the evolution of Earth’s upper mantle remains unclear*” and Hofmann (2007) raises the following questions: “*What happens to the recycled oceanic crust? What happens when subduction ceases? Is it hidden somewhere beneath a continent or homogenised within the ambient mantle?*”. At present, only a few studies have traced subduction modified mantle in MORBs (Andersen et al., 2015; Elliott et al., 2006), which provides a glimpse into what happens in the upper mantle after subduction ceased. However, most of the questions raised by Hofmann (2007) remain unanswered, which is partly due to lack of samples recording such geological events (Brunelli et al., 2018).

The findings from the Western and the Eastern Gakkel Ridge region presented in this thesis provide additional insights into the recycling processes. Element concentration and isotope ratios in basalts from the Western Gakkel Ridge resemble the chemistry of a rear-arc and back-arc (Figures 3.2 and 3.4), suggesting that these basalts sample remnants of a fossil subduction zone, most likely that of a metasomatised mantle wedge (Figure 3.3). Recent subduction zone models indicate that mélangé diapirs rise as blobs into the mantle wedge (Figure 3.3), where arc rocks originate from (Marschall and Schumacher, 2012; Nielsen and Marschall, 2017; Spandler and Pirard, 2013). After subduction ceases, the cold slab material sinks into the deeper mantle, which can then be detected by seismic tomography (e.g., Shephard et al., 2016; Sokolov and Mazarovich, 2016). Conversely, the metasomatically enriched (mélangé diapir) mantle wedge remains stagnant in the upper mantle due to its lower density compared to the ambient mantle. In case of the Gakkel Ridge, between subduction cessation at ~125 Ma (Figure 3.3) and the opening of the ridge occurring at around 50 Ma (Blythe and Kleinspehn, 1998), this mélangé diapir was sheared and integrated into the source of the basalts from the WVZ and the SMZ. These findings suggest a time span of 100 Ma between the commencement of subduction and the switch to divergent tectonics is insufficient to fully integrate a mélangé diapir into the ambient mantle through mantle convection. Instead it is preserved as a large-scale heterogeneity that can be sampled by ocean floor basalts.

In contrary to the findings from the Western Gakkel Ridge region, the Eastern Gakkel Ridge (chapter 4) region is extremely heterogeneous on the scale of km to mm- (Shaw et al., 2010; Wanless et al., 2014). Isotope studies show that the Eastern Volcanic Zone partially represents an ancient mantle of >2.0 Ga (Liu et al., 2008; Stracke et al., 2011; Warren and Shirey, 2012). These parts represent refractory mantle domains that experienced multiple depletion and enrichment events and reside within the upper mantle (Byerly and Lassiter, 2014; Liu et al., 2008). As discussed in chapter 4, these refractory mantle domains do not contribute to the chemical variety of MORBs, which could be either due to that the mantle components are too refractory (Byerly and Lassiter, 2014), or they are volumetrically too small to contribute to the larger scale MORB chemistry. Additionally, elevated Sr and Pb isotopes (in comparison to Atlantic/Pacific MORBs;

Supplementary Figure 4.2) suggest that a similar pollution event, as in the Western Gakkel Ridge region, occurred at a different time and affected the mantle in the Eastern Gakkel Ridge region. At present this pollution can be traced by Sr and Pb isotopes over a larger time-scale.

To conclude, the combined results show that large-scale homogenisation of the mantle requires large time spans (~2 Ga). Nonetheless, I conclude that smaller-scale heterogeneities can be preserved as metasomatically enriched domains and locally contribute to chemical variability in MORBs.

### ***7.1.2 Indian-type mantle/DupAl anomaly and other complexities***

As addressed in chapter 1, the Indian-type mantle signature in ocean floor basalts is characterized by elevated Th/U (high  $^{208}\text{Pb}/^{204}\text{Pb}$ ) and radiogenic Sr isotope ratios. These elevated isotope ratios can only be obtained by a source that became enriched in Th, Sr and Rb (= parent nuclide of  $^{87}\text{Sr}$ ), which results in a higher radiogenic isotope signature over time due to radioactive decay of the parent isotope. Different theories exist explaining the Indian-type mantle isotope signatures. It is possible that subcontinental lithospheric or plume-infused mantle becomes integrated into the MORB source, which results in elevated radiogenic Sr and Pb isotope signatures (e.g., Goldstein et al., 2008; le Roux et al., 2002; Mahoney et al., 1989). A further model suggests that recycled oceanic crust is a cause for an Indian-type mantle signature (Rehkämper and Hofmann, 1997).

The former scenario has been proposed for the Gakkel Ridge (Goldstein et al., 2008). In contrast, the findings from chapters 3 and 4 suggests an alternative model for distinct radiogenic isotope signatures at the Gakkel Ridge. Element enrichment (Ba, Sr, Th; Figures 3.2 and 3.4; Supplementary Figures 3.1 – 3.3) and depletion patterns (Zr/Nb; Supplementary Figure 3.1b) favour the existence of a metasomatic enriched mantle domain underlying the Western Gakkel Ridge and causing the Indian-type mantle signature in the basalts. In this model mantle enrichment took place by Si-rich fluids, transporting mobile elements (Ba, Sr, Th) originating from a subducting oceanic crust (Figures 3.3). The excess Th decayed over time to  $^{208}\text{Pb}$  and caused a higher  $^{208}\text{Pb}/^{204}\text{Pb}$  (Th/U; Figure 3.4).

This model could also be applied elsewhere, where elevated  $^{208}\text{Pb}/^{204}\text{Pb}$  and  $^{87}\text{Sr}/^{86}\text{Sr}$  have been observed. Examples are the Australian Antarctic Discordance, a seafloor depression along the Southeast Indian ridge between Antarctica and Australia, which has previously been linked to fossil subduction zone at around 130 Ma (Gurnis and Müller, 2003), or in back-arc lavas along the Western Pacific plate margin (Nebel et al., 2007), which are related to an active subduction zone. In both cases metasomatized mantle would explain the observed isotope ratios.

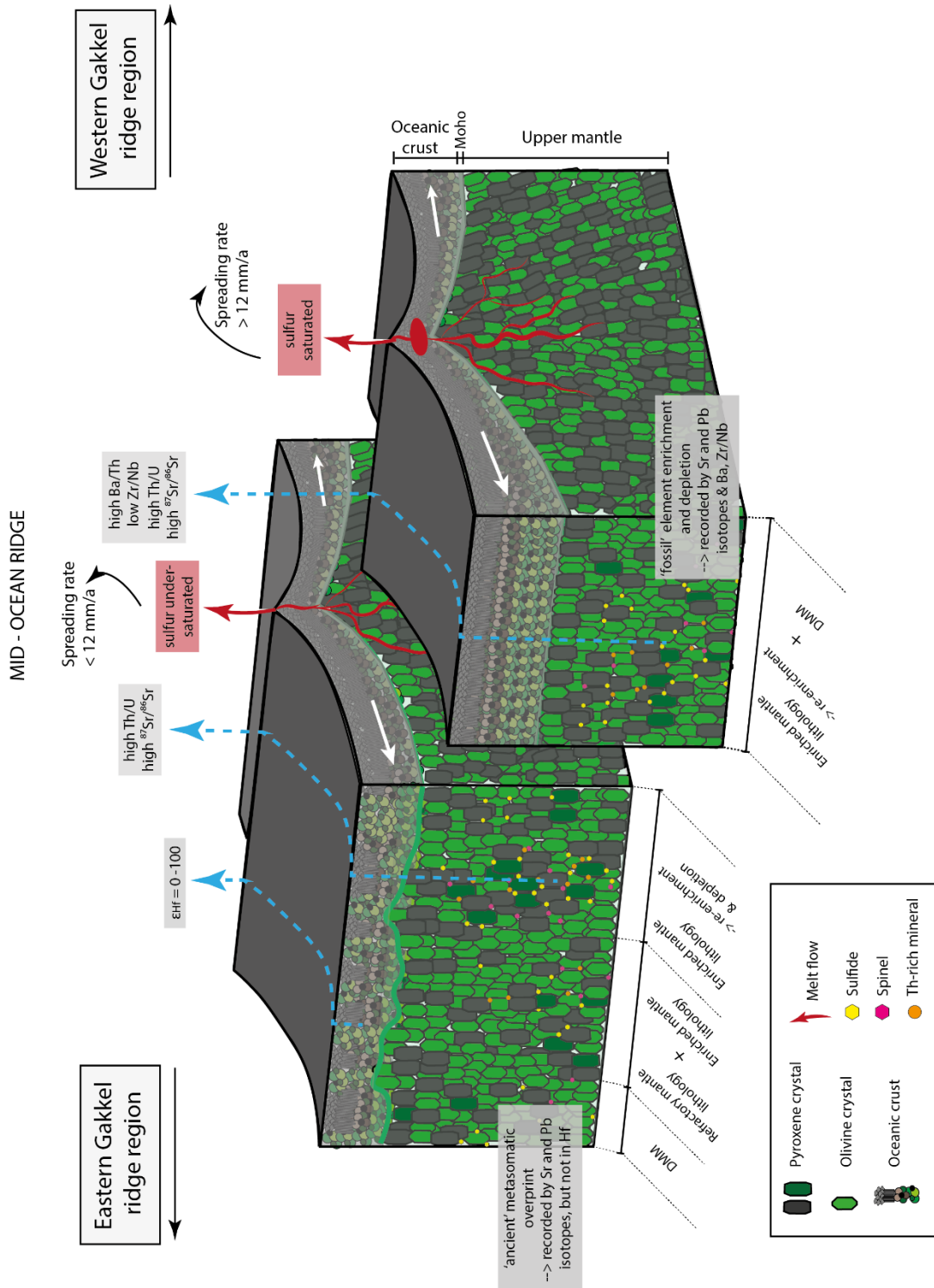


**Figure 7.1 – Schematic overview of all findings from this thesis.** The sketch illustrated two cross-sections of a MORB representing two different melt migrations paths (left: direct magma ascend; right: melt migration through mid-crustal magma chamber). Magma that erupts directly from its source region appears sulfur-undersaturated and is commonly found at spreading rate <math>< 12 \text{ mm/a}</math>, whereas magma that migrates through a magma lens/chamber is sulfur-saturated and commonly found at spreading rates > 12mm/a, as defined here. In addition, the heterogeneity of the upper mantle is highlighted by different phases and its crystal size is exaggerated. Areas showing sulfide, spinel and Th-rich minerals represent the metasomatic enriched domains in the mantle. Melting (blue dotted line) these enriched areas results in elevated Sr and Pb isotope signatures (high Th/U). Area with almost no additional mineral phases represent solely the depleted MORB mantle (DMM). On this note, the model on the left also shows in parts oceanic crust, but is in parts interrupted, representing outcropping abyssal peridotites. Furthermore, the crustal thickness of the left and right model is different, defining the characteristics of ultraslow spreading ridge (left) and slow spreading ridge (right).

## ***PART II: Magmatic differentiation in MORBs***

Only few studies have addressed the iron isotope systematics of ocean floor lavas from spreading ridges (Nebel et al., 2018; Sossi et al., 2016; Teng et al., 2013), but all show a large range in isotopic compositions (0.5 ‰ range in arc lavas, Foden et al. (2018); 0.4 ‰ in back-arc basin lavas, Nebel et al. (2018), and 0.2 ‰ in MORBs, Teng et al. (2013). Since these large isotopic ranges in MORBs cannot only be attributed to fractionation, compositional variation of the source must have a strong control on iron isotopes too. It is however unclear to which extent a heterogeneous mantle contributes to iron isotopic variations in MORBs.

The presented iron isotope data in conjunction with trace element data suggests two distinct magmatic differentiation patterns in basalts from the Gakkel Ridge (rapid ascent versus temporary storage in magma chambers), which show different effects of the mantle source on iron isotopic variation. Here,  $\Delta^{57}\text{Fe}$  ( $\Delta^{57}\text{Fe} = \delta^{57}\text{Fe} - \delta^{57}\text{Fe}_{\text{prim}}$ ) is used as a proxy for the degree of isotopic fractionation that occurs between the source ( $\delta^{57}\text{Fe}_{\text{prim}}$ ) *en route* to surface ( $\delta^{57}\text{Fe}$ ). Rapid ascent from the source region to the crust (Figures 5.6 and 7.1 left), which is typical for ultraslow spreading ridges with spreading rates  $< 12$  mm/a, is characterised by basalts with primitive melt composition (Figure 5.5) and little isotopic fractionation ( $\Delta^{57}\text{Fe} < 0.04$  ‰, Figures 5.1 and 5.5). The iron isotope composition of these basalts show a broad range in  $\delta^{57}\text{Fe}_{\text{prim}}$  suggesting that the chemistry of the basalt from ultraslow spreading ridges are mainly defined by their mantle source. In contrary to this, magma that rises from its source region through the magma chamber *en route* to surface (Figures 5.6 and 7.1 right), typical for slow spreading ridges with spreading rate  $> 12$  mm/a, are more evolved (Figure 5.5) and much stronger affected by fractionation with  $\Delta^{57}\text{Fe} > 0.04$  ‰ (Figures 5.1 and 5.5). The chemistry of these basalts is more defined by crystal fractionation and magma mixing than the mantle source, which is partially reflected in a lower variability of  $\delta^{57}\text{Fe}$  (Figure 5.4).

These observations are in line with platinum group element systematics (Chapter 6). Platinum group elements are highly siderophile elements with a chalcophile character and are divided into two sub-groups: I-PGE (Ir, Os, Ru) and P-PGE (Pd, Pt). In general, I-PGE are more compatible and preferentially remain in the mantle during partial mantle melting compared to P-PGE (Bézos et al., 2005; Lorand et al., 2008). Data show that with increasing magmatic differentiation ( $\Delta^{57}\text{Fe} = 0.01 - 0.04$  ‰), I-PGE concentration in basalts increases, represented by basalts from the SMZ and the WVZ (Figure 6.7), and then decreases with continuous differentiation ( $\Delta^{57}\text{Fe} > 0.04$  ‰), mainly represented by basalts from the WVZ (Figure 6.7). The turning point is in line with a dramatic drop in Cu concentration (Figure 6.7c), suggesting that at  $\Delta^{57}\text{Fe} = 0.04 \pm 0.005$  ‰ sulfide saturation is reached. At sulfide saturation, sulfides start to segregate out and incorporate Cu due to its strong chalcophile affinities. This process is reflected by a sudden drop in Cu. In case of the Gakkel Ridge, the data suggests that these processes occur within a magma chamber, which also leads to the conclusion that basaltic melts that migrate *en route* to surface

through magma chambers become sulfide saturated, which is shown in the WVZ basalts (Figure 6.8). Magma that rapidly ascends from the upper mantle source to the crust without any interaction in magma pools are sulfide undersaturated, as represented by basalts from the SMZ and the EVZ.

This finding is in contrast to previous studies which suggested that MORBs form under sulfide saturated conditions (Li and Ripley, 2005; Reekie et al., 2019; Smythe et al., 2017) and only a few suggested MORBs are sulfide undersaturated and then become sulfide saturated (Reekie et al., 2019). My findings suggest that the ascending melt is sulfide undersaturated and stays sulfur-undersaturated if the magma rises rapidly from the source region to crust, because crystal fractionation is not as effective to change the sulfur content of a MORB. However, if the melt ascends through a magma chamber, in which crystal fractionation effects positively the sulfur content of the magma, then the magma becomes sulfide saturated.

In conclusion, Fe isotope systematics can be used as a tool to define different magmatic evolutions (directly or interactions with mid-crustal magma chambers) in ocean floor basalts, and shows that Fe isotope variabilities in MORBs is affected by the mantle source, which in turn affects the chemistry of the basalts. In conjunction with PGE systematics, the geochemical behaviour of I-PGE and P-PGE can reveal insights into sulfide saturation process in MORBs.

## 7.2 Outlook

Further research should test the hypotheses, how a mélangé diapir can survive in the upper mantle and its effect on the chemical composition of MORBs with respect to its isotope geochemistry; and/or how to form sulfide undersaturated basaltic melts. To find answers for some of these questions an interdisciplinary approach using geodynamic modelling, experimental petrology and isotope geochemistry needs to be applied.

Geodynamic modelling: To test the concept of mantle convection and the development of the upper mantle after subduction ceased, a simple 2D subduction zone model could be developed to further understand the movement of a mélangé diapir/mantle wedge in the upper mantle after slab break-off/subduction cessation.

Experimental petrology: High-pressure and high-temperature experiments could be conducted using different raw materials and changing pressure conditions to experimentally test different melting mechanism, the likelihood of pyroxenite in the source of MORBs and the sulfide saturation in ocean floor lavas.

Isotope geochemistry: Further iron isotope analysis of ocean floor basalts of known source composition (e.g., the East Pacific Rise, the Australian Antarctic Discordance and the Southwest Indian Ridge) could be used to better define the iron isotope variability related to mantle source. Other areas, such as the Southwest Indian Ridge, Central Indian Ridge or South Atlantic ridge can

be targeted to refine magma differentiation processes, with respect to magma chamber processes in MORBs, at spreading rates  $> 15$  mm/a.

Petrology (Gakkel Ridge): To better define the mantle heterogeneity at the Gakkel Ridge, dredged abyssal peridotites from the entire ridge could be mapped and linked to the MORB chemistry to (a) obtain a better overview of the mantle heterogeneity at the Gakkel Ridge and (b) to investigate the relationship between abyssal peridotites and MORBs, because it is thought that abyssal peridotites represent the residue of the MORBs.

### 7.3 Conclusion

This thesis investigates the geochemistry of MORBs from the ultraslow-spreading Gakkel Ridge in the Arctic Ocean to understand geochemical diversity in MORBs. Two different aspects were investigated: (1) source heterogeneity and (2) magmatic differentiation.

To investigate the source composition of the underlying mantle, radiogenic isotope (Pb, Sr, Hf) signatures were linked with trace element systematics and showed that the upper mantle records elemental signatures of fossil (125 Ma) and ancient ( $\sim 2$  Ga) geological events that chemically overprinted the pre-existing mantle composition. Mantle convection slowly integrates these enriched domains, over a time span of  $> 2$  Ga, into the ambient mantle, creating large- and small-scale heterogeneities. The heterogeneous mantle domains can be inherited in upwelling mantle beneath the mid-ocean ridge, creating chemical variety in ocean floor basalts, as discussed with respect to Fe isotope systematics.

Iron isotope signatures and platinum group element concentrations have been used to define two different paths along which magma can ascend, either directly (represented by basalts from the SMZ and the EVZ) or through a magma chamber (as represented by basalts from the WVZ). Magma that rises rapidly from the source region to the crust is commonly observed at ultraslow spreading ridges with a spreading rate  $< 12$  mm/a. The data obtained in this study shows that the chemistry of basalts are mainly affected by their heterogeneous mantle source rather than crystal fractionation, and appear sulfur-undersaturated. On the other hand, magma that migrates through mid-crustal magma chambers *en route* to the surface, tends to be sulfur-saturated and the chemistry is more affected by crystal fractionation than by the heterogeneous source, because of magma replenishment and magma mixing processes in mid-crustal magma chambers. These processes are common at faster spreading rate  $> 12$  mm/a.

Besides these findings, this thesis contributes to the understanding of mantle heterogeneity (DupAl signature) and mantle convection, Fe isotope systematics, and sulfur concentration in MORB. A summary of the key findings is presented below:

- (1) Subduction modified mantle survives in the upper mantle for more than 125 Ma, creating large-scale mantle heterogeneities that can affect the chemistry of ocean floor basalts, as shown by basalts from the Western Gakkel Ridge region (Chapter 3).
- (2) An alternative model that subduction-modified (metasomatised) mantle is the origin for elevated  $^{208}\text{Pb}/^{204}\text{Pb}$  and  $^{87}\text{Sr}/^{86}\text{Sr}$  (Indian-type mantle signature/DupAl isotope signature) isotope signatures in ocean floor lavas has been suggested.
- (3) Iron isotopes systematics can be used to detect differences within magma differentiation.
- (4) Geochemical behaviour of I-PGE can be used as tool to differentiate whether basaltic magma is sulfur-undersaturated or sulfur-saturated

To conclude, the geochemistry of MORBs is in fact dependent on a variety of factors such as the heterogeneity of the mantle source, degree of melting and fractional crystallization. None of these processes solely define the erupting basalt chemistry and cannot be viewed in isolation. With the development of new analytical methods and the improvement of technology in various fields of geosciences, further findings will shed more light into the formation of ocean floor basalts and recycling processes within the Earth's mantle.

## 7.4 References

- Agranier, A. et al., 2005. The spectra of isotopic heterogeneities along the mid-Atlantic Ridge. *Earth and Planetary Science Letters*, 238(1): 96-109.
- Alvey, A., Gaina, C., Kuszniir, N.J., Torsvik, T.H., 2008. Integrated crustal thickness mapping and plate reconstructions for the high Arctic. *Earth and Planetary Science Letters*, 274(3-4): 310-321.
- Andersen, M.B. et al., 2015. The terrestrial uranium isotope cycle. *Nature*, 517(7534): 356-9.
- Bézos, A., Lorand, J.P., Humler, E., Gros, M., 2005. Platinum-group element systematics in Mid-Oceanic Ridge basaltic glasses from the Pacific, Atlantic, and Indian Oceans. *Geochimica et Cosmochimica Acta*, 69(10): 2613-2627.
- Blythe, A.E., Kleinspehn, K.L., 1998. Tectonically versus climatically driven Cenozoic exhumation of the Eurasian plate margin, Svalbard: Fission track analyses. *Tectonics*, 17(4): 621-639.
- Brunelli, D., Cipriani, A., Bonatti, E., 2018. Thermal effects of pyroxenites on mantle melting below mid-ocean ridges. *Nature Geoscience*, 11(7): 520-525.
- Byerly, B.L., Lassiter, J.C., 2014. Isotopically ultradepleted domains in the convecting upper mantle: Implications for MORB petrogenesis. *Geology*, 42(3): 203-206.
- Elliott, T., Thomas, A., Jeffcoate, A., Niu, Y., 2006. Lithium isotope evidence for subduction-enriched mantle in the source of mid-ocean-ridge basalts. *Nature*, 443(7111): 565-8.
- Foden, J., Sossi, P.A., Nebel, O., 2018. Controls on the iron isotopic composition of global arc magmas. *Earth and Planetary Science Letters*, 494: 190-201.
- Goldstein, S.L. et al., 2008. Origin of a 'Southern Hemisphere' geochemical signature in the Arctic upper mantle. *Nature*, 453(7191): 89-93.
- Graham, D.W., Blichert-Toft, J., Russo, C.J., Ruben, K.H., Albarede, F., 2006. Cryptic striations in the upper mantle revealed by hafnium isotopes in southeast Indian ridge basalts. *Nature*, 440(7081): 199-202.
- Gurnis, M., Müller, R.D., 2003. Origin of the Australian–Antarctic Discordance from an ancient slab and mantle wedge. In: Hillis, R.R., Müller, R.D. (Eds.), *Evolution and Dynamics of the Australian Plate*. Geological Society of America.
- Hart, S.R., 1984. A large-scale isotope anomaly in the Southern Hemisphere mantle. *Nature*, 309(5971): 753-757.
- Hofmann, A.W., 2007. The lost continents. *Nature*, 448: 655.
- Hofmann, A.W., 2014. Sampling Mantle Heterogeneity through Oceanic Basalts: Isotopes and Trace Elements. *Treatise on geochemistry*: 67-101.
- le Roux, P.J. et al., 2002. Mantle heterogeneity beneath the southern Mid-Atlantic Ridge: trace element evidence for contamination of ambient asthenospheric mantle. *Earth and Planetary Science Letters*, 203(1): 479-498.
- Li, C., Ripley, E.M., 2005. Empirical equations to predict the sulfur content of mafic magmas at sulfide saturation and applications to magmatic sulfide deposits. *Mineralium Deposita*, 40(2): 218-230.
- Liu, C.Z. et al., 2008. Ancient, highly heterogeneous mantle beneath Gakkel Ridge, Arctic Ocean. *Nature*, 452(7185): 311-6.
- Lorand, J.P., Luguet, A., Alard, O., 2008. Platinum-Group Elements: A New Set of Key Tracers for the Earth's Interior. *Elements*, 4(4): 247-252.
- Mahoney, J.J. et al., 1989. Isotopic and geochemical provinces of the western Indian Ocean Spreading Centers. *Journal of Geophysical Research: Solid Earth*, 94(B4): 4033-4052.
- Marschall, H.R., Schumacher, J.C., 2012. Arc magmas sourced from mélange diapirs in subduction zones. *Nature Geoscience*, 5(12): 862-867.
- Meyzen, C.M. et al., 2007. Isotopic portrayal of the Earth's upper mantle flow field. *Nature*, 447(7148): 1069-74.
- Nebel, O. et al., 2007. Hf–Nd–Pb isotope evidence from Permian arc rocks for the long-term presence of the Indian–Pacific mantle boundary in the SW Pacific. *Earth and Planetary Science Letters*, 254(3-4): 377-392.
- Nebel, O. et al., 2018. Iron isotope variability in ocean floor lavas and mantle sources in the Lau back-arc basin. *Geochimica et Cosmochimica Acta*, 241: 150-163.
- Nielsen, S.G., Marschall, H.R., 2017. Geochemical evidence for mélange melting in global arcs. *Science Advances*, 3(4).
- Reekie, C.D.J. et al., 2019. Sulfide resorption during crustal ascent and degassing of oceanic plateau basalts. *Nature Communications*, 10(1): 82.
- Rehkämper, M., Hofmann, A.W., 1997. Recycled ocean crust and sediment in Indian Ocean MORB. *Earth and Planetary Science Letters*, 147(1–4): 93-106.

- Shaw, A.M., Behn, M.D., Humphris, S.E., Sohn, R.A., Gregg, P.M., 2010. Deep pooling of low degree melts and volatile fluxes at the 85°E segment of the Gakkel Ridge: Evidence from olivine-hosted melt inclusions and glasses. *Earth and Planetary Science Letters*, 289(3-4): 311-322.
- Shephard, G.E., Müller, R.D., Seton, M., 2013. The tectonic evolution of the Arctic since Pangea breakup: Integrating constraints from surface geology and geophysics with mantle structure. *Earth-Science Reviews*, 124: 148-183.
- Shephard, G.E., Trønnes, R.G., Spakman, W., Panet, I., Gaina, C., 2016. Evidence for slab material under Greenland and links to Cretaceous High Arctic magmatism. *Geophysical Research Letters*, 43(8): 3717-3726.
- Shirey, S.B., Bender, J.F., Langmuir, C.H., 1987. Three-component isotopic heterogeneity near the Oceanographer transform, Mid-Atlantic Ridge. *Nature*, 325: 217.
- Smythe, D.J., Wood, B.J., Kiseeva, E.S., 2017. The S content of silicate melts at sulfide saturation: New experiments and a model incorporating the effects of sulfide composition. *American Mineralogist*, 102(4): 795-803.
- Sokolov, S.Y., Mazarovich, A.O., 2016. Cluster analysis of geological and geophysical parameters of the Arctic region as the base for geodynamic interpretation. *Geodynamics & Tectonophysics*, 7(1): 59 - 83.
- Sossi, P.A., Nebel, O., Foden, J., 2016. Iron isotope systematics in planetary reservoirs. *Earth and Planetary Science Letters*, 452: 295-308.
- Spandler, C., Pirard, C., 2013. Element recycling from subducting slabs to arc crust: A review. *Lithos*, 170-171: 208-223.
- Standish, J.J., Dick, H.J.B., Michael, P.J., Melson, W.G., O'Hearn, T., 2008. MORB generation beneath the ultraslow spreading Southwest Indian Ridge (9-25°E): Major element chemistry and the importance of process versus source. *Geochemistry, Geophysics, Geosystems*, 9(5): Q05004.
- Stracke, A. et al., 2011. Abyssal peridotite Hf isotopes identify extreme mantle depletion. *Earth and Planetary Science Letters*, 308(3-4): 359-368.
- Teng, F.-Z., Dauphas, N., Huang, S., Marty, B., 2013. Iron isotopic systematics of oceanic basalts. *Geochimica et Cosmochimica Acta*, 107: 12-26.
- Wanless, V.D., Behn, M.D., Shaw, A.M., Plank, T., 2014. Variations in melting dynamics and mantle compositions along the Eastern Volcanic Zone of the Gakkel Ridge: insights from olivine-hosted melt inclusions. *Contributions to Mineralogy and Petrology*, 167(5).
- Warren, J.M., Shirey, S.B., 2012. Lead and osmium isotopic constraints on the oceanic mantle from single abyssal peridotite sulfides. *Earth and Planetary Science Letters*, 359-360: 279-293.
- White, W.M., 2015. Isotopes, DUPAL, LLSVPs, and Anekantavada. *Chemical Geology*, 419: 10-28.
- Widom, E., 2006. Lost lithium found. *Nature*, 443: 516.

*“The more I learn, the more I realize how much I don't know.”*  
*(Albert Einstein)*

THE END.